CHARACTERIZATION OF FAILURE OF COMPOSITE STRIPS AND SINGLE FIBERS UNDER EXTREME TRANSVERSE LOADING

by

Jinling Gao

A Dissertation

Submitted to the Faculty of Purdue University

In Partial Fulfillment of the Requirements for the degree of

Doctor of Philosophy

School of Aeronautics & Astronautics

West Lafayette, Indiana

August 2021

THE PURDUE UNIVERSITY GRADUATE SCHOOL
STATEMENT OF COMMITTEE APPROVAL

Dr. Weinong Wayne Chen, Chair
School of Aeronautics and Astronautics

Dr. James F. Doyle
School of Aeronautics and Astronautics

Dr. Christopher J. Gilpin
College of Agriculture Administration

Dr. Chelsea Davis
School of Materials Engineering

Dr. Tyler N. Tallman
School of Aeronautics and Astronautics

Approved by:
Dr. Gregory Blaisdell

To all the people appearing in my life.

ACKNOWLEDGMENTS

First, I would like to express my great gratitude to my advisor Weinong (Wayne) Chen for bringing me into Purdue and his research group. This is a big step for me, which changes my mind towards research and my life. Professor Chen has been providing me with a stable platform that allows me to focus on the research progress. He trained me to run experiments, write papers, and make slides for presentations. He placed me in a collaborated project with many researchers from leading universities and institutions and have a solid background in composites' dynamic behaviors. This is significantly beneficial for me to identify the cutting-edge research in the area, learn how to collaborate with people, present to people professionally, and look at a problem from different angles. Professor Chen also trained me to review papers, write proposals, and complete other professional activities as a professor. In addition, he shared with me many tips to face possible challenges in the future. Besides, I really like to talk with Professor Chen since he can illustrate a problem in a way that is very easy to understand and improve my understanding quickly. As an international student, I have been enjoying the life to pursue a Ph.D. degree in Professor Chen's lab at Purdue, and it will be a treasure in my life.

I would also thank Professor James F. Doyle for being one of my committee members. He was really patient and illustrated the difficult concept until I fully understood it. Every time I talked with Professor Doyle, I felt that my scientific understanding of the experimental phenomena improved, and my mechanics background was strengthened. I appreciate Dr. Christopher J. Gilpin's continued support using the micro tensile stage, SEM, and TEM. I also appreciate Professor Tyler N. Tallman for supporting me on composite manufacturing and paper revision. Finally, I would like to thank Professor Chelsea Davis. Although I was not able to work with her to do some experiments on the fiber/matrix interface because of the project requirement, she provided me with the background knowledge, which helped me finish a review paper containing the fiber/matrix interfacial experiments completed by my previous colleagues.

I want to thank all the previous and present members in our lab for the continued help with experiments, discussions, and paper writing and revision. I want to express my special

acknowledgment to Dr. Boon Him Lim and Dr. Nesredin Kedir. Boon Him taught me to use the Kolsky bar, and Nes showed me how to use the gas gun in the lab.

I appreciate Dr. Kamel Fezzaa, Dr. Tao Sun, Dr. Pavel Shevchenko, and Dr. Francesco De Carlo in Argonne National Laboratory for their assistance in the experiments.

I would also like to thank Xiaofan Zhang and Professor Somnath Ghosh from the Johns Hopkins University, Christopher Meyer and Professor Dr. Bazle Haque from the University of Delaware, and Dr. Daniel O'Brien from the U.S. Army Research Laboratory. Exchanging ideas with them can always help me find the method to solve difficult problems.

I really appreciate the understanding and company of my father, Zhongsong Gao, and my mother, Shufeng Zhao, as well as the company of my roommates, relatives, friends, and my cat throughout my Ph.D. study.

This research used resources of the Advanced Photon Source, a U.S. Department of Energy (DOE) Office of Science User Facility operated for the DOE Office of Science by Argonne National Laboratory under Contract No. DE-AC02-06CH11357. Funding for high-speed imaging equipment used in this work was provided by AFOSR Award No. FA9550-16-1-0315 (Dr. Martin Schmidt, Program Officer).

This research was partially funded by US Army PEO Soldier with a grant number W91CRB-14-C-0025. This research was also sponsored by the Army Research Laboratory and was accomplished under Cooperative Agreement Number W911NF-12-2-0022. The views and conclusions contained in this document are those of the authors and should not be interpreted as representing the official policies, either expressed or implied, of the Army Research Laboratory or the U.S. Government. The U.S. Government is authorized to reproduce and distribute reprints for Government purposes notwithstanding any copyright notation herein.

TABLE OF CONTENTS

LIST OF TABLES

LIST OF FIGURES

ABSTRACT

When a composite laminate is transversely impacted by a projectile at the ballistic limit, its failure mode transits from global conical deformation to localized perforation. This Ph.D. dissertation aims to reveal the fundamental material failure mechanism at the ballistic limit to control perforation. First, transverse impact experiments were designed on composite strips to isolate the interaction between plies and tows. Three failure modes were identified, divided by no, partial, and complete failure before the transverse wave deformed the entire composite strip. The failure phenomenon and critical velocity region can differ with the fiber type and projectile nose geometry and dimension. In most impact events, the composite strips all failed in tension in the front of the projectiles, although they failed at different positions as the projectile nose geometry and fiber type changed. A special failure phenomenon was uncovered when the composite strips were impacted onto razor blades above the upper limit of the critical velocity region: the composite strips seemed to be cut through completely by the razor blades. To further investigate the failure by razor blade, a microscopic method was developed to cut a single fiber extracted from the composite strip and simultaneously image the failure process inside a Scanning Electron Microscope (SEM). The experiments revealed that the razor blade cannot cut through the inorganic S-2 glass fibers while can partially incision the aramid Kevlar® KM2 Plus fibers and completely shear through the ultra-high-molecular-weight polyethylene (UHMWPE) Dyneema® SK76 fibers. Further investigations on the fiber's failure under dynamic cut revealed that there was no variation in the failure mode when the cut speed was increased from 1.67 μm/s to ~5.34 m/s. To record the local dynamic failure inside the composite strips and single fibers at high-velocity impact, an advanced imaging technique, high-speed synchrotron X-ray phase-contrast imaging, was introduced, which allows to capture the composite's internal failure with a resolution of up to 1.6 μm/pixel and at a time interval 0.1 μs. Integrated with a reverse impact technique, such an advanced imaging technique is believed to be capable of revealing the mechanism involved in the impact-induced cut in single fibers, yarns, and composite strips. The relevant studies will be the extended work of this Ph.D. dissertation and published in the future.

CHAPTER 1. INTRODUCTION

1.1 FRCs at extreme dynamic environments

Continuous fiber-reinforced polymer matrix composites, or simplified as fiber-reinforced composites (FRCs), open up the great material potential of the high strength and modulus, the excellent penetration resistance and energy absorption capabilities as well as the lightweight characteristics. Beginning in the 1940s, FRCs have been applied as the backing materials of ceramic or metal in ballistic protective equipment such as soft body armor, helmets, and military vehicles and aircraft [1-3]. A typical armor system [4] is schematically illustrated in Figure 1.1. With high hardness and compressive strength, a ceramic tile provides immediate containment of blast fragments and prevention of bullet penetration. An FRC layer serves for secondary energy absorption, spreading the energy from the impact point. However, when the armor system was impacted at a sufficiently high velocity, after the projectile destroys the ceramic tile, the FRC layer can be completely perforated and lose the impact resistance. Therefore, except for the damage resistance to the low-velocity impact, the ballistic performance of the FRCs at extreme impact environments is another critical property in the design of an armor system.

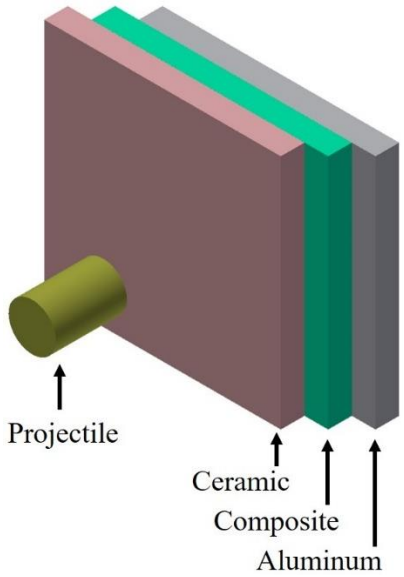

Figure 1.1. Schematic of a typical armor system

1.2 Impact response of an FRC laminate at the ballistic limit

The ballistic limit (V_{50}) is a commonly used parameter to evaluate the ballistic performance of an FRC structure, being defined as a specific impact velocity at which the probability of a projectile halted by the FRC structure is 50% [5]. Previous experimental efforts reveal that the ballistic limit of a composite laminate can be affected by the fiber type [6-10], laminate thickness [11-12], stacking sequence [12-13], weave pattern [14-15] and hybridization [16-19] of the composite, projectile mass [18], size [20], and nose geometry [21], and impact angle [22-23]. The effect of each factor is illustrated below. First, the rapid development of fiber synthesis technology provides high-performance organic and inorganic reinforcements for composite manufacturing. The primary organic fibers include aramid (Kevlar®, Zylon®, Twaron®, Technora®, AuTx®), ultra-high-molecular-weight polyethylene (UHMWPE) (Dyneema®, Spectra®), and Poly (p- phenylene-2, 6-benzobisoxazole), or PBO (Vectran, Zylon®, M5) fibers. On the other hand, glass (S-2, E), ceramic (Nextel, Slyramic), carbon (Celion, Aksaca), carbon nanotube fibers are the inorganic fibers. Although there has been a general rule that fibers with high strength and failure strain and low density are ideal reinforcements for energy absorption, comparing the ballistic limits of the corresponding FRCs are difficult, which is due to the diversity of laminate plane size and thickness, matrix type and projectile employed in different experiments. Secondly, increasing the laminate thickness can significantly increase the ballistic limit of FRCs. Sikarwar et al. [12] reported a 78% increase of V_{50} when the glass/epoxy laminate thickness increased from 1.5 mm to 5 mm. They also found that the laminate with (0/90) lay-up sequences was more effective in impact resistance than other laminates with different stacking sequences such as 0/90/45/-45, 30/-60/60/-30. Yaghoubi et al. [13] impacted GLARE 5 FML plates using 0.22-caliber copper bullets and obtained a higher average ballistic limit for the 0/±45/90 plate than the 0/90 plate. Besides, the effect of weave pattern was examined by Flanagan et al. [14] and Udatha et al. [15], revealing that the ballistic limit of a composite can be slightly increased by weaving the fibers in three dimensions. There has been a considerable number of experimental studies showing that the ballistic limit can be significantly improved by employing hybrid composites [16-18]. An optimal design was proposed to place tough layers such as Kevlar® composites as the backing material of glass or carbon composites [19]. In addition, the impact conditions are also critical factors influencing V_{50}. For example, Pandya et al. [18] impacted the E-glass/epoxy composite by utilizing three right circular cylinders with increasing masses from 3.61 g, 3.83 g, to 6.42 g. The V_{50} of the composite

laminate was uncovered to decrease from 110 m/s, 90 m/s, to 72 m/s. Gellert et al. [20] reported that a 4.5-mm-thickness GFRC's V_{50} decreased from 210 m/s to 175 m/s when the flat-ended cylindrical projectile diameter was reduced from 6.35 mm to 4.76 mm. Ulven et al. [21] utilized a flat, conical, hemispherical, and fragment simulation projectile to impact the carbon/epoxy composite panels with a thickness of 3.2 mm. The corresponding V_{50} was measured to be 91 m/s, 90 m/s, 79 m/s, and 77 m/s, respectively. Zhikharev et al. [22] performed oblique impact experiments on GFRC plates and examined five impact angles of 0°, 15°, 30°, 45°, and 60°. The ballistic limit was measured correspondingly as 290, 295, 300, 314, 378 m/s. An increasing trend of V_{50} against the impact angle was also reported by Xie et al. for CFRCs under oblique impact [23].

With a considerable number of experimental investigations, a detailed description of the penetration and perforation process of a composite laminate was provided by researchers [24-26], schematically illustrated in Figure 1.2. As a generalized illustration, the target is a two-dimensional woven composite, and the projectile is a rigid cylinder with a flat end. As shown in Figure 1.2*a*, the projectile is contacting the composite. Figure 1.2*b* is a planer view of the impact event: the yarns underneath the projectile and along the wrap and fill directions are called primary yarns and referred to region 1, while the remaining yarns in the surrounding region are the secondary yarns and indicated as region 2. The entire failure process of the composite can be divided into three stages. During stage 1 (see Figure 1.2*c*), a compressive and shear stress wave are generated and propagate along the laminate thickness direction. The shear stress wave follows the compressive stress wave. The material below the projectile is compressed with the propagation of the compressive wave. On the other hand, the material surrounding the impact location is also compressed due to the shear stress wave propagating in the in-plane direction. Compression of the laminate also produces in-plane tensile deformation. The material could fail under compression, tension, or shear plugging whenever the induced strains exceed the corresponding failure strains of the composite. Stage 2 starts when the shear stress wave reaches the back surface of the composite laminate, which is shown in Figure 1.2*d*. Depending on the initial kinetic energy available with the projectile and the number of layers that failed in stage 1, the material could be deformed into a conical shape in Figure 1.2*e* or completely fail by shear plugging in Figure 1.2*f*.

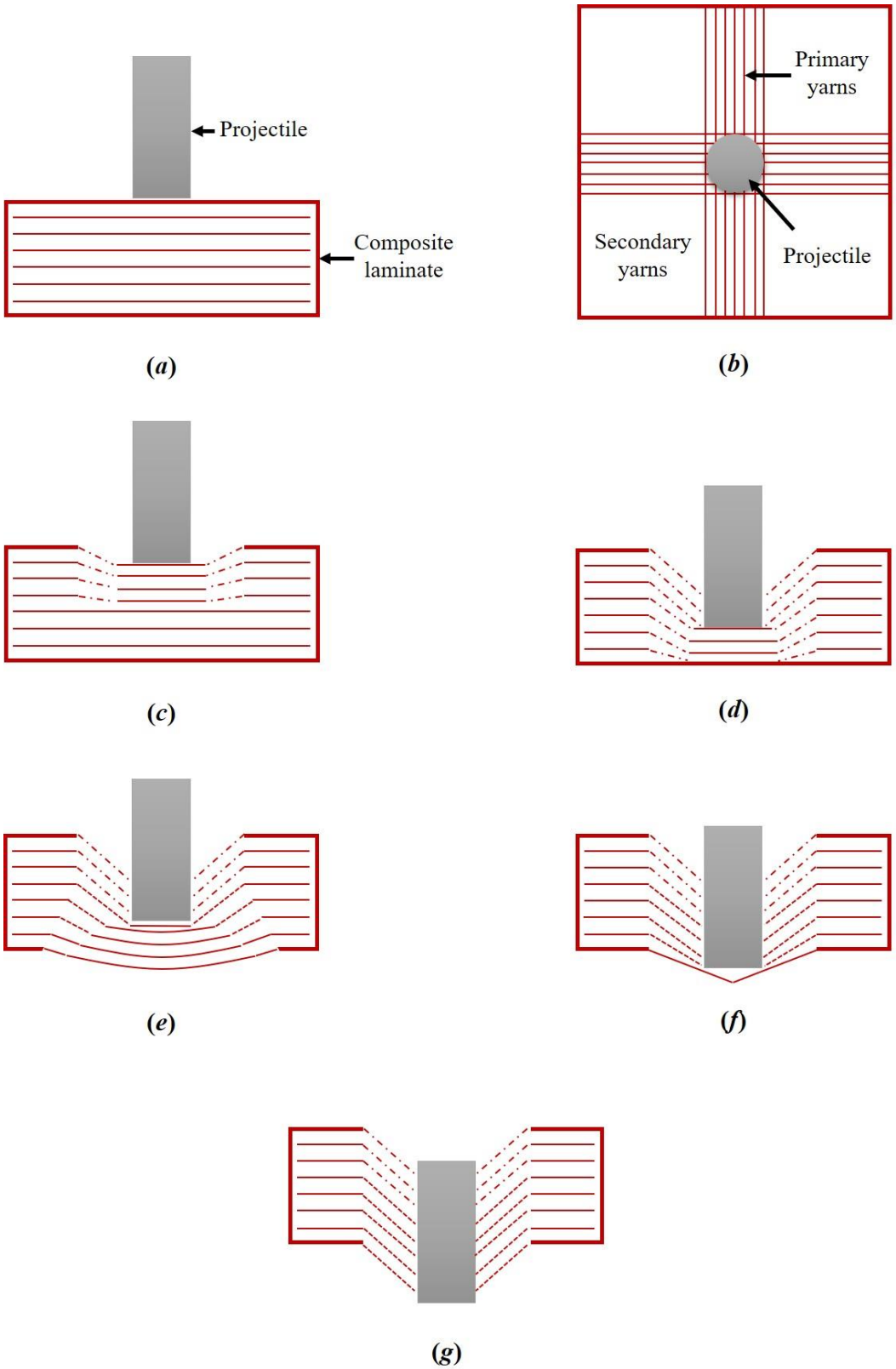

Figure 1.2. Schematic of the penetration and perforation process of the composite laminate.

Stage 3 is counted when the projectile tip perforates through the laminate in Figure 1.2*g*, during which the kinetic energy is dissipated by the projectile/composite friction. It has been identified that during the ballistic impact event, the loss of the projectile's kinetic energy is due to the composite's energy absorption via various deformation and failure mechanism, including the transverse compression below and surrounding the impact region, shear plugging, stretching, and tensile failure of primary and secondary yarns, conical deformation, delamination, matrix cracking, and the projectile/composite friction. However, owing to complicated weaving structures and inter-penetration between plies and tows close to the impact region, the transition from the conical deformation in Figure 1.2*e* to the local perforation in Figure 1.2*f* has not been understood.

1.3 Impact response of a yarn-scale FRC structure

In 2013, Chocron et al. [26] conducted transverse impact experiments on Dyneema® HB90/epoxy strips, isolating the interactions between plies and tows. The global deformation and failure of the composite strips under fragment simulating projectiles (FSPs) were imaged by a high-speed camera. The wave propagation and global material failure in the composite strips were believed to be similar to that in yarns. Therefore, in this section, the mechanical behavior of a yarn under transverse impact was introduced, including the classical Smith's theory to describe the wave propagation and failure in the yarn and the critical factors that influence the yarns' failure and make the Smith's theory overpredict the yarn's impact performance.

1.3.1 Smith's theory

In the 1950s, Smith et al. proposed a one-dimensional (1D) analytical model to describe the wave propagation in a long textile yarn impacted transversely [27]. The theory assumes that the yarn has an infinite length so that there are no clamps to reflect the waves. It also idealizes the yarn to be a 1D wire having the linear elastic stress-strain relation along the longitudinal direction. The dimension and deformation perpendicular to the yarn was ignored. The loading configuration was sketched in Figure 1.3.

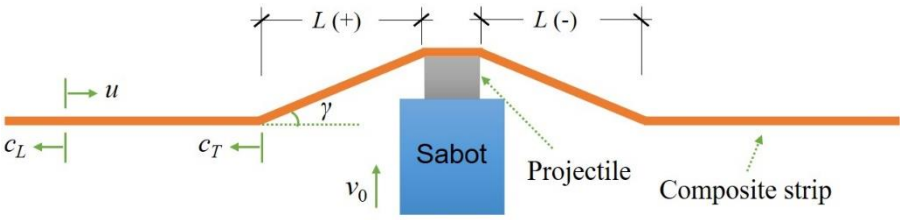

Figure 1.3. Schematic of wave propagation in a yarn.

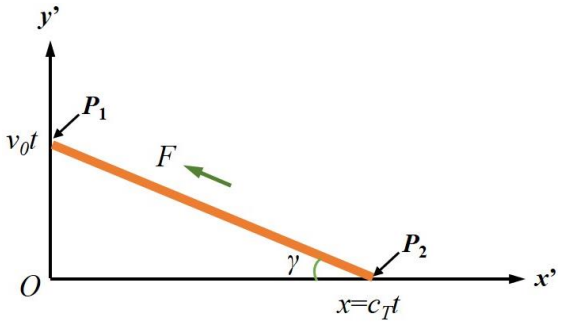

Figure 1.4. Configuration of half of the yarn after impacted by the projectile.

When the yarn contacts an RCC projectile coming with a velocity of v_0, a longitudinal wave is generated at the projectile corner, moving outwards until the end of the yarn with a velocity of c_L. c_L represents the elastic wave speed of the yarn and can be calculated by

$$c_L = \sqrt{\frac{E}{\rho}} \tag{1-1}$$

where E and ρ are the tensile modulus and density of the yarn, respectively. The material behind the wake of the longitudinal wave is set in motion with a particle velocity u, pulling the material towards the impact site. The magnitude of the particle velocity (u) can be calculated by the tensile strain inside the yarn and the longitudinal wave speed according to Eq. (1-2).

$$u = c_L \varepsilon \tag{1-2}$$

On the other hand, a transverse wave is also developed at the time of impact, usually propagating with a much lower velocity c_T described in Eq. (1-3). Materials at the transverse wavefront, previously moving inwards to the projectile after the faster longitudinal wave passes, currently start motion in the direction of the projectile with the impact velocity v_0. The yarn is deformed into a tent shape with a tent angle of γ, which is ideally symmetrical to the projectile axis. Regarding the wave propagation inside the yarn, half of the yarn is selected. A Cartesian coordinate system (x-O-y) is established: the x axis lies along the yarn before impact, and the original point was located at the projectile's corner upon the projectile/yarn contact, which is shown in Figure 1.4. Consider the movement of a point on the yarn before impact. The point was at a distance of x away from the original point. At any time t, the displacement of the point can be represented as

$$x' = x + \xi(x,t) \tag{1-3}$$

$$y' = \eta(x,t) \tag{1-4}$$

Consider an element with an initial length of Δx and studies its deformation. After impact, the element is stretched, and the tensile strain developed inside the element is

$$\varepsilon = \frac{\Delta x' - \Delta x}{\Delta x} = \sqrt{\left(1+\frac{\partial \xi}{\partial x}\right)^2 + \left(\frac{\partial \eta}{\partial x}\right)^2} - 1 \tag{1-5}$$

The angle of the element, which is also the tent angle, can be represented as

$$\cos\gamma = \frac{1}{1+\varepsilon}\left(1+\frac{\partial \xi}{\partial x}\right) \tag{1-6}$$

$$\sin\gamma = \frac{1}{1+\varepsilon}\frac{\partial \eta}{\partial x} \tag{1-7}$$

The equilibrium equations in the x' and y' directions are

$$m\frac{\partial^2 \xi}{\partial t^2} = \frac{\partial}{\partial x}\left(F\cos\gamma\right) \tag{1-8}$$

$$m\frac{\partial^2 \eta}{\partial t^2} = \frac{\partial}{\partial x}\left(F\sin\gamma\right) \tag{1-9}$$

where m is the mass of the element, and F is the cross-section force of the yarn.

Substitute Eq. (1-6) and Eq. (1-7) into Eq. (1-8) and Eq. (1-9), respectively, and obtain

$$\frac{\partial \xi^2}{\partial t^2} = \frac{\partial}{\partial x}\left[\frac{F}{m\left(1+\varepsilon\right)}\left(1+\frac{\partial \xi}{\partial x}\right)\right] \tag{1-10}$$

$$\frac{\partial \eta^2}{\partial t^2} = \frac{\partial}{\partial x}\left[\frac{F}{m\left(1+\varepsilon\right)}\frac{\partial \eta}{\partial x}\right] \tag{1-11}$$

By assuming a 1D wave propagation in the yarn, the tensile strain and cross-section force are independent of the x-axis. Furthermore, the material is considered homogeneous so that m is a constant and not related to the x-aixs. As a result, Eq. (1-10) and Eq. (1-11) can be simplified as

$$\frac{\partial \xi^2}{\partial t^2} = \frac{F}{m\left(1+\varepsilon\right)}\frac{\partial^2 \xi}{\partial x^2} \tag{1-12}$$

$$\frac{\partial \eta^2}{\partial t^2} = \frac{F}{m\left(1+\varepsilon\right)}\frac{\partial^2 \eta}{\partial x^2} \tag{1-13}$$

To solve the above equations, it is first assumed that η has the form below

$$\eta = f + g + At + Bx + K \tag{1-14}$$

where f and g are the non-linear functions of the variables $\beta_1 = t - \frac{x}{\sqrt{F/\left[m\left(1+\varepsilon\right)\right]}}$ and $\beta_2 = t + \frac{x}{\sqrt{F/\left[m\left(1+\varepsilon\right)\right]}}$, respectively. A, B, and K are unknown constants. To determine these

unknown functions and constants, the boundary conditions and continuous conditions are applied below.

As shown in Figure 1.4, at the position of x=0, the yarn followed the projectile's movement. The vertical displacement of the yarn is $\eta = v_0 t$. Hence, the boundary condition at the projectile's corner is

$$x=0,\ \eta = v_0 t \tag{1-15}$$

Substituting Eq. (1-14) into Eq. (15) generates

$$f(0,t) + g(0,t) + At + K = v_0 t \tag{1-16}$$

To satisfy Eq. (1-16), there should be

$$\begin{cases} A = v_0 \\ K = 0 \\ f(0,t) = -g(0,t) \end{cases} \tag{1-17}$$

Hence, f and g must be the same function except for the sign. η can be represented as

$$\eta = f(\beta_1) - f(\beta_2) + v_0 t + Bx \tag{1-18}$$

At the transverse wave front, the yarn has not been activated in motion, so the vertical displacement should be zero, which induces a boundary condition

$$x = c_T t,\ \eta = 0 \tag{1-19}$$

By combining Eq. (1-18) and Eq. (1-19), it is obtained

$$\eta = f(\beta_1) - f(\beta_2) + v_0 t + Bc_T t \tag{1-20}$$

Equation (1-20) can only be satisfied when

$$\begin{cases} f\left(\beta_1\right) \equiv f\left(\beta_2\right) = 0 \\ B = -\dfrac{v_0}{c_T} \end{cases} \tag{1-21}$$

Therefore, the analytical solution of η is determined

$$\eta = v_0\left(t - \frac{x}{c_T}\right) \tag{1-22}$$

Based on the compatibility of deformation in Eq. (1-5), the derivative of the movement in the x-axis can be calculated via η in Eq. (1-22)

$$\frac{\partial \xi}{\partial x} = \sqrt{\left(1+\varepsilon\right)^2 - \left(\frac{v_0}{c_T}\right)^2} - 1 \tag{1-23}$$

The general solution of Eq. (1-23) becomes

$$\xi = x \cdot \left[\sqrt{\left(1+\varepsilon\right)^2 - \left(\frac{v_0}{c_T}\right)^2} - 1\right] + H\left(t\right) + J \tag{1-24}$$

It is noted that the material's horizontal displacement at the projectile's corner is zero. Such a boundary condition can be described as

$$x=0,\ \xi=0 \tag{1-25}$$

This requires that the $H(t)+J$ in Eq. (1-24) must be zero, giving the expression of ξ as

$$\xi = x \cdot \left[\sqrt{(1+\varepsilon)^2 - \left(\frac{v_0}{c_T}\right)^2} - 1 \right] \tag{1-26}$$

As shown in Figure 1.3, the horizontal displacement at the transverse wave front must satisfy the continuous condition.

$$\xi_+ \left(x = c_T t \right) = \xi_- \left(x = c_T t \right) \tag{1-27}$$

$\xi_- = \left(x = c_T t \right)$ represents the material of which the motion in the horizontal direction has been activated by the longitudinal wave. Its expression can be determined by Eq. (1-26)

$$\xi_- \left(x = c_T t \right) = c_T t \cdot \left[\sqrt{(1+\varepsilon)^2 - \left(\frac{v_0}{c_T}\right)^2} - 1 \right] \tag{1-28}$$

On the other hand, the longitudinal wave also stretches the material before the transverse wave front arrives. At any point with a distance of x away from the original point before impact, the longitudinal wave arrives at the time $t = x/c_L$. The inward velocity of material flow (particle velocity) is increased by an amount $-c_L d\varepsilon$ during the time $t - x/c_L$. Therefore, the horizontal displacement of the material ahead of the transverse wave front can be determined by integrating the particle velocity against the time after the arrival of the longitudinal wave.

$$\xi = -\int_0^{\varepsilon} c_L \left[t - \frac{x}{c_L} \right] d\varepsilon \tag{1-29}$$

Hence, the inward flow of the material at the transverse wave front ($x=c_L t$) can be obtained as

$$\xi_+ \left(x = c_T t \right) = c_T t \varepsilon - c_L t \varepsilon \tag{1-30}$$

Substituting Eq. (1-30) and Eq. (1-28) into Eq. (1-27), the impact velocity can be represented by the longitudinal wave speed, transverse wave speed, and the tensile strain developed in the yarn

$$v_0 = \sqrt{(1+\varepsilon)^2 c_T^2 - \left[(1+\varepsilon)c_T - c_L\varepsilon\right]^2} \tag{1-31}$$

Besides, the force at the transverse wave front must also be continuous. Therefore, in the vertical direction, there is

$$mc_T v_0 = -F\sin\gamma \tag{1-32}$$

Combining Eq. (1-32) with Eq. (1-7) and Eq. (1-22), the transverse wave speed can be related to the tensile strain in the yarn

$$c_T = \sqrt{\frac{F}{m(1+\varepsilon)}} = c_L\sqrt{\frac{\varepsilon}{1+\varepsilon}} \tag{1-33}$$

The continuous condition of the horizontal component of the force is automatically satisfied, which is

$$F - mc_T u = F\cos\gamma \tag{1-34}$$

By substituting Eq. (1-33) to Eq. (1-31), the impact velocity can be related to the tensile strain in the yarn

$$v_0 = c_L\sqrt{\varepsilon(1+\varepsilon) - \left[\sqrt{\varepsilon(1+\varepsilon)} - \varepsilon\right]^2} \tag{1-35}$$

The tent angle in Eq. (1-7) can thereby also expressed by the yarn's tensile stain, transverse wave, or impact velocity.

$$\sin\gamma = \frac{v_0}{c_L\sqrt{\varepsilon(1+\varepsilon)}} = \frac{1}{1+\varepsilon}\frac{v_0}{c_T} \tag{1-36}$$

1.3.2 Transverse impact experiments on yarns

By correlating the impact velocity with the yarn's tensile strain, Smith's theory assumes the only failure mode of a yarn to be the tensile fracture during the impact. However, actual transverse impact experiments show that a yarn can have three different failure modes, relying on the impact velocity [28-32]. Hudspeth et al. [32] reported the yarn's deformation and failure at varied velocities. As shown in Figure 1.5*a*, the yarn's mechanical behavior at a low impact velocity usually matches well with Smith's theory: the yarn was deformed with a tent-like geometry and failed in a tensile fracture mode. The failure mode is labeled as Mode 1. When the impact velocity was increased to an intermediate level, the yarn was observed to fail partially upon impact. As the transverse wave propagated from the impact area to the yarn's ends, the global geometry of the yarn changes from a tent to a dome due to the unloading by the rarefaction waves, which is categorized as failure Mode 2 in Figure 1.5*b*. The material still failed in tension in front of the projectile. If the projectile's velocity was extremely high, the yarn experienced an immediate rupture before the transverse wave reached the two ends of the yarn (see Mode 3 in Figure 1.5*c*). Therefore, two impact velocity boundaries can be determined from the experiments to differentiate the three failure modes, which generated a critical velocity region. It is noted that a yarn is different from a composite laminate during transverse impact because the yarn can consistently be failed by a projectile. Therefore, the concept of the ballistic limit for the composite laminate's impact response cannot be adopted to evaluate the impact resistance of a yarn. Instead, the concept of the critical velocity region provides a type of quantification.

Except for the impact velocity, the failure mechanism of a yarn also changes with the fiber type [31-32] and projectile nose shape [32-34] and dimension [35-36]. Carr [31] assembled 0.68 g steel spheres onto the nylon sabots and impacted various Kevlar® and Dyneema® yarns. The Kevlar® yarns failed in fibrillation, and the Dyneema® yarns failed in shear with shear bands and melt damage. By using a razor blade, FSP, and round-nose projectile, Hudspeth et al. [32] determined the critical velocity regions of the Kevlar® KM2 yarns to be 145-310 m/s, 480-645 m/s, and 540-700 m/s, respectively, which were all lower than Smith's prediction. Furthermore, it was found that the fibers experienced a rupture fracture at the FSP's corners, while the yarn failed at

various locations throughout the yarn/round-nose projectile contact area. The difference in the failure surface was believed to be due to the stress concentration near the projectile corners [34]. Lim et al. [35] performed transverse impact experiments on Twaron® 2040 yarns by utilizing round-nose projectiles having a radius of curvature of 2 μm, 20 μm, 200 μm, and 2 mm. The critical velocity region had an increasing trend as the projectile nose radius increased. Moreover, the failure surfaces of the yarns changed from the local shear to fibrillation. The effect of the projectile nose diameter on the yarn's impact response is suggested to be considered via the projectile/yarn contact.

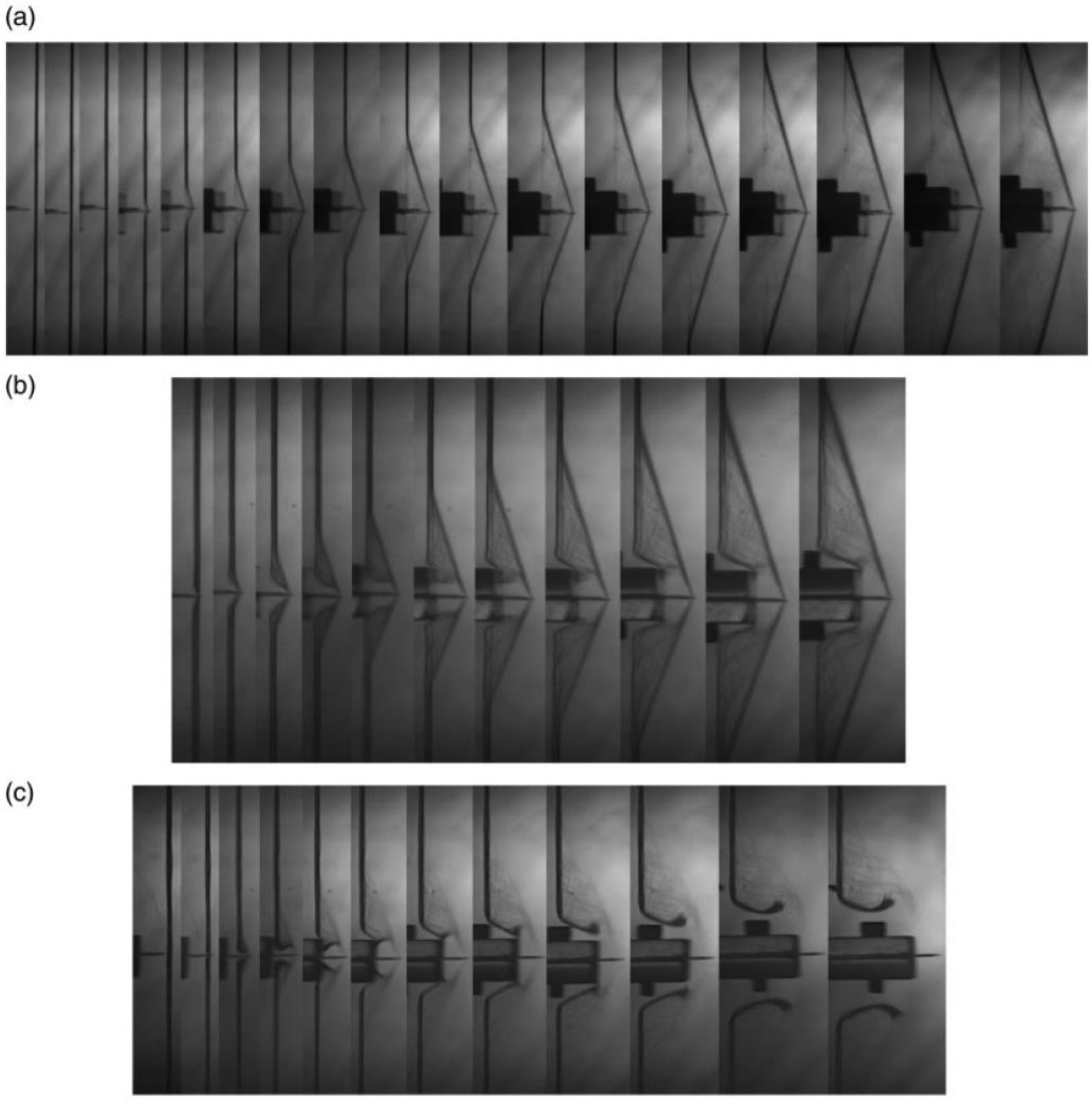

Figure 1.5. Failure processes of yarns at different impact velocities [32].

1.4 Research gaps

From the literature review, it is identified the importance of understanding the transition of a composite laminate's impact response from the conical deformation to the local perforation. It is also identified that the low-scale composite strip or yarn impact experiments provide the possibility to characterize the laminate-scale transition mechanism. However, it is noted that current experiments on composite strips are only available for Dyneema®/epoxy composites. The failure of the composite can be affected by the fiber type. It is also interesting to know whether the matrix properties such as fracture toughness and ductility can influence the wave propagation and failure in the composite impacted at the critical velocities. Furthermore, despite a number of experimental efforts, current studies on the composite strips or yarns have been focused on the samples' global deformation and failure as well as the post-fracture analysis. The experiments merely identified that as the impact velocity increases, the failure of the composite strips or yarns transits from a tensile fracture due to the tent deformation to a local rupture. The transition mechanism, which needs the real-time observations of the local materials' failure process, has not been investigated. In addition, characterization on the yarns' fracture surfaces reveals that the local rupture process can be different, relying on the fiber type and projectile nose shape and dimension, which also needs further investigations.

This Ph.D. dissertation presents the continued efforts to understand the transition mechanism of the composite material in and below the yarn-scale level. First, transverse impact experiments were conducted on S-glass and Kevlar® FRC strips. Glass fibers are inorganic fibers and are regarded as isotropic materials, while Kevlar® fibers belong to the aramid group and have different nanostructures with the Dyneema® fibers. Therefore, such a study extends the work by Chocron et al. [26] and investigates the impact responses of composite strips with different reinforcement types at the critical velocities. Besides, the matrix effect on wave propagation and material failure is explored by examining composite strips made by different matrix systems. Secondly, the composite strips are impacted by round-nose projectiles with various nose diameters to identify the tensile failure and local rupture at different impact velocities. The experiments adopt a reverse impact method, enabling the composite strips to appear always within the camera window so that the failure processes are not missed. The experiments reveal the apparent local rupture when the projectile is a razor blade with an average nose diameter of ~4 μm. Transverse impact experiments on Kevlar® KM2 yarns by Song and Lu [37] revealed that a yarn behaved with fibers

progressively impacted instead of a solid component. The lower-scale single constituent fiber's response under cut is believed to provide a fundamental understanding of the relevant mechanism determining the system-level response of yarns or fabrics. Consequently, in the following two chapters (Chapter 4 and Chapter 5), to identify the local rupture mechanism, transverse impact experiments are performed directly on a variety of single fibers by using razor blades. In Chapter 4, a microscopic method is developed to slowly load a single 10-μm-scale fiber by a razor blade and simultaneously visualize its local failure process. In Chapter 5, a modified Kolsky compression bar setup was integrated with high-speed optical imaging to observe the single fibers' failure by razor blades at an increased loading speed up to ~5.34 m/s. As the last technical chapter of this Ph.D. dissertation, Chapter 6 introduced an advanced imaging technique, high-speed synchrotron X-ray phase-contrast imaging. Such a technique was successfully integrated with a modified Kolsky bar loading and characterized the microscale cracking behavior inside a composite laminate subjected to the low-velocity impact. It is believed that an integrated technique of the high-speed X-ray imaging with the light gas gun loading can provide a sufficient resolution to tracking the local material failure in a composite strip, yarn, and single fiber at high impact velocities, which is expected in the future work.

CHAPTER 2. TRANSVERSE IMPACT BY RCCS ON S-GLASS AND KEVLAR® FRC STRIPS

The following chapter contains content reproduced with permission from the journal article:
Gao J, Guo Z, Hernandez JA, Zhou F, Nie Y, Gao J, Lim BH, Kedir N, Zhai X, Wang J, Tsai JT, De Carlo F, Shevchenko PD, Tallman TN, Jun MBG, Palmese GR, Chen, W. (2021). Transverse impact by RCCs on S-glass and Kevlar® FRC strips. *Composites Part A: Applied Science and Manufacturing*, 146, 106425. DOI: 10.1016/j.compositesa.2021.106425

2.1 Introduction

As mentioned in Chapter 1, continuous fiber-reinforced composite (FRC) structures are exposed to impact loads during their service life. Bird striking and hail dropping on the aircraft as well as shrapnel, bullets, and missiles striking on the military vehicle armors are typical examples of impact events of FRCs [1-3]. Fast evaluation and accurate prediction of impact behaviors of FRCs have been identified as key parts of the frontiers of materials research from 2020 to 2030 by the United States National Academy of Sciences [3].

Traditional experimental approaches to investigate the ballistic performance of FRCs are to shoot various standard bullets onto composite panels at different velocities [25, 38-46]. Such experiments identified two failure modes of target composite structures: complete perforation by the projectile with a certain residual velocity or partial penetration, in which case the projectile would be trapped inside the target or bounced back [25, 38]. The ballistic limit (V_{50}) of a composite panel was quantified as the velocity at which the projectile completely perforated the target 50% of the times [39-40]. Energy absorption of the composite was determined by either the trauma depth and diameter value created on the back of the unperforated panel [41-42] or the projectile speed reduction by the target [43]. The ballistic limit and energy absorption capability were revealed to rely on fiber types [44-46] and orientations [47], fiber hybridization [18], plain or spatial weave [48], fabric areal density [49], composite thickness [11, 20], projectile mass [50] and nose geometry [11, 35, 51], impact angle [52-53], and boundary conditions [54]. Researchers used high-speed cameras to capture the panel behavior in real time during impact [55]. They also conducted post-fracture analysis via optical microscopy [56], scanning electron microscopy (SEM) [57], or X-ray computed tomography [58] to identify impact-induced damage in recovered samples. Multiple energy dissipation mechanisms were identified, including the failure of primary plies

under multi-axial loading, primary ply matrix cracking, deformation of secondary plies, delamination, and friction between the projectile and target [2, 59]. However, experiments also show that the lamina nesting, random tow placement, and interpenetration and overlapping of tows in multiple plies added errors to characterize the strain field close to the impact area [55]. As a result, experiments were suggested to be performed at a lower scale to minimize sources of error due to ply-to-ply interaction and provide a better understanding of the underlying impact-induced material damage mechanisms [55]. Meyer et al. [60] performed ballistic impact experiments on single-ply woven composite panels to isolate the ply-to-ply interaction. They examined the perforation-dominated mesoscale damage modes and mechanisms associated with thin woven fabric composites. However, the interpenetration and overlapping of tows still made it difficult to capture in real time the perforated damage details at or below the yarn scale level.

Researchers have also used numerical methods to study the deformation and failure of the composite under impact due to the attractive efficiency in time and cost compared with experimental approaches. Two main numerical models were developed, including three-dimensional (3D) continuum model [61-63] and multiple constituent model (MCM) [54, 56, 64]. The 3D continuum model constructs the woven fabric with warp and weft yarns and then assembles it with the matrix [61-63]. On the other hand, MCM builds up the composite structure using a representative volume element (RVE) and assumes multiple RVEs exist at a single continuum point in the macroscopic structure. This provides microscale constituent (i.e., fiber and matrix) level responses of a composite microstructure without the need to model the micromechanical details explicitly during a macroscale simulation [64]. For plain weave composites, the RVE can either be an assembly of crossovers [54] or a mesoscale yarn-level model [56]. By sacrificing sophisticated details of the weave and the yarn, the MCM was demonstrated to have higher efficiency in predicting the failure of a composite panel at the ballistic limit in comparison with the 3D continuum model. However, since yarns are not explicitly modeled, the stress distribution and mechanical behavior of yarns and fabrics inside the matrix cannot be predicted with accuracy. Grujicic [65] attributed these shortcomings of current models to be a lack of inclusion of the contribution of various phenomena and processes occurring at different length scales to the overall behavior/performance of a composite.

To the best of the author's knowledge, few studies on FRCs isolated interactions between both plies and tows to focus on the damage mechanisms at the yarn scale level when the composite

was transversely impacted at different velocities. To fill in this data gap, Chocron et al. [26] transversely impacted the ultra-high molecule weight polyethylene (UHMWP) Dyneema® HB80/polyurethane composite strips and reported the waves in the material. The work presented in this paper studied two other reinforcement fiber types: S-glass and Kevlar® fibers. Glass fibers are generally regarded to be isotropic and have high strength and failure strain at high strain rates, while Kevlar® fibers belong to the aromatic polyamide (aramids) family and have rod-like polymer molecules in almost perfect crystalline packing during spinning, which are different from extremely long chain structures of Dyneema® fibers with shish-kebab configurations [66]. Four types of composite strips were manufactured by the aforementioned two reinforcements and two impact-resistant matrixes, as commercialized SC-15 and newly developed monoamine functionalized partially reacted substructures (mPRS) modified TGDDM-Jeffamine® D230 matrix, respectively. Samples were characterized by optical photography, 3D synchrotron X-ray computed tomography, and SEM to record the initial conditions. Transverse impact experiments on FRC strips were then conducted by shooting RCCs at varied velocities perpendicularly onto the centers of clamped strips. The deformation and failure behaviors of the strips were captured in real time by a high-speed camera. The concept of critical velocity region used to describe the impact behaviors of yarns was introduced to define different failure modes and estimate the ballistic limits of these composite strips. Wave propagations and load histories in the strips were quantified. Finally, critical velocities of the composite strips were compared with that of single fibers and yarns and the ballistic limits of single-ply and multi-ply composite panels to provide insight into the design of impact-resistant fabrics and composites.

2.2 Materials

2.2.1 Fibers and matrix systems

Non-woven sheets of S-Glass and Aramid (Kevlar®) “Uni-web” unidirectional fibers were supplied by ACP Composites, Inc. (Livermore, CA, USA). SC-15 was received from Kaneka Aerospace (Benicia, CA, USA) as SC-15 resin (Part A) and hardener (Part B). On the other hand, to obtain the mPRS modified TGDDM-Jeffamine® D230 matrix, tetraglycidyl diaminodiphenylmethane (TGDDM) (Sigma-Aldrich, St. Louis, MO, USA) was used as the epoxy resin and poly (propylene oxide) diamine Jeffamine® D230 was provided by Huntsman

Corporation (Austin, TX, USA) as the primary curing agent. mPRS was prepared by partially reacting a stoichiometric mixture of TGDDM and Jeffamine® M1000 also from Huntsman with the degree of conversion of 75%.

2.2.2 Composite manufacturing and sample preparation

The composite manufacturing process included fabric and matrix preparation, prepreg formation, vacuum bagging, and curing and post-curing progression. First, S-Glass and Kevlar® fabrics in 254 mm × 254 mm (1 ft × 1ft) were cut from the received non-woven sheets. SC-15 matrix was obtained by mixing the resin part with the hardener in a weight ratio of 100:30. TGDDM has an epoxy equivalent weight (EEW) of 105.63 g/eq, while Jeffamine® D230 possesses an amine equivalent weight (AEW) of 59.5 g/eq. TGDDM and Jeffamine® D230, as the epoxy and amine, respectively, were mixed in a weight ratio of 1:1. mPRS was added into the TGDDM-Jeffamine® D230 matrix in a content of 15% by weight. Both the SC-15 and TGDDM-Jeffamine® D230 with mPRS (m T&J) matrixes were well stirred and then placed inside a vacuum chamber at room temperature and approximately 0.1 MPa below the atmospheric pressure for 30 minutes. This procedure effectively removed bubbles from the liquid matrix and avoided possible voids in the manufactured composites. Afterward, the two types of fabrics were uniformly wetted by corresponding matrixes to form prepregs and vacuum bagged for curing. The curing cycle for the S-Glass/SC-15 and Kevlar®/SC-15 prepregs included a 24-hour curing time at room temperature and a vacuum pressure of 80 kPa, additional 24-hour curing time at room temperature and atmospheric pressure, and post-curing for 2 hours at 120 ℃ and atmosphere pressure [67-68]. On the other hand, the S-Glass and Kevlar® fabrics pre-impregnated with m T&J were applied with a curing time of 24 hours at a temperature of 80 ℃ and a vacuum pressure of 80 kPa, followed by a post-curing process for 2 hours at 160 ℃ and atmospheric pressure, as suggested in [69]. Finally, composite strips were cut from the thin composite panels by razor blades and then machined down to 50 mm in length × 1 mm in width by either a polisher or a femtosecond laser.

2.3 Experiments

2.3.1 Material characterization

Microstructures of different composite strips were characterized by 3D synchrotron X-ray computed tomography at beamline 2-BM at Advanced Photon Source (APS), Argonne National Laboratory, Lemont, IL, USA. The strip was first mounted on a rotational stage and rotated over 180°. During this process, a monochromatic X-ray beam with an energy of 40 keV penetrated the sample and reconstructed the composite's interior structures within 3000 projections, including the fiber distribution and alignment, voids, and defects. The X-rays were then converted into visible light by a single-crystal scintillator, magnified by a 5X microscope objective lens, and recorded by a FLIR Oryx ORX-10G-51S5M camera in a fly scan mode where projections were recorded while the sample was continuously rotated. Each composite strip was reconstructed by the commercialized software Dragonfly (Object Research Systems Inc., Montreal, Quebec, Canada). The fiber volume fraction (V_f) was quantified by counting fibers in voxel size.

SEM was also employed to help determine the fiber volume fraction. Test strips were cut using a diamond-coated wheel and potted using an epoxy resin system. The end-faces of the potted strips were polished by using conventional metallographic procedures. Samples were then placed inside the Quanta 3D FEG Dual Beam SEM (FEI, Hillsboro, OR, USA) for imaging. Image analysis was conducted by ImageJ to obtain the fiber volume fraction from a minimum of 5 images with an identical size of 150 × 130 μm^2 from random locations per sample. Additionally, the sample thickness was measured under an optical microscope with a total sample number of 10.

Table 2.1. Mechanical properties of fibers and matrixes

Material	S-Glass	Kevlar®	SC-15 [72-73]	m T&J [69]
Diameter (μm)	9.38 ± 0.57	15.31 ± 0.63		
Density ρ (kg/m^3)	2460 [70]	1440 [71]	1140	1157
Areal density A_d (kg/m^2)	99.56	75.85		
Elastic modulus E (GPa)	66.43 ± 2.70	67.06 ± 5.95	2.5 ± 0.6	2.25 ± 0.06
Tensile strength σ (GPa)	4.17 ± 0.74	2.98 ± 0.44	(60.0 ± 11.6) × 10^{-3}	(57.6 ± 1.5) × 10^{-3}
Failure strain ε (%)	7.69 ± 0.81	5.55 ± 0.54	3.4 ± 0.2	21.3 ± 1.6
Elastic wave speed c_L(m/s)	5167	6824		

*E, σ, ε, and c_L were measured at a strain rate of 500 s^{-1}.

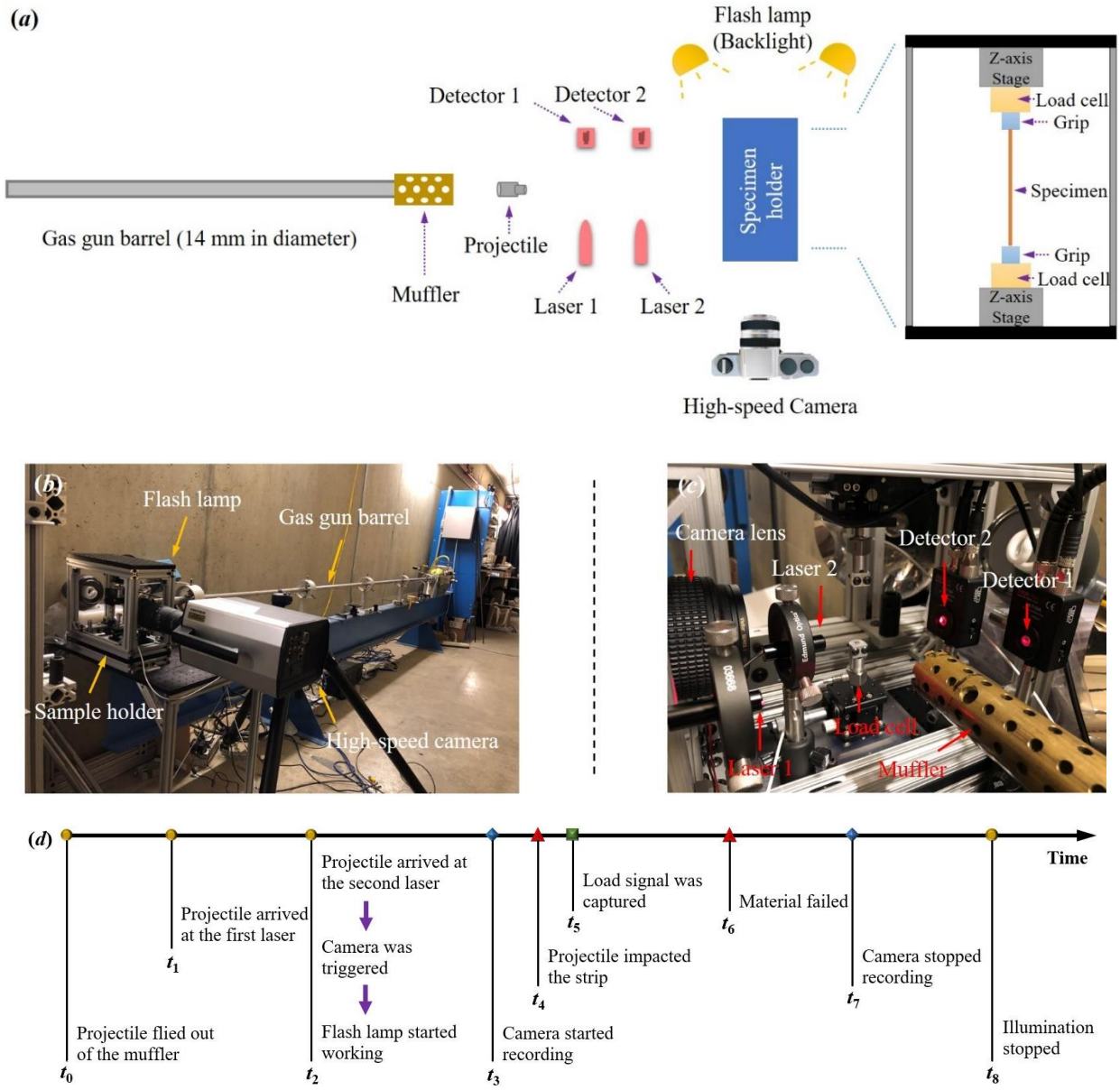

Figure 2.1. Transverse impact experiment on the composite strip. (*a*) Schematic of the experimental setup; (*b*) Real picture of the experimental setup; (*c*) Details inside the sample holder; (*d*) Timing sequence used throughout the experimental duration.

Since the product information about the S-Glass and Kevlar® fabrics are not available except for the areal densities shown in Table 2.1, in this work, we pulled out single fibers from the fabrics and measured the fiber diameters by using NovaNano SEM (FEI, Hillsboro, OR). High-rate tensile experiments on single fibers with an identical gauge length of 6.35 mm were performed to obtain the fiber stress-strain curves at a strain rate of ~500 s^{-1}. The diameters and mechanical

properties of different fibers were presented in Table 2.1. Densities of fibers and matrix properties were also provided in Table 1 based on either literature [70-73] or previous experimental investigations [69].

2.3.2 Transverse impact experiments

Transverse impact experiments on the composite strips were conducted by using a light-gas gun having a barrel diameter of 14 mm, as presented schematically in Figure 2.1*a* with a photograph of the setup in Figure 2.1*b*. 16 grain RCCs were adopted as projectiles, which are cylinders with a standardized size of 5.575 ± 0.025 mm (0.219 ± 0.001 inch) in diameter and 5.625 ± 0.025 mm (0.221 ± 0.001 inch) in length. Projectiles were shot from the gun barrel, passing two laser beams with a distance of 50 mm apart. Two detectors were placed opposite the two lasers, respectively, and detected the beam intensity decrease on the arrival of a projectile. The decreases of the beam intensity were recorded as reduced voltage signals in an oscilloscope. The projectile velocity (v_0) was determined by dividing the 50-mm distance with the time intervals between which the two laser beams were blocked. Afterward, the projectile transversely impacted onto the composite strip mounted inside the sample holder. It is noted that the sample was located as close to the second laser as possible so that the impact velocity can be closely represented as v_0. A muffler was assembled directly downstream of the barrel muzzle to attenuate the muzzle blast created from the firing system. In order to reduce trajectory instability and the tumbling of the RCC projectiles, each RCC was glued to a sabot having a diameter of 14 mm and shaped by polyurethane foam FOAM-iT!™ 26 (Smooth-On, Inc., Macungie, PA, USA) inside a steel mold. The total weight of the RCC and sabot was measured as 3.76 ± 0.27 g. Additional effort to enhance the trajectory stability included minimizing the distance between the barrel muzzle and sample. Deformation and failure of the composite strip during impact were magnified by a close-up lens and then captured by a high-speed camera (Shimadzu HPV-X2, Kyoto, Japan) from the side with an exposure time of 200 ns at a frame rate of 2-5 million fps (frames per second). For each sample type, two close-up lenses with magnifications of 1X and 10X, respectively, were utilized. The 1X lens enabled to record the global configuration of each sample under impact. The 10X lens was focused on a partial sample where the RCC corner was expected to impact so that the strip sample's localized failure behavior can be captured. A strobe light (flash lamp) system (Cordin Company, Salt Lake City, USA) was installed to provide a backlight source with a typical 42-μs ramp-up

time to reach full lamp intensity such that the sample can be illuminated throughout the entire loading event.

The framework of the sample holder was constructed by T-slotted framings and breadboards. Figure 2.1*c* presents the components inside the sample holder, including Z-axis stages (Optics Focus Instruments Co., Ltd., Beijing, China), piezoelectric load cells (Kistler, Kistler Instrument Corp., Novi, MI, USA), and grips. Before each impact experiment, the strip sample needed to be clamped by grips. The grips were designed with files to insert to prevent sample slippage. Details of the grip design can be found in [74]. To prevent the strip sample from being damaged by the grips, before clamping, the strip ends were enveloped by epoxy adhesive DP190 (3 M Inc., St. Paul, MN, USA) and then covered by aluminum foils. The processed ends were then directly clamped onto the grips. The two grips were connected to two load cells by set screws, respectively. Each load cell was assembled on a Z-axis stage via a set screw. The Z-axis stages were used to align the center of the sample with the gun barrel vertically. Moreover, the movements of the Z-axis stages can control the pretension in the sample so that the sample had a smaller transverse deflection by air before the impact. The pretension was recorded by the load cells to be ~3% of the composite strip's average tensile strength reported in Table 2.2. The load cells were also capable of recording the sample's load histories at the two ends during transverse impact. The whole sample holder was fixed on a static plate to minimize signal disturbance.

Table 2.2. Material properties of composite strips

Sample type	S-Glass/SC-15	S-Glass/m T&J	Kevlar®/SC-15	Kevlar®/m T&J
V_f (%)	55.70 ± 2.46	50.99 ± 3.60	61.79 ± 2.35	57.86 ± 2.72
Thickness T (μm)	178.13 ± 10.56	210.75 ± 17.14	185.40 ± 23.44	207.20 ± 14.86
Density ρ (kg/m^3)	1891	1836	1325	1321
Elastic modulus E (GPa)	38.01	34.98	42.42	39.75
Tensile strength σ_P(GPa)	2.35	2.16	1.87	1.75
Elastic wave speed c_L (m/s)	4484	4365	5658	5486

*E, σ_P, and c_L were measured at a strain rate of 500 s^{-1}.

A successful high-velocity impact experiment with the integration of high-speed imaging highlights the timing sequence/synchronization of velocity measurement, light source, impact event, load history recording, and image detection for the deformation and failure analysis. Figure

1*d* illustrates the triggering scheme and time sequence throughout a complete impact experiment, starting from the projectile flying out of the muffler at t_0. When the projectile arrived at the second laser at t_2, the oscilloscope immediately released a trigger signal to the high-speed camera working in a trigger-trigger mode. However, instead of being activated for recording, the camera was preset with a delay time (t_3-t_2) for recording, which was close to but larger than the projectile's traveling time from the second laser to the sample. Simultaneously, the high-speed camera output a positive signal to discharge the flash lamps, providing high-intensity visible light to illuminate the sample. As demonstrated in Figure 2.1*d*, the light source had a duration of (t_8-t_2) equivalent to 5-7 ms, which was sufficient to cover camera imaging endurance (t_7-t_3) and the loading event spanning from t_4 to t_6. The camera ended up imaging with a steady signal output at t_7 detected by the oscilloscope, enabling the correlation of the laser signal with the image sequence. The load histories were captured separately by another oscilloscope, starting from t_5 when the longitudinal in-plane waves propagated from the impact area to the sample ends.

2.3.3 SEM fractographic analysis

Fractographic studies were conducted by analyzing failure surfaces of representative samples. Selected samples after impact experiments were sputter-coated with platinum for 90 seconds. The morphologies of the fractured surfaces were imaged by Quanta 3D FEG Dual Beam (SEM/FIB) (FEI, Hillsboro, OR, USA).

2.4 Results

2.4.1 Microstructures and mechanical properties of composite strips

Figures 2.2*a* and 2.2*b* show the reconstructed 3D tomographic and SEM images of an S-Glass/SC-15 composite strip, respectively. Single fibers can be identified because of the high resolution of the beam source that can reach 1.3 μm/voxel size. Moreover, with different X-ray attenuations, fibers and matrices in the FRC strips can be differentiated in X-ray images. Besides, compared to glass fibers, polymer fibers such as Kevlar® embedded inside the matrix have a lower X-ray attenuation. As shown in Figures 2.2*c*-2.2*d*, the X-ray image of the Kevlar® FRC had a lower contrast to reveal the distribution of fibers and matrix in the composite. The difference of the X-ray attenuation between S-Glass or Kevlar® fibers and the surrounding matrix was quantified

on the basis of greyscale value (GV) along corresponding paths A_1B_1 and A_2B_2, respectively, as demonstrated in Figure 2.2*e*. Fiber volume fractions of different strips were extracted in Table 2.2. Previous research efforts characterized the dynamic constitutive parameters of unidirectional FRCs through traditional dynamic tensile experiments [75] or short-beam bending experiments [76] based on bi-modulus theory [77-79]. These experiments proved that the elastic moduli of composites at high loading rates along the fiber direction matched well with the Voigt model [80]. In this work, the densities, dynamic elastic moduli, and dynamic tensile strength of FRCs were calculated by the Voigt model and summarized in Table 2.2. The fiber and matrix properties used for the calculation can be found in Table 1, and the fiber volume fractions are reported in Table 2.2.

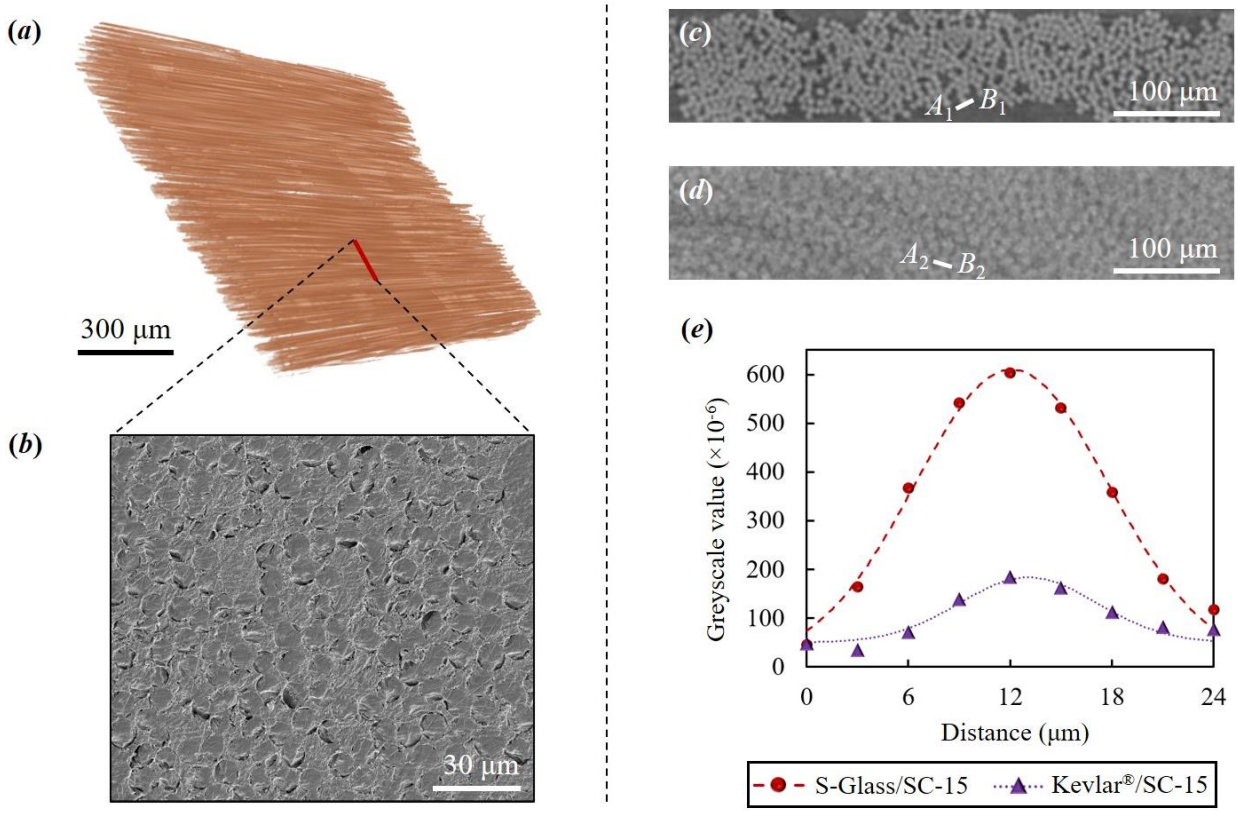

Figure 2.2. Microstructures of composite strips. (*a*)-(*c*) S-Glass/SC-15 composite strips: (*a*) 3D reconstructed structure, (*b*) SEM image, (*c*) An X-ray tomography slice; (*d*) An X-ray tomography slice for a Kevlar®/SC-15 composite strip; (*e*) Variations of greyscale value along the paths A_1B_1 in (*c*) and A_2B_2 in (*d*), respectively.

2.4.2 Global deformation and failure behaviors of composite strips

This section presents the failure processes of representative composite strip samples experiencing transverse impact by RCC projectiles at various velocities. Mechanical behaviors of these strips were projected to a 1X close-up lens and then recorded by the high-speed camera as image sequences shown in Figs. 3-6. An identical field of view, ~17 × 28 mm^2, made it possible to vertically locate more than half of a sample's length and capture the variation of the global configuration of the sample in real time. It is noted that the projectile may still be accelerated after passing the second laser upon arrival at the sample. The projectile's velocity can be computed from high-speed images and was compared with the measurements by lasers for calibration. Results show that global failure behaviors of the composite strips differed based on the material type and impact velocity.

As depicted in Figure 2.3*a*, an S-Glass/SC-15 composite strip was impacted by an RCC projectile at a velocity of 197 m/s. The projectile contacted the composite strip at the time $t = 0$. Afterward, the projectile activated the lateral movement of the strip to form a tent-like shape. Over time, the jumping point of the tent, which was the transverse wavefront, was observed to move outwards until the strip ends. The area that the tent encompassed was thereby increased. An identical tent angle γ was identified during impact and indicated in Figure 2.3*a*. The composite strip's failure was initiated in front of the projectile's flat face as partial materials were tensioned to break. Such damage then propagated along the strip length and delaminated the strip. The composite strip eventually failed due to the tensile failure of the residual materials and intralaminar delamination [81].

Figure 2.3*b* presents the fracture process of a representative S-Glass/SC-15 composite strip sample impacted by an RCC projectile at v_0 = 405 m/s. The sample was delaminated after contacting the projectile, indicating a portion of the material failed transversely during impact and then separated from the strip. The residual material was still able to resist the projectile. As the projectile advanced, the particle velocity of the residual strip increased to the projectile velocity, resulting in the material in the vicinity of the impact area reached a dynamic equilibrium state. The composite strip finally failed in tension in front of the projectile's flat face. Compared with the strip impacted at the lower velocity of 197 m/s, the material experienced more severe damage by spall-like intralaminar delamination. The global configuration of the composite strip was initially

like a tent while gradually became a dome. The jumping point of the dome can still propagate out of the field of view.

When the impact velocity increased to 497 m/s, as presented in Figure 2.3*c*, the composite strip cannot dissipate the high kinetic energy of the projectile. The strip was deformed into a ridge shape and failed locally before the transverse wave propagated out of the field of view. The damage extent was lower than that observed when the impact velocity was 405 m/s. Besides, the strip was found to fracture at the flat surface of the RCC but not the RCC corners.

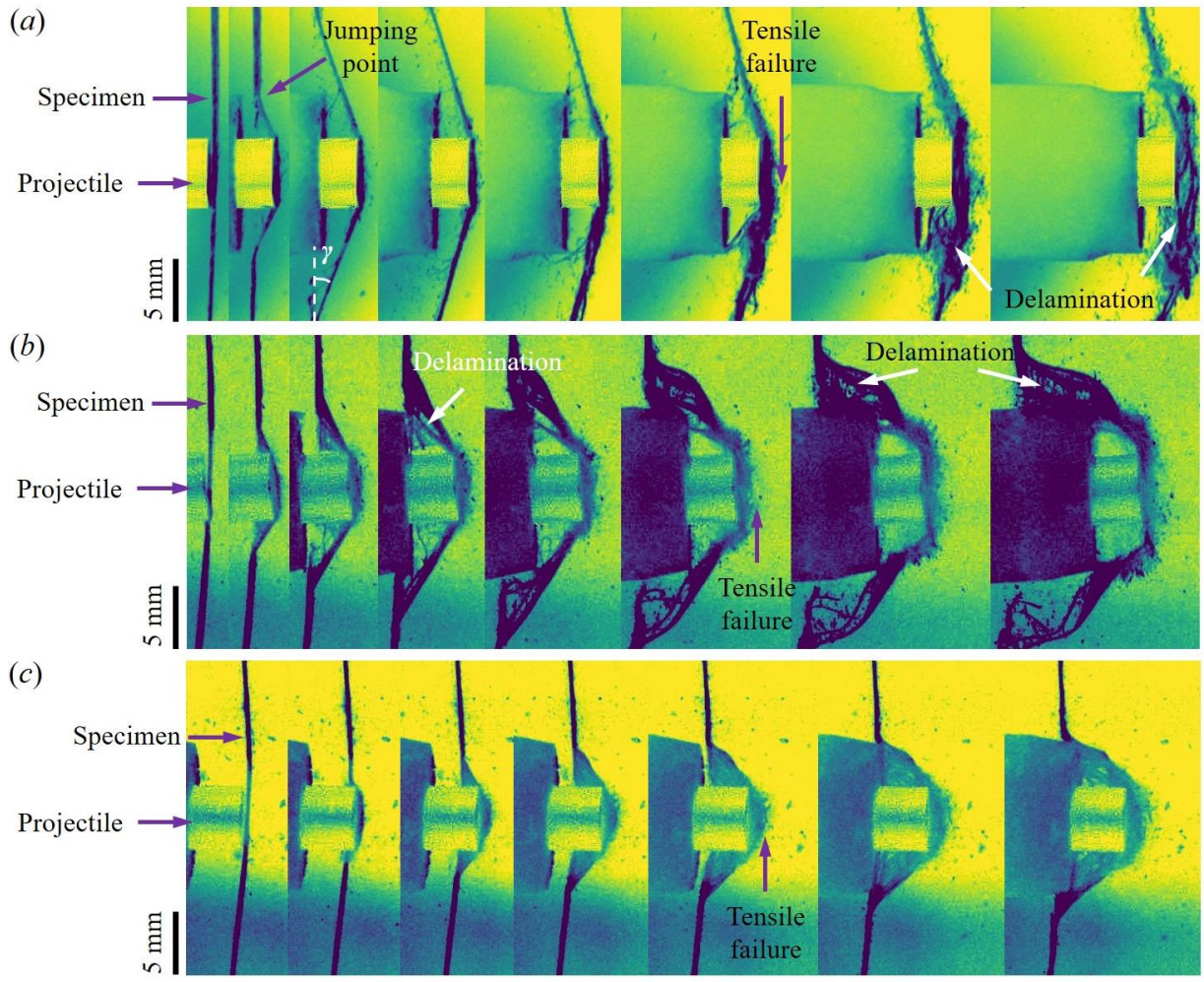

Figure 2.3. Failure processes of S-Glass/SC-15 composite strips tranversely impacted by RCC projectiles at various velocities. (*a*) v_0 = 197 m/s, inter-frame spacing is 10 μs; (*b*) v_0 = 405 m/s, inter-frame spacing is 4 μs; (*c*) v_0 = 497 m/s, inter-frame spacing is 2 μs.

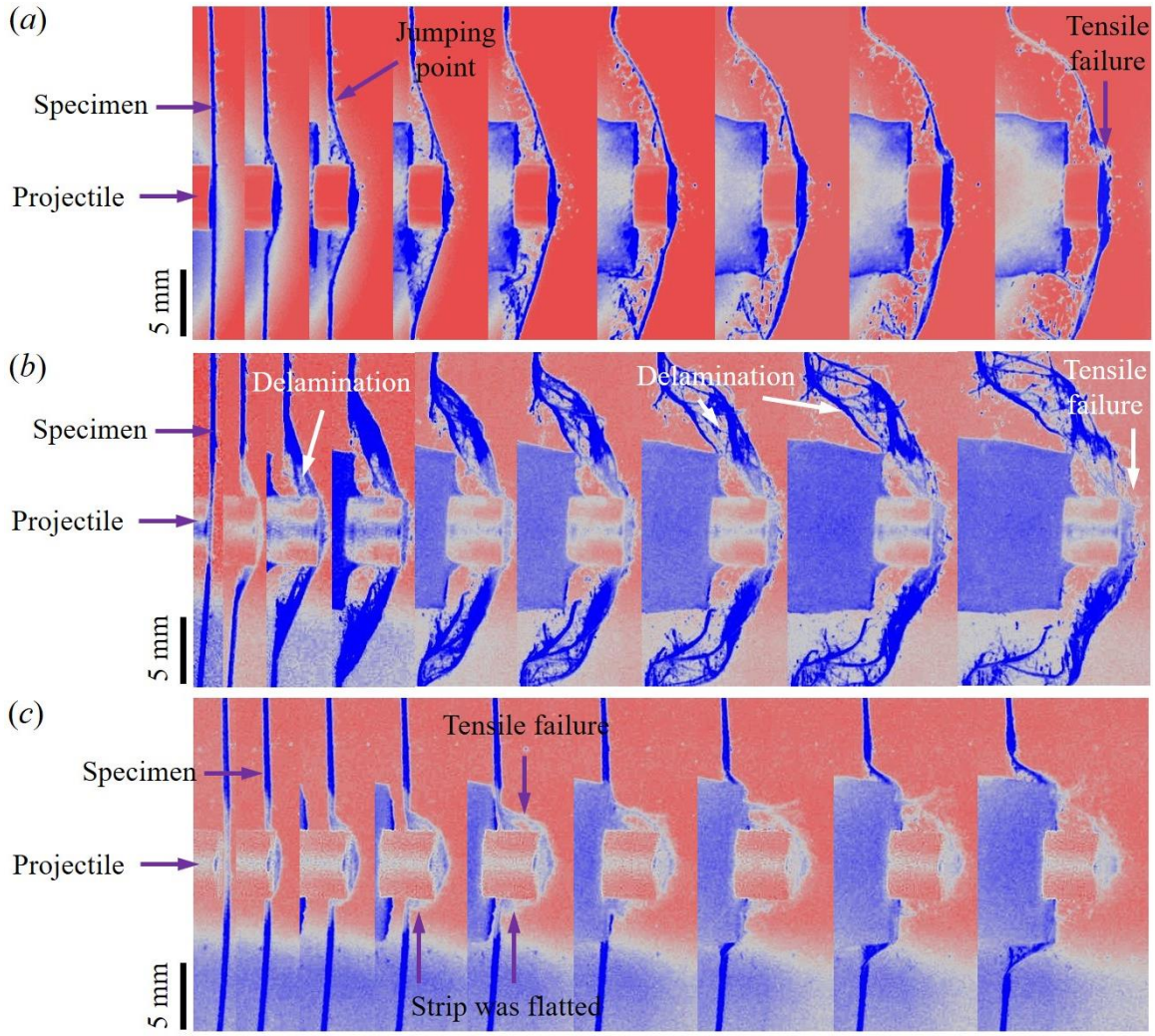

Figure 2.4. Failure processes of Kevlar®/SC-15 composite strips tranversely impacted by RCC projectiles at various velocities. (*a*) v_0 = 173 m/s, inter-frame spacing is 5 μs; (*b*) v_0 = 336 m/s, inter-frame spacing is 5 μs; (*c*) v_0 = 485 m/s, inter-frame spacing is 2 μs.

Similar to the S-Glass/SC-15 composite strips, when the impact velocity increased in order from 173 to 336 and then to 485 m/s, the global configuration of Kevlar®/SC-15 composite strips changed from a tent to a dome and then to a ridge shape, respectively, which is recorded in Figure 2.4. The damage extent of the material increased when the impact velocity increased from 173 m/s to 336 m/s. However, it reduced when the impact velocity continuously increased to 485 m/s. Three different failure features were identified for the Kevlar®/SC-15 composite strips compared with the S-Glass/SC-15 composite strips. First, when the Kevlar®/SC-15 composite strip was impacted at a low velocity of 173 m/s in Figure 2.4*a*, the tent angle at the early stage after the

projectile/strip contact was ~10° smaller than that of the S-Glass/SC-15 composite sample. Furthermore, the global configuration of the Kevlar®/SC-15 composite strip cannot maintain straight as that of the S-Glass/SC-15 composite strip, which was possibly because the Kevlar® fibers are more flexible and softer and have a lower transverse stiffness than the glass fibers. Second, at an intermediate impact velocity of 336 m/s, the Kevlar®/SC-15 composite strip was delaminated to a larger extent than the S-Glass/SC-15 composite strip (see Figure 2.4*b*). This indicates that more material damage and failure were involved in dissipating the kinetic energy of the projectile. Third, the Kevlar®/SC-15 composite strips were observed to fail in tension at the projectile corners rather than the projectile front surface.

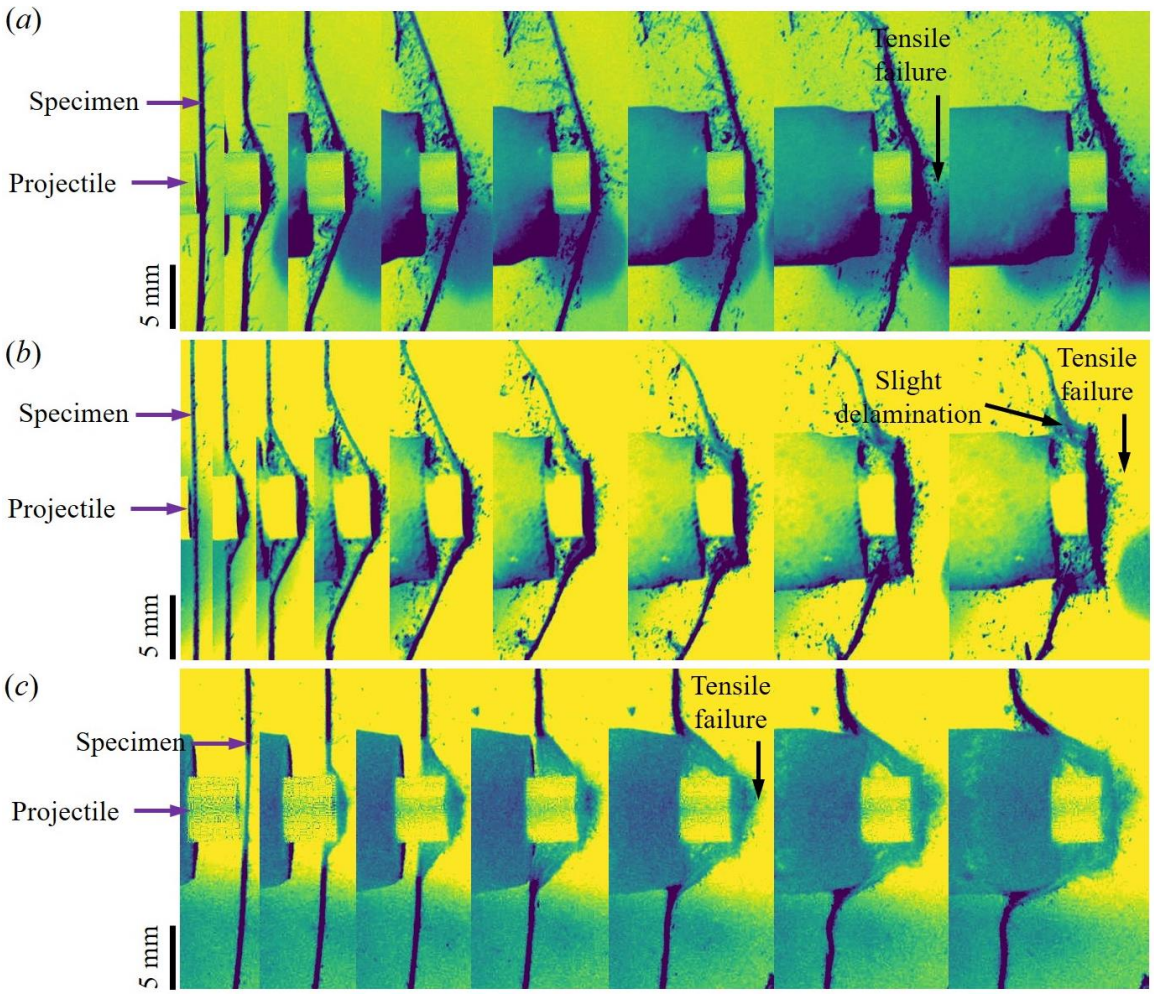

Figure 2.5. Failure process of S-Glass/m T&J composite strips transversely impacted by RCC projectiles at various velocities. (*a*) *v*=197 m/s, inter-frame spacing is 10 μs; (*b*) *v*=292 m/s, inter-frame spacing is 5 μs; (*c*) *v*=461 m/s, inter-frame spacing is 3 μs. The scale bar is 5 mm.

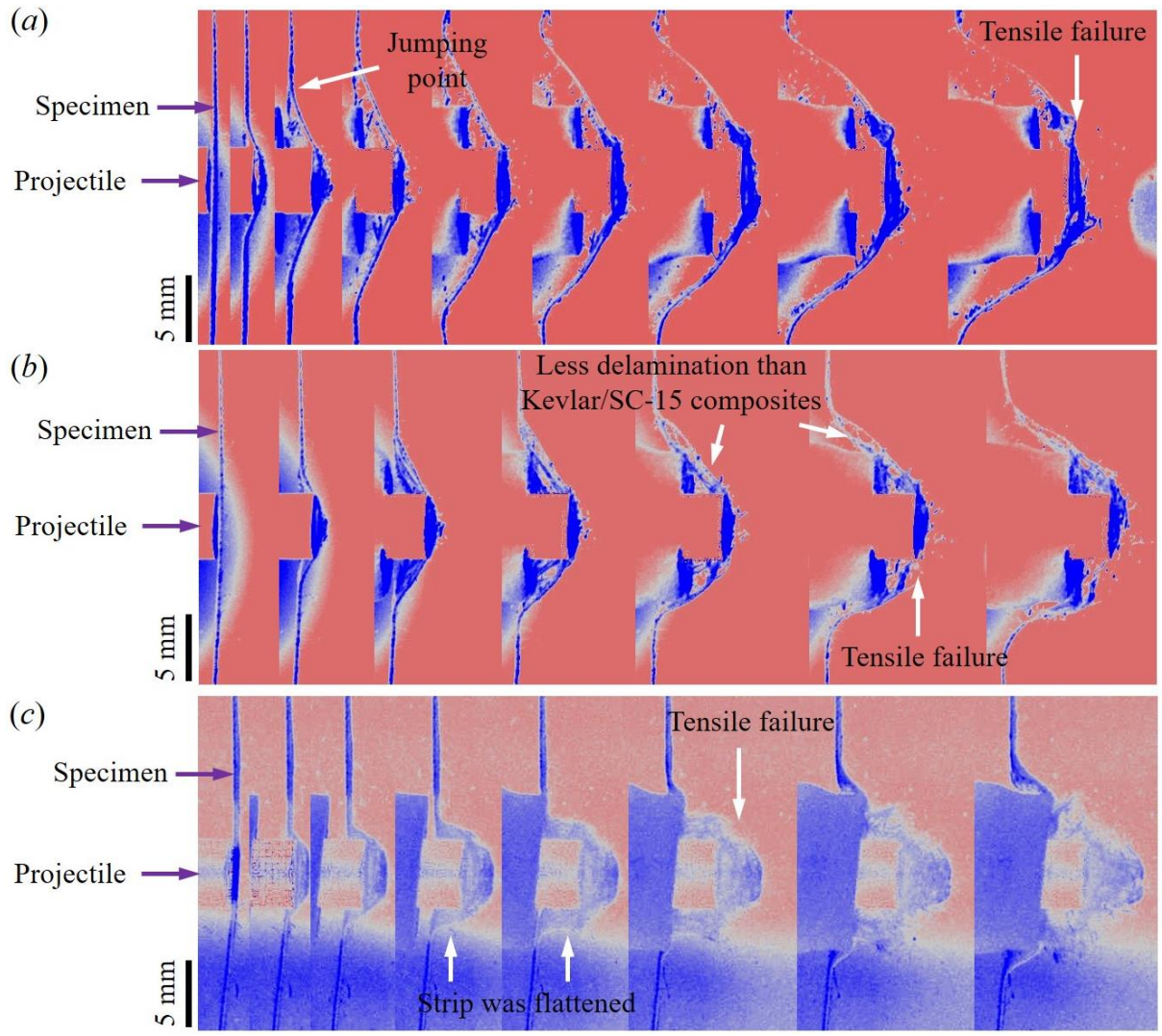

Figure 2.6. Failure process of Kevlar®/m T&J composite strips tranversely impacted by RCC projectiles at various velocities. (*a*) *v*=212 m/s, inter-frame spacing is 5 μs; (*b*) *v*=330 m/s, inter-frame spacing is 5 μs; (*c*) *v*=532 m/s, inter-frame spacing is 2 μs.

Compared with the SC-15 matrix, the m T&J matrix seemed to bond fibers well. Under transverse impact by RCCs at similar impact velocities, the strip samples made of m T&J had less intralaminar delamination than the strips manufactured by the SC-15 matrix. The deformation and failure processes of the S-Glass/m T&J and Kevlar®/m T&J composite strips were exhibited in the supplementary data as Figure 2.5 and Figure 2.6, respectively.

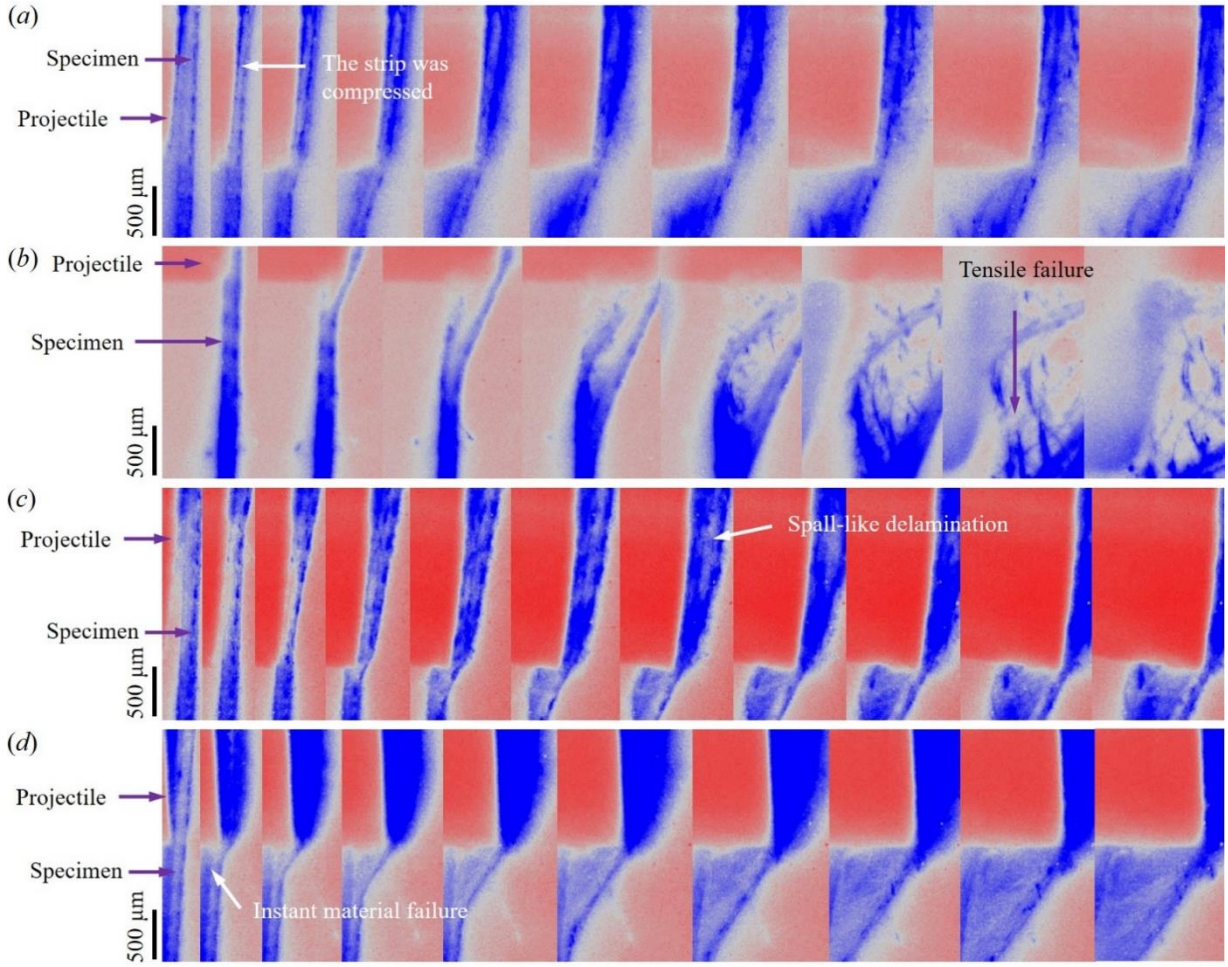

Figure 2.7. Physical behaviors of Kevlar®/SC-15 composite strips at projectile corners when tranversely impacted at various velocities. (*a*) v_0 = 226 m/s, inter-frame spacing is 1 μs; (*b*) v_0 = 291 m/s, inter-frame spacing is 2 μs; (*c*) v_0 = 325 m/s, inter-frame spacing is 500 ns; (*d*) v_0=520 m/s, inter-frame spacing is 500 ns.

2.4.3 Mechanical behavior of the composite strip at the projectile corner

In an impact event, a multi-axial stress state is likely to develop at the projectile corner and fail the material [34]. Characterization of the strip behavior at the projectile corner is critical to identify the stress state of the material, especially for Kevlar® FRCs, since such material was revealed to fail in the vicinity of the projectile corner in Figure 2.4. A 10X close-up lens was used to focus down to one corner of the projectile and magnify the local material's response during impact. The field of view had a size of 1.4 × 2.3 mm^2.

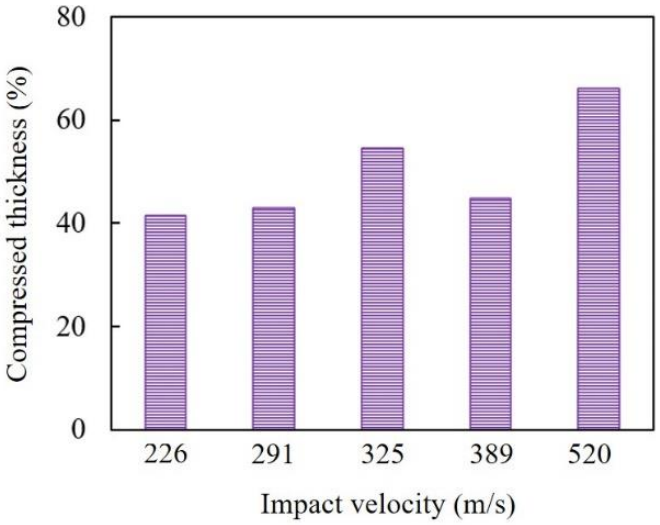

Figure 2.8. Compressed thicknesses of Kevlar®/SC-15 composite strips impacted at various velocities.

Figures 2.7*a*-2.7*d* show the local responses of the Kevlar®/SC-15 composite strips at the projectile corners under impact at velocities of 226, 291, 325, and 520 m/s, respectively. The image sequences reveal that all the composite strips first experienced transverse compression. When the impact velocity was very low as 226 m/s, the compressed strip was promoted without apparent damage, as observed in Figure 2.7*a*. At an intermediate impact velocity of 291 or 325 m/s, a partial composite strip failed during transverse compression by the RCC. Intralaminar delamination was observed in the composite strip contacted by the projectile corner. The material in front of the projectile's flat surface possessed spall-like intralaminar delamination, and a portion of the delaminated strip material bounced off the flat surface of the projectile (see Figure 2.7*c*). On the other hand, the delaminated material beside the corner but away from the impact region may fail in tension and snap back, which is recorded in Figure 2.7*b*. When the impact velocity was further increased to 520 m/s, a partial composite failed very quickly after the projectile contacted the strip. Due to the limited contrast and magnification and the distortion by the material debris, it is not feasible to identify that such a quick failure was originated from the tensile fracture of the strip after fast transverse compression or from the transverse shear. As time progressed, the surviving strip was continuously compressed by the projectile. Because of the small field of view, the fracture of the strip was not caught by the camera before the projectile propelled the strip out of the screen. The maximum compressed thicknesses of Kevlar®/SC-15 composite strips during

impact at various velocities were measured within the field of view and are presented in Figure 2.8. Similar failure behaviors were also captured for S-Glass FRC strips.

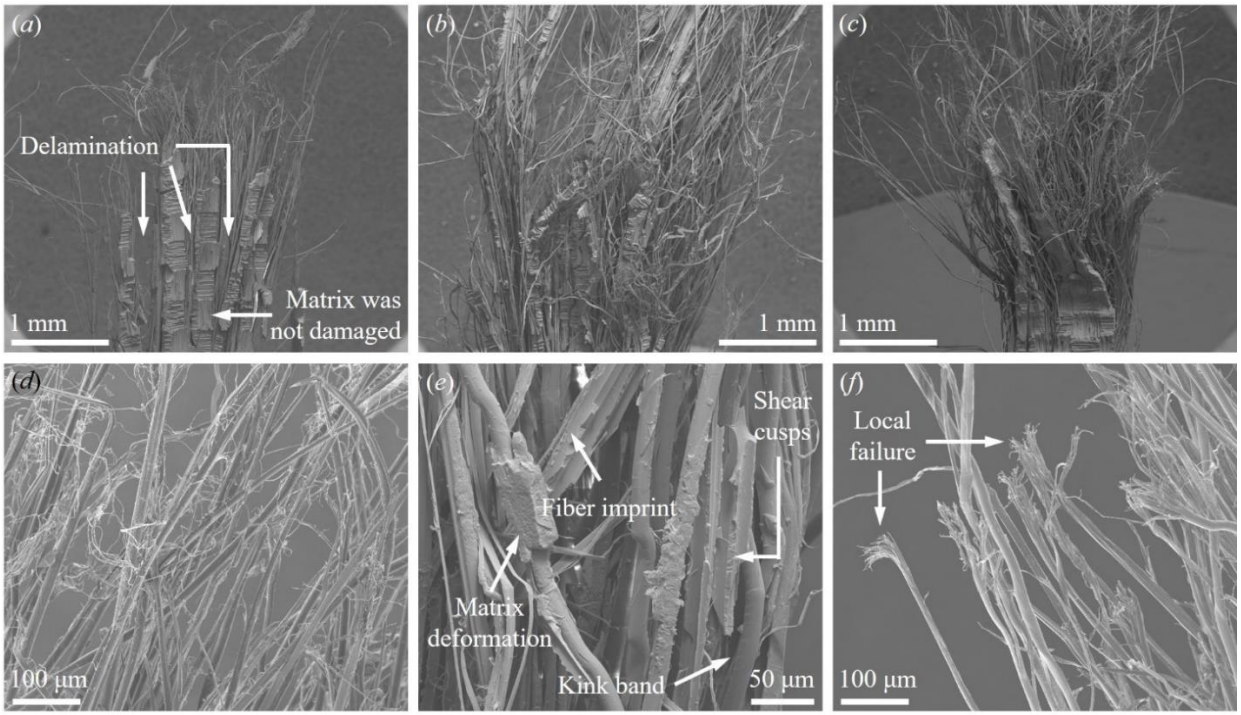

Figure 2.9. Post-fracture images of the Kevlar®/m T&J composite strip impacted at different velocities. (*a*) v_0 = 191 m/s; (*b*) v_0 = 305 m/s; (*c*) v_0 = 537 m/s; (*d*) Fibrillated fibers; (*e*) Microscale fiber and matrix deformation and failure inside the strip; (*f*) Local failure of fibers inside the composite strip impacted at 537 m/s.

2.4.4 Fracture morphologies of composite strips

Figures 2.9*a*-2.9*c* present fracture morphologies of Kevlar®/m T&J composite strips impacted at velocities of 191, 305, and 537 m/s, respectively. Impacted at a low velocity of 190 m/s, the fibrillated fibers at the impact region in Figure 2.9*a* indicate the tensile failure of the strip. The strip was delaminated into several parts. The matrix in the neighborhood of the impact area was not destroyed, meaning less damage was introduced by the impact loading. When the impact velocity increased to 305 m/s, the strip was damaged to a larger extent at the impact site, which is revealed by Figure 2.9*b*. Fibers were severely fibrillated (see Figure 2.9*d*) and kinked (see Figure 2.9*e*) and debonded with the matrix, leaving the fiber imprint in Figure 2.9*e*. The matrix was deformed and separated from the strip, which was observed as shear cusps in Figure 2.9*e*. When

the impact velocity was 537 m/s, the damage extent decreased, as demonstrated in Figure 2.9*c*. The fracture concentrated at the impact site without the intralaminar delamination developing through the strip length. Furthermore, although the Kevlar® fibers still exhibited a tensile failure mechanism, an increased number of fibers were detected in Figure 2.9*f* to fracture locally rather than have several cracks propagating through the fiber length. Except for the fibrillated fibers, the damages developed in the S-Glass FRC strips at different impact velocities had similar characteristics with that of Kevlar® FRC strips, which was illustrated in the supplementary data as Figure 2.10. Compared with fibers in the Kevlar®/m T&J composite strips, fibers in the Kevlar®/SC-15 composite strips experienced more severe debonding with the matrix, which is consistent with the real-time observation mentioned in Section 4.2. Fracture morphologies of Kevlar®/SC-15 composite strips impacted at different velocities were shown in Figure 2.11.

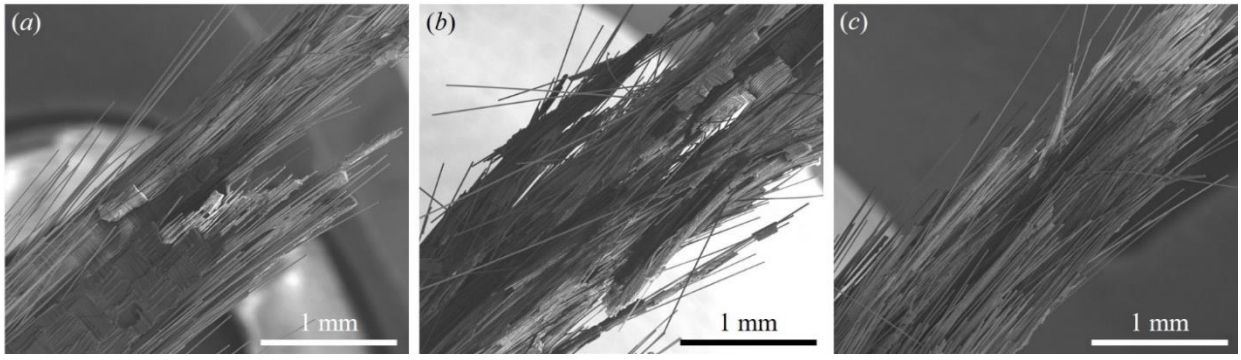

Figure 2.10**.** Post-fracture images of S-Glass/m T&J composite strips impacted at different velocities. (*a*) v_0=236 m/s; (*b*) v_0=425 m/s; (*c*) v_0=573 m/s.

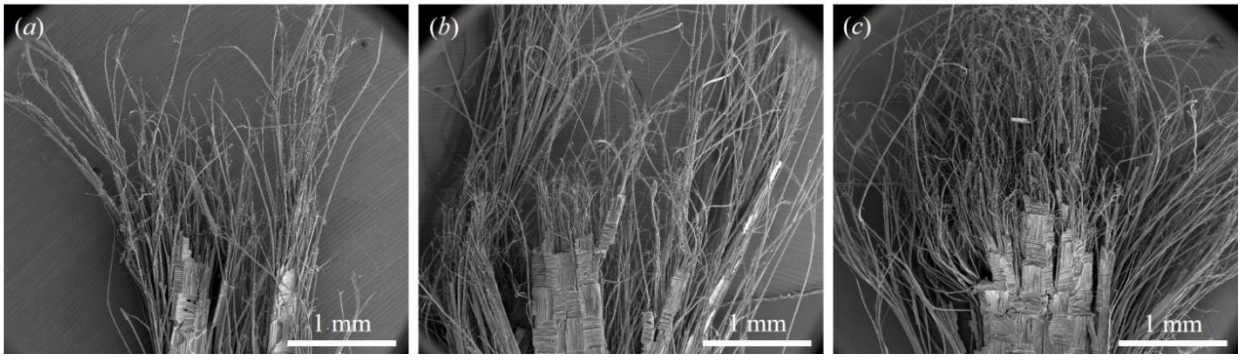

Figure 2.11**.** Post-fracture images of Kevlar®/SC-15 composite strips impacted at different velocities. (*a*) v_0=187 m/s; (*b*) v_0=344 m/s; (*c*) v_0=481 m/s.

2.5 Discussions

2.5.1 Critical velocity region of each type of composite strip

A critical velocity region [v_c^l , v_c^u] was defined in [32] to describe different failure mechanisms of yarns under impact at various velocities, where v_c^l and v_c^u represented the lower and upper limits of the critical velocity region, respectively. This concept can be introduced to conclude the composite strip behaviors under the transverse impact. When the impact velocity was lower than v_c^l , the composite strip was loaded with minimum damage developed upon the projectile/strip contact. The strip globally formed a tent-like configuration. Tensile deformation was fully developed inside the composite material until it fractured in front of the projectile, which happened after the transverse wave propagated out of the field of view. When the projectile impacted the composite strip at a velocity between v_c^l and v_c^u , the composite strip experienced a partial failure in the transverse direction during impact, followed by intralaminar delamination. The stiffness of the strip was thus reduced, and the global configuration of the strip changed quickly from a tent shape to a dome shape. The transverse wave can still propagate out of the field of view. Material failed in tension beside or in front of the projectile. More damages were developed in the strip to dissipate the kinetic energy of the projectile. Impacted by the projectile at a velocity above v_c^u , the composite strip was locally shaped into a ridge-like geometry and tensioned to fracture near the projectile before the transverse wave propagated out of the field of view. The damage extent was lower than that when the impact velocity was within v_c^l and v_c^u . Obviously, v_c^l relates the damage extent and energy dissipation to the impact velocity, while v_c^u indicates the instant fracture of the composite strip. Moreover, such a definition enables to quantify the critical velocity directly through the global geometry and failure mode of the composite strip during impact. It is important to note that the damage extent mentioned in this work was based on the observable mesoscale failure of the strip. Before the impact velocity reached v_c^l , there might also be microscale matrix cracking, fiber breakage, or fiber/matrix interfacial debonding inside the strip, which was not counted here.

The critical velocity regions of four types of composite strips were summarized in Figure 2.12. The aforementioned three failure modes were denoted as 1, 2, and 3, which were corresponding to the

impact velocities below, within, and above the critical velocity region, respectively. Each demarcation was determined by averaging the velocities of two adjacent shots. To obtain the accurate two boundaries of the critical velocity region, impact experiments were performed as many times as possible. The maximum velocity difference between the two shots used to define the upper or lower limit of the critical velocity region was less than 45 m/s, although most boundaries were calculated within a range differing by less than 10 m/s.

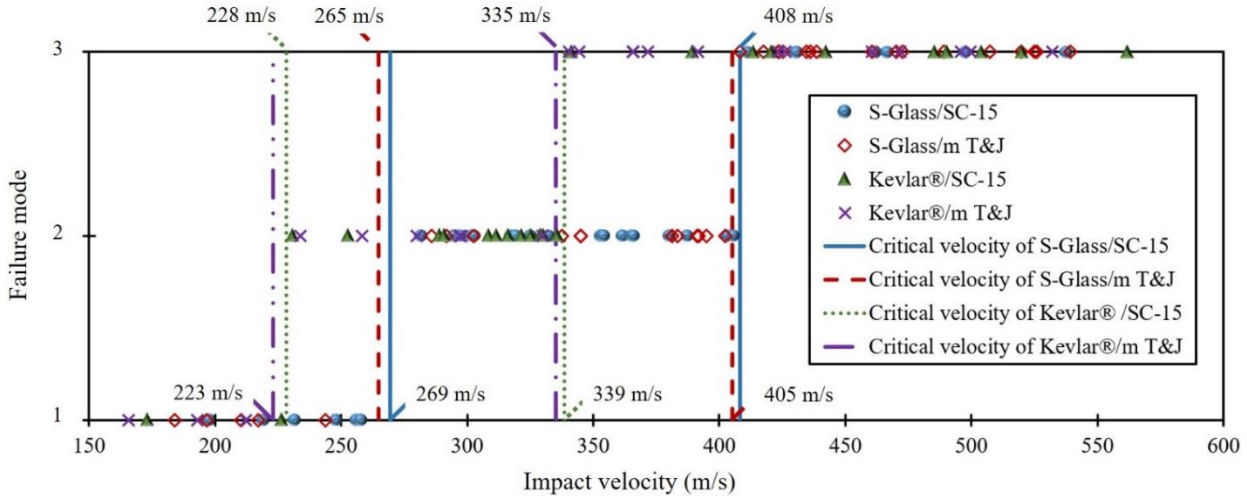

Figure 2.12**.** Critical velocities of different composite strips.

As shown in Figure 2.12, v_c^l of S-Glass/SC-15 and S-Glass/m T&J composite strips were 269 and 265 m/s, respectively. In contrast, v_c^l of Kevlar®/SC-15 and Kevlar®/m T&J composite strips were 228 and 223 m/s, respectively. This reveals that the Kevlar® strips developed damage much more easily upon impact. Moreover, compared with S-Glass FRC strips, Kevlar® FRC strips had a narrower critical velocity region, which means the intralaminar delamination damage was more sensitive to the impact velocity. This can be validated by comparing the damage extent through the morphologies of the damaged S-Glass/SC-15 strip in Figure 2.3*b* with that of the Kevlar®/SC-15 strip in Figure 2.4*b*. v_c^u of the S-Glass FRC strips were ~22% larger than that of the Kevlar® FRC strips. On the other hand, the composites with the same reinforcement fibers but the two different matrixes were uncovered to possess a less-than-3% difference in both the lower and upper limits of the critical velocity region. This indicates that the composite strip's critical velocity mainly depended on the reinforcement fiber type, while the matrix type played a less influential role. The results are reasonable since the strengths

and moduli of the matrixes were reported to be ~1% of that of the fibers, as summarized in Table 2.1. Furthermore, compared with the case of impact on a thick composite panel, the matrix in the composite strip was in such a small amount that it may not exhibit distinctive energy dissipation capability under impact. It is noted that for each fiber type in this work, the composites made by either the SC-15 or m T&J matrix did not have a significant difference in the fiber volume fraction, which is shown in Table 2.2. It is based on these fiber volume fractions that the matrix type was measured to have a negligible effect on the critical velocity of composite strips. However, a possibility that the matrix volume fraction in composites changes the ballistic resistance of composite materials should be noted.

2.5.2 Wave propagation in the composite strips during impact

As mentioned in Section 1.3, Smith's theory has been adopted to study the deformation and failure of yarns during impact [81, 34, 84], and the predicted wave propagation in the yarn matched well with experimental results at low-velocity impacts [27, 84]. In this study, the wave propagation in the composite strip was tracked in the experiment, and the tent angle of the deformed strip was measured, which was the compared with Smith's predictions.

Figure 2.13 describes the transverse wavefronts in composite strips in different impact events. In order to avoid the effect of tension-induced fiber breakage on the strip geometry and also ensure that the transverse wave propagation occurred within the camera frame, only the first several microseconds after the projectile/sample contact were selected to track the transverse wave, namely 16-20 μs for $v_0 < v_c^l$, 12-16 μs for $v_c^l \le v_0 \le v_c^u$, and 4-6 μs for $v_0 > v_c^u$. The zero point in Figure 2.13 represents the two corners of RCC projectiles where the transverse waves were activated. As the transverse waves propagated upwards and downwards, the positions of wavefronts were denoted

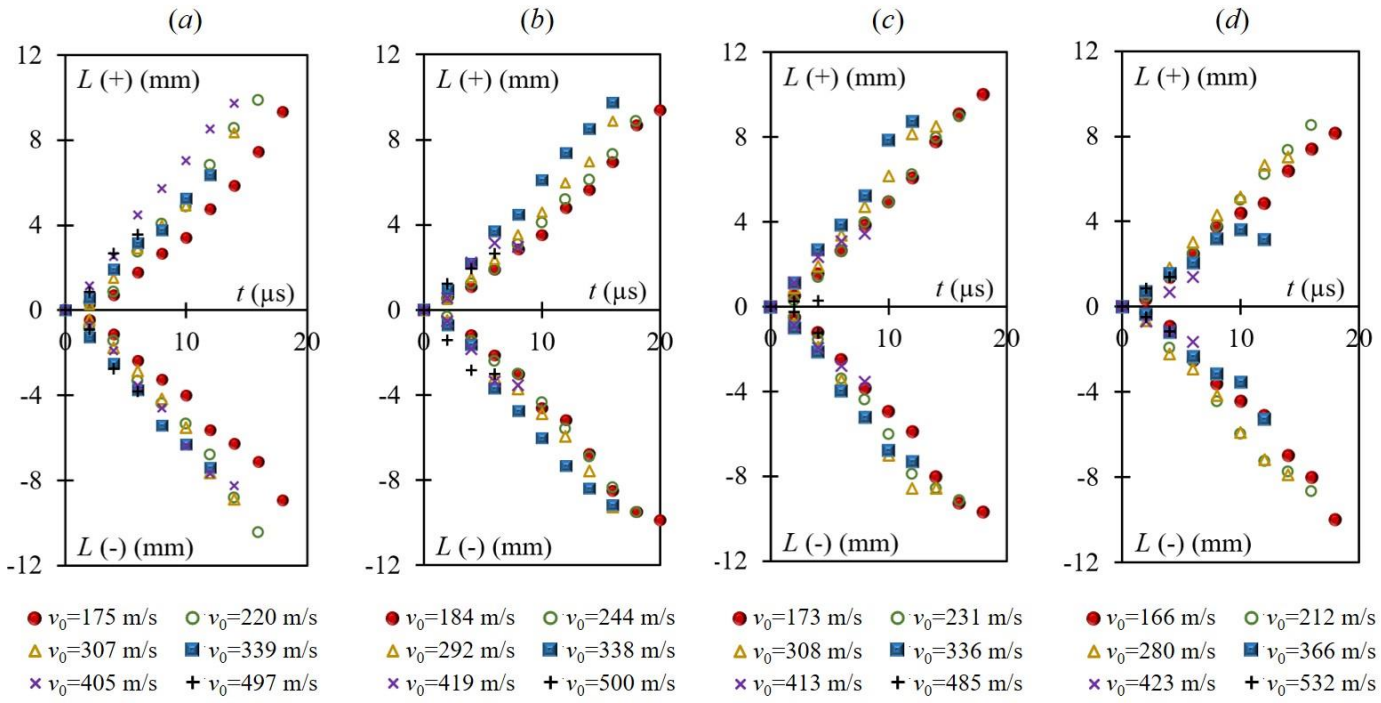

Figure 2.13. Transverse wave positions in different samples impacted at various velocities. (*a*) S-Glass/SC-15; (*b*) S-Glass/m T&J; (*c*) Kevlar®/ SC-15; (*d*) Kevlar®/m T&J.

as positive and negative, respectively. Transverse wave speed was then experimentally determined by measuring the average slope of the fitted L^{+}-t and L^{-}-t straight lines in Figure 2.13 and plotted against the impact velocity in Figure 2.14. The relationship between the transverse wave speed in the composite strip and impact velocity was also theoretically determined according to Eqs. (3) and (4). The elastic wave speed of the composite strip used for the calculation can be found in Table 2.2. Figure 2.14 compares experimental results with theoretical solutions. It is revealed that the transverse wave propagations in different composite strips were consistent with the predictions by Smith's theory when the impact velocities were less than v_c^u. Above the critical velocity region, the strips failed abruptly underneath the projectiles, making the transverse wave difficult to propagate.

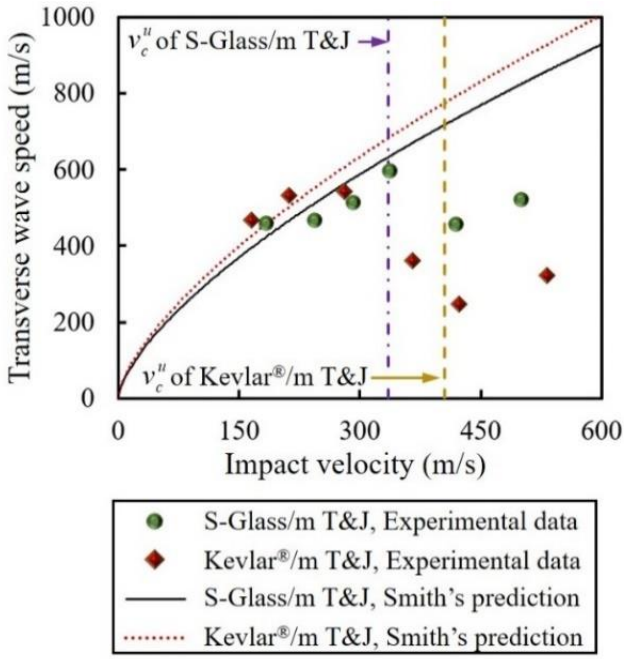

Figure 2.14. Transverse wave speed in composite strips.

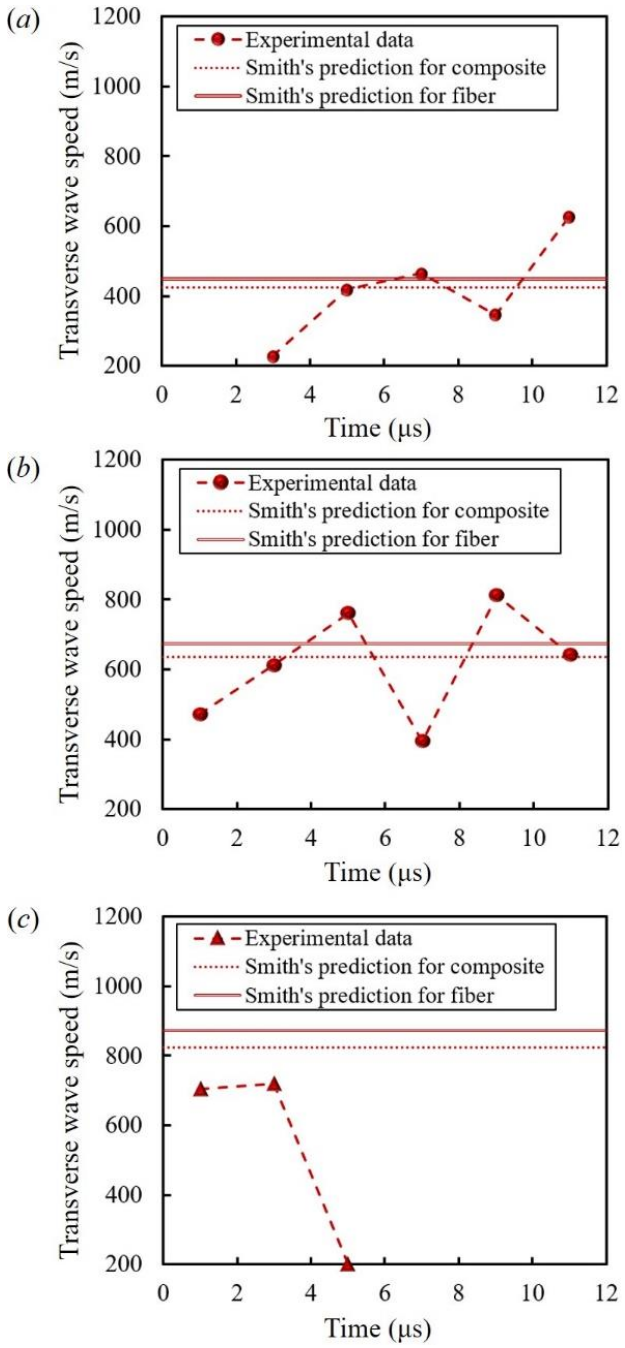

Figure 2.15. Transverse wave speeds in S-Glass/m T&J composite strips impacted at different velocities. (*a*) v_0 = 184 m/s; (*b*) v_0 = 292 m/s; (*c*) v_0 = 500 m/s.

The variation of the transverse wave speed was tracked in single shots and compared to Smith's predictions in Figure 2.15. The fibers' and composite strips' transverse wave speeds predicted by Smith's theory were calculated based on the corresponding fiber properties in Table 2.1 and composite properties in Table 2.2, respectively. For each impact experiment, the transverse wave speed was

measured every 2 μs by computing *dL*/*dt* between every two points in Figure 2.13. The timing spacing of 2 μs allows the transverse wavefront to travel to a sufficiently large distance that can be adequately measured by the software ImageJ. Besides, only the transverse wave speeds before 12 μs were presented, which considered a longitudinal stress wave propagation process that a longitudinal stress wave was generated upon the initial projectile/strip contact and reflected at the clamping area, and then the reflected stress wave returned to the projectile corner. As shown in Figures 2.15*a* and 2.15*b*, when v_0 was below and within the critical velocity region, respectively, despite a limited number of sampling points, it seems to have a trend that the transverse wave speed was initially close but smaller than Smith's prediction while then oscillated around the Smith's predictions until the returning of the longitudinal wave reflected back from the clamp. When $v_0 > v_c^u$, the transverse wave propagated no longer than 5 μs and then the strip failed, as demonstrated in Figure 2.15*c*.

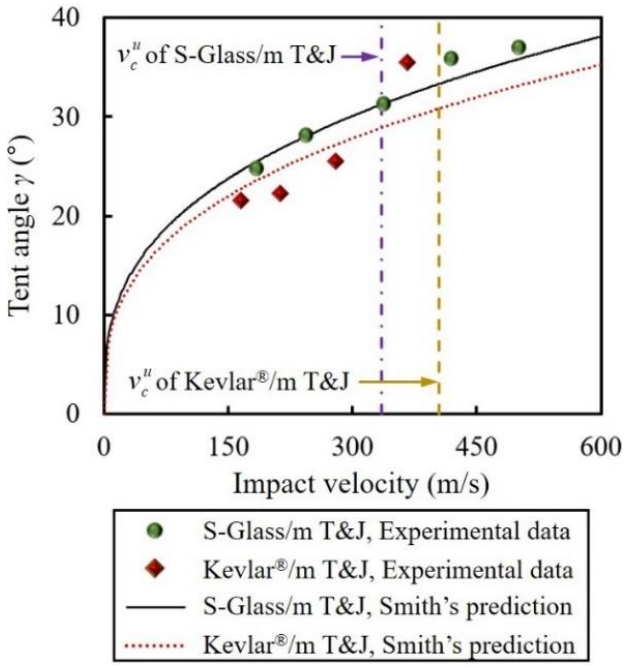

Figure 2.16. Tent angles formed in composite strips.

During the transverse wave propagation, the tent angle varied accordingly, which is depicted in Figures 2.16-2.17. Computation of the tent angle at each impact velocity was according to Eqs. (4) and (5). Smith's predictions for different composite strips in Figure 2.16 were determined based on the elastic wave speed of corresponding composites in Table 2.2. On the other hand, S-Glass fiber and S-Glass/m T&J composite properties utilized to obtain Smith's predictions in Figure 2.17 can be found

in Table 2.1 and Table 2.2, respectively. Impacted at a velocity below v_c^u, the strip initially formed a tent angle larger than Smith's prediction for composite strips. The angle then decreased to Smith's prediction.

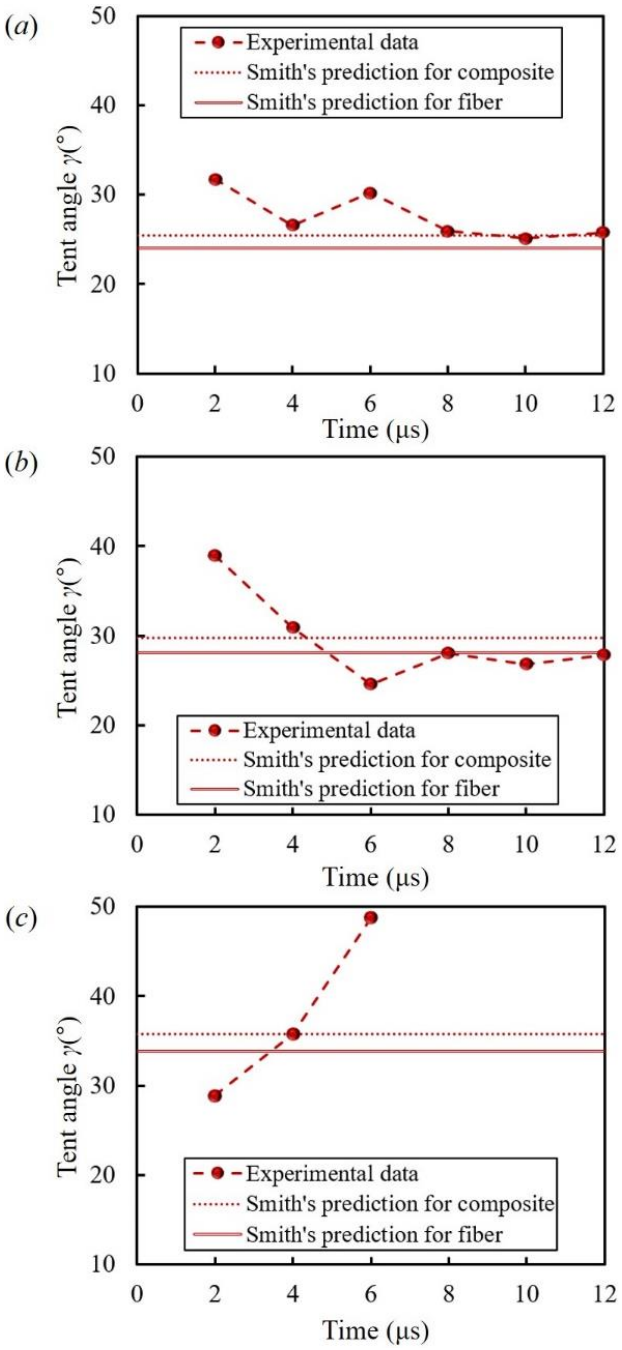

Figure 2.17. Tent angles formed in S-Glass/m T&J composite strips impacted at different velocities. (*a*) v_0 = 184 m/s; (*b*) v_0 = 292 m/s; (*c*) v_0 = 500 m/s.

Compared with single fibers, composite strips were predicted to have a lower transverse wave speed and larger tent angle during impact, which was presented in Figures 2.15 and 2.17. This indicates that introducing the matrix may prevent the tensile strain from fully developing in fibers and intensify the localized deformation, thereby leading to a lower v_c^u. However, the utilization of matrix is still necessary since the matrix bonds fibers to form composite structures with sufficient transverse stiffnesses that can be applied to actual products. Instead of not using the matrix, the design of ductile matrix may be an alternative scheme so that the manufactured composite structures can be flexible enough to deform during impact and dissipate more kinetic energy from the projectile [85-86].

2.5.3 Load history in the composite strip

Figure 2.18 presents the load histories of representative S-Glass/m T&J composite strip samples. The impact velocities were namely 197, 292, and 461 m/s, which are below, within, and above the critical velocity region, respectively. Failure behaviors of these strip samples have been presented in Figure 2.5. For the cases when the impact velocity v_0=197 and 292 m/s, image sequences showing more detailed material behaviors were extracted from Figure 2.5 and reproduced with shorter inter-frame spacings in Figure 2.19*a* and Figure 2.19*b*, respectively. The first image of each image sequence indicates the initial contact between the projectile and composite strip sample when a longitudinal stress wave was generated. The longitudinal wave then propagated from the projectile corner to the clamping area at a velocity of 4365 m/s shown in Table 2.2. The time duration was calculated to be 5.73 μs. Before arriving at the load cell, the longitudinal wave passed through the grip with a length of 22.9 mm (0.9 inches), which took 4.50 μs computed based on the elastic wave speed of aluminum of ~ 5092 m/s. It is also noted that the stress wave needed to transmit a layer of epoxy glue when traveling from the strip end to the grip. Due to the small thickness of the glue (less than 300 μm), this process should not take more than 3 μs. Therefore, the load recording was estimated to start at t=~10-14 μs after the projectile/sample contact. The image sequences in Figure 2.19 were approximately correlated with the load signals in Figure 2.18 starting from t=12 μs. It is revealed that the strip sample had a lower peak load magnitude when v_0=292 m/s, compared with the case when the impact velocity was 197 m/s. This is possibly due to the partial failure of the strip. The fractured material cannot transmit tensile load to the load cell, so the load magnitude was decreased. Furthermore, the loading duration was also reduced. As shown in Figure 2.19, the tensile fracture of the strip sample impacted at v_0 = 197 m/s was observed at t = 62 μs, while the sample had already fractured at t = 33 μs when v_0 = 292 m/s. When the impact velocity was 461 m/s, the strip was significantly damaged upon impact (see Figure

2.19*c*). The stress wave generated at the projectile/strip contact had a very short duration. It was highly dissipative in the composite strip and became non-detectable when it arrived at the load cell. Therefore, no load signal was shown in Figure 2.18 for the case when v_0=461 m/s.

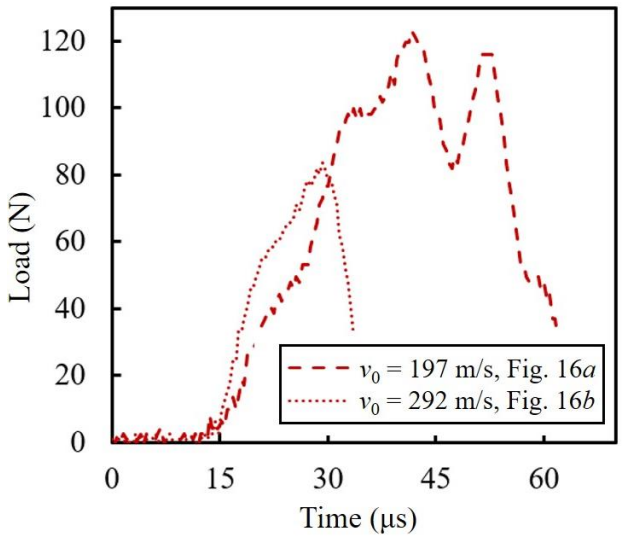

Figure 2.18. Load histories recorded by the load cell for S-Glass/m T&J composite strips impacted at different velocities.

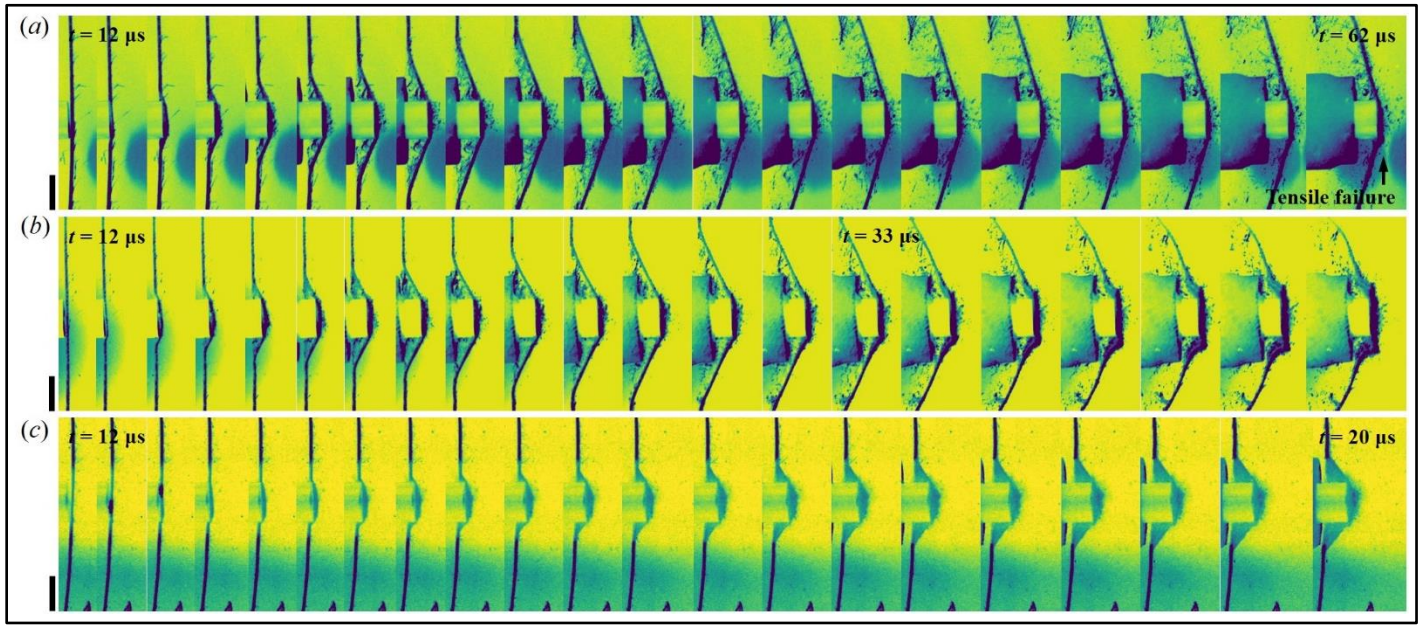

Figure 2.19. Physical behaviors of S-Glass/m T&J composite strips corresponding to the load histories in Figure 2.18 when transversely impacted at different velocities. (*a*) v_0 = 197 m/s, inter-frame spacing is 2.5 μs; (*b*) v_0 = 292 m/s, inter-frame spacing is 1.5 μs; (*c*) v_0 = 461 m/s, inter-frame spacing is 400 ns. The scale bar is 5 mm.

2.5.4 Critical velocities of single fibers, yarns, and FRC strips and ballistic limits of fabrics and composite panels

From the FRC strip transverse impact results obtained in this paper, we noticed that the critical velocities are significantly lower than those of the yarns and fibers. To examine this issue further, we collected available literature data on transverse impact critical velocities of single fibers, yarns, and FRC strips and ballistic limits of fabrics and composite panels with aramid and glass fiber reinforcements. The results are presented in Figure 2.20. It should be noted that the literature data were not obtained under identical conditions. We can only use them to identify qualitative trends. From the data in Figure 2.20, we see that the general trend exists: as the size scale increases from a single fiber to a single-ply composite panel, the critical velocity or ballistic limit decreases. We believe that the fiber mobility and structural interactions, such as weaving patterns, affect the full utilization of the properties of each single fiber, and thus degraded the critical velocity or ballistic limit. We also noticed that increasing ply numbers of fabrics and composite panels can significantly improve the V_{50}.

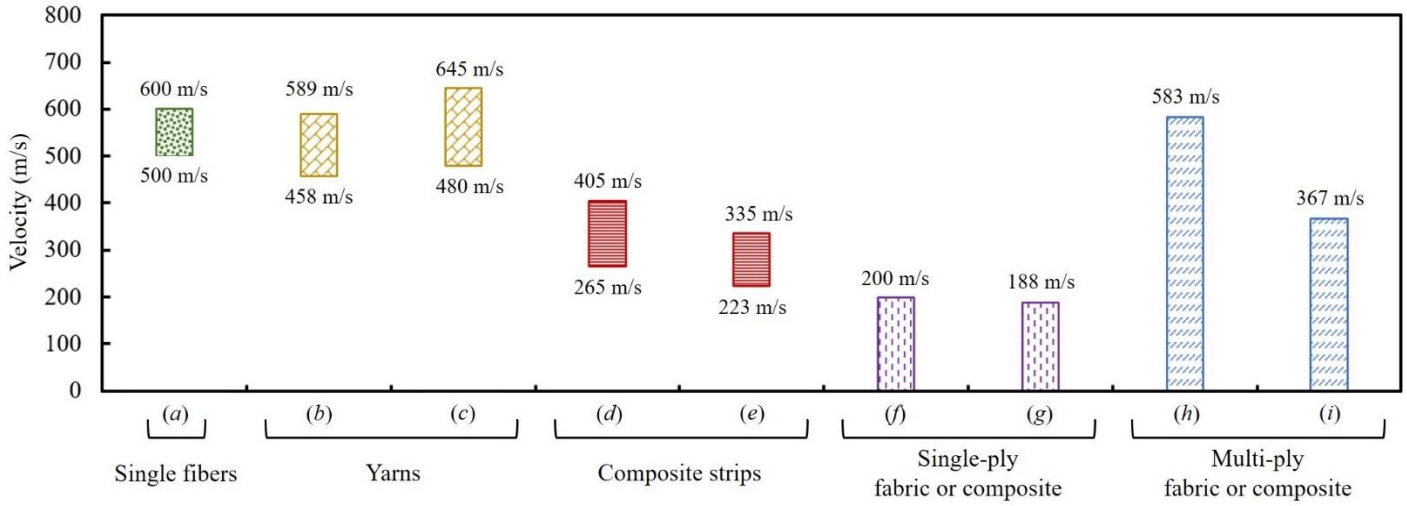

Series Name	Material	Sample size	Projectile	References
a	Single Kevlar® KM2 fibers	Length: 2.25 mm	Spheres; Diameter: 28.9 μm	Xie et al. [61]
b	Twaron® 2040 yarns	Length: 190 mm	Round nose; Diameter: 2 mm	Lim et al. [21]
c	Kevlar® KM2 yarns	Length: 850 mm	FSPs, 0.30 cal	Hudspeth et al. [54]
d	S-Glass/m T&J composite strips	Length: 50 mm; Width: 1 mm	RCCs, 16 grain	This study
e	Kevlar®/m T&J composite strips	Length: 50 mm; Width: 1 mm	RCCs, 16 grain	This study
f	Single-ply woven Kevlar® 29 fabrics	Length: 147 mm; Width: 147 mm	FSPs (size was not clear)	Cunniff [62]
g	Single-ply woven S-2 Glass/SC-15 composites	Diameter: 203 mm	RCCs, 16 grain	Meyer et al. [31]
h	Multi-ply woven Kevlar® 29 fabrics	U.S. Army personnel armor system for ground troops (PASGT) vest	RCCs, 16 grain	Cunniff [64]
i	Multi-ply woven S-2 Glass/SC-15 composites	Diameter: 101.6 mm; 22 plies	RCCs, Diameter: 12.7 mm	Gama et al. [63]

Figure 2.20. Ballistic limits of single fibers, yarns, composite strips, and single-layer and multi-layer woven fabrics and composites.

2.6 Conclusions

Transverse impact experiments on FRC strips were performed in this study to isolate interactions between plies and tows and provide insight into the fundamental material failure mechanism involved in transverse impact on large-scale FRC structures. Four single-ply unidirectional composite panels, namely S-Glass/SC-15, S-Glass/m T&J, Kevlar®/SC-15, Kevlar®/m T&J, were manufactured, sectioned into composite strips, and characterized by optical photography, 3D synchrotron X-ray computed tomography and SEM. Each composite strip was then assembled inside a sample holder and transversely impacted by an RCC projectile launched by a gas gun and speeded up to the velocity ranging from ~150 to 600 m/s. The failure progress of the strip was captured in real time from the side by high-speed optical imaging. By switching different close-up lens in front of the high-speed camera, the global deformation and failure of the strip as well as localized material behavior near the projectile corner were recorded. A pair of load cells installed at the sample ends enabled to detect the tensile load developed in the composite strip during impact. Fractured composite strip samples were collected and characterized by SEM. The main findings are concluded as below:

1) Under transverse impact, both the two FRC strips failed in tension. S-Glass FRC strips were observed to fail ahead of the RCC projectiles' flat surfaces while Kevlar® FRC strips fractured at the projectile corners.
2) The concept of critical velocity region, $[v_c^l, v_c^u]$, previously used for yarn impact, can be introduced to describe three failure modes captured in the transverse impact experiments on the composite strips. The three failure modes were mainly differentiated by no, partial, and complete failure of the composite strips after contacting the projectiles.
3) The damage extent of the composite strip increased with the impact velocity and reached the maximum at v_c^u. Above v_c^u, the damage extent decreased as the impact velocity continued to rise.
4) Wave propagations in the composite strips during impact were quantified and compared with Smith's theory.
5) The ballistic limit depended on the fiber material rather than the matrix type based on the fiber volume fraction of composites in this work. In contrast, the matrix in composites was uncovered to decrease the transverse wave propagation and intensify the local deformation during impact.

6) Load history in the strip was measured in the experiment during impact. When the impact velocity increased from a value below v_c^l to a value within the critical velocity region, both the peak load magnitude and loading duration decreased. When the impact velocity was above v_c^u, no load signal was detected because the strip failed locally in a short time, and the stress wave was dispersed and dissipated on its way to the load cell.

7) A general trend was revealed that the critical velocity and ballistic limit decreases as the size scale increases from a single fiber to a single-ply composite panel. Future work on the impact responses of composites needs to investigate materials at different scale levels under identical conditions so that the results can be comparable.

CHAPTER 3. REVERSE IMPACT ON S-GLASS COMPOSITE STRIPS BY ROUND-NOSE PROJECTILES WITH DIFFERENT NOSE DIAMETERS

3.1 Introduction

The transition of a fabric and FRC laminate's failure from the conical deformation to the local perforation is not only governed by the impact velocity but also coupled to the projectile nose geometry and dimension. Impact experiments on aramid fabrics by Montgomery et al. [90] and Tan et al. [91] reveal that a sharper projectile was easier to shear the yarns and cause a pronounced fabric windowing, thereby reducing the energy absorption and ballistic limit of the fabric or FRC laminate. Abbott [92] conducted impact experiments on Nylon 6/6 composite laminates and undisclosed dry aramid fabrics, reporting a decreasing V_{50} as the chamfer angle of the conical-nose projectiles and FSPs increased. Such a variation of V_{50} against the projectile's chamfer angle was expected to be due to the increased local cutting and shear explained by Prosser [93]. By utilizing a razor blade, 0.30-cal FSP, and 0.30-cal round-nose projectile, Hudspeth et al. [32] impacted the Kevlar® yarns at a variety of velocities. The recovered failure surface of the yarn indicates a local shear failure mode for the impact by a razor blade above the critical velocity, while the yarn failed in fibrillation under the impact by the round-nose projectile. Furthermore, the critical velocity experienced a reduction as the projectile changed in order from the razor blade, FSP, to the round-nose projectile. The difference in the failure mode and critical velocity were speculated to be the varying stress concentration due to the radius curvature of the projectile nose. Lim et al. [94] then examined the stress concentration developed in Twaron® yarns under the indenters with different nose diameters. The effect of the projectile nose diameter on the critical velocity and failure mode of the Twaron® yarns was also investigated [35].

This work studies the projectile nose diameter effect on the impact response of the composite strips. The composite strips were sectioned from a single-ply S-glass/SC-15 composite panel manufactured in Section 2.2. Projectiles with three nose diameters of 4 μm, 40 μm, and 400 μm were prepared to apply the impact loadings to the composite strips. A reverse impact technique was adopted by impacting the composite strip samples onto static projectiles. The deformation and failure processes of the composite strips were captured by a high-speed camera from the side. The

critical velocity regions of the composite strips were quantified. Finally, the influence of the projectile nose diameter on the composite strip's failure at the critical velocity was discussed.

3.2 Materials

The composite material investigated in this study is S-glass/SC-15 composite. As an inorganic reinforcement, S-glass fibers are regarded as an isotropic material with super strength in all directions, which is different from the many polymer fibers in yarns or fabrics studied by previous researchers [32, 35, 94]. Consequently, although there is a transition from the tensile fracture to local rupture, the detailed local failure phenomenon and mechanism of the material may differ from previous researchers' observations, as revealed in conclusion 1 in Chapter 2. The composite strip samples were sectioned from the same composite panel mentioned in Section 2 of Chapter 2. Therefore, the composite strip samples have the same V_f and mechanical properties in Table 2.2. The properties of the fibers and matrix can also refer to Table 2.1. The composite strips were machined into two lengths of 30 mm and 50 mm, respectively. The samples had an identical width of 1 mm and an average thickness of 178.13 ± 10.56 μm, which is identical to that presented in Section 2.2.

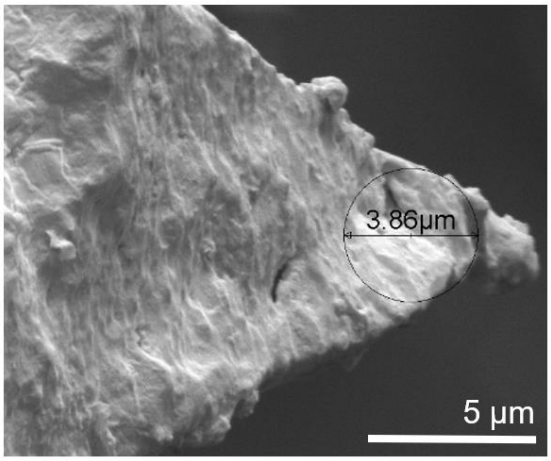

Figure 3.1. Dimension of the razor blade tip.

There were three types of projectiles utilized for experiments: razor blades, 40-μm- and 400-μm-diameter round-nose projectiles. These projectiles were the same as that used in the experimental work on Twaron® yarns by Lim et al. [35, 94]. It is noted that the razor blade is

actually a type of round-nose projectile with a nose diameter of ~ 4 μm, which was measured by the SEM and shown in Figure 3.1. The other two projectiles are custom-made projectiles provided by PTI Machine, Inc. (Delta, PA, USA).

3.3 Experiments

As shown in Figure 2.7, when assembling a 10X objective lens to observe the local failure mechanism close to the RCC projectile's corner, a normal impact technique made the composite sample easily moved outside the camera window by the projectile. To make the sample always appear within the observation field, a reverse impact technique was employed in this study. In each event, the camera with the close-up lens was focused on a static projectile. The composite sample was mounted on a sabot and accelerated to impact the static projectile. During impact, the camera captured the composite strip's deformation and failure in the surrounding of the projectile nose.

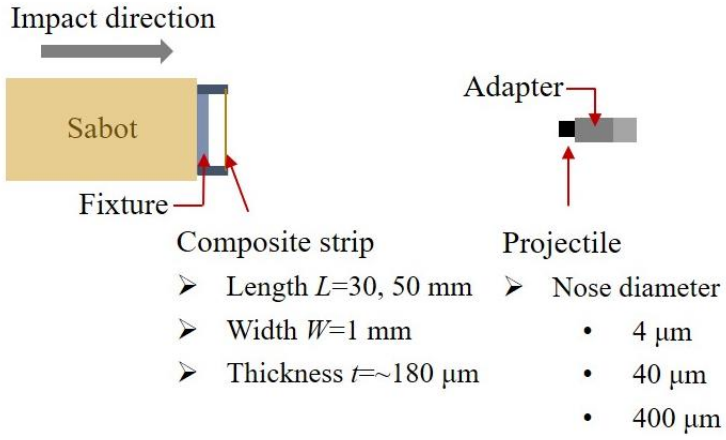

Figure 3.2. Schematic of the loading configuration.

Figure 3.2 schematically illustrates the loading configuration. The first step was to make sabots for experiments. By mixing the two liquid parts of FOAM-iT!™ 15 (Smooth-On, Inc., Macungie, PA, USA) and pouring the mixture inside a steel mold, followed by a two-hour curing process at room temperature and atmospheric pressure, a rigid polyurethane foam sabot was obtained in Figure 3.3. The cylindrical sabot had a diameter of 63.5 mm (2.5 inch) and a length of 6.0 inch. It was hollow at one end with a wall thickness of 6.35 mm (0.25 inch). Second, two types of fixtures were designed and 3D-printed, which enabled to mount the composite strip samples

with different lengths. As shown in Figure 3.3, the 30-mm and 50-mm composite strip samples were fixed onto the corresponding fixture arms at two ends by pouring SC-15 matrix into the cavities on the fixture and making the composite strip samples embedded in the cured SC-15 matrix. Afterward, each fixture with a sample was adhered to a sabot by the epoxy glue. During the impact experiment, the composite strip assembly was projected by a single-stage light gas having a 63.5-mm-diameter barrel, as presented in Figure 3.4*a*. Two pairs of laser diodes and sensors were installed at the end of the barrel to measure the composite strip's velocity when it flew out of the barrel. The impact event occurred within a steel chamber attached to the end of the barrel. The projectile was attached by the plasticine to a steel adapter which was rigidly connected to an aluminum backstop. The steel rod protruded through a 19.0-mm (0.75-inch) hole on a ballistic shield placed in front of the aluminum backstop, which can be seen in Figure 3.4*b*. The ballistic shield served as a barrier and successfully halted the movement of the sabot during the impact experiment. The projectile assembly was placed close to the gun barrel end to ensure that the actual impact velocity can be approximated to the measured velocity by the laser diodes and sensors. As shown in Figure 3.4*a*, the sides of the chamber were covered by the polycarbonate plates, allowing the high-speed camera to capture the real-time deformation and failure of the composite strip in the impact event. The Cordin flash lamp system mentioned in Chapter 2 was also used in the current experiments to provide a front light source to illuminate the composite strip. The impact velocity in this study was determined to change from 50 – 400 m/s, while the frame rate of the camera was adjusted to 1-5 million fps.

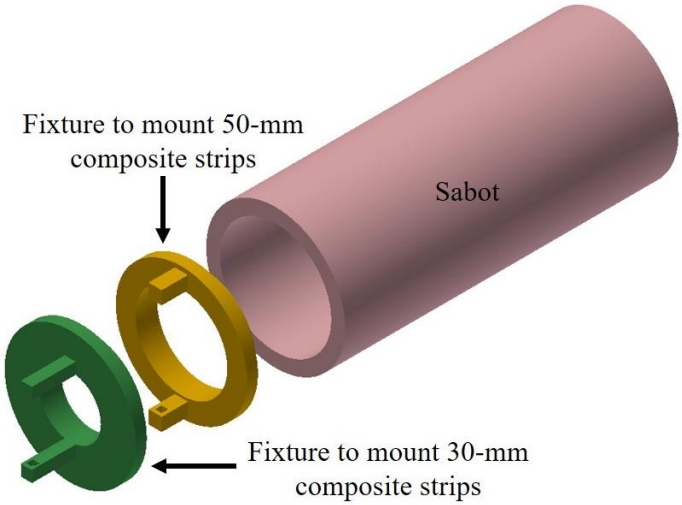

Figure 3.3. Schematic of the sabot and fixtures to mount 30-mm or 50-mm composite strips.

The triggering scheme was illustrated in Figure 3.4*c*. The impact experiment started from the solenoid releasing the gas to launch the composite strip assembly at t_0. The decreasing signal at the second laser diode and sensor was selected to trigger the oscilloscope at t_2. Afterward, the oscilloscope sent out another trigger signal to trigger the high-speed camera. The high-speed camera worked in a trigger-trigger mode. It sent out a rising signal immediately to activate the flash lamp to provide an instant illuminating source with a typical 42-μs ramp-up time to reach the full intensity. Due to a preset delay time carefully determined before the experiment (t_3-t_2), the camera did not start recording until the composite strip was close enough to the projectile. Finally, the entire impact event was successfully captured by the high-speed camera within 256 frames.

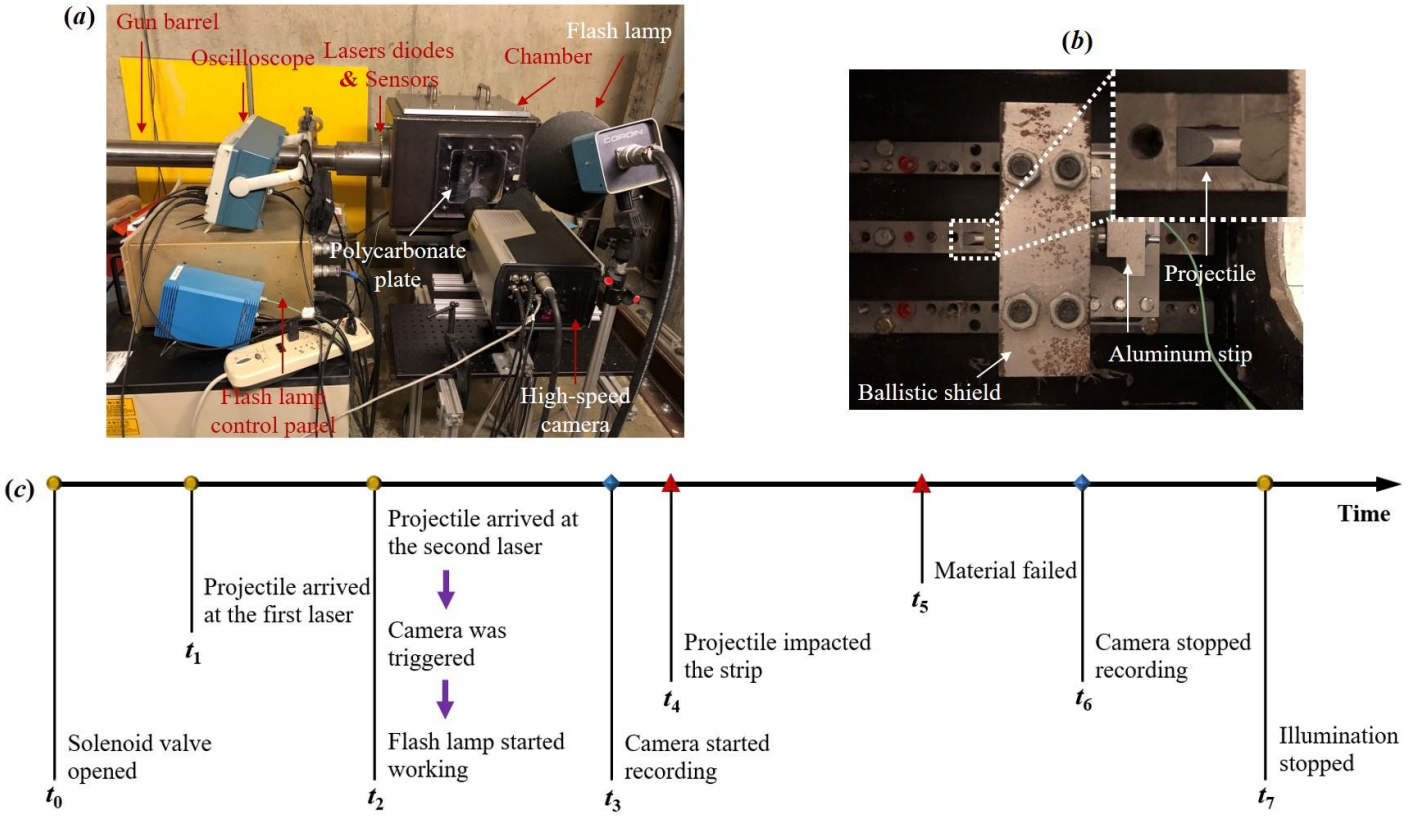

Figure 3.4. Reverse impact experiment on the composite strip. (*a*) Real picture of the experimental setup; (*b*) A close image at the projectile side; (*c*) Timing sequence used throughout the experimental duration.

3.4 Results and Discussions

3.4.1 Failure processes of the composite strips

In this section, the composite strips' failure processes under transverse impact by various projectiles are demonstrated in Figures 3.5-3.7. For each projectile type, the composite strip was identified to have three different failure modes as the impact velocity increased. Each failure mode was described with a representative composite strip sample. The effect of the projectile nose diameter on the composite strip's failure process is discussed.

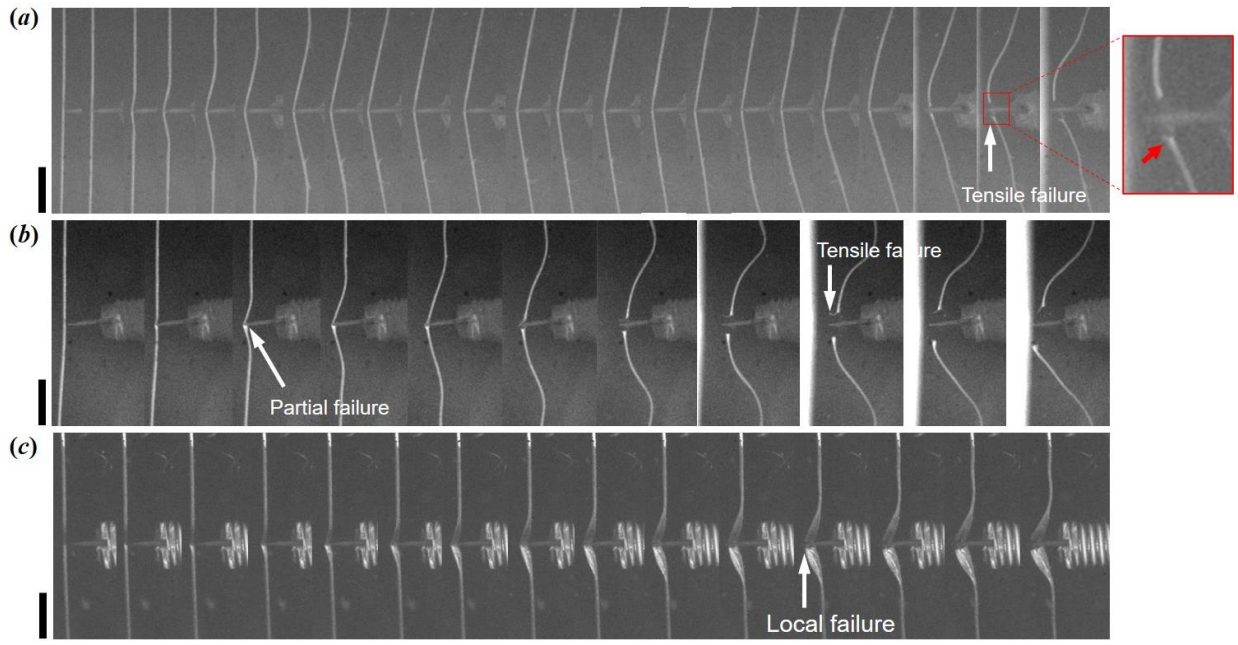

Figure 3.5. Failure processes of the composite strips by the razor blades at different impact velocities. (*a*) v = 72 m/s; (*b*) v = 134 m/s; (*c*) v = 165 m/s. The scale bar is 5 mm.

3.4.1.1 Failure processes of the composite strips by the razor blades

Figure 3.5 shows the failure processes of the representative composite strip samples by the razor blades. The razor blades were located at the right side of the image sequences, and the composite strip samples flew from the left and impacted onto the razor blades. As described in Figure 3.5*a*, the composite strip was transversely impacting a razor blade at a low velocity of 72 m/s. After the initial contact with the razor blade, longitudinal and transverse waves were generated at the same time but traveled with different velocities. As the transverse wave propagated to the

strip's ends, it deformed the composite strip into a tent-like shape. The sample then experienced tension along the fiber direction. Finally, the sample failed in front of the blade tip. The fracture surface had a small tail, indicating the tensile fracture despite a possible transverse compression by the blade tip. When the velocity of the strip sample was at an intermediate level of 134 m/s, the sample failed also due to tension, which can be identified by the small tail of the fracture surface in Figure 3.5*b*. However, at the initial contact of the strip sample with the razor blade, the strip was partially failed in the transverse direction by the razor blade. The rarefaction waves then quickly unloaded the strip sample. Therefore, as the transverse wave propagated to the strip ends, the geometry of the composite strip changed from a tent shape to a dome shape. Flying at a high velocity of 165 m/s, the composite strip sample seemed to be fully cut through by the razor blade, resulting in a very flat fracture surface in Figure 3.5*c*. The transverse wave can only propagate to a very short distance within the camera window before the strip failed.

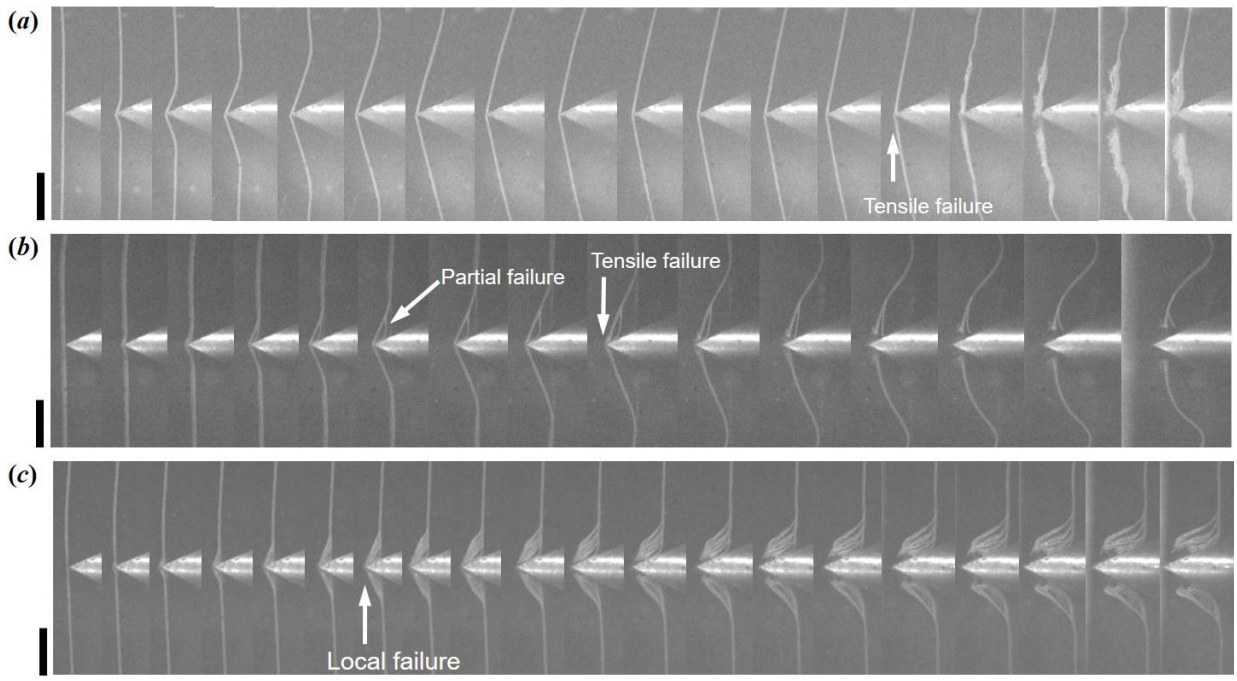

Figure 3.6**.** Failure processes of the composite strips by the 40-μm round-nose projectiles at different impact velocities. (*a*) *v* = 144 m/s; (*b*) *v* = 196 m/s; (*c*) *v* = 360 m/s. The scale bar is 5 mm.

3.4.1.2 Failure processes of the composite strips by the 40-μm round-nose projectiles

The composite strip's failure at a low velocity by a 40-μm round-nose projectile was similar to that by a razor blade. As shown in Figure 3.6*a*, after the transverse wave was activated and then propagated to the strip ends, the strip sample was deformed into a tent shape. With the longitudinal wave propagation back and forth within the sample, the tensile stress accumulated and finally failed the sample in front of the projectile nose. Figure 3.6*b* is the failure process of the composite strip at an intermediate velocity of 196 m/s. At a time 6 μs after the sample/projectile initial contact, the composite strip was identified to experience the intralaminar delamination. This is believed to be due to the partial failure of the composite strip by the projectile. Similar to that observed in Figure 3.5*b*, the rarefaction wave quickly unloaded the strip sample. The shape of the strip then changed from a tent to a dome as the transverse wave continued to propagate to the strip ends.

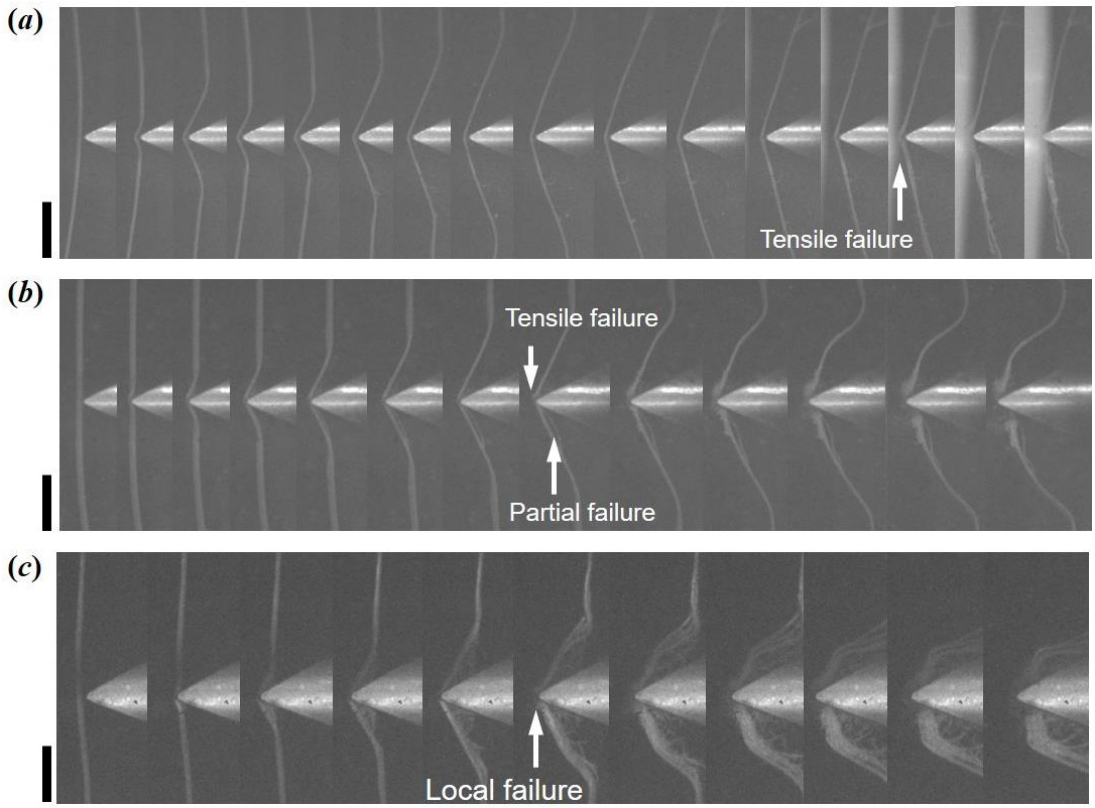

Figure 3.7. Failure processes of the composite strips by the 400-μm round-nose projectiles at different impact velocities. (*a*) v = 228 m/s; (*b*) v = 246 m/s; (*c*) v = 324 m/s. The scale bar is 5 mm.

When the composite strip's velocity was increased to 310 m/s, the strip failed locally before the transverse wave can propagate to the strip ends. The tail feature and significant delamination of the fracture surface in Figure 3.6*c* indicate the strip failed in tension.

3.4.1.3 Failure processes of the composite strips by the 400-μm round-nose projectiles

Failure processes of the composite strips by the 400-μm round-nose projectiles were quite similar to that by the projectiles with the 40-μm-diameter round noses. When the strip's velocity was at a low level, such as 228 m/s, the transverse wave deformed the strip into a tent shape (see Figure 3.7*a*). The strip failed in the projectile's front due to the accumulated tensile stress. In Figure 3.7*b*, the composite strip impacted a 20-μm round-nose projectile at a velocity of 246 m/s. The strip was partially failed by the projectile and delaminated. The geometry of the composite varied from a tent to a dome. If the strip's velocity was further increased to 324 m/s in Figure 3.7*c*, the strip experienced tensile breakage ahead of the projectile nose before the transverse wave can deform the entire sample. The failure was local, and the strip was significantly delaminated.

3.4.2 Critical velocity regions of the composite strips

By identifying the three failure modes of the strips moving at a variety of velocities, a critical velocity region can be determined for the impact by each projectile type, which is presented in Figure 3.8. The failure modes 1, 2, and 3 are corresponding to the three failure modes revealed in Section 3.4.1, namely as tensile failure in the projectile's front without initial damage upon the strip/projectile contact, a partial failure upon the initial strip/projectile contact and eventually the tensile failure in the projectile's front, and complete local failure before the transverse wave can deform the entire strip. The two velocity boundaries were calculated by averaging the nearest two impact velocities when the failure mode changed from one to another. It is revealed that both the lower and upper boundaries of the critical velocity region increased with the projectile nose diameter. This indicates that a sharper projectile was easier to induce initial damage to the composite strip. However, the mechanism generating the initial damage has not been identified. Besides, a sharper projectile rendered the ultimate failure of the strip more localized in the projectile's front. It is noted that at the upper boundary of the critical velocity region, the strips failed ahead of 40-μm and 400-μm round-nose projectiles because of tension. However, the strip's fracture surface by the razor blade had a different morphology from that by the other two

projectiles. Such a different fracture surface is suspected due to the transverse shear by the razor blade, which requires further investigation.

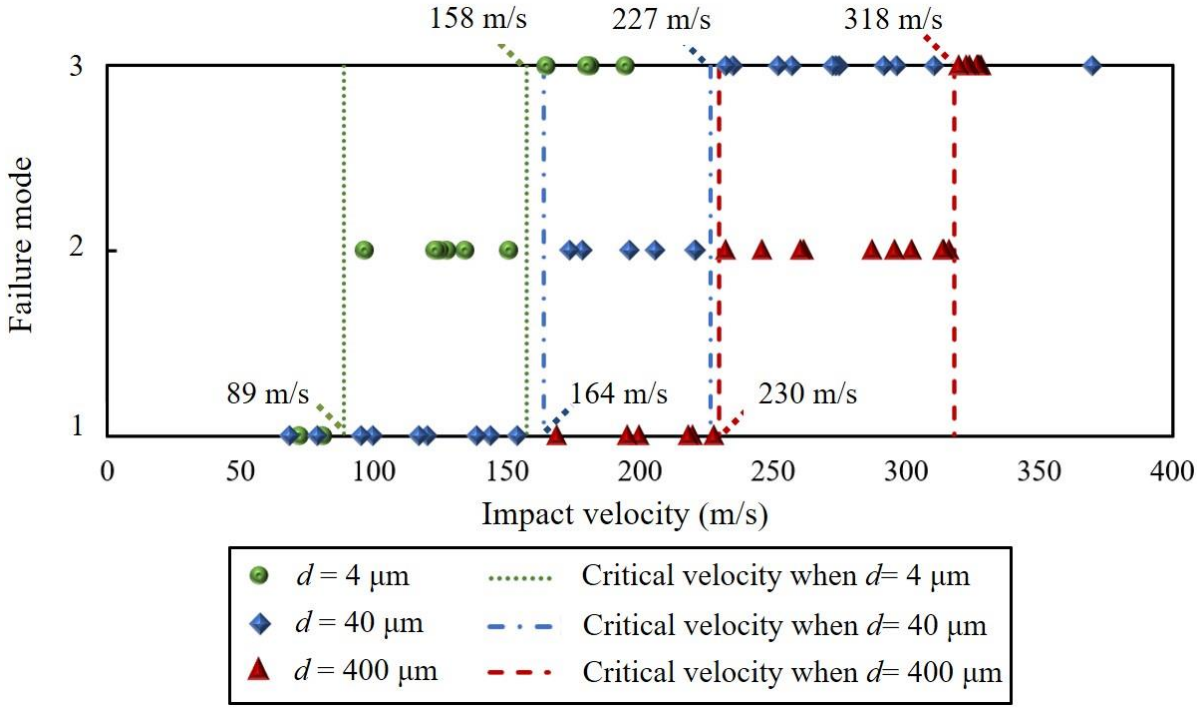

Figure 3.8. Critical velocity regions of the composite strips under impact by different projectiles.

3.5 Conclusions

In this study, transverse impact experiments were performed on S-glass/SC-15 composite strips by three types of round-nose projectiles with different nose diameters of 4 μm, 40 μm, and 400 μm. A reverse impact technique was utilized to impact the composite strip samples to the static projectiles. During each experiment, the camera with the lens was focused on the projectile nose from the side and captured the real-time deformation and failure process of the composite strip. The composite strip's failure by different projectiles and the corresponding critical velocity region were compared and discussed. The main findings are concluded below:

1) For each projectile type, there were three failure modes identified at different impact velocities. At a low velocity, the composite strip did not experience the initial damage upon impact. It was deformed into a tent and failed in tension in the front of the projectile. When the velocity was at an intermediate level, the composite strip was partially failed

by the projectile at its initial contact with the projectile. Its geometry changed from a tent to a dome, and the strip finally failed in tension ahead of the projectile. As the velocity further increased to a very high level, the strip failed locally at the projectile nose within a short time before the transverse wave can deform the strip to a tent or dome shape.

2) Both the lower and upper boundaries of the critical velocity region increased with the projectile nose diameter.
3) The partial failure of the composite strip by different projectiles within the critical velocity region needs further investigation.
4) At the upper boundary of the critical velocity region, the composite strip was failed in the front of the 40-μm and 400-μm round-nose projectile due to tensile fracture. However, the razor blade seemed to completely cut through the strip, which also requires further investigation.
5) The reverse impact technique is deemed to provide the possibilities to identify the local failure mechanisms of the composite strips at the critical velocities mentioned in (3) and (4).

CHAPTER 4. IN-SITU OBSERVATION OF CUTTING-INDUCED FAILURE PROCESSES OF SINGLE HIGH-PERFORMANCE FIBERS INSIDE AN SEM

The following chapter contains content reproduced with permission from the journal article:
Gao J, Nie Y, Lim BH, Kedir N, Chen W. (2019). A microscopic experimental method transversely loading on single high-performance fibers. *Experimental Mechanics*, 59(5), 669-679. DOI: 10.1007/s11340-019-00518-y
Gao J, Nie Y, Lim BH, Zhai X, Nie Y, Kedir N, Chen, W. (2020). In-situ observation of cutting-induced failure processes of single high-performance fibers inside an SEM. *Composites Part A: Applied Science and Manufacturing*, 131, 105767. DOI: 10.1016/j.compositesa.2020.105767

4.1 Introduction

Transverse impact experiments on aramid and UHMWPE yarns by Hudspeth et al. [32], Twaron® yarns by Lim et al. [35], and S-glass FRC strips in Chapter 3 revealed a transition from tensile fracture to local cut and shear when the projectile nose diameter decreased from the million-meter scale to ~4 μm. Tensile experiments on the fibrous materials have been well developed, providing an in-depth understanding of the tensile fracture of a variety of fibers [95-99]. However, the failure mechanism by transverse cut has not been explored sufficiently.

In an impact event, the cut-induced failure mechanism has significant differences from the mechanism of bullet penetration. First, in the actual application, during a bullet penetration event, the material is subject to the transverse impact by a light-weight projectile at a high velocity, while in the case of the knife attack, the instrument has a substantially larger mass but moves at a velocity generally less than 20 m/s [100]. Furthermore, upon impact, the bullet is likely to be flattened and interact with the target at a wide surface area. On the contrary, the sharp knife or spike remains rigid and less affected, "windowing" or displacing the materials and passing through the structure. Therefore, the textiles or composites withstanding ballistic impact may still not provide sufficient protection against shape-edge threats [101].

Cut resistance of fabrics made by commercialized fibers was investigated by Anctil et al. [102], including Kevlar®, Twaron®, Spectra®, Dyneema®, and Zylon®. A number of modification strategies were examined to obtain enhanced fabrics exhibiting increasing energy absorption during the cut, which contains incorporating ceramic and cermet coatings [103-104], impregnating fabrics with shear-thickening fluid [105-106] or thermoplastic films [107-108], laminating with

mental fabrics, placing woven wool fabrics over the penetration of armor panels [109]. The cut resistances of different materials were evaluated by peak load [110], penetration work [111], and "window" geometry [104]. However, in order to understand material failure mechanism under cut in more detail, research efforts on the yarn scale are required, which isolates the complicated inter-penetration between multiple layers and tows [32, 34-35, 94, 113-114] and focuses on the failure of the constituent material. The cut resistance of a yarn was reported to be highly sensitive to the indenter morphology [35, 46, 51] and related to the slicing angle [112-115] and pre-tension within the material [113]. As the indenter became blunter, the yarn was stressed, transitioning from axial tension and shear to tension and transverse compression. The initiation of fiber breakage was delayed, and higher peak stresses were sustained, which resulted in increased cut energy determined from the stress-strain curves. Shin et al. [113] observed a dramatically 75% drop in the cut energy when the slice angle only changed slightly from 90° to 82.5°. They attributed it to the sawing action and the continual exposure of a new sharp blade edge to the yarn. They also demonstrated that pre-tension shifted the stress-strain curves of a Zylon® yarn to a lower value and led to earlier fiber failure, therefore decreasing the cut energy.

Similar to the experiments on composite laminates, the interaction between yarns makes it challenging to identify the material failure mechanism during the cut. Transverse impact experiments on Kevlar® KM2 yarns by Song and Lu [37] revealed that a yarn behaved with fibers progressively impacted instead of a solid component. Therefore, the lower-scale single constituent fiber's response under cut is believed to be able to provide a fundamental understanding of the relevant mechanism determining the system-level response of yarns or fabrics. Mayo et al. [116] cut single high-performance fibers with various types at different angles. They examined several inorganic fibers, such as carbon fiber, S-glass, and organic fibers including Kevlar®, Twaron®, Vectran®, Technora®, Zylon®, Dyneema®. The inorganic fibers were found to be less sensitive to the cut angle and have higher average cut resistance due to their higher relative hardness and transverse mechanical properties. Effects of indenter nose shape, initial loading angles, the compliance of the substrate supporting the fiber were evaluated by Hudspeth et al. [46] and Lu et al. [117]. A statistical analysis by continual experiments after Mayo et al. [116] was conducted by increasing the number of investigated samples and reducing the scope of cut angles to three types [118]. One big challenge of the study in the fiber level is the characterization of such a fine

dimension and force scale, which refines failure observations of fibers through post-fracture analysis.

In this study, a microscopic way was developed to transversely cut single fibers by using razor blades and simultaneously image the failure processes inside an SEM. Such a method provides a detailed *in-situ* observation of the initial fiber/blade contact, fiber deformation, crack initiation and propagation in the fiber until the ultimate fiber failure. Two types of fibers were investigated, namely aramid (Kevlar® KM2 Plus) and UHMWPE (Dyneema® SK76). The effects of cut angle and sample length on the fiber's failure were also studied. The cut resistance was evaluated by the specific energy absorption during the cut. Failure surfaces were imaged in higher resolutions to provide further insight into the relation of the microscale fiber's failure behavior to the fiber's nanostructures.

4.2 Materials

Single Kevlar® KM2 Plus fibers (DuPont™, Delaware, USA) and Dyneema® SK76 fibers (DSM, Geleen, the Netherlands) were pulled out from the yarns as received. Both two fibers are widely used as constituent materials of armor or cutting-resistance gloves. The fiber morphology was investigated by a Quanta 3D FEG SEM (FEI, Hillsboro, OR). The diameters of the Kevlar® KM2 Plus and the Dyneema® SK76 fiber in average were measured as 10.82±0.37 μm and 16.99±0.67 μm, respectively.

4.3 Experiments

4.3.1 Single-fiber quasi-static tensile experiments

Single fiber samples were adhered onto cardboards with circular holes punched at the center using the epoxy adhesive DP190 (3 M Inc., St. Paul, MN, USA). The gauge length of the sample was determined by the diameter of the hole as 6.35 mm. At the same time, A bond length ~1.5 times of the gauge length was carefully decided, which effectively reduced the effect of the fiber's being pulled out into an undetectable level. The cardboard with the fiber sample was then mounted onto a Deben Microtest tensile stage (Deben UK Ltd., Oxford, UK). The cardboard was then snipped along the dashed line. Figure 4.1 schematically illustrates the construction of the

Deben tensile stage with the assembly of the cardboard and fiber sample. The tensile stage has two stages (left stage and right stage) connected by a threaded rod. As a step motor rotates the threaded rod, the two stages either move towards each other or separate. On the top of each stage, there are mounting threaded holes to house the fixtures on which the sample fiber and indenter are mounted, respectively. Five relative moving velocities of the left and right stages are available in the software to load the single fiber at different rates, namely 0.1, 0.2, 0.5, 1.0, and 2.0 mm/min. During the entire loading process, the linear scale extensometer mounted across the two stages measures the relative displacement between two stages with a 300-nm resolution. A 20-N strain-gauge load cell with the 0.01-N resolution was mounted at the right side of the right stage to record the transverse load on the fiber as experienced by the indenter. The entire tensile stage was installed inside the chamber of a Quanta 3D FEG SEM (FEI, Hillsboro, OR). Before each experiment, the SEM measured each sample's diameter, eliminating the source of error by the usage of the fiber diameter on average. In this study, the loading speed was selected to be 0.1 mm/min, generating a tensile strain rate of 2.6×10^{-4} s^{-1}.

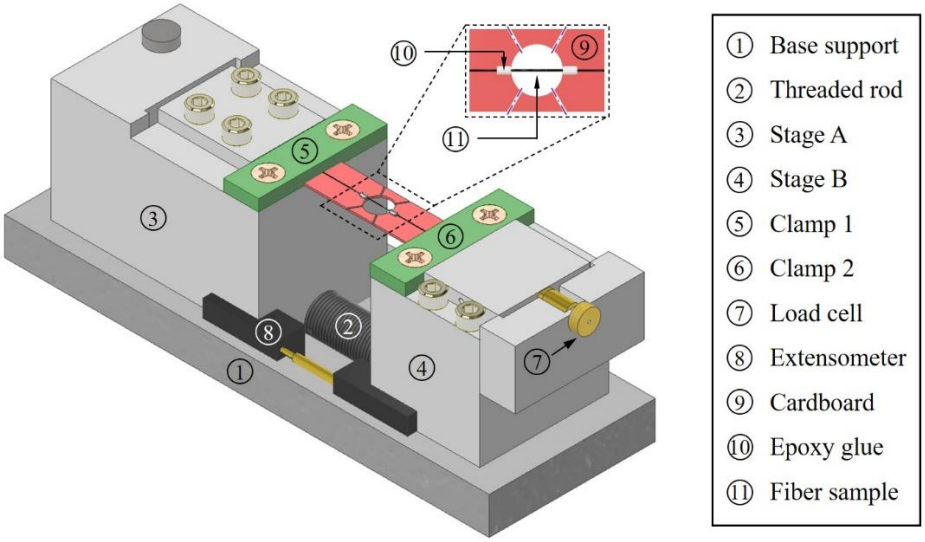

Figure 4.1. Schematic of single-fiber quasi-static tensile experiments on the Deben loading stage.

4.3.2 Single-fiber quasi-static cut experiments

A successful singe-fiber quasi-static cut experiment includes designing the adapted fixtures, mounting fibers and indenters, reconstructing the Deben tensile stage, integrating the loading process with the SEM. The fibers had an identical gauge length of 50 mm. The cut angle effect was studied by loading the 50-mm single fibers at three different angles to the razor blades, namely 30°, 60°, and 90°.

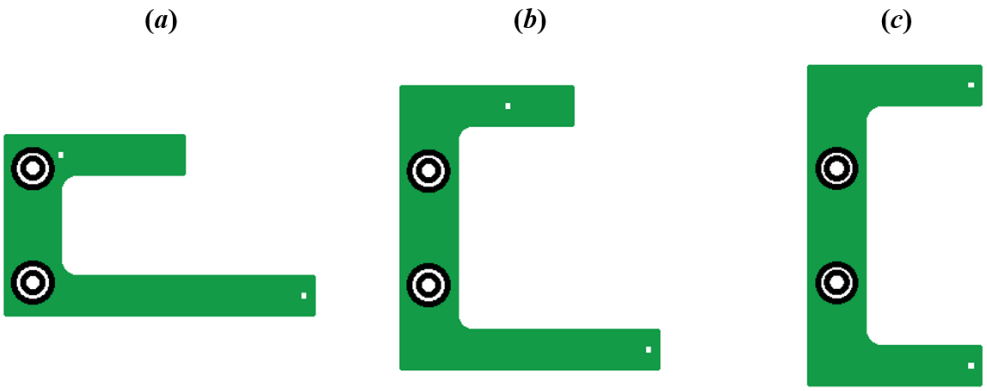

Figure 4.2. Fixtures to mount the fiber samples with different angles. (*a*) 30°; (*b*) 60°; (*c*) 90°.

A variety of C-shape fixtures were designed to mount the fiber samples with different angles. As shown in Figure 4.2, these fixtures were designed with a 1-mm^2 square hole on each arm. Before fiber mounting, two 1-mm-diameter stainless pins were inserted into the square holes and cured with the ZAP superglue (Frank Tiano Enterprises, Lakeland, FL). A three-step fixing method was adopted to fix a single fiber onto the two pins, which is described in Figure 4.3. First, the single fiber was wrapped on each of the pins and then secured with ZAP superglue. To ensure that the fiber deformed on the plane of the fiber fixture's surface during the subsequent loading process, the fiber testing section should be at the fixture surface during the wrapping process (see Figure 4.3*a*). Secondly, a carbon tape was wrapped on the pin and the unwrapped fiber in Figure 4.3*a* was then wrapped spirally on the tape, as illustrated in Figure 4.3*b*. Figure 4.3*c* presents the fixture with the actual fiber fixed when the second step was finished. The purpose of this step is to prevent the fiber's sliding at two ends during transverse loading by the added friction between the fiber and the carbon tape, which has been proven to be effective in our experiments. Finally, in

Figure 4.3*d*, the ZAP superglue was dropped on the surface of the carbon tape to enhance the fixing strength further.

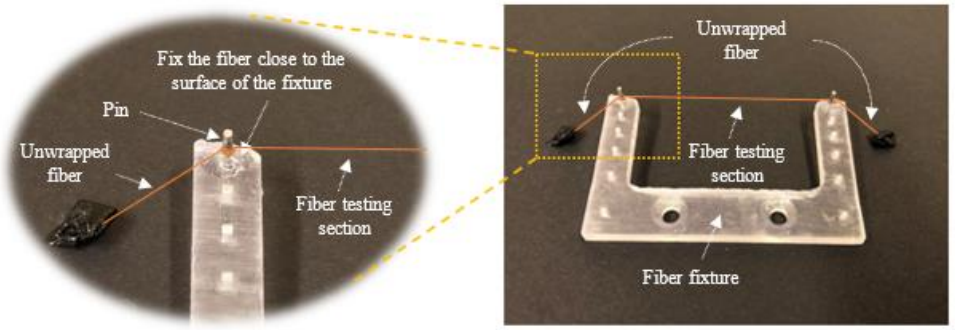

(*a*) Step 1 Wrap the fiber on the pin and close to the fixture surface

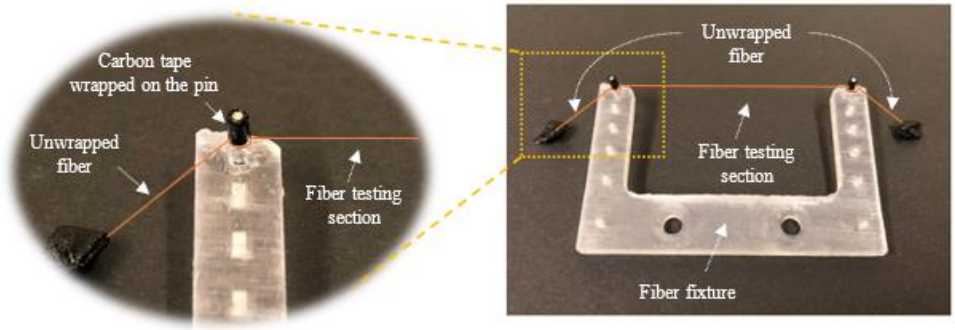

(*b*) Step 2-1 Wrap a carbon tape on the pin

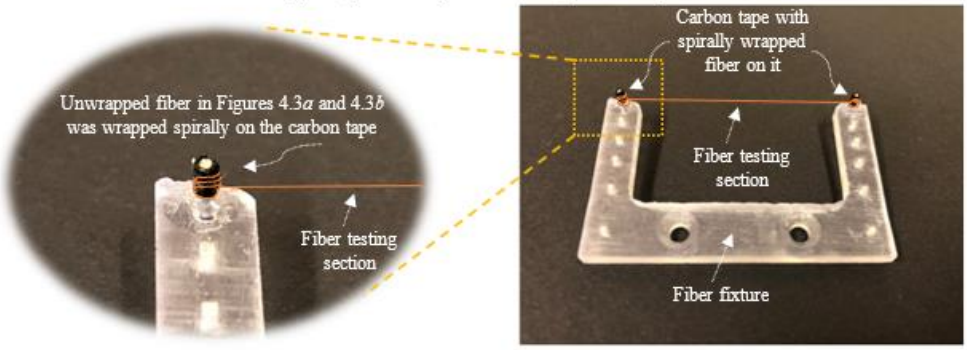

(*c*) Step 2-2 Warp spirally the unwrapped fiber on the carbon tape

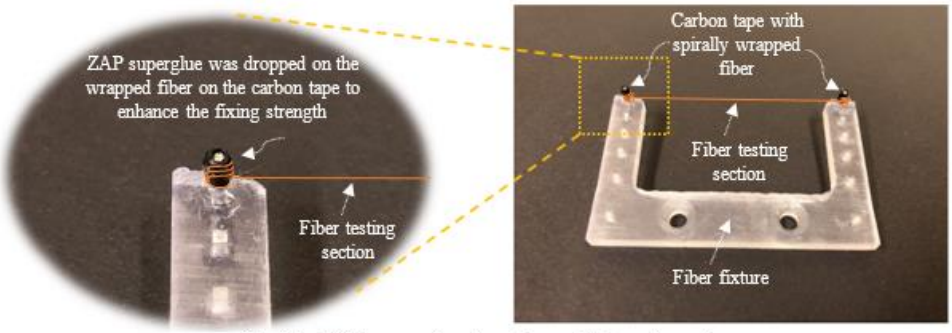

(*d*) Use ZAP superglue to enhance fixing strength

Figure 4.3. Three-step fiber mounting method.

Figure 4.4 is the fixture to hold the razor blade to cut the fiber sample. The razor blade fixture had a gap with its width equal to the blade's thickness so that the blade can be inserted into the gap. ZAP superglue was applied close to the blade/fixture contact area for additional fixing. The reconstruction of the Deben tensile stage requires replacing the two clamps in Figure 4.1 with the fiber and blade fixtures. The schematic of the modified Deben tensile stage is shown in Figure 4.5. In each experiment, the blade fixture needs to be installed before the fiber fixture. The two loading stages were set in a tensile loading mode. When the loading started, the two fixtures moved apart simultaneously. The blade then contacted the fiber sample at the center and transversely cut the fiber until failure. The same loading speed to the tensile experiments, 1.67 μm/s (0.1 mm/min), was employed in the cut experiments. The entire loading setup was installed inside the chamber of a Quanta 3D FEG SEM (FEI, Hillsboro, OR). The fiber's failure process was captured by the secondary electron detector located at the top of the fiber. The SEM worked in an environmental mode so that the non-conductive fiber did not need to be sputter-coated for imaging. A progressive loading was adopted, providing sufficient time for the SEM to image the fiber morphology once the loading was suspended. Force (F) at the blade tip was recorded by the load cell. The deflection of the fiber (S) at the loading point was measured by the extensometer.

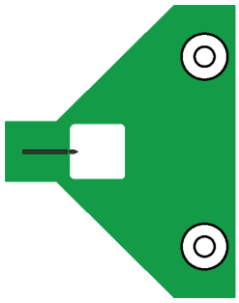

Figure 4.4. Blade fixture

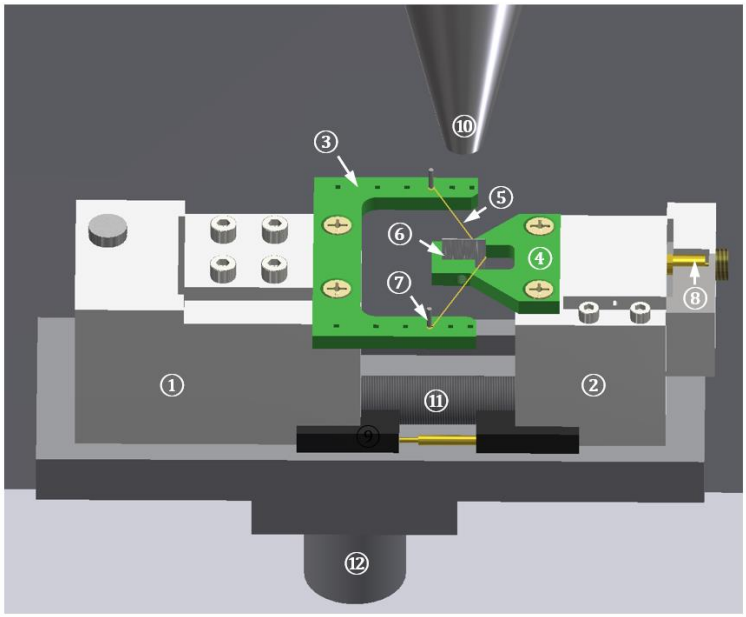

① Left stage ② Right stage ③ Fiber fixture ④ Blade fixture
⑤ Fiber ⑥ Razor blade ⑦ Pin ⑧ Load cell
⑨ Extensometer ⑩ Electron beam ⑪ Thread rod ⑫ 5-axis stage

Figure 4.5**.** Schematic of the experimental setup.

4.3.3 Post-fracture imaging on the fiber failure surface

Each broken fiber was sputter-coated for 60-120 seconds and placed in a NovaNano 200 Series SEM (FEI, Hillsboro, OR). A secondary electron detector (SED) was used to image the entire failure surface of the fiber. More details reflecting the post-fracture state of fibrils around the fracture surface were revealed at a higher-resolution Through-the-Lens detector (TLD). The beam accelerating voltage and spot size were 5 kV and 3.0 - 4.0, respectively.

4.4 Results

4.4.1 Tensile property of a single fiber

Figure 4.6 records the stress-strain curves of different samples for each type of fiber. The stress (σ_T) was calculated as Eq. (4-1) by assuming a constant cross-section area, where F_T is the load signal; d is the diameter of the fiber. The strain (ε_T) in the fiber was transferred as Eq. (4-2)

from the time-resolved displacement (S_T) detected by the extensometer, divided by an initial gauge length L_T.

$$\sigma_T = \frac{4F_T}{\pi d^2} \tag{4-1}$$

$$\varepsilon_T = \frac{S_T}{L_T} \tag{4-2}$$

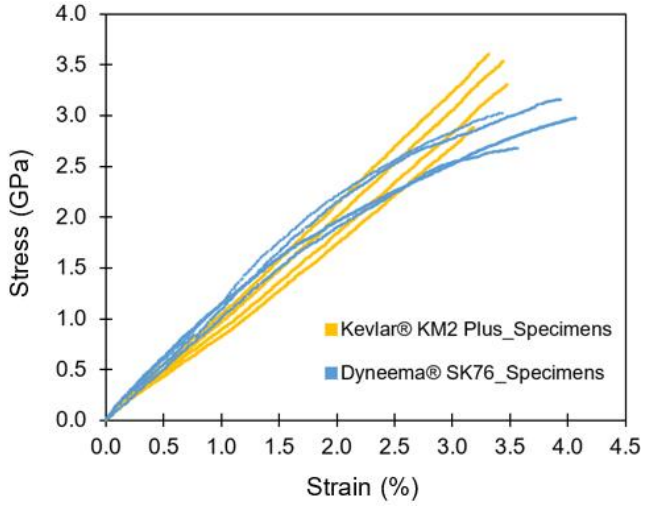

Figure 4.6. Stress-strain curves of different fibers.

The ultimate stress and failure strain of two fibers on average were compared with existing references as Table 4.1.

Table 4.1 Tensile properties of Kevlar® KM2 Plus and Dyneema® SK76 fibers

Author	Fiber type	Gauge length (mm)	Strain rate (s^{-1})	Fiber diameter (μm)	Tensile strength (GPa)	Failure strain (%)
This work	Kevlar® KM2 Plus	16	1.04×10^{-4}	10.82 ± 0.37	3.33 ± 0.32	3.36 ± 0.13
This work	Dyneema® SK76	16	1.04×10^{-4}	16.99 ± 0.67	2.96 ± 0.20	3.76 ± 0.29
Cline et al. [119]	Kevlar® KM2 Plus	5, 15	3×10^{-4}	11.18 ± 0.53	3.0 ± 0.3	3.4 ± 0.4
Mayo and Wetzel [116]	Dyneema® SK76			18.8	2.62	3.6
Sanborn et al. [120]	Dyneema® SK76	5	0.001	14.5-16.9	3.63 ± 0.19	3.48 ± 0.42
		10			3.64 ± 0.31	3.93 ± 0.96
		50			3.69 ± 0.17	3.96 ± 0.36
Hudspeth et al. [121]	Dyneema® SK76	5, 10	0.001		3.12-3.15	

4.4.2 Force-Displacement Curve

Figure 4.7*a* is the schematic illustration of the loading process. A single fiber was fixed at two ends. A razor blade transversely normally loaded the single fiber at the midpoint until the fiber broke. The force at the tip of the razor blade and its displacement relative to the fiber fixing points were recorded as F and S, respectively. S_{max} is the maximum of S before the fiber broke. A breaking angle θ is defined to describe the ultimate state of the fiber:

$$\theta = \arctan\left(\frac{S_{max}}{L}\right) \tag{4-3}$$

where $2L$ is the gauge length of the fiber, which is 50 mm in the experiments reported here.

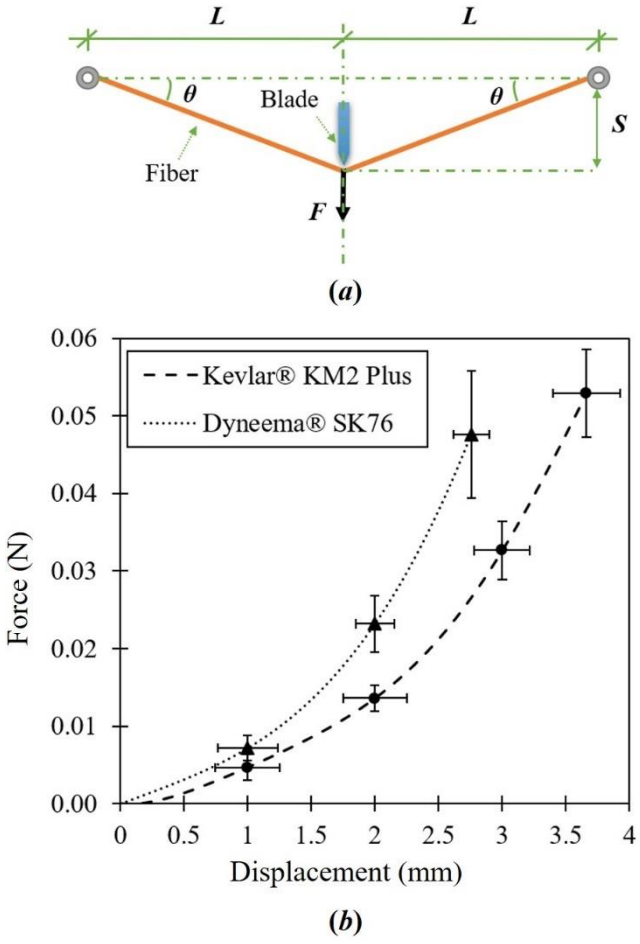

Figure 4.7. Force and displacement in a single fiber. (*a*) Sketch of deformation of a fiber before the break, (*b*) Force-displacement curves of two different fibers.

Four to five experiments were performed for each kind of fiber. The force (*F*) and displacement (*S*) data were input into Origin Pro 2017 for further data processing. The equations of force-displacement curves were obtained by curve fitting. The maximum displacement was then calculated by averaging the maximum displacement obtained in the experiments. Finally, the average force-displacement curves were plotted within the maximum displacement, as shown in Figure 4.7*b*.

As shown in Figure 4.7, the Kevlar® KM2 Plus and Dyneema® SK76 fiber are capable of withstanding the maximum shear forces of 0.053 N and 0.047 N, respectively, with the ultimate displacements at the midpoint correspondingly at 3.6618 mm and 2.7338 mm. The breaking angles calculated according to Eq. (1) are 8.330° and 6.241°, respectively.

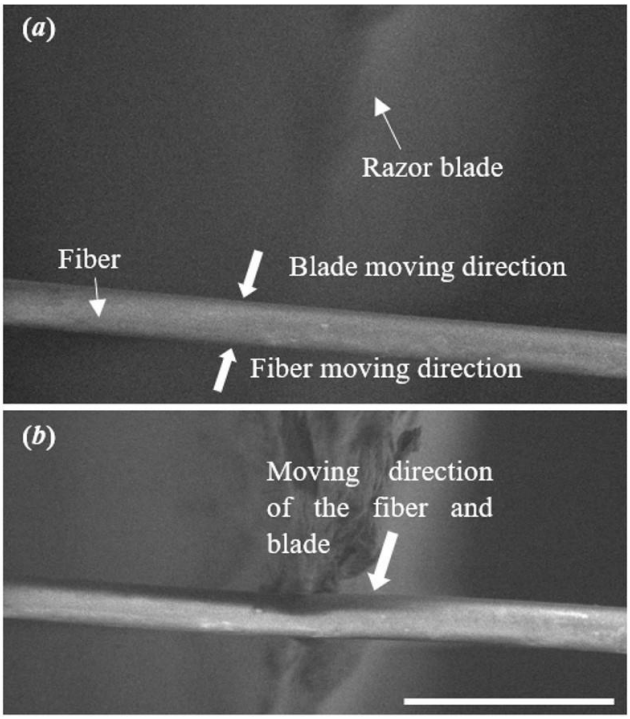

Figure 4.8. Characteristics of the blade and fiber before (*a*) and after (*b*) initial touch. The scale bar is 50 μm.

4.4.3 The starting point of the loading process (*S*=0)

At the fiber scale, naked-eyes observation cannot accurately identify the initial contact of the razor blade tip and the sample, which was used in previous single fiber experiments [116]. The low vacuum SE detector in the SEM facilitates the precise determination of the exact instant of contact, which is regarded as the starting point of the loading process. The blade tip and the fiber sample were placed very close to their engaging positions (less than 1 mm observed from naked eyes) in advance. The experimental set-up moved the blade and the fiber towards each other, as shown in Figure 4.8*a*. Since the blade had higher stiffness and stability, once it touched the fiber, it drove the soft fiber to shift the moving direction by pushing the fiber at the contact point. Figure 4.8*b* shows the movement of the blade and the fiber after contact. The point when the fiber transfers from its independent motion to moving with the blade tip is regarded as the starting point of the loading process, which is indicated as *S*=0.

4.4.4 Fracture process of a Kevlar® KM2 Plus fiber

Figures 4.9-4.10 show the fracture process of a Kevlar® KM2 Plus fiber cut by a razor blade. The fracture process can be sub-divided into four phases: localized compression, cutting and sliding; further cutting and bending; crack initiation and propagation until fiber failure.

First, after the initial touch with the blade tip, the fiber was cut from the contact point. Theoretically, the fiber should be cut along the cross-section. However, in reality, the fiber may not be strictly symmetrically cut by the blade, causing the stress to distribute unevenly astride the blade tip. It is also possible that the fiber was not perfectly perpendicularly cut. Either one of or both these factors caused the observed fiber to slide at the blade tip as it was being cut through. As a result, with the fiber cut more profound in the cross-section, the cut fibrils piled up at one side of the blade tip because of blade sliding, forming a resistance to the relative sliding between the blade and the fiber along the fiber length. Simultaneously, the blade-fiber friction increased with the augment of cutting depth. Eventually, the fiber stopped sliding and contacted with the blade tip at a ‘stable’ point for being further cut, which is viewed as the end of the first phase of the cutting process. Figure 4.9 presents the recorded maximum sliding distance away from the initial contact point as 11 μm. In addition to the fiber being cut and sliding, localized compressive deformation was

observed on the Kevlar® KM2 Plus fiber, which is displayed in Figure 4.9. This process sustained until S reached 28% of the maximum displacement S_{max}.

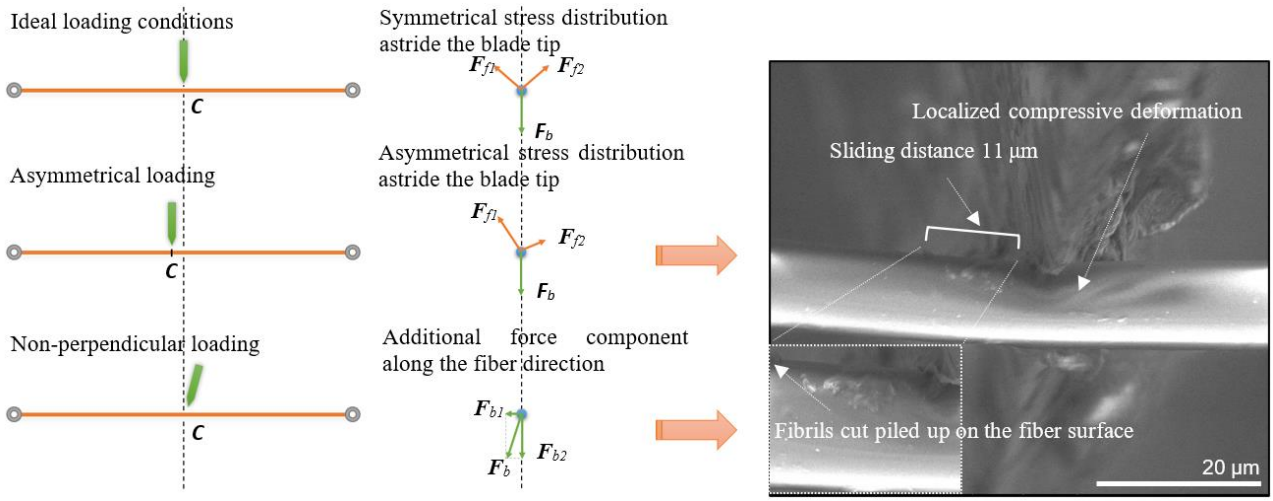

Figure 4.9**.** Blade sliding on the fiber surface. Insets: *C*, fiber-blade contact point; F_b, force at the blade tip; F_{f1}, F_{f2}, fiber cross-section force at two sides of the blade tip; F_{b1}, force component along the fiber length direction; F_{b2}, force component along the fiber cross-section.

The second phase of the process began from S=28% S_{max} when the fiber cut from the 'stable' point at the end of the first process without sliding and lasted until 85%S_{max}. At the same time, as more and more fibrils in the fiber were cut, the entire fiber progressively lost its structural stiffness to resist bending around the contact area, resulting in the fiber bending more at this 'stable' point (see Figure 4.10*a*) and the increasing transverse compressive deformation in Figure 4.10*b*.

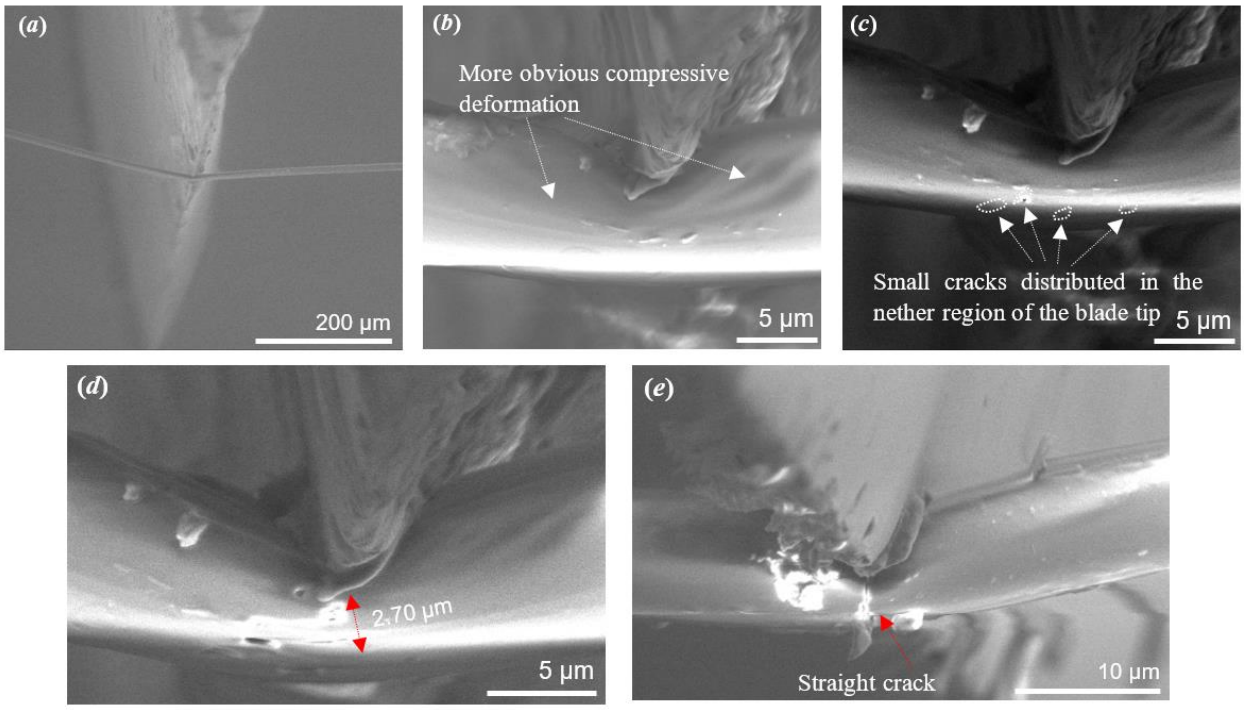

Figure 4.10. Fracture process of a single Kevlar® KM2 Plus fiber. (*a*) Global image of the fiber when $S = 50\%S_{max}$, (*b*) Local image of the fiber when $S = 50\%S_{max}$, (*c*) Crack initiated when $S = 85\%S_{max}$, (*d*) Crack propagated along a stair-stepping path, (*e*) Crack propagated straightly.

Cracks initiated beneath the blade-fiber contact area when S reached 85% S_{max}, which is regarded as the start of the process's third phase. These cracks are caused by the tensile failure of fibrils in the fiber and are marked to be easily discernable in Figure 4.10*c*. In four of the five experiments performed, cracks appeared at the bottom region of the fiber but were not exactly below the blade tip. Initial defects in the fiber, as well as imperfectly perpendicular and inexactly symmetrical loading, are considered the main contributors to this phenomenon. As the blade pushed the fiber to move forward, these cracks expanded, connected, and propagated to the blade tip along a stair-stepping path, finally causing the tensile failure of the fiber. Conversely, a relatively symmetric and perpendicular loading rendered the crack initiate at the fiber bottom, which is also right under the blade tip, and propagate to the tip when the fiber failed, forming a straight crack connecting the bottom of the fiber to the blade tip. Figures 4.10*d* and 4.10*e* demonstrate the stair-stepping and the final straight crack propagating paths, respectively, at the moment before the fiber broke.

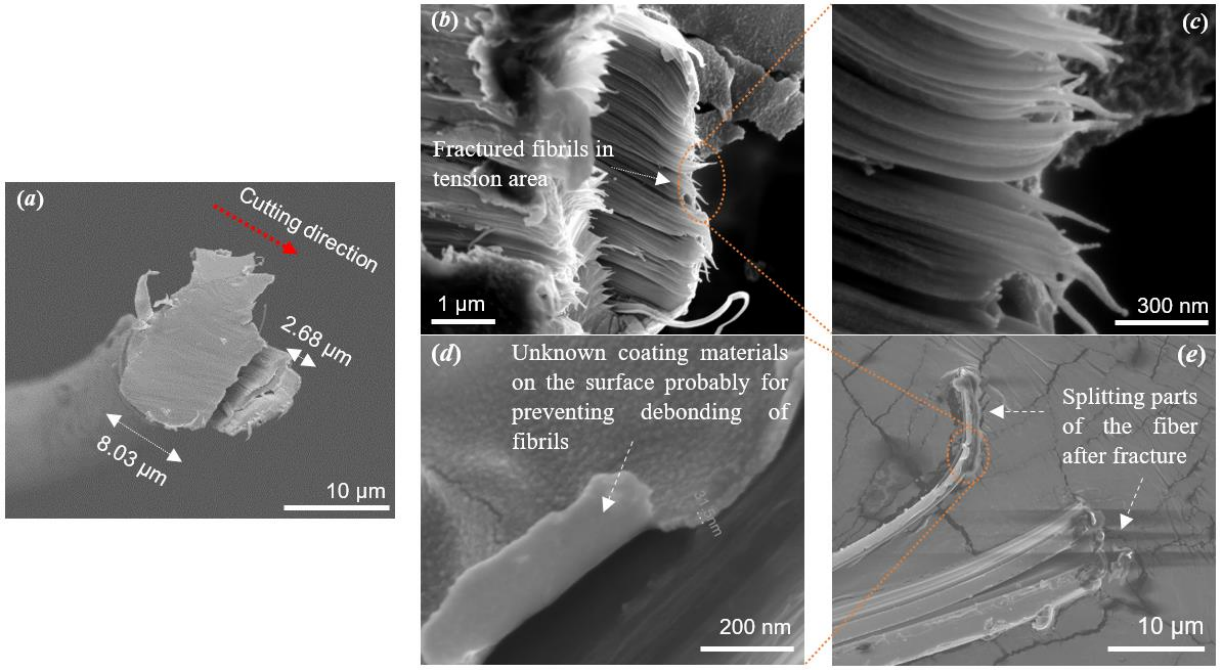

Figure 4.11. Post-fracture images of the single Kevlar® KM2 Plus fiber. (*a*) Failure surface, (*b*) Tension-induced failure of fibrils, (*c*) Fractured fibrils on a larger scale, (*d*) A layer of coating material on the fiber surface, (*e*) Fiber splitting.

4.4.5 Post-fracture images of the Kevlar® KM2 Plus fiber

Combining the pre- and post- fracture images of the single fiber around the failure region in Figures. 4.10*d*-4.10*e* and Figure 4.11*a*, respectively, it is found that, along the cutting direction, the fiber was cut through by the blade nearly 75% of the diameter while the remaining 25% part was stretched to break. Apparent tension-induced failure of fibrillation with fibrils of 20 - 30 nm diameter (Figure 4.11*c*) was shown in Figure 4.11*b*. A 30-nm-thick special coating in Figure 4.11*d* was on the fiber's surface, probably preventing the debonding of fibrils during material processing and manufacturing. In particular, the post-fracture analysis provides the information that part of the fiber split from the entire structure, as exhibited in Figure 4.11*e*, which is not reflected in pre-fracture images. The mechanism can be interpreted as below. At the end of the failure process, the fiber resisted the blade with many small cracks at the bottom, and a main crack propagates to the blade tip. In regions close to those many small cracks, compressive stresses on the nether part of the fiber along the cross-section direction are very large. As the fiber fails abruptly from the blade-fiber contact area, the two separated parts of the fiber snapped back [98]. Simultaneously, the

bottom part of the separated fiber cannot stand the significant compressive stresses and split from the entire fiber.

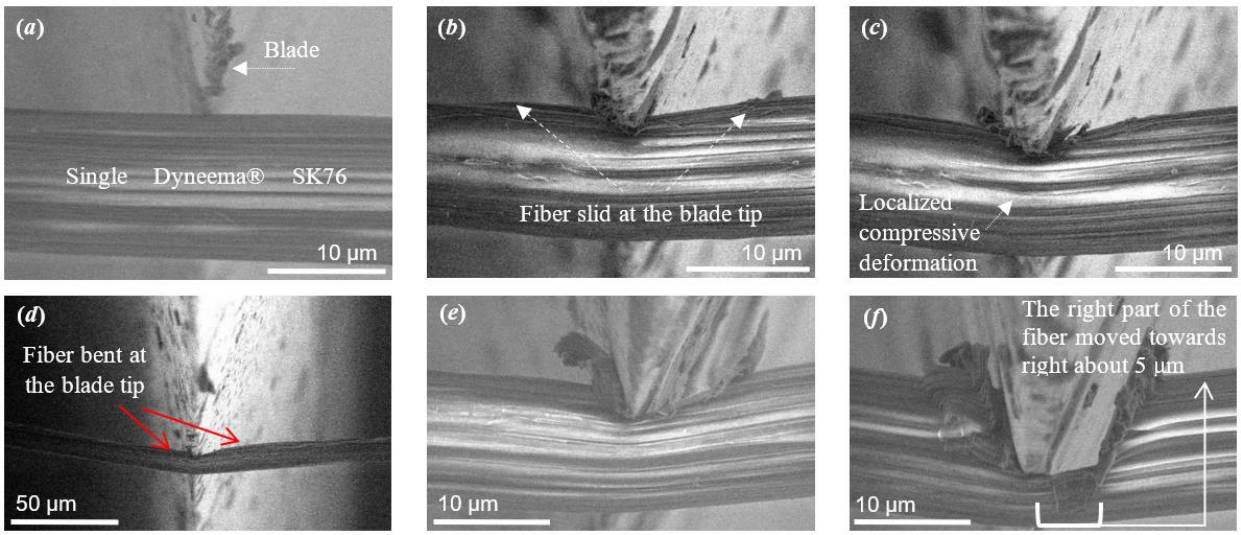

Figure 4.12. Fracture process of a single Dyneema® SK76 fiber. (*a*) initial contact $S = 0$, (*b*) $S = 50\ \%S_{max}$ fiber sliding and being cut, (*c*) $S = 66\%S_{max}$ fiber further being cut, (*d*) $S = 82\%S_{max}$ obvious bending behavior of the fiber at the fiber-blade contact area, (*e*) $S = 87\%S_{max}$ fiber further being cut, (*f*) $S = 95\%S_{max}$ a special case happening close to the final failure.

4.4.6 Fracture process of a Dyneema® SK76 fiber

A similar cutting and sliding process is found in the experiments on Dyneema® SK76 fiber when S increased until 50% S_{max} (see Figures. 4.12*a*-4.12*b*). Different from Kevlar® KM2 Plus fiber, three of the four single Dyneema® SK76 fiber samples were cut through by a razor blade without clearly identifiable tension-induced failure. The typical failure process is shown in sequence as Figures 4.12*a*-4.12*e*. Only one sample, presented in Figure 4.12*f*, with a thin slice (less than 5% of the diameter) interacting with the blade, ultimately sliding on the tip and tensioned to break. This was attributed to the fact that the blunter blade tip after cutting can no longer cut the remaining of the fiber while, at the same time, the thin slice of fiber was subjected to a very large tensile stress, which has been mentioned in [44].

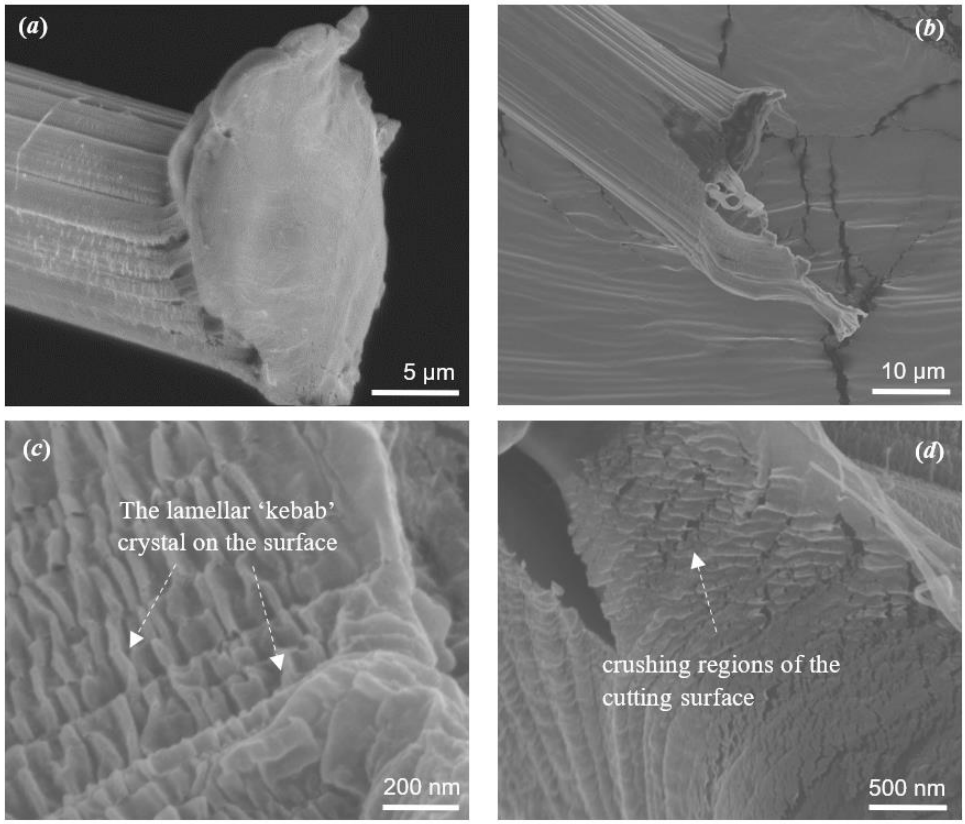

Figure 4.13. Post-fracture images of a single Dyneema® SK76 fiber. (*a*) Typical failure surface, (*b*) A special failure surface, (*c*) Shish-kebab structures of the fiber, (*d*) A crushed surface.

4.4.7 Post-fracture images of the Dyneema® SK76 fiber

A typical failure surface of a Dyneema® SK76 fiber is presented in Figure 4.13*a*. Figure 4.13*b* is about the post-fracture image corresponding to Figure 4.12*f*. As mentioned in Section 4.6.6, this one of the four fiber samples finally failed because of the tensile failure of the thin slice. Different from the observed fibril-form fracture in the Kevlar® KM2 Plus fiber, the shish-kebab structure of the Dyneema® SK76 fiber in Figure 4.13*c* displayed a crushing surface after indented by the razor blade (see Figure 4.13*d*).

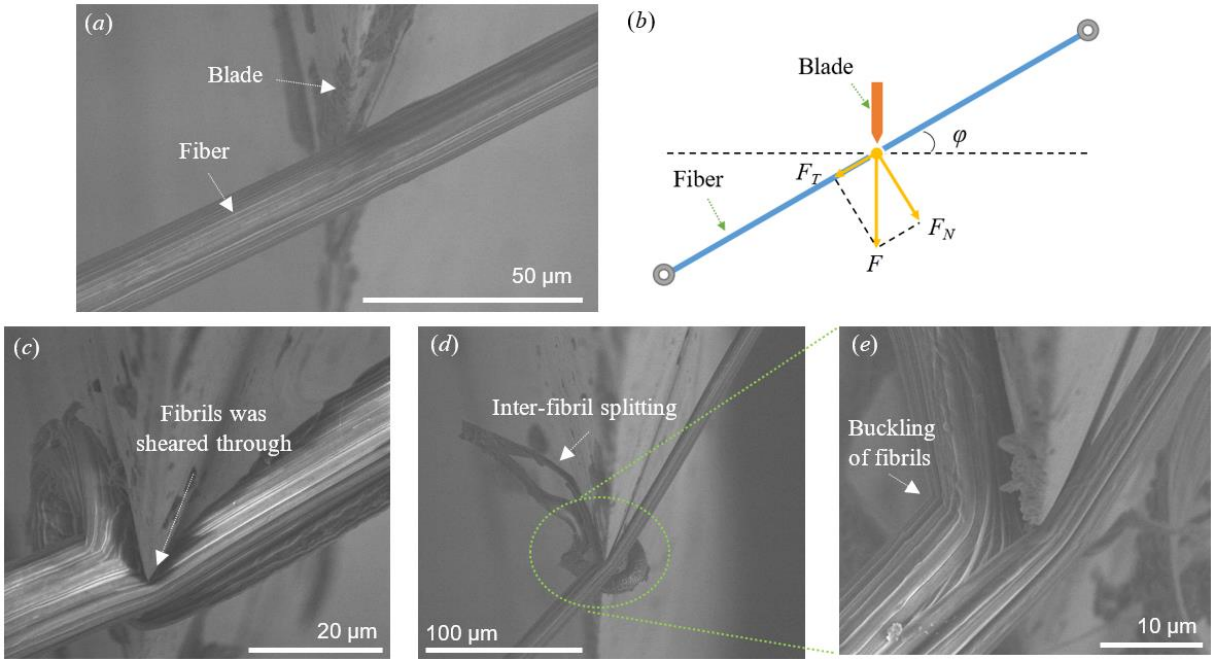

Figure 4.14. Failure process of a single Dyneema® SK76 fiber under oblique cutting. (*a*) Initial contact ($\varphi = 30^{\circ}$), (*b*) Schematic of a single fiber under cut, (*c*) Fiber configuration before failure ($\varphi = 30^{\circ}$), (*d*) Fiber configuration before failure ($\varphi = 60^{\circ}$), (*e*) Magnified image around the blade tip ($\varphi = 60^{\circ}$).

4.4.8 Fracture processes of single fibers under oblique cutting

Figure 4.14 presents typical failure processes of single Dyneema® SK76 fibers transversely cut by razor blades at angles of 30˚ and 60˚. After contact (Figure 4.14*a*), the force at the blade tip was divided into two components perpendicular to and along the fiber length, respectively, represented as F_N and F_T in Figure 4.14*b*. During cutting, F_N failed the fibrils transversely while F_T caused inter-fibril splitting, as shown in Figures 4.14*c*-4.14*e*. The Dyneema® SK76 fiber failed when it was sheared through by the razor blade. As the cutting angle increased from 30˚ to 60˚, the blade was observed to travel a longer distance along the fiber, causing more fibrils to split from the fiber. Different from Dyneema® SK76 fiber, the damage due to the inter-fibril splitting on the Kevlar® KM2 Plus fiber around the blade tip was more likely to evolve along the fiber direction, forming a crack propagating through the fiber length. The residual fibrils were tensioned to break before being cut through by the razor blade. The fiber configurations before fracture were captured and presented in Figure 4.15.

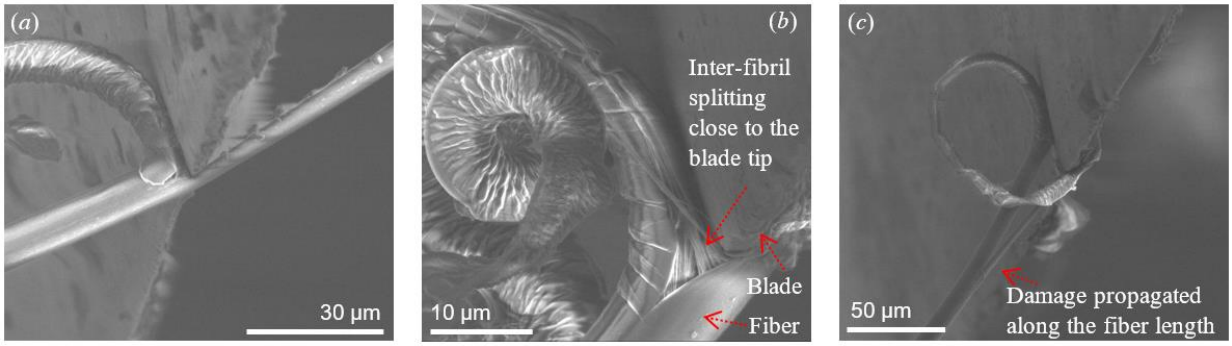

Figure 4.15. A single Kevlar KM2 Plus fiber before failure under oblique cutting. (*a*) Fiber configuration before failure ($\varphi = 30^{\circ}$), (*b*) Fiber configuration during cutting ($\varphi = 60^{\circ}$), (*c*) Fiber configuration before failure ($\varphi = 60^{\circ}$).

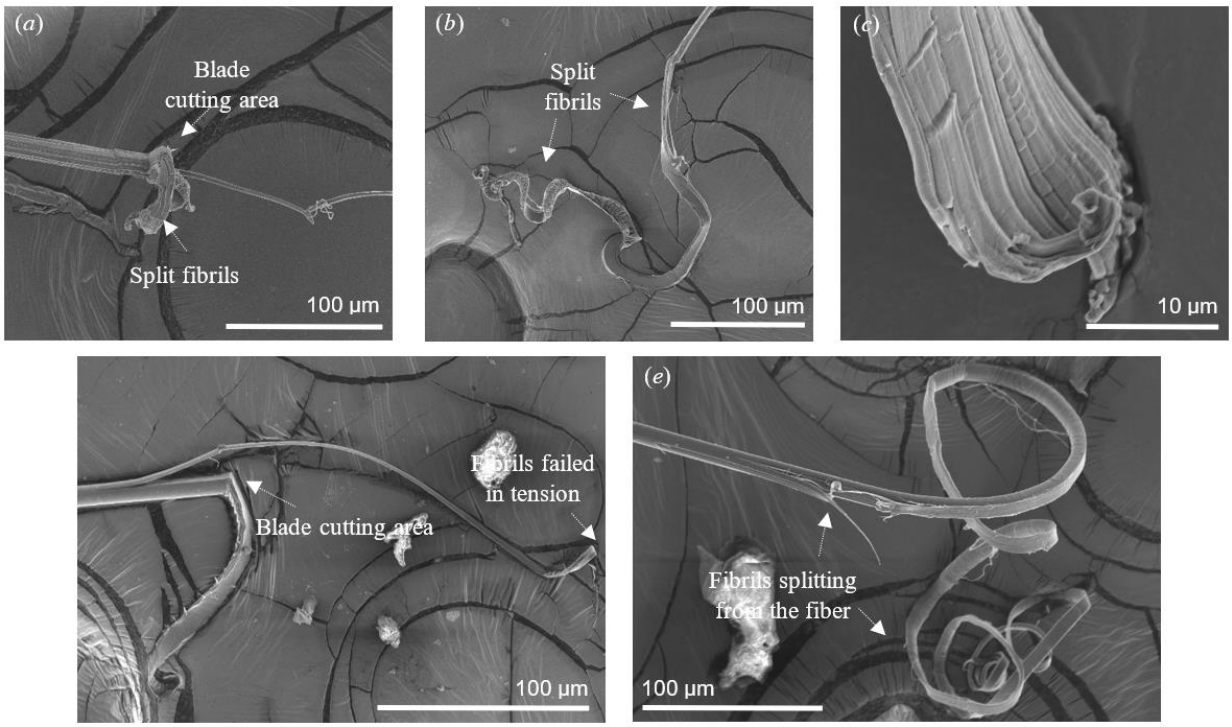

Figure 4.16. Post-fracture images of single fibers after oblique cutting. (*a*) Dyneema® SK76 fiber cut at $\varphi = 30^{\circ}$, (*b*) Dyneema® SK76 fiber cut at $\varphi = 60^{\circ}$, (*c*) Failure surface of a Dyneema® SK76 fiber cut at $\varphi = 60^{\circ}$, (*d*) Kevlar® KM2 Plus fiber cut at $\varphi = 30^{\circ}$, (*e*) Kevlar® KM2 Plus fiber cut at $\varphi = 60^{\circ}$.

4.4.9 Post-fracture images of single fibers after oblique cutting

Figure 4.16 documents the fracture surfaces of two types of fibers after oblique cutting. When the cutting angle was 30˚, there were fewer fibrils splitting from the Dyneema® SK76 fiber before it was cut through, as shown in Figure 4.16*a*, comparing with the case when φ = 60˚, demonstrated in Figure 4.16*b*. Figure 4.16*c* is the magnified failure surface of a Dyneema® SK76 fiber after the cut, revealing that the fiber was cut through by the razor blade instead of failing by tensile stresses in fibrils. Figure 4.16*d* clearly indicates that the Kevlar® KM2 Plus fiber was not cut through by the razor blade. After the crack propagated through the fiber and caused fibrils to split from the fiber from the blade tip, these fibrils were not fully cut through but tensioned to break at a position away from the fiber-blade contact area. When the cutting angle was increased to 60˚, the blade was able to travel along the fiber length direction over a longer distance, making more fibrils split from the Kevlar® fiber, which is displayed in Figure 4.16*e*.

4.5 Discussions

4.5.1 Gauge length effect on the fiber failure

Table 4.2 compares the breaking force and angle obtained in this work with the experimental data in [116]. Although different gauge lengths were studied in each work, the Dyneema® SK76 fiber failed at a similar force and break angle with the corresponding error of 15% and 2%, respectively, which means the fiber, despite possessing different gauge length as 50 mm and 140 mm, failed in a similar triangular geometry. Close to the blade tip, Kevlar® fibers were observed to have nearly the same post-fracture surfaces, showing a combination failure mode, including shearing through by the blade and tensile failure of fibrils.

Table 4.2 Break force and break angle of fibers with a different gauge length

Author	Gauge length (mm)	Kevlar® KM2 Plus fiber		Kevlar® KM2 fiber		Dyneema® SK76 fiber	
		Break force F (N)	Break angle θ (˚)	Break force F (N)	Break angle θ (˚)	Break force F (N)	Break angle θ (˚)
This study	50 mm	0.053	8.33			0.047	6.24
Mayo and Wetzel [116]	140 mm			0.039	6.76	0.055	6.36

4.5.2 Differences of failure between the two fibers

Dyneema® fibers are composed of a number of 8-100-nm-diameter extended chain fibrils (shish or nanofibrils), and the epitaxial crystallizes (lamellar 'kebab') on the surface [122], which are called shish-kebab structures. These fibrils form a larger-scale fibril (microfibril) with the diameter varying from 100 nm to 3 μm by mechanically interlocked kebabs protruding from the shish structure. Furthermore, tie chains rise and fall across these nanofibrils, providing another mechanical connection [123-124]. Therefore, when the blade loads the Dyneema® fiber, the kebab on the shish and the tie chain behave like the natural bridges among neighboring kebabs and enhance the physical interaction among nanofibrils. When the blade loads the Dyneema® fiber, this nature of the connectivity provided by the folded lamellar and the tie chain finally firmly bundles the nanofibrils together transversely during the entire loading process, increasing the interactions between the blade tip and front fibrils. Along the fiber length direction, the shish and the tie chain share the tensile stress with the kebab by self-deformation. In this way, the kebab along the fiber axial direction was strictly constrained and cut through by the blade before tensioned to fail. The schematic of the failure process illustrating these physics is shown in Figure 4.17.

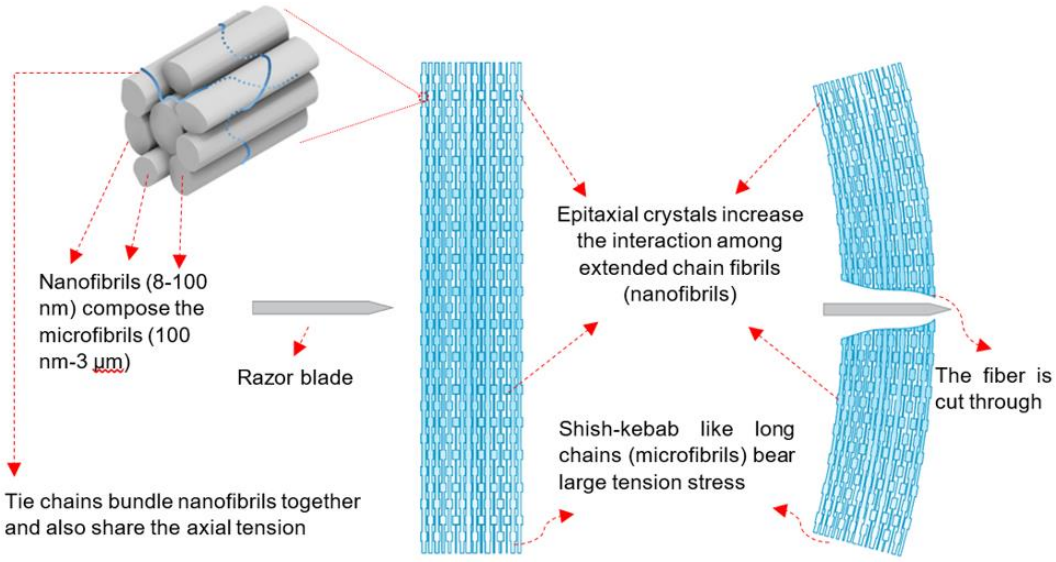

Figure 4.17. Fracture mechanism of a single Dyneema® SK76 fiber under transverse normal cutting.

Kevlar® fibers have short-rod fibrils aligning at the fiber length direction with the end distributing randomly but without the transverse connection [125-126]. In addition, Kevlar® KM2 Plus fibers have a 10.82 μm diameter measured in the SEM before mechanical loading, with a reported axial tensile modulus as 99 GPa in Table 4.1. In comparison, Dyneema® SK76 fibers are larger and stiffer with a 16.99-μm diameter and 113-GPa axial initial tangent modulus in Figure 4.6, respectively. Therefore, the bending stiffness of the Kevlar® KM2 Plus is 86 % less than that of the Dyneema® SK76 fiber. Subject to the blade tip's transverse loading, a single Kevlar® KM2 Plus fiber behaves in a more flexible manner with larger bending deformation. This microstructure lack of physical constraints in the transverse direction and the large bending deformation finally caused the lower-level fiber-blade interaction comparing with the Dyneema® SK76 fiber experiments while the internal damage of the fiber dominates the failure process. At the same time, owing to the poor natural connections among fibrils close to the fracture surface, the Kevlar® KM2 fiber is easier to split into separated parts after failure, which has been shown in Figure 4.11*e*. The schematic explanation of the failure of the Kevlar® KM2 Plus fiber is sketched in Figure 4.18.

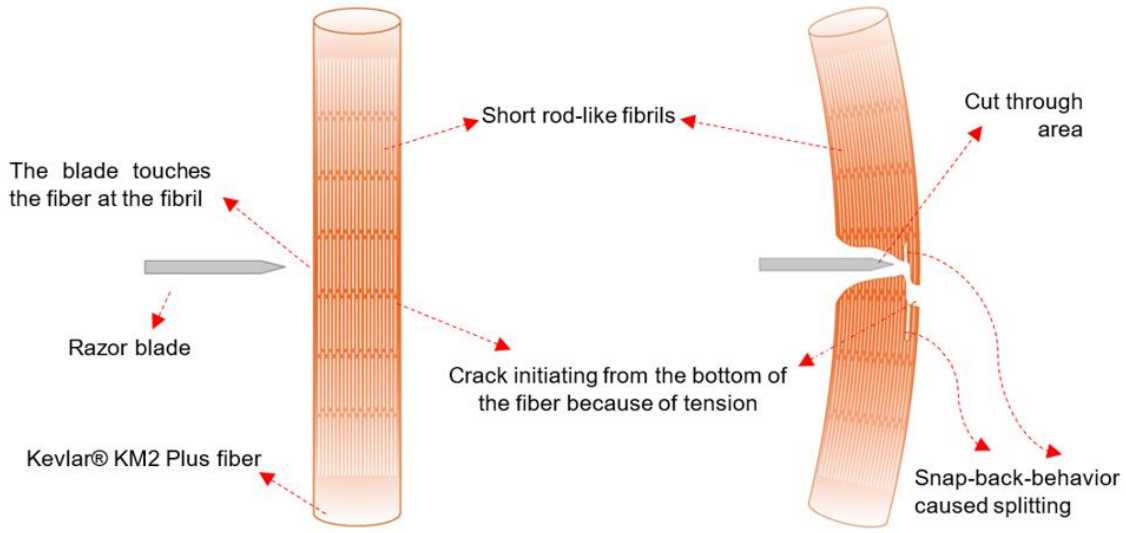

Figure 4.18. Fracture mechanism of a single Kevlar® KM2 Plus fiber under transverse normal cutting.

Based on the load and deformation information provided in Figure 4.7*b*, we obtain the energy to break a single Kevlar® KM2 Plus and Dyneema® SK76 fiber as 0.060 N·mm and 0.042 N·mm, respectively. For Dyneema® SK76 fiber, the energy is consumed to cut the fiber. On the

other hand, the 0.060-N·mm-energy for the Kevlar® KM2 Plus fiber is distributed into two parts working for two separated process with a boundary at S=85%S_{max}, involving a 0.036-N·mm-energy to cut into about 75% of the fiber diameter and a 0.024-N·mm energy to push the residual 25% of the fiber until it fails in tension. Hence, compared with the 0.042-N·mm-energy to cut the Dyneema® SK76 fiber, although the Kevlar® KM2 Plus fiber cutting process spends 14% less energy, the tension-induced failure requires up to 57% additional energy from outside and eventually leads to a 43% higher energy consumption.

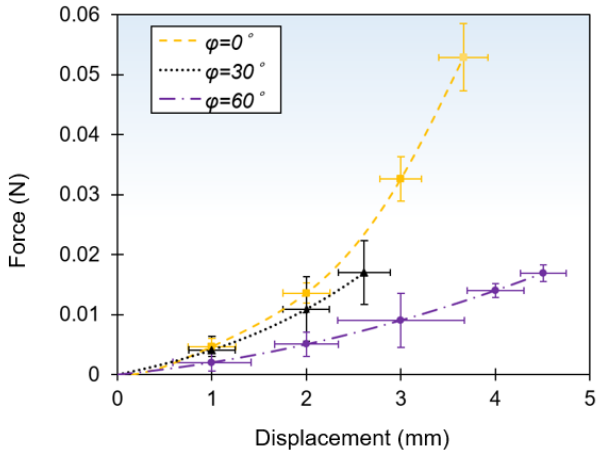

Figure 4.19. Force-displacement curves of Kevlar® KM2 Plus fibers cut at different angles.

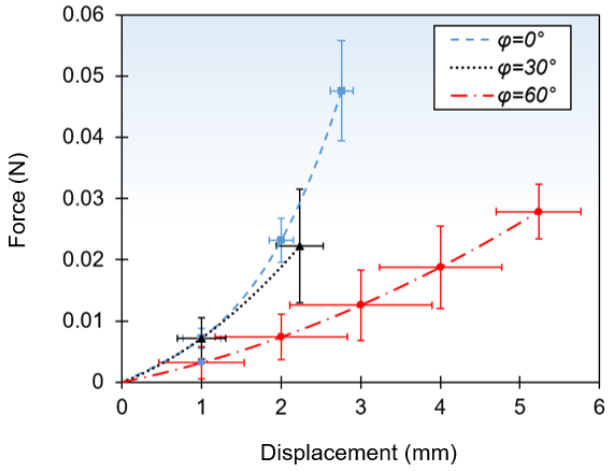

Figure 4.20. Force-displacement curves of Dyneema® SK76 fibers cut at different angles.

4.5.3 Cutting angle effect on the fiber failure

Subjected to oblique cutting, the fiber was sheared in both longitudinal and transverse directions. When the cutting angle was small, the normal shear force, F_N, represented in Figure 4.14*b*, dominated the fiber failure, driving the blade tip to cut through fibrils of fiber transversely. On the other hand, the fiber was cut along the longitudinal direction due to the tangential component F_T of the blade tip force. As the blade moved in, the cutting depth increased, and more fibrils were cut, piling at the blade tip. At the same time, the fiber bent at the blade tip, decreasing the cutting angle and therefore F_T. At one moment, the initially small and continuously decreasing F_T, distributed around the blade tip over an increasing contact area between the fractured fibrils and the blade side, was not large enough to separate fibrils in the longitudinal direction of the fiber. Instead of cutting along the fiber, the blade was trapped inside the fiber. The fibrils already being cut were experiencing axial compressive stress from F_T and then buckled. This buckling failure of fibrils added the complexity of the stress state of fibrils at the frontier of the blade tip by introducing extra inter-fibril friction and transverse compression. Combined with shearing from the blade, the fiber was much easier to fail and showed a poorer cutting resistance, as revealed in Figures 4.19-4.20. The corresponding failure mechanism is schematically portrayed in Figure 4.21*a* and Figure 4.22.

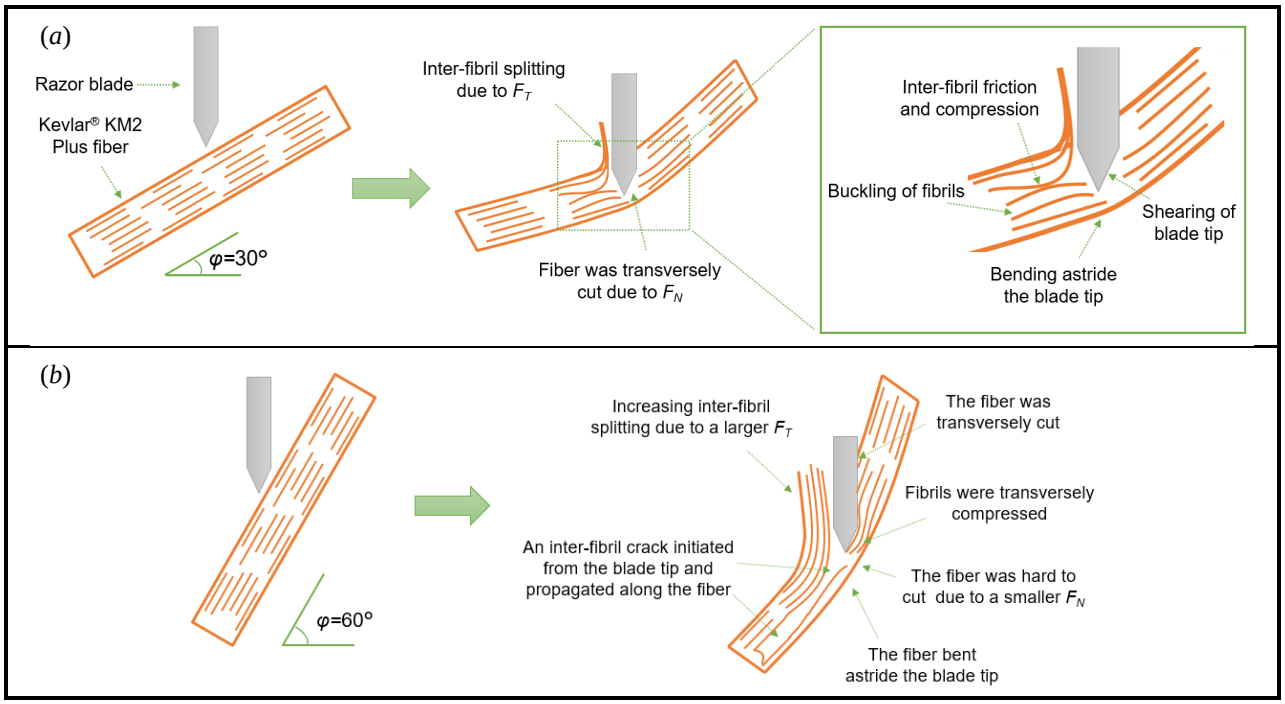

Figure 4.21. Fracture mechanism of a single Kevlar® KM2 Plus fiber experiencing oblique cutting. (*a*) φ = 30°, (*b*) φ = 60°.

When the cutting angle increased, the normal force component F_N decreased, extending the time before the fiber was cut through. On the contrary, an increasing value of F_T enabled the blade to cut the fiber longitudinally over a longer distance before getting trapped inside the fiber. For Kevlar® KM2 Plus fiber, the large F_T was also able to generate an inter-fibril crack, initiating at the blade tip and transiently propagating through the fiber length, as experimentally presented in Figure 4.15*c* and schematically portrayed in Figure 4.21*b*, respectively, which resulted from the weak connection between fibrils. However, due to the random inter-fibril strength, the crack did not propagate exactly along the fiber axis. Once the crack developed into a critical length, causing fast decreasing of the effective cross-section of the fiber, the residual fibrils were not capable of resisting the dramatically increasing tensile stress and finally failed instantaneously. For Dyneema® SK76 fiber, the shish-kebab structure and tie chains [122-124] constrained the fiber transversely and prevented the inter-fibril splitting. The fiber finally failed locally at the blade tip (see Figure 4.22). As demonstrated in Figures 4.19-4.20, compared with the normal cutting and small-angle oblique cutting, both types of fibers got more likely to be stretched and became much tougher due to the slow cutting by the reduced F_N. Dyneema® SK76 fiber shows a better oblique

cutting resistance at larger angles, benefiting from the specific transverse nanoscale physical bridge, which constrained fibrils from splitting so that more fibrils can be involved to dissipate more energy from the blade by tension.

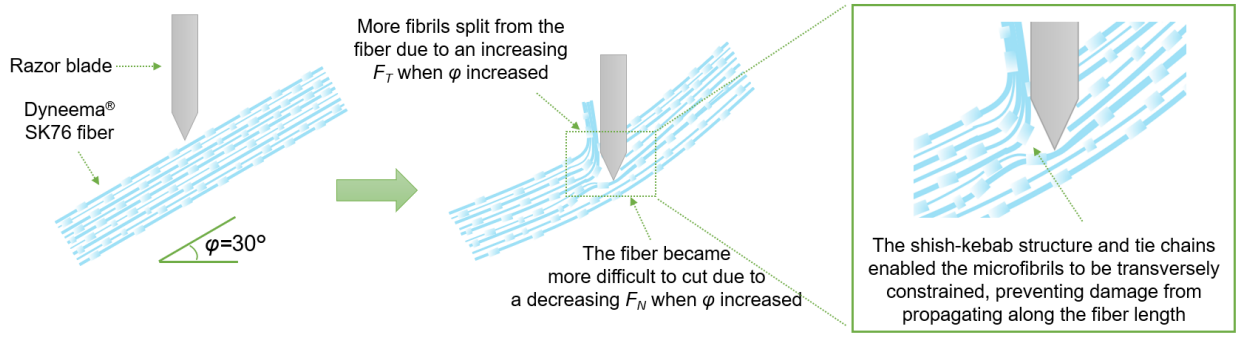

Figure 4.22. Fracture mechanism of a single Dyneema® SK76 fiber experiencing oblique cutting.

4.5.4 Cutting resistance of fibers

4.5.4.1 Specific energy of a single fiber under cut

Transversely cut by a razor blade, the fiber dissipates the energy from the blade via deformation and failure. The amount of energy dissipated (E), which is a critical indicator to reflect the cutting resistance of the fiber, can be calculated by integrating the force-displacement curve as Eq. (4-4).

$$E = \int_0^{S_{\max}} F dS \tag{4-4}$$

For the application of high-performance fibers as armor, mass is a crucial factor in evaluating material performance. Therefore, the specific energy (e) is defined as Eq. (4-5) to consider the mass competence in the cutting resistance of a single fiber, where ρ is the density of the fiber and $2L$ is the fiber length.

$$e = \frac{4E}{\rho \pi d^2 \cdot (2L)} \tag{4-5}$$

Figure 4.23 compares the specific energy of two-type fibers under transverse normal or oblique. The Kevlar® KM2 Plus fiber possessed a specific energy ~2.3 times that of the Dyneema®

SK76 fiber when the fiber was normally cut. When the cut angle increased, the specific energy experienced an undulation of falling first, followed by rising. Such undulation was possibly due to the variation of F_N and F_T against the cut angle, either accelerating the local failure and reducing the energy dissipation or extending the cut duration and increasing the specific energy, as analyzed in Section 4.7.3. When the cut angle increased to 60°, the decrease of F_N made the Dyneema®

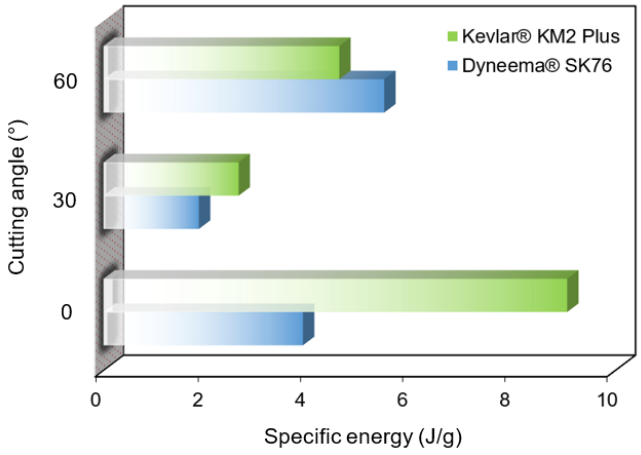

Figure 4.23. Specific energy of two fibers under the normal or oblique cut.

SK76 fiber difficult to be cut, involving the tensile failure of more fibrils. The specific energy of the Dyneema® SK76 fiber was improved above that of the Kevlar® KM2 Plus fiber and also exceeded its own specific energy under the normal cut.

High-performance fibers are usually designed for load-bearing structures because of their superior mechanical properties under axial tension. Hence, there is a necessity to compare the specific energy of a single fiber under cutting with that subject to the tensile loading, e_0. The specific energy of a fiber under tension can be computed as Eq. (4-6), where U_0 represents the strain energy by integrating the tensile stress-strain curve of a single fiber, as described in Eq. (4-7).

$$e = \frac{U_0}{\rho} \tag{4-6}$$

$$U_0 = \int_0^{\varepsilon_{max}} \sigma d\varepsilon \tag{4-7}$$

It is noted that the ultimate span between the two clamps on the tensile stage is ~38 mm. As a result, investigating the stress-strain curve of a fiber with the same gauge length of 50 mm under cut is difficult. Calculation of e_0 is based on the assumption that the 50-mm-length fiber sample for the cut experiment has the same stress-strain curve as Figure 4.6.

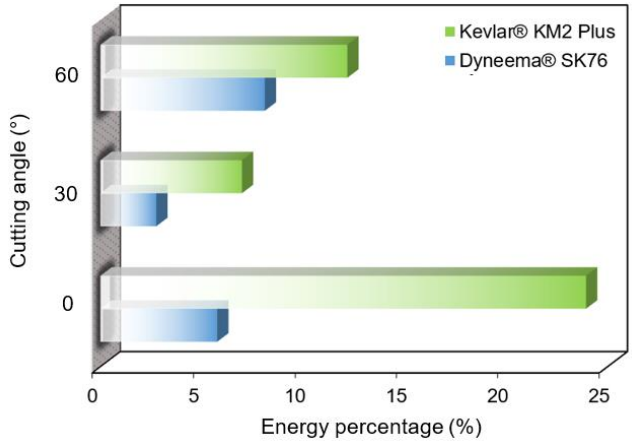

Figure 4.24. Percentage of the specific energy of the fiber under the cut to the specific energy under tension.

As shown in Figure 4.24, a unit mass Kevlar® KM2 Plus fiber under cut can only dissipate the amount of energy at most 24% of its specific energy under tension, which means the localized cut significantly decreased the tensile deformation developed in the entire fiber. At the same time, introducing the cutting angle further reduced e / e_0 into a half. On the other hand, e / e_0 of a Dyneema® SK76 fiber kept below 10% when the cutting angle changed. Such a low level of e / e_0 indicates a poor usage of the tensile properties of the fiber in resisting cut-like loads. Regarding many current efforts in improving the fiber tensile strength, it is supposed to be more efficient to enhance the fiber anti-penetration capability, which ensures more portion of the fiber is involved in dissipating energy via tensile deformation before being cut through and thereby increases the specific energy of the structure under the cut.

4.5.4.2 Axial tensile strain developed inside the fiber

When the single fiber was cut transversely, the blade sheared through the fiber while, synchronously, drove the movement of the fiber at the blade tip. Such movement promoted the variation of the relative position between the loading point and two fixed fiber ends, resulting in

the tension developed inside the fiber. By assuming a constant cross-section area, the tension inside the fiber can be approximately evaluated with quantification.

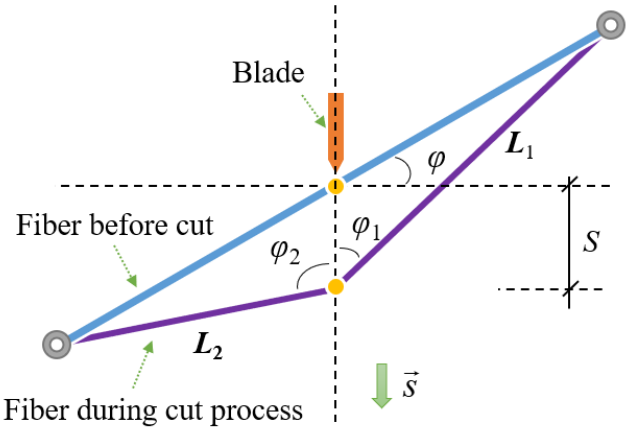

Figure 4.25. Sketch of a fiber under transverse cut at an angle of φ.

Figure 4.25 sketches a single fiber transversely cut by a razor blade at an angle φ being at the initial contact and cut in the process, respectively. The fiber has an initial length of $2L$. After activated in motion for a distance of S by the blade in the direction of $\vec{s}$, the fiber bent at the blade tip. The upper section of the fiber, L_1, forms an angle φ_1 with $\vec{s}$, while the lower section L_2 has an angle with $\vec{s}$ as φ_2. The length of L_1 and L_2 can be calculated via Eq. (4-8) and Eq. (4-9), respectively.

$$L_1 = \frac{L\cos\varphi}{\sin\varphi_1} \tag{4-8}$$

$$L_2 = \frac{L\cos\varphi}{\sin\varphi_2} \tag{4-9}$$

According to the measured displacement S by the extensometer on the tensile stage, the new lengths of the fiber astride the blade tip after deformation, L_1, L_2, can be individually related to the angle φ_1 and φ_2, as Eq. (4-10) and Eq. (4-11).

$$S = L\cos\varphi\cdot\left(\frac{1}{\tan\varphi_1} - \tan\varphi\right) \tag{4-10}$$

$$S = L\cos\varphi \cdot \left(\frac{1}{\tan\varphi_2} + \tan\varphi \right) \tag{4-11}$$

Incorporating Eq. (4-10) with Eq. (4-8), Eq. (4-11) with Eq. (4-9) provides the length of the deformed fiber expressed by the recorded displacement history as Eq. (4-12) and Eq. (4-13).

$$L_1 = L\cos\varphi \sqrt{1 + \left(\frac{S}{L\cos\varphi} + \tan\varphi \right)^2} \tag{4-12}$$

$$L_2 = L\cos\varphi \sqrt{1 + \left(\frac{S}{L\cos\varphi} - \tan\varphi \right)^2} \tag{4-13}$$

Consequently, the tensile strain ε_f developed in the fiber can be given by Eq. (4-14).

$$\varepsilon = \frac{L_1 + L_2}{2L} - 1 \tag{4-14}$$

When the cutting angle φ=0°, Eq. (4-14) can be simplified as Eq. (4-15), which was mentioned as Eq. (4-3) in Mayo and Wetzel [116].

$$\varepsilon_f = \sqrt{1 + \left(\frac{S}{L} \right)^2} - 1 \tag{4-15}$$

It is noted that the axial tensile strain derived here is used to approximately describe the tensile behavior of the fiber outside the cutting area. In the cutting region, the fiber in front of the blade tip was also subject to tension, which was even with a much higher value because of the reduced cross-section area by the blade cut. However, due to the small tip radius of the razor blade, the localized deformation was limited in a ~10-μm-length region astride the blade tip, as observed in Figure 4.10 and Figure 4.12. Considering the gauge length of 50 mm, it is assumed here that the residual part of the fiber had a homogeneous stress distribution, thereby obtaining the axial tensile strain described in Eq. (4-14).

Figure 4.26 portrays the maximum tensile strain developed inside different fibers under various cut conditions. Compared with the normal cut, it is revealed that the oblique cut loading condition failed the fiber with smaller axial tensile strain developed, indicating that the combination of shear force along (F_T) and perpendicular (F_N) to the fiber axis added the complexity of the stress state in the local cut area and caused an earlier failure in the fiber.

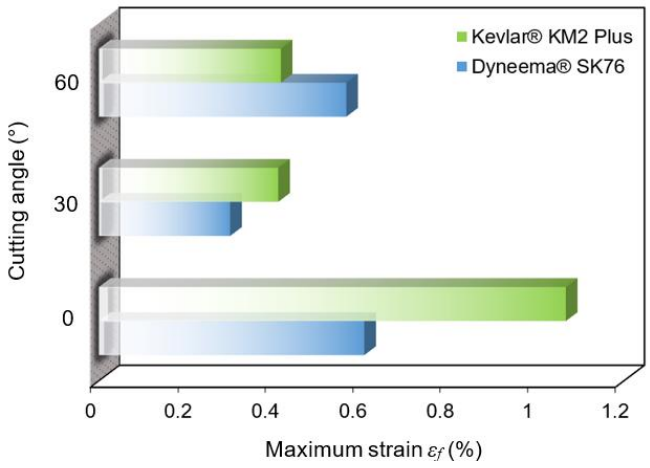

Figure 4.26. Maximum axial tensile strain in the fiber before failure.

4.5.4.3 Tension-induced specific energy

As assumed in Section 4.7.4.2, the fiber astride the cut region is subject to a uniform axial tension. The constitutive model is supposed to consist of the stress-strain curve shown in Figure 4.6. Accordingly, the strain energy store by tension outside the cutting area can be calculated through Eq. (4-16), via integrating the stress-strain curve in a strain region ranging from 0 to ε_f.

$$e_T = \frac{\int_0^{\varepsilon_f} \sigma d\varepsilon}{\rho} \tag{4-16}$$

4.5.4.4 Localized cut-induced specific energy

The specific energy resulting from the localized cut, e_C, is given by Eq. (4-17), which eliminates the contribution of the tension-induced portion in the total specific energy (e) computed as Eq. (4-5).

$$e_C = e - e_T \tag{4-17}$$

Figure 4.27 describes the distribution of e_C and e_T of different fibers under three cut conditions. It is revealed that the localized deformation and failure dominated the energy dissipation during the cut, except for the case when the Dyneema® SK76 fiber was normally cut, where actually there was still 42% total specific energy contributed by e_C. As the cutting angle increased, e_T all decreased even though the maximum strain was large when φ=60°. This is because the decreasing of F_N led to a larger tensile strain in the fiber distributing not only outside but also inside the cut region. The growth of the tensile strain inside the cut region is supposed to be more significant as a result of the complicated stress state analyzed in Section 4.7.3, which enables the fiber to store more strain energy and contributes to the rising of e_C. However, e_T did not significantly reduce the Dyneema® SK76 fiber compared with the Kevlar® KM2 Plus fiber. This indicates a more effective energy dissipating mechanism of the Dyneema® SK76 fiber through axial tension, which possibly attributes to the physical transverse bridges provided by the shish structures and the tie chain inside the Dyneema® SK76 fiber, as illustrated in Section 4.7.2.

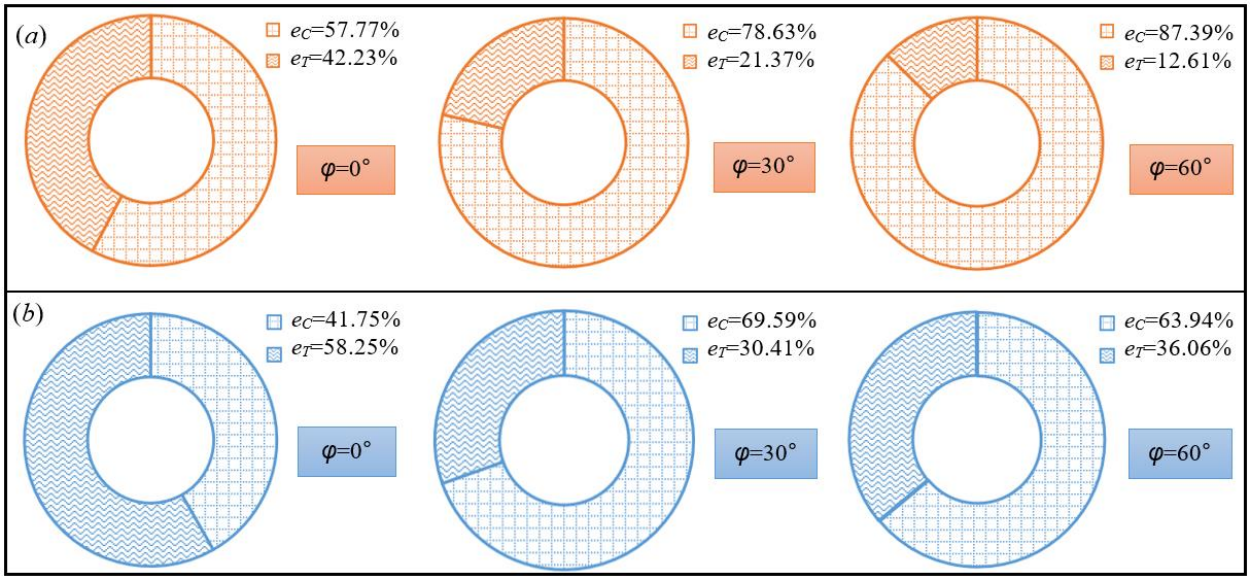

Figure 4.27. Distribution of e_C and e_T of two fibers under the normal and oblique cut. (*a*) Kevlar® KM2 Plus fiber; (*b*) Dyneema® SK76 fiber

4.6 Conclusions

This study demonstrates and compares the in-situ observation of the failure processes of a single Kevlar® KM2 Plus and Dyneema® SK76 fiber cut by razor blades at various angles, including the initial contact, deformation, crack initiation and propagation until final failure. Failure modes and quantitative load and displacement signals were verified by comparing the data with existing work on post-fracture analysis on single fibers and performing the same experiments on sputter-coated fibers inside the SEM to capture the fiber failure in high resolution.

Under transverse normal cutting, the Kevlar® KM2 Plus fiber is observed to be cut into about 75% of the fiber diameter, and the residual part was tensioned to break, while the Dyneema® SK76 fiber is completely cut through by the razor blade. It is physically demonstrated that the shear force from the cutting blade dramatically suppresses the high performance of fibers in tension. For Dyneema® SK76 fiber, the microstructural characteristics, including the shish-kebab fibrils and tie chains, are considered to be the nature of an entirely cutting-through phenomenon by maximizing the connection among the extended chain fibrils to resist cutting. Although these physical bridges improve the transverse stiffness of the fiber, they decrease the transverse displacement of the fiber and cause fibrils to fail by cutting long before their high performance in tension was fully developed. In comparison, to resist a razor blade, the Kevlar® KM2 Plus fiber, with a smaller diameter and a parallel-short-rod nanostructure, behaves more flexible with a larger deformation and makes full use of its tensile performance to absorb more energy from the razor blade.

Experiencing oblique cutting, a smaller cutting angle is more likely to cause a more localized complex stress state around the blade tip, decreasing the cutting resistance of the single fiber. When the cutting angle gets larger, the fiber resists the coming blade in a much tougher manner. In the transverse direction, the fiber becomes more resistant to cut, while along the fiber length, the blade easily cuts the fiber, splitting the fibrils from the entire fiber. The different cutting-resistant performance is considered to result from variations of two components of the blade tip force against the cutting angle. Besides, Dyneema® SK76 fibers are revealed to have better large-angle oblique cutting resistance than Kevlar® KM2 Plus fibers, which is assumed to be attributed to the transverse constraints provided by the shish-kebab structure and tie chains inside the fiber.

The mass-competent cutting resistance of a single fiber was evaluated via the specific energy (e), which is further disintegrated into a localized cut-induced specific energy component (e_C) and another tension-induced specific energy (e_T). Despite a lower specific energy e, the distributions of e_C and e_T inside the Dyneema® SK76 fiber was less sensitive to the cutting angle, indicating a more effective energy dissipating mechanism of the fiber through axial tension, which possibly attributes to the effective physical bridges provided by the shish structures and the tie chain.

CHAPTER 5. FAILURE BEHAVIORS OF SINGLE HIGH-PERFORMANCE FIBERS UNDER DYNAMIC TRANSVERSE CUT

The following chapter contains content reproduced with permission from the journal article:
Gao J, Lim BH, Zhai X, Nie Y, Kedir N, Chen, W. (2020). Failure behaviors of single high-performance fibers under transverse dynamic cut. *International Journal of Impact Engineering*, 144, 103660. DOI: 10.1016/j.ijimpeng.2020.103660

5.1 Introduction

Chapter 4 has visualized the local cut mechanism of single aramid (Kevlar® KM2 Plus) and UHMWPE (Dyneema® SK76) fibers with high resolution. However, the loading speed was very low as 1.67 μm/s. In an impact event, the high loading speed may influence the mechanical response of a single fiber. Therefore, this chapter is to study the dynamic cut mechanism of single fibers.

A reverse impact experimental setup was developed to transversely cut single fibers by using a miniature modified Kolsky compression bar loading system. Upon the strike's impact, the incident bar drove a fiber sample mounted at the bar end to a razor blade. The blade was fixed ahead of a dynamic force transducer (load cell) on a three-axis stage. The load history at the blade tip during each dynamic cut event was accurately recorded after placing an acoustic noise barrier and anti-vibration foams to isolate air and table vibration noises, respectively. The real-time failure behavior of the single fiber was captured by a high-speed camera with a 50X objective lens, illuminated by a visible light source originated from a flash lamp and then condensed by a self-constructed light condensing and bending system. Three types of fibers, namely Kevlar® KM2 Plus, Dyneema® SK76, and S-2 Glass fiber, were cut in varied angles. Loading rate effect on the cut-induced fiber failure was studied by comparing the fiber's dynamic failure process and fracture surface with those under the quasi-static loading condition. The fiber length and cut angle effects on the failure and energy absorption of a single fiber were also discussed. To avoid the cyclic loading on the single fibers on the Kolsky bar, the gauge length of the fiber sample was reduced to 6.35 mm, which was much shorter than that in Chapter 4. Therefore, to identify the loading rate effect on the fiber’s failure under the cut, additional quasi-static tensile and cut experiments on single fibers were both performed on the 6.35-mm samples by using the technique introduced in

Chapter 4. The experimental results were compared with those obtained by dynamic cut experiments in this work.

5.2 Materials

Aramid fibers of Kevlar® KM2 Plus (DuPont™, Delaware, USA), ultra-high-molecular-weight polyethylene (UHMWPE) fibers of Dyneema® SK76 (DSM, Geleen, the Netherlands), Glass fibers of S-2 Glass (AGY, Aiken, USA) were provided in the form of roving wherein the fibers were straight and untwisted. The former two types are currently heavily used as the constituent fibers of body armor. The S-2 Glass roving, as received, was treated with a sizing compatible with epoxies or polyesters and has wide application in vehicle armor [6]. Single fiber samples were carefully pulled out from the corresponding roving and then glued onto the fixtures designed for different experiments, which will be introduced in detail in Sections 5.3.3 and 5.3.4. The average diameters of the Kevlar® KM2 Plus, Dyneema® SK76, and S-2 Glass fibers were namely 10.82±0.37 μm, 16.99±0.67 μm, 9.83±0.28 μm, measured from micrographs obtained using a Quanta 3D FEG SEM (FEI, Hillsboro, OR) in a low vacuum mode, with the chamber pressure 0.23 Torr, accelerating voltage 5 kV.

5.3 Experiments

5.3.1 Quasi-static tensile experiments

Single fiber samples were adhered onto cardboards with circular holes punched at the center using the epoxy adhesive DP190 (3 M Inc., St. Paul, MN, USA). The gauge length of the sample was determined by the diameter of the hole as 6.35 mm. At the same time, A bond length ~1.5 times of the gauge length was carefully decided, which effectively reduced the effect of the fiber's being pulled out into an undetectable level. The cardboard with the fiber sample was then mounted onto a Deben Microtest tensile stage (Deben UK Ltd., Oxford, UK) and assembled inside the chamber of the Quanta SEM, as shown in Figure 5.1*a*. The cardboard was then snipped along the dashed line in Figure 5.1*a*. Before each experiment, the SEM measured the diameter of each sample, eliminating the source of error by the usage of the fiber diameter on average. The fiber was tensioned at a rate of 2.6×10^{-4} s^{-1}.

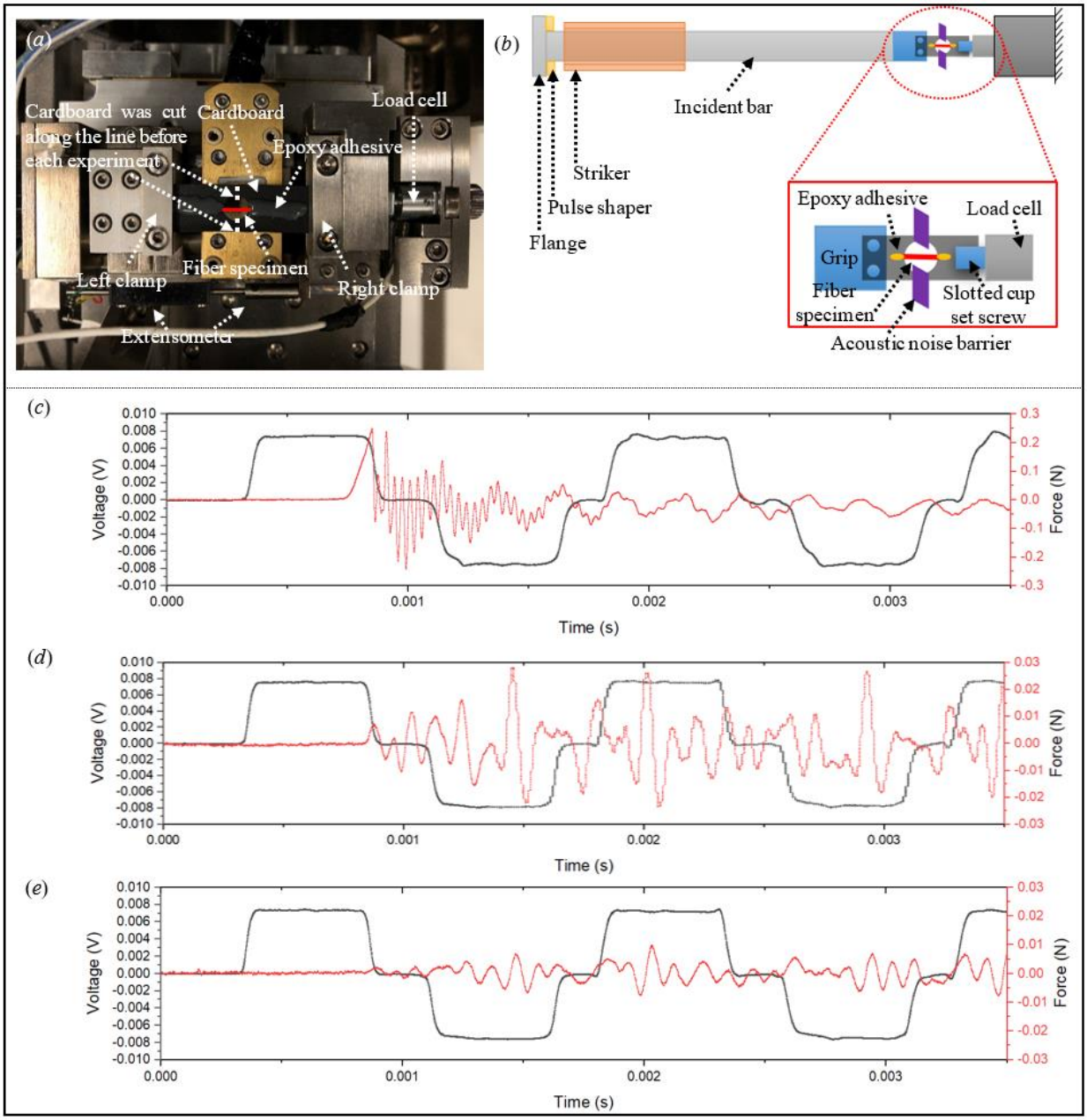

Figure 5.1. Experimental setup of tensile experiments. (*a*) Quasi-static tensile experimental setup; (*b*) Dynamic tensile experimental setup; Oscilloscope record of the incident waveform and the transferred load signal (*c*) in an actual experiment; (*d*) without mounting a sample and placing the acoustic noise barrier; (*e*) without mounting a sample but with the acoustic noise barrier placed.

Stress (σ_0) in each fiber sample was calculated by Eq. (5-1), where F is the load history recorded by the load cell; d is the diameter of each fiber sample.

$$\sigma_0 = \frac{4F}{\pi d^2} \tag{5-1}$$

Correspondingly, the time-resolved strain (ε_0) in an individual fiber can be tracked by the displacement history (S_0) based on Eq. (5-2), where L_0 is the gauge length of 6.35 mm.

$$\varepsilon_0 = \frac{S_0}{L_0} \tag{5-2}$$

5.3.2 Dynamic tensile experiments

The dynamic tensile experiments on single fibers were performed using a modified Kolsky tension bar apparatus schematically depicted in Figure 5.1*b*. Before experiments, a cardboard, attached with a fiber sample having the same gauge length of L_0=6.35 mm in quasi-static tensile experiments, was gripped onto the end of the incident bar. The other end of the cardboard was glued to a slotted cup set screw connected with a 22.24 N (5 lbf) quartz–piezoelectric load cell (Kistler 9712B5). The cardboard was then cut off, similar to the procedure in the quasi-static tensile experiment. Upon loading, the incident bar was activated in motion after the air-propelled strike tube impacted its flange end, as present in Figure 5.1*b*. Simultaneously, the fiber sample mounted at the opposite end was tensioned with an average strain rate of ~420 s^{-1}. It is noted that the movement of the incident bar caused the surrounding air to flow onto the load cell. Figure 1*d* reveals the noise by the air reached 0.005 N, which is ~2% of the peak force to fail a Kevlar® KM2 Plus fiber in tension (see Figure 5.1*c*). In order to eliminate such noise, an acoustic noise barrier (ANB) made by multiple layers of cardboard was installed ahead of the load cell. Figure 5.1*e* verifies the effectiveness of the ANB in insulating the air noise. Other techniques include placing anti-vibration foams under the three-axis stage to isolate the noise due to the vibration of the optical table.

The stress inside each fiber was computed via Eq. (5-1) based on the recorded load history and the measured fiber diameter before the experiment. The strain in the fiber was related to the

bar strain via the assumption of 1D wave propagation theory. During the dynamic tensile experiment, the bar strain associated with the stress wave was recorded with strain gauges on the bar surface through a Wheatstone bridge in a half-bridge configuration. The loading rate $v(t)$ can be calculated as Eq. (5-3) from magnitudes of the measured incident strain $\varepsilon_I(t)$ and reflected strain $\varepsilon_R(t)$,

$$v(t) = c_B\left[\varepsilon_I(t) - \varepsilon_R(t)\right] \tag{5-3}$$

where c_B indicates the elastic bar wave speed.

By assuming a constant strain rate loading, the strain of the fiber sample was given by Eq. (5-4).

$$\varepsilon_0 = \frac{\int_0^t v(\tau)d\tau}{L_0} \tag{5-4}$$

5.3.3 Quasi-static cut experiments

5.3.3.1 Fiber fixture and mounting method

The hexagon fiber fixture for the quasi-static normal cut experiment was designed as Figure 5.2*a* and then printed by a Form 2 SLA 3D printer (Formlabs, Somerville, MA). A three-step fiber mounting method [44] was employed to fix the fiber sample onto the fixture, which was presented in detail in Figure 5.2*b*: ① Wrapped the fiber on a pin and secured the wrapped area with ZAP glue; ② wrapped a carbon tape onto the pin and wrapped the residual fiber at both ends onto the carbon tape; ③ dropped ZAP glue onto the wrapped area for final secure. It is noted that the tiny fiber in Figure 5.2*b* is represented as a line in the convenience of presenting. The interaction between the wrapped fiber and the carbon tape was able to prevent the slide of the sample, which has been demonstrated in [44].

For the oblique cutting experiment, a cardboard with a 6.35-mm-diameter punched hole was utilized to hold the fiber sample. Lines were pre-drawn on the cardboard to determine the fiber

direction for the cut. The cardboard was then partially cut along the lines, forming small incisions as shown in Figure 5.2*d*①. The fiber was then wrapped between the small incision and the punched hole edge and mounted onto the cardboard in the same three steps described in the normal cut experiment. The entire cardboard with the fiber in Figure 5.2*d*② was then carefully inserted into the slot of the designed fiber fixture in Figure 5.2*c* and cured with the ZAP glue. Finally, the cardboard was tailored as in Figure 5.2*d*③ for the oblique cut experiment.

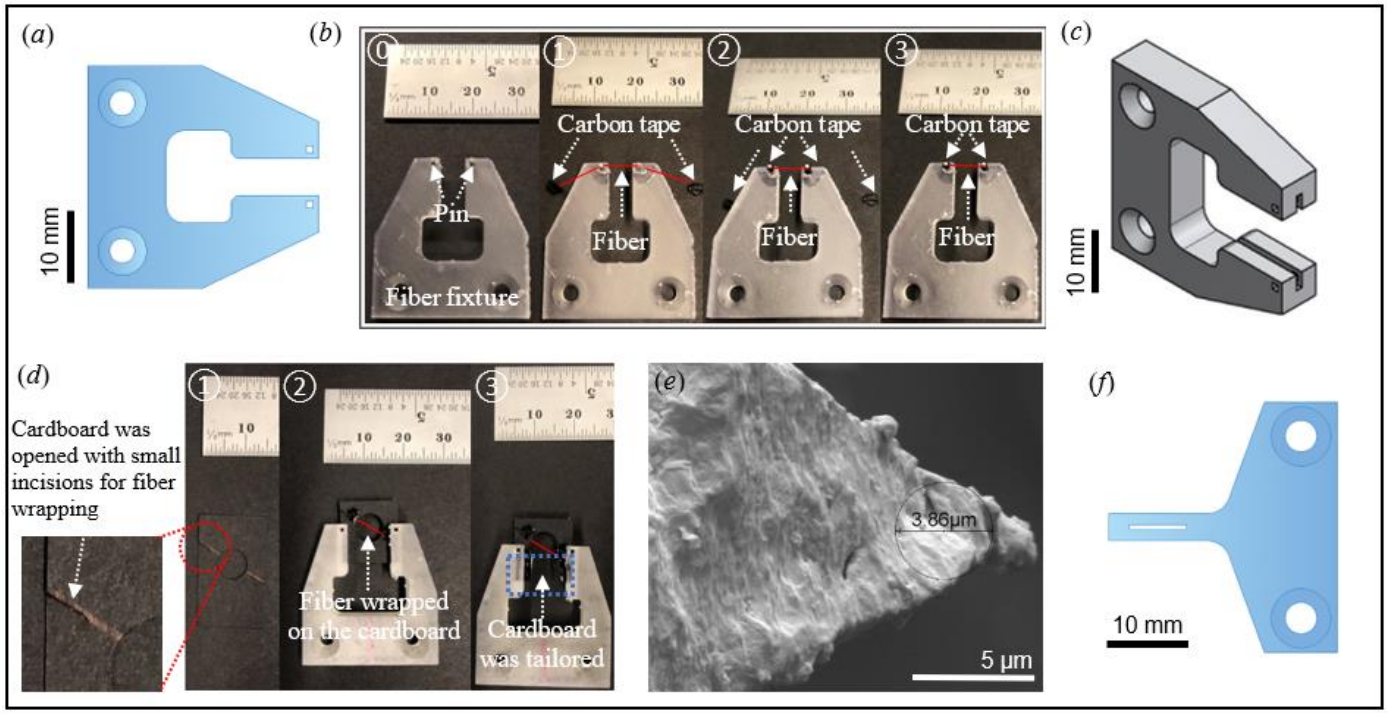

Figure 5.2. Sample and indenter preparation for quasi-static cut experiments. (*a*) Sketch of fiber fixture for normal cut experiments; (*b*) Three-step fiber mounting method; (*c*) Sketch of fiber fixture for oblique cut experiments; (*d*) Installment of the fiber onto the fiber fixture designed for oblique cut experiments; (*e*) Blade geometry; (*f*) Sketch of the blade fixture.

5.3.3.2 Indenter and indenter fixture

A blade (TED PELLA, INC., Redding, CA) was used as the indenter in experiments. The tip radius of the razor blade on average was measured as 2 μm from SEM micrographs, presented in Figure 5.2*e*. Figure 5.2*f* provides a schematic of the 3D printed blade fixture for quasi-static experiments. The large blade was cut into small pieces, which were then individually assembled into the reserved hole on each blade fixture and secured using ZAP glue.

5.3.3.3 Experimental setup

Quasi-static transverse loading experiments on single fibers were performed by modifying fixtures on the Deben Microtest tensile stage used in the fiber tensile experiments. The newly designed fiber fixture with an uncoated fiber sample and blade fixture (with the blade) were first assembled onto the left and right stage of the setup, respectively. During the experiment, the left stage and right stage moved apart, driving the fiber and the blade tip to approach. The blade then contacted and loaded the fiber in the middle until the fiber broke. The deformation, damage, and failure of the fiber in real time were captured by the secondary electron detector (SED) in the Quanta SEM under a low vacuum mode. Simultaneously, the load and displacement history were recorded by a load cell at the blade fixture side and an extensometer. The method in detail was illustrated in [44]. Figure 5.3 is the schematic illustration of the experimental setup with the newly designed fiber and blade fixtures.

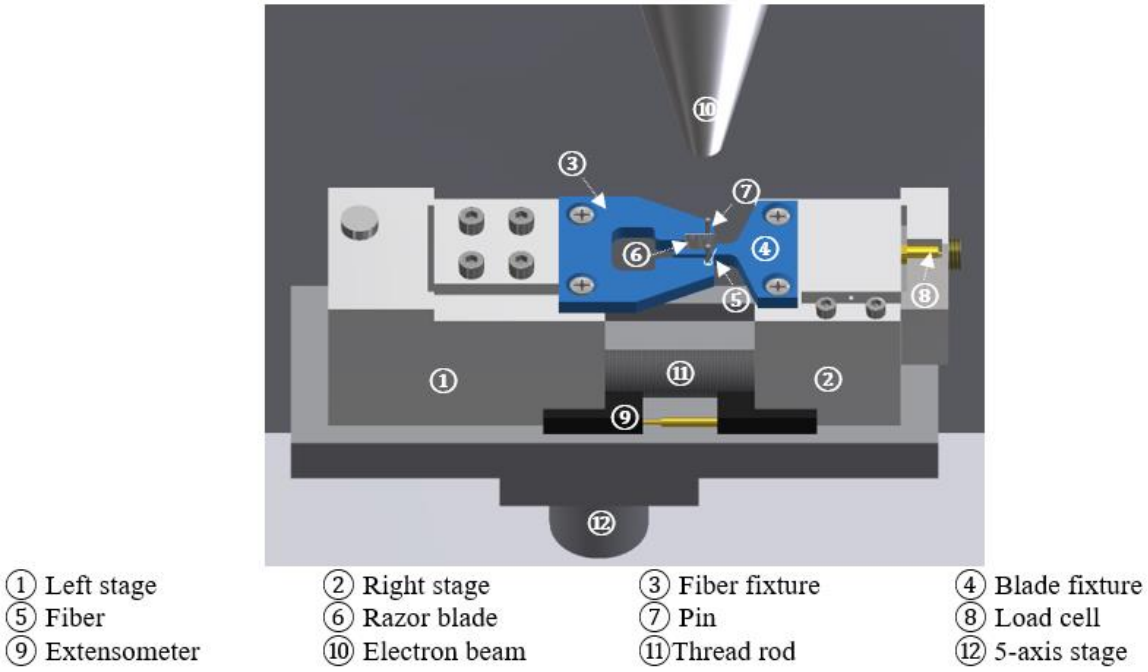

Figure 5.3. Schematic of the quasi-static experimental setup.

5.3.4 Dynamic cut experiments

5.3.4.1 Fixtures for the fiber and blade

By using a similar method in Figure 5.2*d*, the fiber was wrapped and mounted, normally or obliquely, onto a cardboard with a 6.35-mm-diameter hole punched at the center. The cardboard with the fiber sample was then screwed inside the slot of the fiber fixture designed for dynamic cut experiments in Figure 5.4*a*. Finally, the cardboard on the fixture was tailored into a C-shape for the normal or oblique cut as Figures 5.4*b* and 5.4*c*, respectively.

The blade fixture for the dynamic cut is displayed in Figure 5.4*d*, where the small blade was inserted and glued into the slotted groove of a 10-32 Nylon Plastic set screw (McMaster Carr, Elmhurst, IL).

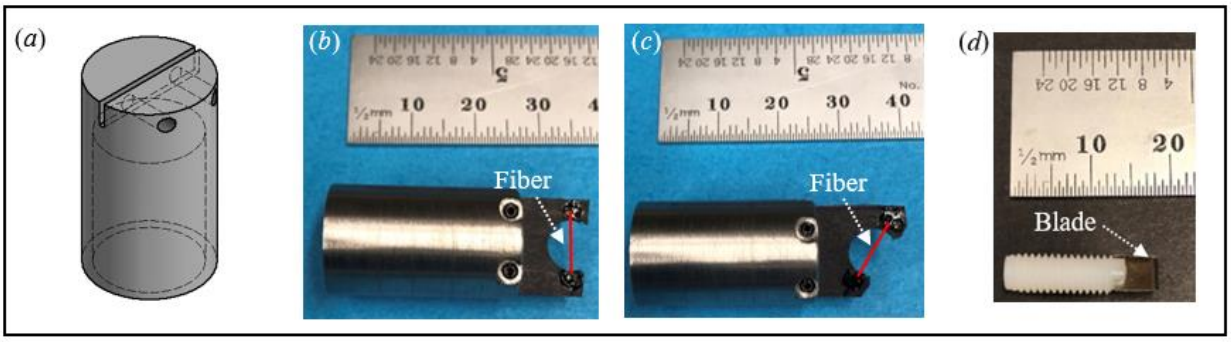

Figure 5.4. Sample and indenter preparation for dynamic cut experiments. (*a*) Fiber fixture for dynamic cut experiments; (*b*) Fiber fixture with fiber sample mounted for normal cut experiments; (*c*) Fiber fixture with fiber sample mounted for oblique cut experiments; (*d*) Blade fixture with the blade mounted.

5.3.4.2 Experimental setup for dynamic loading

A modified miniature Kolsky compression bar technique was used to deliver the dynamic loading to the fiber sample, which is schematically illustrated in Figure 5.5*a*. In order to obtain the load history at the fiber/blade contact area, a reverse impact method was employed. Before each experiment, the fiber fixture with the sample in Figure 5.4*b* or Figure 5.4*c* was screwed onto the end of the incident bar. Unlike a traditional Kolsky bar, the miniature device replaced a transmission bar with a load cell, of which the front was assembled with the blade fixture, and the back was mounted onto a three-axis stage. The three-axis stage controlled the movement of the blade to contact the fiber before loading. By using a gas firing system, a strike was accelerated to a certain speed and impacted onto the incident bar, activating a reverse impact process: the incident bar drove the fiber to impact the blade tip. The maximum traveling distance was controlled by the reserved space between the flange at the opposite end of the incident bar and the single loading stop. Similar to the dynamic tensile experiment, the air noise needed to be insulated by a T-shaped ANB printed by the 3D printer and installed ahead of the load cell on the three-axis stage. Another ANB made by multi-layer cardboards was designed to provide additional insulation of the air pressure, with a fitting hole punched for the blade to head out of the barrier for fiber cut. In addition, anti-vibration foams were used to clear up the noise due to the vibration of the optical table to capture the accurate load signal F_0. The displacement of the bar, which was supposed to represent the relative traveling distance of the fiber at the blade tip to the fiber end, S, was gained as Eq. (5-5) by integrating the velocity calculated through Eq. (5-3).

$$S(t) = \int_0^t v(\tau) d\tau \tag{5-5}$$

The failure behavior of the fiber was captured by a high-speed camera (Shimadzu HPV-X2, Kyoto, Japan) combined with a 50X long working distance objective lens (Mitutoyo, Kawasaki, Japan), which is displayed in Figure 5.5*b*. The objective lens focused on the fiber/blade contact area. The reverse impact method guaranteed the fiber/blade contact area to always appear within the camera screen, ensuring the entire cut event was captured. Since the fiber was tiny and the magnification of the objective lens was very large, high-intensity light was required to illuminate the field of view. A light condensing and bending system was built to condense the light source from a high photon-flux flash bulb and then transit the light to the target scope as illumination, which was schematically described in Figure 5.5*b*. The light condensing system is composed of three convex lenses. First, a 75-mm diameter plano-convex lens (*f*=85mm) was placed in front of the flash bulb to collect the light and another 75-mm diameter plano-convex lens (*f*=200mm) was for condensing the light from the previous lens. Then the condensed light passed through a bi-convex lens (*f*=10mm) with a small diameter of 6 mm and became a parallel light. Since the light had been condensed and needed to shoot onto the fiber accurately, the light bending system was constructed by three prisms installed in the corresponding 3D printed holders. The first prism was used to bend the light down to the height of the fiber sample. The second prism was an intermediate between prism 1 and prism 2. The third prism was assembled on a T-slotting framing so that it can move left and right and accurately deliver the condensed light onto the target scope. The whole light path was covered by either black paper or slip-on lens tube covers (Thorlabs, Newton, NJ) to obtain a better contrast.

The trigger method was carefully designed to capture the cut event. After the strike impacted the incident bar, the incident wave passed the strain gauge adhered on the bar surface at its middle span. The signal of the strain gauge was then recorded by the oscilloscope which sent out a trigger signal to the camera. Subsequently, the camera generated a rising pulse and triggered the flash bulb. An appropriate time delay (due to the travel time of the waveform down to the incident bar end) was cautiously determined to visualize the dynamic failure process of the fiber at frame rates between 1M and 5M fps (frames per second). The flash has a 5-7 ms duration, which ensured a lasting illumination through the entire cut event.

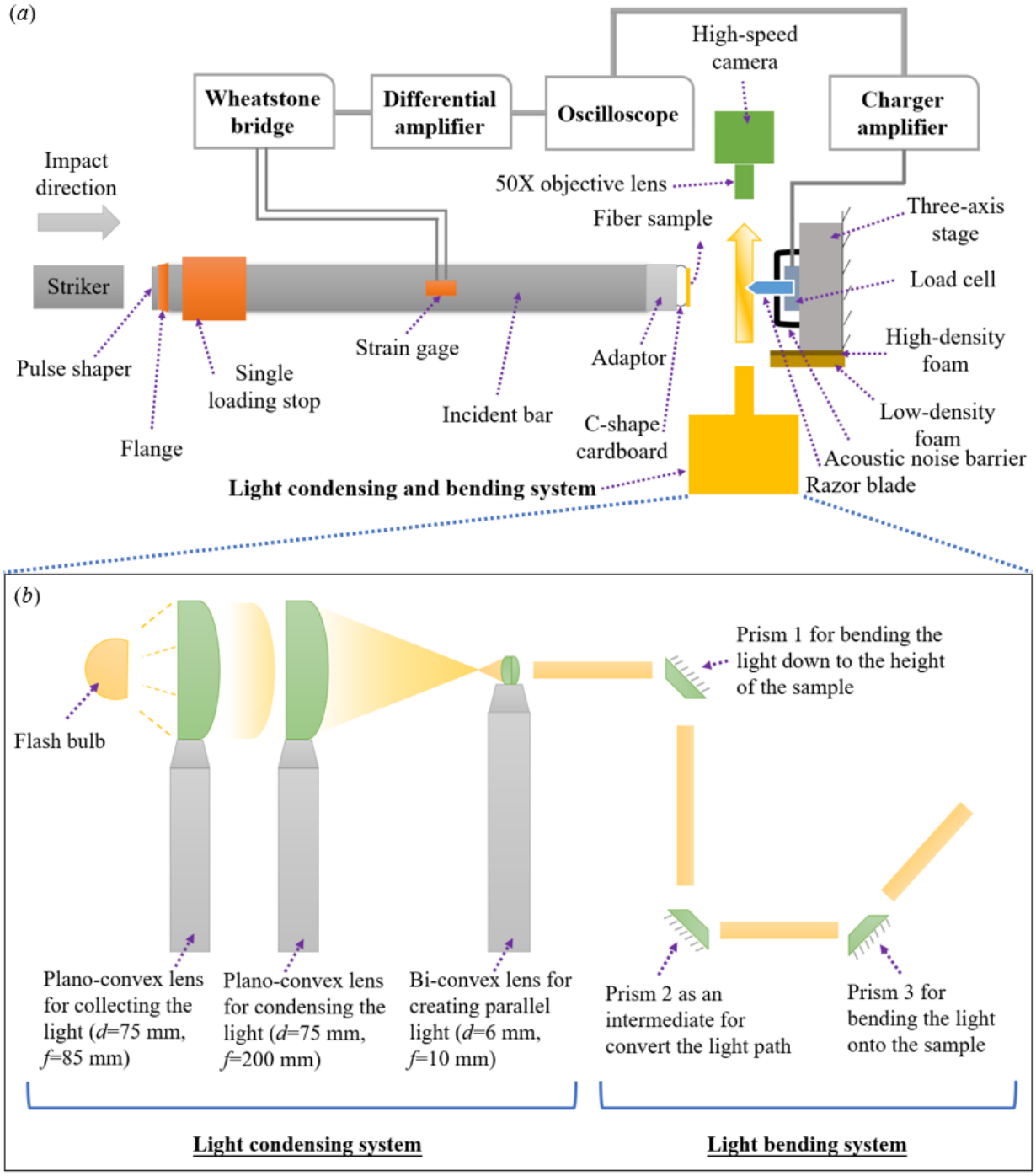

Figure 5.5. Experimental setup for dynamic loading. (*a*) Schematic of the entire experimental setup. (*b*) Light condensing and bending system.

Table 5.1. Tensile properties of Kevlar® KM2 Plus, Dyneema® SK76, S-2 Glass fibers

Author	Fiber type	Grip method	Gauge length (mm)	Strain rate (s^{-1})	Fiber diameter (μm)	Tensile strength (GPa)	Failure strain (%)
This work	Kevlar® KM2 Plus	Epoxy glue	6.35	2.6×10^{-4}	10.64 ± 0.21	3.98 ± 0.29	4.49 ± 0.30
		Epoxy glue	6.35	420	10.64 ± 0.21	4.19 ± 0.63	4.29 ± 0.49
Gao et al. [45]	Kevlar® KM2 Plus	Epoxy glue	16	1.04×10^{-4}	10.82 ± 0.37	3.33 ± 0.32	3.36 ± 0.13
Cline et al. [119]	Kevlar® KM2 Plus	Direct gripping	5, 15	3×10^{-4}	11.18 ± 0.53	3.0 ± 0.3	3.4 ± 0.4
This work	Dyneema® SK76	Epoxy glue	6.35	2.6×10^{-4}	16.39 ± 0.51	2.16 ± 0.36	4.37 ± 0.67
			6.35	420	16.39 ± 0.51	3.72 ± 0.43	5.99 ± 0.73
Gao et al. [45]	Dyneema® SK76	Epoxy glue	16	1.04×10^{-4}	16.99 ± 0.67	2.96 ± 0.20	3.76 ± 0.29
Mayo and Wetzel [116]	Dyneema® SK76				18.8	2.62	3.6
Sanborn et al. [120]	Dyneema® SK76	Direct gripping	5	0.001	14.5-16.9	3.63 ± 0.19	3.48 ± 0.42
			10			3.64 ± 0.31	3.93 ± 0.96
			50			3.69 ± 0.17	3.96 ± 0.36
			5	1		4.28 ± 0.30	2.92 ± 0.23
			10			3.96 ± 0.35	3.35 ± 0.75
			50			4.14 ± 0.50	3.29 ± 0.25
			10	775		4.08 ± 0.17	3.00 ± 0.24
			5	913		4.24 ± 0.39	2.58 ± 0.31
			7	1156		4.25 ± 0.21	3.51 ± 0.57
Hudspeth et al. [121]	Dyneema® SK76	Epoxy glue	5, 10	0.001		3.12-3.15	
			5, 10	0.01		3.31-3.40	
			5, 10	400		3.63-3.67	
			5	600		3.56	
			10	600		3.92	
This work	S-2 Glass	Epoxy glue	6.35	2.6×10^{-4}	9.83 ± 0.28	3.76 ± 0.27	7.40 ± 0.71
			6.35	420	9.83 ± 0.28	4.54 ± 0.51	6.21 ± 0.62
Mayo and Wetzel [116]	S-2 Glass				9.3	4.8	5.5
Hearle et al. [127]	S-2 Glass				10	4.0	5.4

5.4 Results

5.4.1 Tensile properties of single fibers

Figure 5.6 shows the raw data of axial tensile stress-strain curves of three-type fibers under quasi-static and dynamic loading conditions. The loading rate effect was not obviously observed for the Kevlar® KM2 Plus fiber with an elastic modulus ~90 GPa. In contrast, the ultimate strength and failure strain of the Dyneema® SK76 fiber are highly rate-dependent. As the loading rate increased from 2.6×10^{-4} s^{-1} to 420 s^{-1}, the ultimate strength of Dyneema® SK76 fibers rose from an average value of 2.16 GPa to 3.72 GPa, while the failure strain had an increase from 4.37% to 5.99%. On the other hand, the S-2 Glass fiber became stiffer with the loading rate: the average tensile stiffness increased by 45.77% when subject to the dynamic axial tension. Table 5.1 compares the tensile strength and failure strain reported in the literature, revealing that the measurement of fiber tensile properties relies on the grip method, sample gauge length, and strain rate.

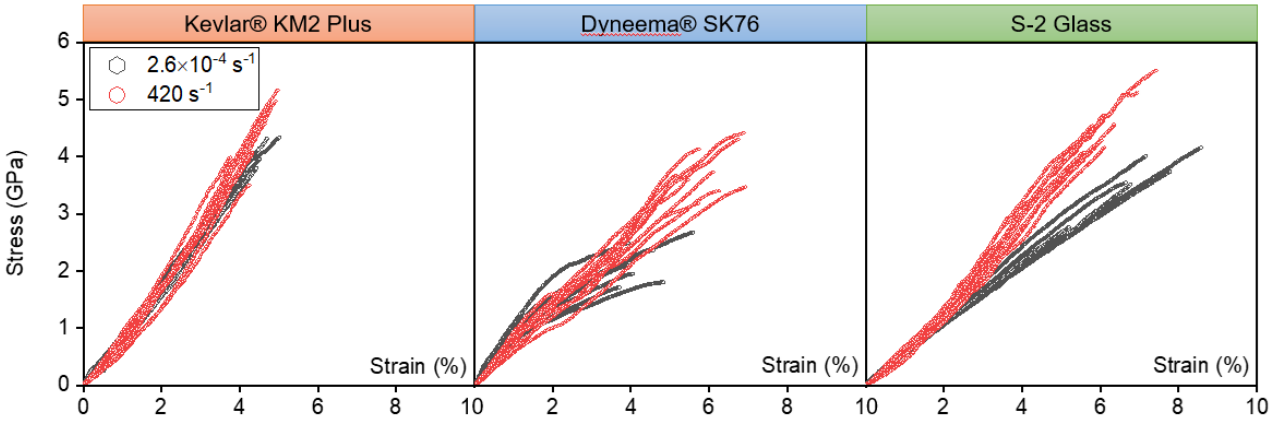

Figure 5.6. Raw data of tensile stress-strain curves of different fibers.

5.4.2 Load-displacement curve

Figure 5.7*a* is the schematic of a single fiber experiencing transverse normal cut, where F represents the force at the blade tip in real time, S is the traveling distance of the fiber at the blade tip. During the loading process, the fiber bent at the blade tip, forming a triangle shape and offsetting the initial position at an angle of θ. F_{max} and S_{max} are the maximum force and

displacement measured before the fiber failure, respectively. Correspondingly, θ_{max} represents the breaking angle of the fiber.

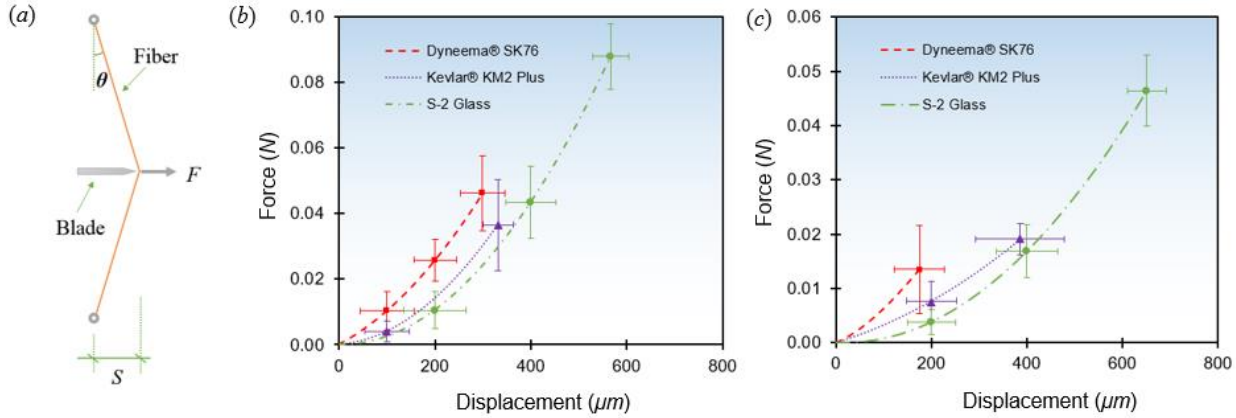

Figure 5.7. Load-displacement curves of different fibers transversely cut at different rates. (*a*) Schematic of a single fiber subjected to transverse loading of a razor blade; (*b*) Dynamic loading; (*c*) Quasi-static loading.

Five to ten experiments were repeated for each type of fiber under one specific cut condition. For the quasi-static cut experiment, the force and displacement data were recorded directly by the load cell and the extensometer. On the other hand, in a dynamic cut experiment, the force history was also directly captured by the load cell, while the time-resolved displacement was transferred from the output voltage signal from the strain gauge. The equation of the average force-displacement curve of a single fiber was obtained by curve fitting in Origin 2017. The average force-displacement curves of different fibers were plotted within the corresponding maximum displacements on average, as shown in Figures 5.7*b* and 5.7*c*.

5.4.3 Failure process of single fibers under the quasi-static normal cut

Figure 5.8 demonstrates the failure processes of three types of fibers under the quasi-static transverse cut. The initial contact between the blade and the fiber can be identified by the SE detector inside SEM, which has been illustrated in [44]. The morphologies of different fibers initially contacted with the blade are namely shown in Figures 5.8*a*, 5.8*b*, and 5.8*c* when S=0. Afterward, the Kevlar® KM2 Plus and Dyneema® SK76 fibers were observed to be penetrated transversely. Around the blade tip, the fiber was in a very complicated stress state (see Figures

5.8*a* and 5.8*b* when S=95% S_{max}), including axial tension, transverse compression, bending, and shearing by the blade. Before the failure, a crack initiated and propagated along the Kevlar® KM2 Plus fiber, causing the inter-fibril splitting followed by the tensile failure of the fiber. On the other hand, the Dyneema® SK76 fiber was completely cut through in spite of the observable tension-induced fibril failure around the cut region. Different from Kevlar® and Dyneema® fiber, S-2 Glass fiber was difficult for the blade to penetrate, with merely the thin sizing swept off the fiber. The fiber was bent astride the blade tip and stretched until breakage in a brittle manner, as observed in Figure 5.8*c*.

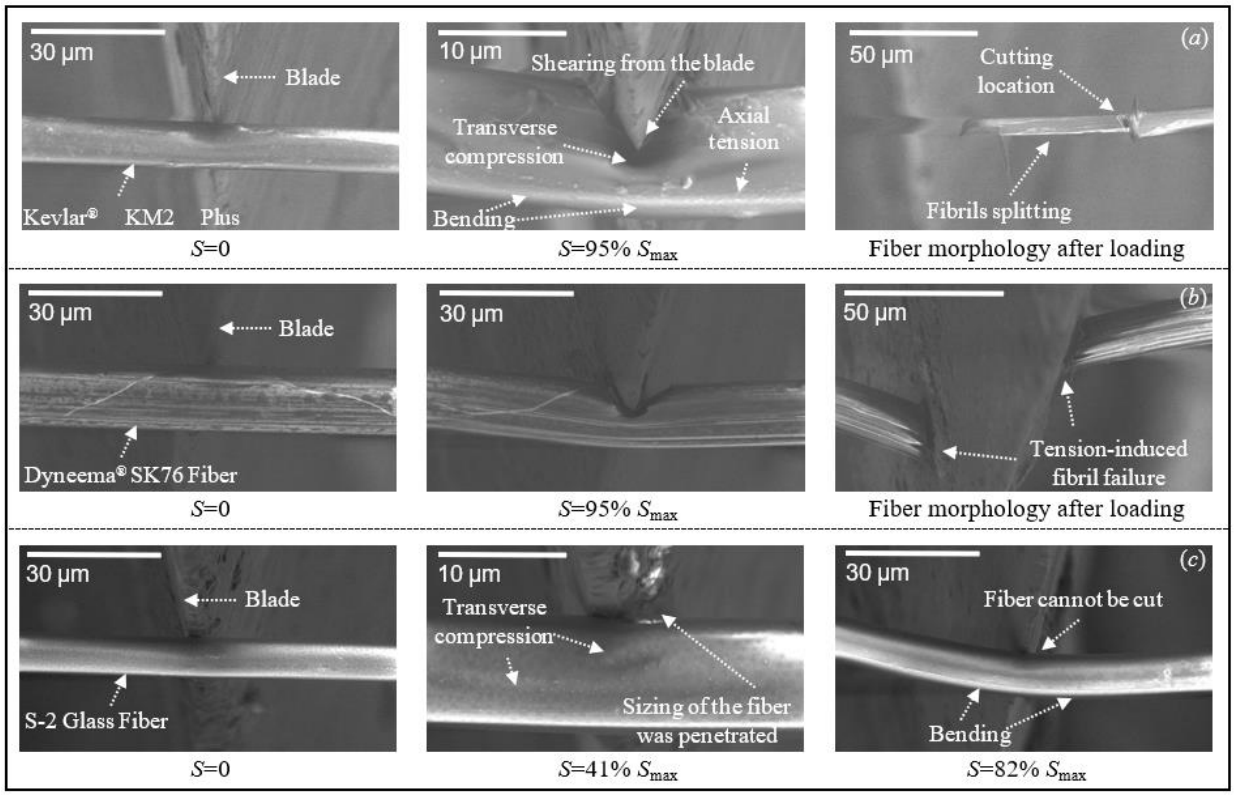

Figure 5.8. Failure processes of different fibers under quasi-static loading. (*a*) Kevlar® KM2 Plus fiber; (*b*) Dyneema® SK76 fiber; (*c*) *S*-2 Glass fiber.

5.4.4 Failure process of single fibers under quasi-static oblique cut

Under the oblique cut, the failure processes of the single Kevlar® KM2 Plus and Dyneema® SK76 fibers with the short length of 6.35 mm in this work were similar to those of the 50-mm-length fibers reported in [45]. The blade was able to penetrate through the individual fiber at the specific

cut angle φ. The cut force at the blade tip, F, as sketched in Figure 5.9*a*(2), had two components along and perpendicular to the fiber length as F_T and F_N, respectively. When φ was small, F_N dominated the fiber failure behavior, resulting in the continuous penetration of fiber in the transverse direction. The tangential component, F_T, albeit with a small value, buckled the fibrils around the blade tip, adding extra complexity to the multi-axial stress state of fibrils inside the cut region, including transverse compression, axial compression, inter-fibril compression and friction, axial tension, bending and shearing by the blade. The deformations of Kevlar® KM2 Plus and Dyneema® SK76 fibers under oblique cut at φ=30° are demonstrated in Figures 5.9*a*(2) and 5.9*b*(2). Comparing with the fiber under the normal cut, the fiber subject to the small-angle oblique cut failed within a short displacement S measured by the extensometer. The Kevlar® KM2 Plus fiber was split along a longitudinal crack and failed in tension away from the cut region (see Figure 5.9*a*(3)), while the Dyneema® SK76 fiber was completely cut through without axial splitting as exhibited in Figure 5.9*b*(3).

As φ increased to 60°, F_N decreased, making the fiber difficult to be cut transversely. The fiber failed after the blade traveled a larger distance. In contrast, the increasing F_T intensified the buckling of fibrils in Figures 5.10*a*(2) and 5.10*b*(3). For Kevlar® KM2 Plus fiber, such fibril buckling mechanism induced a crack in Figure 5.10*a*(3), initiating from the cut area and propagating along the fiber. At last, the fiber was tensioned to break at the longitudinal crack tip as Figure 5.10*a*(4) because the fibrils in front of the tip lost the resistance to the rapidly growing tensile stress after the effective cross-section of the fiber was dramatically reduced upon the arrival of the crack. For Dyneema® SK76 fiber, although observable inter-fibril splitting in Figure 5.10*b*(3) was caused by fibril buckling, no crack was found along the fiber axial direction until the fiber failure in Figure 5.10*b*(4).

S-2 Glass fiber was observed to have an essentially similar failure behavior under oblique cut with that under normal cut since the fiber cannot be penetrated by the blade. The blade was only able to slide on the fiber surface. The fiber was bent at the blade tip and stretched until failure in a brittle manner. As the cut angle increased, the blade slid at a larger distance on the fiber surface, but it became difficult to bend the fiber. The failure processes of the single S-2 Glass fibers under oblique cut at φ = 30° and 60° were demonstrated in Figure 5.9*c* and Figure 5.10*c*, respectively.

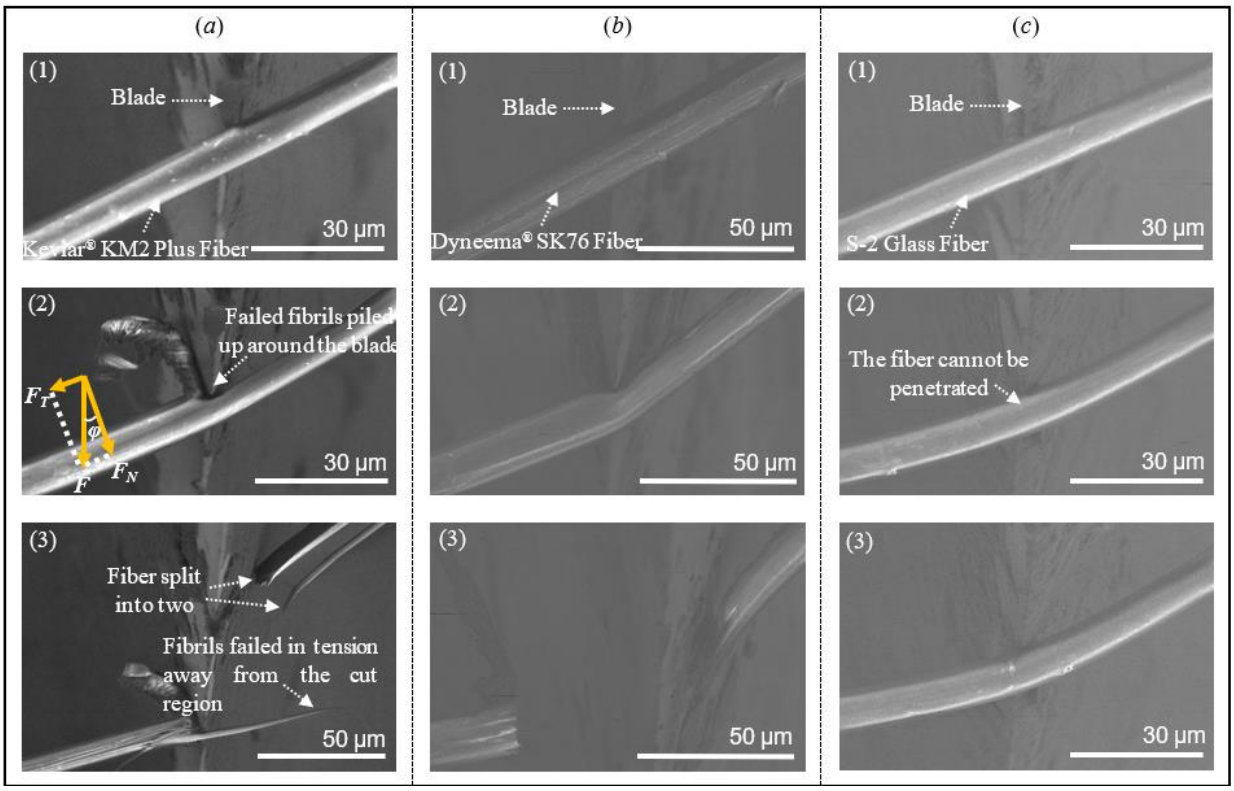

Figure 5.9. Failure processes of single fibers under oblique cut at an angle of φ=30°. (*a*) Kevlar® KM2 Plus fiber: (1) Fiber and blade morphology before loading, (2) S = 85% S_{max}, (3) Fiber morphology after loading; (*b*) Dyneema® SK76 fiber: (1) Fiber and blade morphology before loading, (2) S= 89% S_{max}, (3) Fiber morphology after loading; (*c*) S-2 Glass fiber: (1) Fiber and blade morphology before loading, (2) S = 63% S_{max}, (3) S = 85% S_{max}.

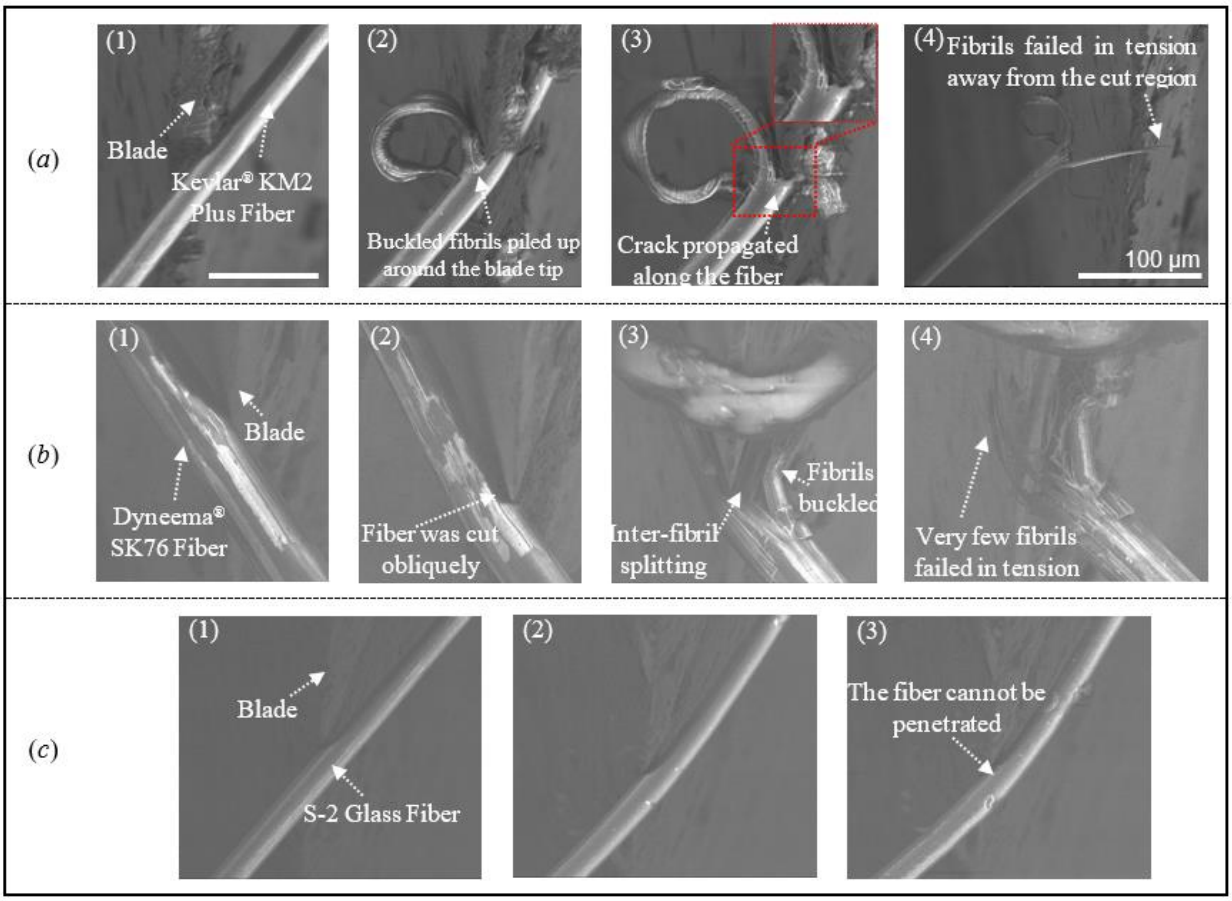

Figure 5.10. Failure processes of single fibers under oblique cut at an angle of φ=60°. (*a*) Kevlar® KM2 Plus: (1) Fiber and blade morphology before loading, (2) S = 93% S_{max}, (3) S = 99% S_{max}, (4) Fiber morphology after loading; (*b*) Dyneema® SK76: (1) Fiber and blade morphology before loading, (2) S = 56% S_{max}, (3) S = 97% S_{max}, (4) Fiber morphology after loading; (*c*) S-2 Glass: (1) Fiber and blade morphology before loading, (2) S = 33% S_{max}, (3) S = 69% S_{max}. Scale bar is 30 μm.

5.4.5 Failure surfaces of single fibers after the quasi-static transverse cut

Figure 5.11 displays failure surfaces of different fibers after being cut transversely under the quasi-static loading condition. Kevlar® KM2 Plus fiber subject to normal cut was observed to have a longitudinal crack splitting the fiber into two parts. As revealed in Figure 5.11*a*, such crack was not located in the center-plane of the recovered fiber but in a parallel plane offsetting away from the fiber edge by a distance of 25%*d*. The fiber was deformed considerably from a circular shape to an ellipse, which indicates the transverse compression by the razor blade. On the fiber/blade contact surface, the failed fibrils were flattened. Tension-induced fibril failure was identified on the fiber fracture surface located at the end of the travel path of the blade. In comparison, fibrils inside the Dyneema® SK76 fiber did not split with each other. Identical flattened fibrils and tension-caused fibril failure were detected as Figure 5.11*d*. When the cut angle increased, both the Kevlar® KM2 Plus and Dyneema® SK76 fiber had more fibrils cut off from the fiber, as compared in Figures 5.11*b* and 5.11*c*, Figures 5.11*e* and 5.11*f*, respectively. The difference is that the Kevlar® KM2 Plus fiber was not fully cut through but split into fibril bundles that broke in tension away from the cut region, while the Dyneema® SK76 fiber was completely sheared through by the razor blade. S-2 Glass fibers were found to have a brittle fracture surface as Figure 5.11*g*, no matter how the cut angle changed.

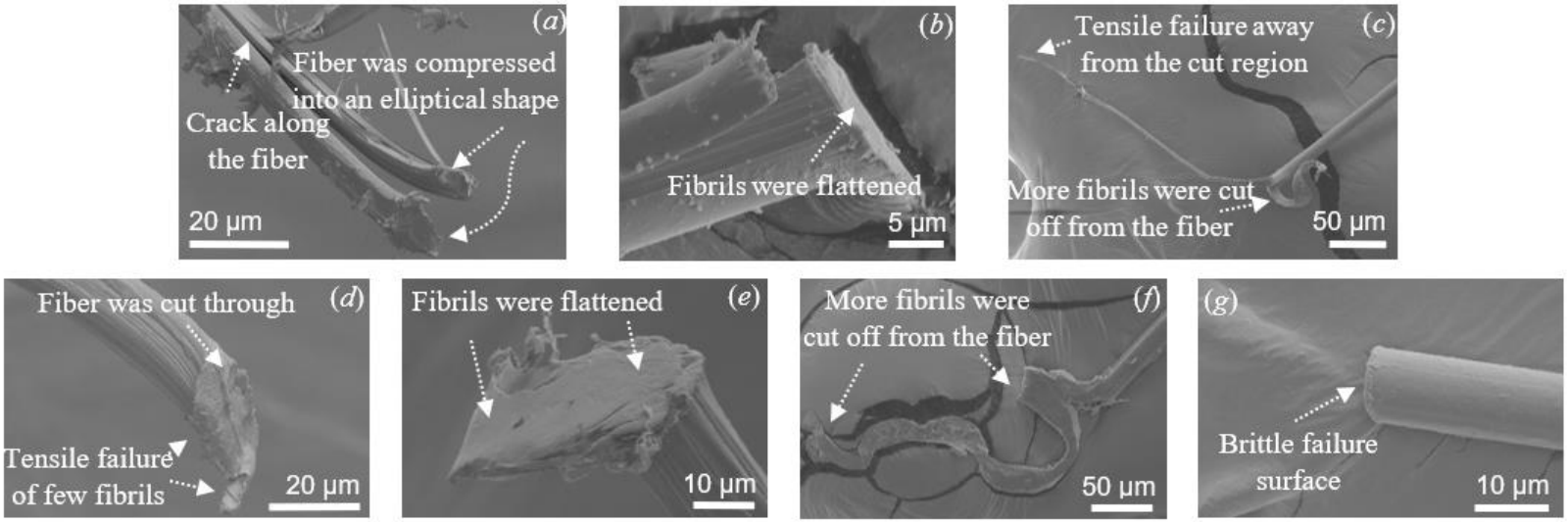

Figure 5.11. Failure surfaces of different fibers after quasi-static transverse cut. (*a*)-(*c*) Kevlar® KM2 Plus fiber: (*a*) φ=0°, (*b*) φ=30°, (*c*) φ=60°; (*d*)-(*e*) Dynema® SK76 fiber: (*d*) φ=0°, (*e*) φ=30°, (*f*) φ=60°; (*g*) S-2 glass fiber.

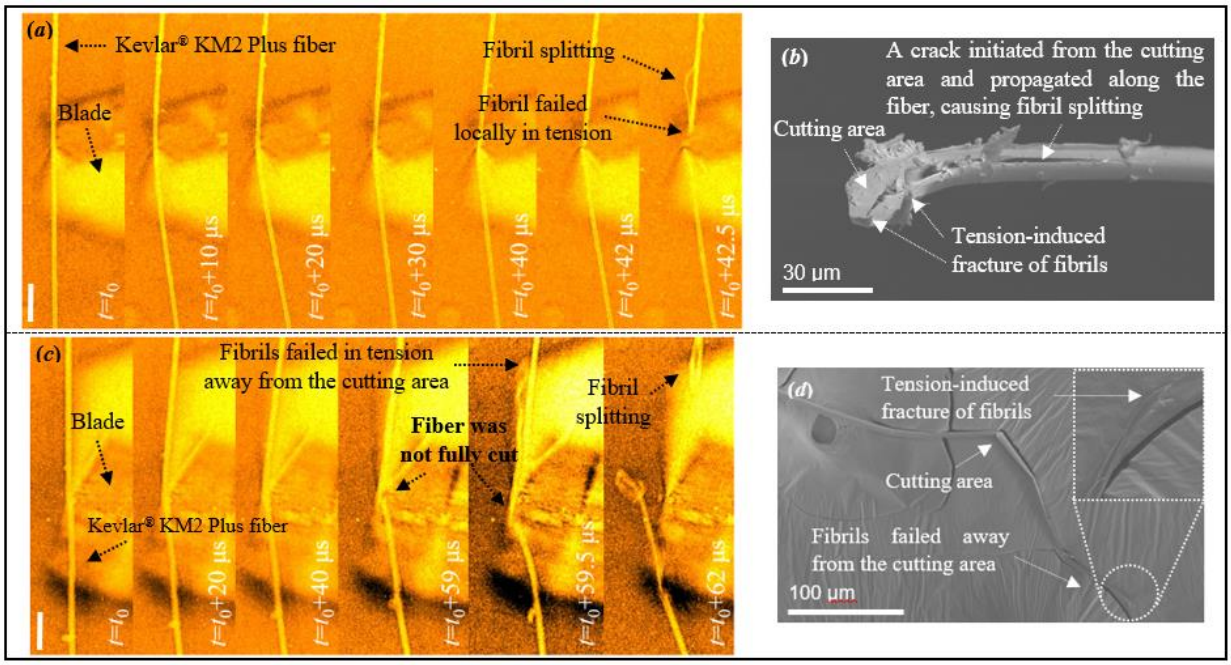

Figure 5.12**.** Failure of a single Kevlar® KM2 Plus fiber under dynamic cutting. (*a*) Failure process of the fiber when fibrils failed in tension beneath the blade tip; (*b*) Failure surface of the fiber when fibrils failed around the cutting area; (*c*) Failure process of the fiber when fibrils failed in tension away from the blade tip; (*d*) Failure surface of the fiber when fibrils failed away from the cutting area. The scale bar is 50 μm.

5.4.6 Failure of single fibers under the dynamic normal cut

The dynamic failure processes of single fibers under the transverse normal cut were very similar to those observed under the quasi-static loading condition. The initial contact between the fiber and the blade was identified by moving the 3-axis stage and observing the relative position of the fiber and the blade through the high-speed camera in live mode. Upon loading, both the Kevlar® KM2 Plus and Dyneema® SK76 fiber were penetrated by the razor blade. The fiber bent at the blade tip, forming a V-shape geometry. The Kevlar® KM2 Plus fiber failed due to tension-caused breakage of fibrils instead of being fully cut through by the blade. A longitudinal crack was recognized before fiber failure, similar to that subject to quasi-static cut, initiating from the cut area and splitting the Kevlar® KM2 Plus fiber. The fiber breakage happened either beneath or away from the blade tip, depending on whether the strength of fibrils in front of the longitudinal crack was sufficient to resist the tensile stress developed in the fiber. The corresponding failure processes of the Kevlar® KM2 Plus fibers are physically presented in Figures 5.12*a* and 5.12*c*, respectively.

Failure surfaces of the recovered fibers were observed by the SEM as Figures 5.12*b* and 5.12*d*. Compared with the failure under the quasi-static cut, the fiber became easier to fibrillate when subjected to dynamic cut.

For the Dyneema® SK76 fiber, fibrils did not split from the entire fiber as Kevlar® KM2 Plus fibers. The fiber failed locally at the blade tip as Figure 5.13*a*. Compared with the failure under the quasi-static cut, fibrils seemed to be difficult to be penetrated, forming a crater-like fracture surface shown in Figure 5.13*b*.

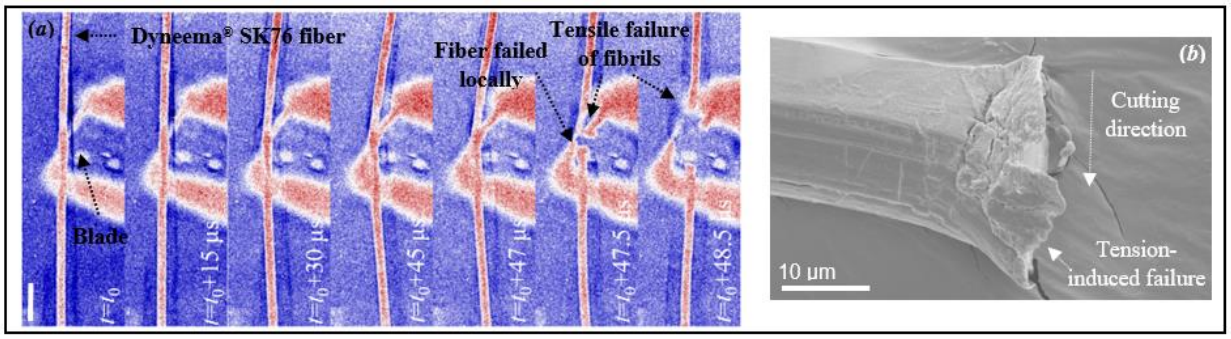

Figure 5.13. Failure of a single Dyneema® SK76 fiber under dynamic cutting. (*a*) Failure process; (*b*) Failure surface. The scale bar is 50 μm.

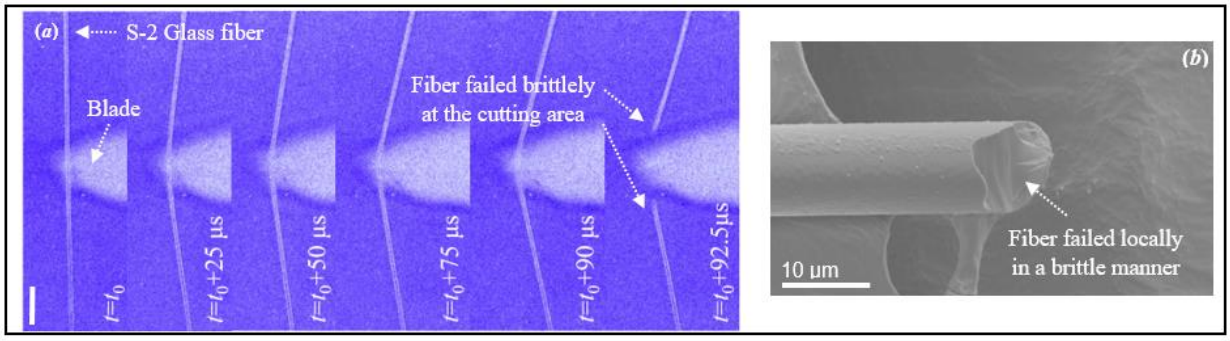

Figure 5.14. Failure of a single S-2 Glass fiber under dynamic cutting. (*a*) Failure process; (*b*) Failure surface. The scale bar is 50 μm.

S-2 Glass fibers had the same failure process in both quasi-static and dynamic cut conditions. The fiber bent at the blade tip without being penetrated and finally failed in a brittle manner because of tension. The failure surface in Figure 5.14 was clean and did not show any plastic deformation resulting from the transverse compression or shearing by the razor blade.

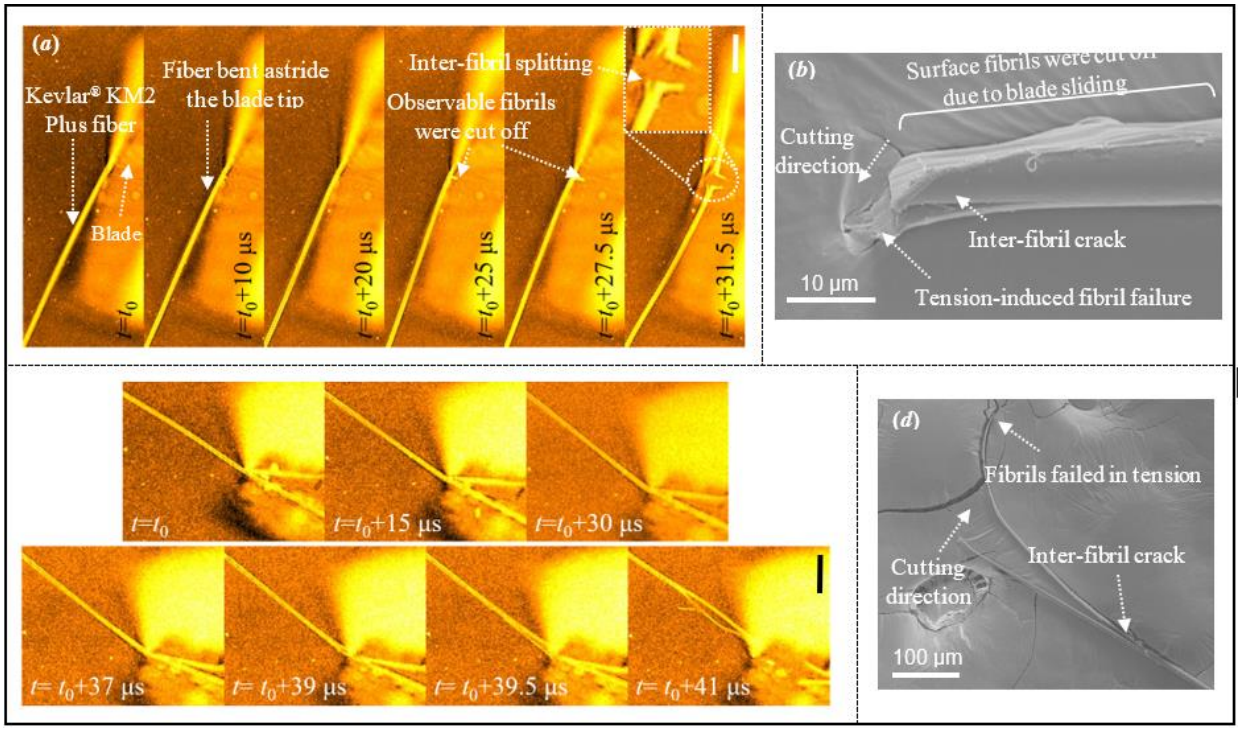

Figure 5.15. Failure of single Kevlar® KM2 Plus fibers under dynamic oblique cutting. (*a*) Failure process when φ=30°; (*b*) Failure surface of the fiber when φ=30°; (*c*) Failure process when φ=60°; (*d*) Failure surface of the fiber when φ=60°. The scale bar is 50 μm.

5.4.7 Failure of single fibers under dynamic oblique cut

Transversely cut at an angle dynamically, the failure process of the fiber was also very similar to that under quasi-static conditions. When φ was small as 30°, the Kevlar® KM2 Plus fiber first slid on the blade tip. The fiber was then cut in the transverse direction by F_N, while along the fiber, fibrils were split from the fiber surface by F_T. As the fibrils piled up around the blade tip, the blade was finally trapped inside the fiber. Afterward, the fiber bent astride the blade tip with continuous transverse penetration, as shown in Figure 15*a*. The post-fracture image in Figure 5.15*b* revealed an inter-fibril crack and tension-induced fibril failure during the cut. When the cut angle was 60°, the Kevlar® KM2 Plus fiber slid at a longer distance at the blade tip. The increased tangential component F_T due to the rising of φ compressed the fibrils axially simultaneously as the fiber was slowly sheared through by the decreased F_N in the transverse direction. Before the failure, a crack along the fiber length was detected to propagate and thereby split the fiber into fibril bundles. The fiber then lost its cut resistance when these fibrils broke in tension before the fiber was completely cut through.

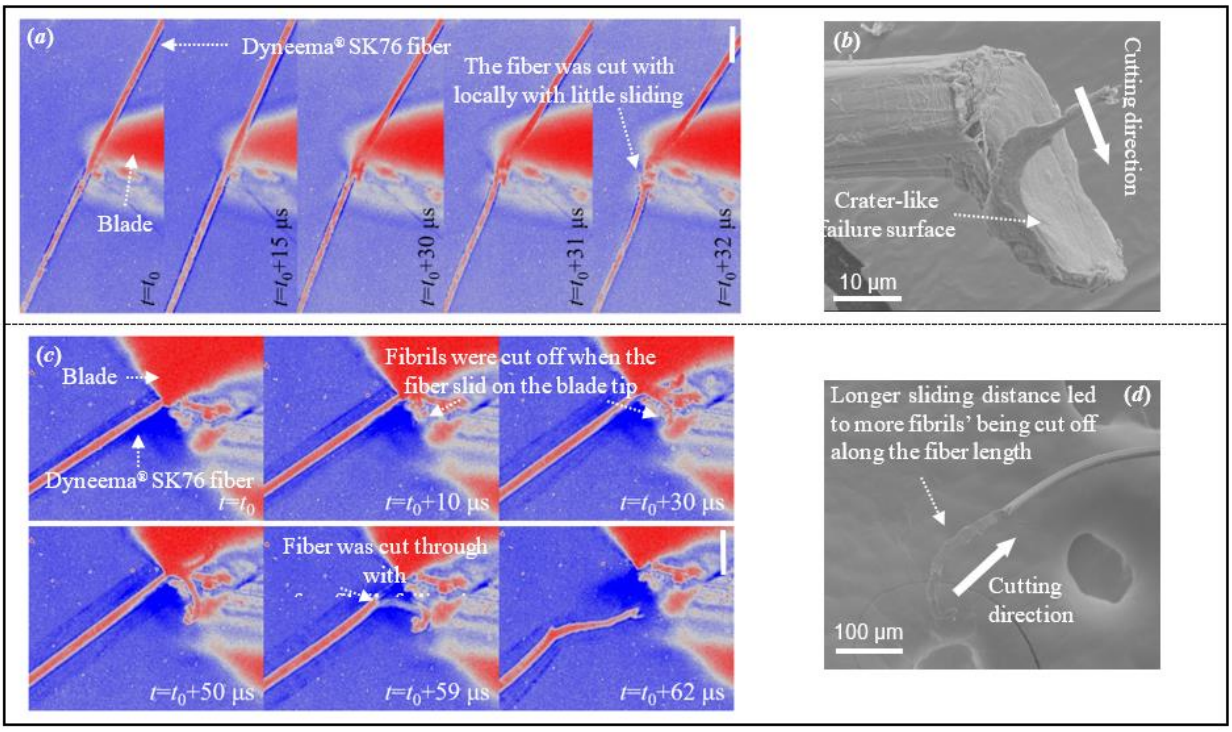

Figure 5.16. Failure of single Dyneema® SK76 fibers under dynamic oblique cutting. (*a*) Failure process when φ=30°; (*b*) Failure surface of the fiber when φ=30°; (*c*) Failure process when φ=60°; (*d*) Failure surface of the fiber when φ=60°. The scale bar is 50 μm.

Despite similar axial compression by F_T, transverse compression by F_N, transverse cut, and tensile failure of fibrils, the Dyneema® SK76 fiber did not have inter-fibril cracks splitting the entire fiber. The failure processes of the Dyneema® SK76 fibers transversely cut at two different angles were presented in Figure 5.16, together with SEM images demonstrating the failure surfaces. The S-2 Glass fiber still kept the same failure mode when experiencing oblique cut dynamically. The fiber cannot be cut by the blade and failed in tension in a brittle manner, as shown in Figure 5.17.

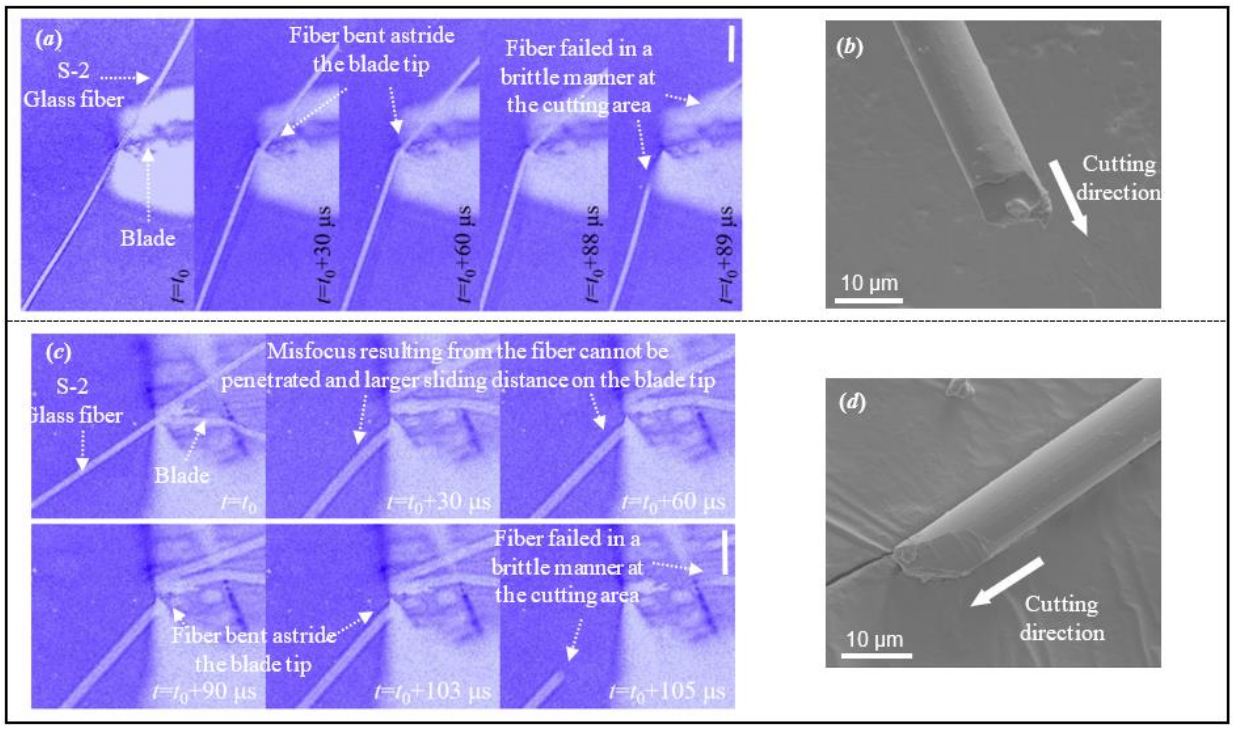

Figure 5.17. Failure of single S-2 Glass fibers under dynamic oblique cutting. (*a*) Failure process when φ=30°; (*b*) Failure surface of the fiber when φ=30°; (*c*) Failure process when φ=60°; (*d*) Failure surface of the fiber when φ=60°. The scale bar is 50 μm.

5.5 Discussions

5.5.1 Failure mechanism of different fibers under dynamic normal cut

Time-resolved failure processes of different fibers, reported in Figures 5.12-5.14, reveal three typical cut-induced fiber failure modes: partially cut through followed by tensile failure, fully cut through, and tensile failure without penetration.

Kevlar® KM2 Plus fiber is an organic fiber in the aromatic polyamide (aramids) family. In order to achieve maximum tenacity and initial modulus, the polymer molecules possess an extended-chain configuration and are in almost perfect crystalline packing during spinning [125-126, 128]. The rod-like polymer molecules are transversely connected via van der Weals forces and form aligned fibrils shown in Figure 5.18*a*. Subjected to transverse normal cut, as the fiber was penetrated a depth, an increasing number of fibrils were condensed, failed, and then piled up at the frontier of the blade tip, preventing the blade from further plugging into the fiber. Simultaneously, the blade may become blunt. As a result, the fiber became increasingly difficult

to be cut. In the vicinity of the cut location, the blade tip can be regarded as an indenter with a round nose. The residual fibrils behaved similar to a curve beam, subjected to a radial stress σ_{rr} and a circumferential stress $\sigma_{\theta\theta}$ schematically illustrated in Figure 5.18*a*: σ_{rr} transversely compressed the fibrils and messed up the crystal structure inside the fiber; $\sigma_{\theta\theta}$ caused the inter-fibril debonding and generated a longitudinal crack. The entire fiber failed as the inter-fibril crack propagated to a position where the tensile stress rapidly rose to the strength of the fibril as the crack dramatically decreased the effective cross-section. Therefore, the fiber breakage was observed randomly either beneath the blade tip or away from the cut region. The failure process of Kevlar® KM2 Plus fiber was schematically portrayed in Figure 5.18*a*.

Dyneema® SK76 fiber is composed of ultra-high-molecular-weight polyethylene with extremely long chains aligned in the same direction. The long-chain molecules form the nanofibrils with diameters varying from 8 to 100 nm and then further consist of microfibrils in 0.1-3-micron diameter. Except for the van der Weals forces between the long-chain molecules, the Dyneema® SK76 fiber was characterized via SEM, AFM, TEM with incorporated lamellar crystals on the surfaces of microfibrils, assembling with the fibrils into a shish-kebab structure [122-123]. Such lamellar crystal structures provided mechanical interlocking between microfibrils and prevented inter-fibril splitting. Moreover, there are tie chains detected by Stockdale et al. [123] and Strawhecker et al. [124], which transversely bundle the nanofibrils. This inter-fibril structure is able to supply extra mechanical connections in the fiber transverse direction. As a result, although Dyneema® SK76 fibers experienced similar transverse cut, compression, bending, and stretch, they did not split into small fibril bundles. The schematic illustration of the failure process of Dyneema® SK76 fiber was shown in Figure 5.18*b*.

S-2 Glass fiber is a magnesium alumino-silicate produced for textile substrates or reinforcements in composite applications [129-130]. The received S-2 Glass fiber was applied with a sizing material to protect the fiber and be compatible with the matrix during the manufacture of the glass fiber reinforced polymer composites. The sizing material includes silane coupling, film former, surfactant, and other processing aids. When the blade dynamically loaded onto the S-2 Glass fiber, it cannot penetrate the fiber since the material is even harder than the metal blade. Therefore, the blade merely stayed on the fiber, bending the fiber at the tip until the fiber was tensioned to break, as schematically described in Figure 5.18*c*.

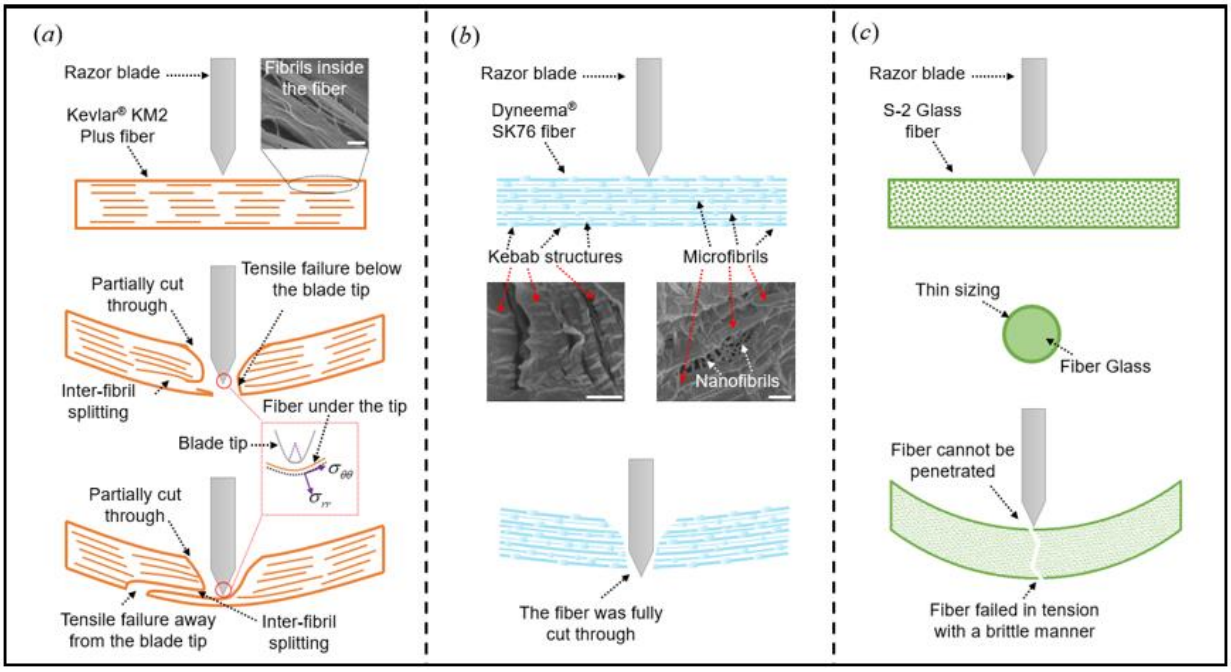

Figure 5.18. Failure mechanisms of different fibers under the dynamic normal cut. (*a*) Kevlar® KM2 Plus; (*b*) Dyneema® SK76; (*c*) S-2 Glass. The scale bar is 500 nm.

5.5.2 Energy dissipation of different fibers under the dynamic normal cut

5.5.2.1 Specific energy of a single fiber under cut

During the dynamic cut, the fiber dissipated energy from the blade via deformation. The dissipated energy (E) can be calculated by integrating the force-displacement curve in Figure 5.7*c*, as shown in Eq. (5-6).

$$E = \int F(S)dS \tag{5-6}$$

For textiles or composites designed for armor applications, the weight of the material is a critical factor supposed to be considered. Equation (5-7) gives the specific energy (e) of a fiber experiencing transverse normal cut, defined as the dissipated energy of a fiber per unit mass.

$$e = \frac{4E}{\pi d^2 \rho \cdot (2L)} \tag{5-7}$$

where ρ is the density of the fiber material; d is the diameter of the fiber; $2L$ is the sample length before the cut, which is 6.35 mm in this work.

Table 5.2 compares the total energies dissipated during cut processes of three fibers and the corresponding specific energies. A single S-2 Glass fiber is demonstrated to have the highest performance in energy dissipation. The energy dissipated by an individual S-2 Glass fiber was 2.5-4 times that of the other two fibers. Despite the highest density, the specific energy of the S-2 Glass fiber was still 2.5-3 times that of the Kevlar® KM2 Plus and Dyneema® SK76 fibers. On the other hand, a single Dyneema® SK76 was able to dissipate the energy with an amount of 5.733 μJ, which was 36% higher than the energy of the Kevlar® KM2 Plus fiber. However, due to a larger diameter, in spite of the light weight in density, a single Dyneema® SK76 fiber per unit mass will dissipate less energy than the Kevlar® KM2 Plus fiber.

Table 5.2. Comparison of energy dissipation of different fibers

Fiber type	d (μm)	ρ (g/cm^3)	E (μJ)	e (J/kg)	e_0 (J/kg)	δ	ε_f (%)	η (%)
Kevlar® KM2 Plus	10.64 ± 0.21	1.45	4.225	5157.498	58591.172	0.088	0.544	1.609
Dyneema® SK76	16.39 ± 0.51	0.98	5.733	4368.374	117996.531	0.037	0.441	0.593
S-2 Glass	9.83 ± 0.28	2.48	16.374	13692.783	55498.145	0.247	1.579	5.150

5.5.2.2 Cut energy factor

High-performance fibers have extraordinary mechanical properties in the axial direction. After manufactured into textiles or composites and subject to normal service loading conditions, such as cut, indentation, and low-velocity impact, such fibers are expected to develop material potentials in tension and dissipate energy via tensile deformation. As a result, it is necessary to compare the energy dissipation of a fiber under cut and pure tension and simultaneously evaluate the tensile deformation developed in a fiber during a transverse cut event.

In consideration of the mass efficiency of a single fiber in energy dissipation, here, the energy dissipating capabilities of the same fiber subject to transverse cut and axial tension based on the specific energy were compared. A cut energy factor δ was defined in Eq. (5-8) as the ratio of the specific energy of a single fiber under the cut to its specific energy (e_0) under tension.

$$\delta = \frac{e}{e_0} \tag{5-8}$$

where e_0 was computed via Eq. (5-9) as the strain energy density (U_0) over the mass density of a single fiber. Furthermore, U_0 was given by integrating the tensile stress-strain curve of a single fiber, as described in Eq. (5-10).

$$e_0 = \frac{U_0}{\rho} \tag{5-9}$$

$$U_0 = \int_0^{\varepsilon_{\max}} \sigma d\varepsilon \tag{5-10}$$

The cut energy factors of different fibers were calculated in Table 5.2. Compared with the dynamic tensile loading condition, all fibers had poor energy dissipation when subjected to the transverse normal cut, with the maximum δ being less than 0.25, which indicates the huge weakening effect of the localized compression/cut on the energy dissipation of a single fiber. Regarding three fiber types, S-2 Glass fiber had a δ being ~2.8 times of the Kevlar® KM2 Plus fiber and ~6.7 times of the Dyneema® SK76 fiber. Such the highest δ should be attributed to the none-penetration failure mechanism of the S-2 Glass fiber during the dynamic cut, which, to the largest extent, enabled the fiber to dissipate the energy by tensile deformation. In contrast, the Dyneema® SK76 fiber, albeit the highest specific energy under dynamic tension, was sheared through transversely by the razor blade before the tensile deformation in the axial direction was developed.

5.5.2.3 Tensile deformation of a single fiber under cut

In order to assess the tensile deformation developed during the transverse cut, in our previous work in [45], we considered a homogeneous tensile stress distributed inside the fiber, except for the multi-axial stress state within the cut region. Such assumption is reasonable, based on the observation that the localized deformation was constrained within a ~10-μm-length region around the blade tip, which is ignorable comparing with the sample gauge length [45]. The total specific energy e in Eq. (5-7) is then divided into two components, e_c and e_T, corresponding to the contribution of the local cut and uniform tensile deformation, respectively.

Under the axial tension, the mechanical behavior of a single fiber essentially matches the tensile stress-strain curve. Therefore, the energy dissipated by tensile deformation, e_T, can be calculated via integrating the stress-strain curve within the strain from 0 to ε_f.

$$e_T = \frac{\int_0^{\varepsilon_f} \sigma d\varepsilon}{\rho} \tag{5-11}$$

where ε_f represents the maximum tensile strain developed outside the cut region before the fiber failure, which is given by Eq. (5-12).

$$\varepsilon_f = \sqrt{1+\left(\frac{S_{\max}}{L}\right)^2} - 1 \tag{5-12}$$

Finally, the energy dissipated via localized deformation/penetration is obtained via eliminating the contribution of tensile deformation from the total specific energy as Eq. (5-13).

$$e_C = e - e_T \tag{5-13}$$

Therefore, the localized deformation/penetration contribution and the tensile deformation in the energy dissipating of a single fiber can be quantified as κ_C in Eq. (5-14) and κ_T in Eq. (5-15), based on the specific energy.

$$\kappa_C = \frac{e_C}{e} \tag{5-14}$$

$$\kappa_T = \frac{e_T}{e} \tag{5-15}$$

Here, we also defined a tensile deformation factor η as Eq. (5-16) by comparing the tensile component of the specific energy e_T during a dynamic cut event with the specific energy under pure tension, e_0.

$$\eta = \frac{e_T}{e_0} \tag{5-16}$$

As shown in Table 5.2, due to the none-penetration failure mechanism, the S-2 Glass fiber had the highest tensile strain of 1.579% developed inside the entire fiber before failure, which activated merely η = 5.150% of the specific energy under pure tension during the cut event. The Dyneema® SK76 fiber was completely cut through before the tensile deformation was effectively deformation in the fiber and thereby had the lowest ε_f as 0.441%, with e_T being only 0.593% of e_0. Failed in a partially-cut-through manner, the Kevlar® KM2 Plus had an intermediate ε_f equal to 0.544%, enabling 1.609% of the e0 to be involved in the energy dissipation under the transverse cut. Obviously, the high performance of the fiber in tension was extremely poorly utilized during the cut, while the penetration failure mechanism further decreased the usage of the fiber potential in tension dramatically. For the material design of fibers served to resist cut, it is possibly much more effective to prevent the blade penetration instead of continuously developing new fibers with high tensile strength.

5.5.3 Fiber length effect

Under transverse cutting by a razor blade, the fiber is in a multi-axial stress state within the cut region, including tension, transverse compression, and bending. As a major component to promote fiber failure, bending of the fiber at the blade tip changes the blade/fiber contact area and thereby influences the distribution of the transverse compressive stress in the fiber. At the same time, bending controls the development of the tensile deformation inside the fiber by varying the fiber failure angle. Basically, bending deformation is determined by the fiber's flexural stiffness, which is highly related to the sample length for a specific type of fiber. Comparison of cut-induced failure behaviors of fiber samples with various lengths contributes to optimizing fiber length in larger-scale textiles and composites served for extreme dynamic cut conditions.

There was a majority of work by Mayo and Wetzel [116] and Gao et al. [44-45], cutting single fibers with the sample length of 140 mm and 50 mm, respectively, under quasi-static loading conditions. However, such longer samples are not adaptable for current dynamic experimental techniques presented in Figure 5.5. The main issue is that the diameter of the miniature Kolsky bar used in this work is only 12.7 mm. Fixing a single fiber longer than 50 mm will cause considerable sample vibration and air noise applied onto the fiber, making it difficult to quantify the failure behavior of the fiber. Therefore, the effect of fiber length was studied by comparing the quasi-

static experimental results in this work with those presented in Mayo and Wetzel [116] and Gao et al. [44-45].

Figure 5.19*a* compares the triangular geometries of fibers before failure by nominalizing all the initial sample lengths to 1. The maximum displacement in Figure 5.19*a* was calculated via the failure angle θ in each experiment described as Eq. 5-(17) during nominalization.

$$\theta = \arctan\left(\frac{S_{\max}}{L}\right) \tag{5-17}$$

The maximum tensile strains given by Eq. (5-12) in different experiments are correspondingly compared in Figure 5.19*b*. It is clearly shown that when the fiber length exceeded 50 mm, the fiber failed at a similar angle with identical tensile strain developed inside the fiber. However, when the fiber length decreased to 6.35 mm in this work, both the Kevlar® KM2 Plus and Dyneema® SK76 fiber failed at a smaller angle, while the failure angle of the S-2 Glass fiber increased. Simultaneously, the maximum tensile strain in the Kevlar® KM2 Plus and Dyneema® SK76 fiber decreased by 31% and 75%, respectively. On the contrary, the maximum tensile strain within the S-2 Glass increased by 61%.

The variation of the fiber's mechanical response against the fiber length is considered as a result of the difference in the stiffness. When the fiber was experiencing a transverse cut, the blade deformed the fiber in a localized region. The fiber outside the cut region can be regarded as a constrain with a stiffness depending on the fiber length. Spanned a short length, the fiber had a larger stiffness to resist different deformation, such as bending stiffness (EI/L), torsional stiffness (GJ/L), and axial stiffness (EA/L). Once deformed by the blade, such higher stiffness was equivalent to a strong constrain applied at the end of the fiber within the cut region. Subjected to the same blade force, both the Kevlar® KM2 Plus and Dyneema® SK76 fiber then responded with a larger localized deformation and stored a correspondingly increasing amount of energy, which made the fiber easier penetrated and fail at a small angle without the tensile deformation homogeneously developed along the entire fiber. This failure mechanism was physically supported by the abrupt breakage of the Kevlar® KM2 Plus fiber in Figure 5.8 with the tension-induced fibrils failure merely being identified in post-fracture images in Figure 5.11*a*, compared to the visible crack propagating process on the fiber reported in [45]. On the other hand, the S-2 Glass fiber

cannot be penetrated. The fiber stored the energy through bending deformation, physically generating a larger offsetting angle before failure. When the fiber was cut in a long span, the constrain effect from the outward fiber was reduced. The Kevlar® KM2 Plus and Dyneema® SK76 fiber were then slowly cut and failed at a larger angle, while the S-2 Glass fiber was less bent before failure. As the sample length continuously increased, the equivalent constrain effect decreased to a stable level. The failure angle and the axial tensile deformation inside the fiber both became insensitive to the sample length. The effect of the fiber length on the fiber failure behavior was schematically illustrated in Figures 5.19*c*-5.19*d*.

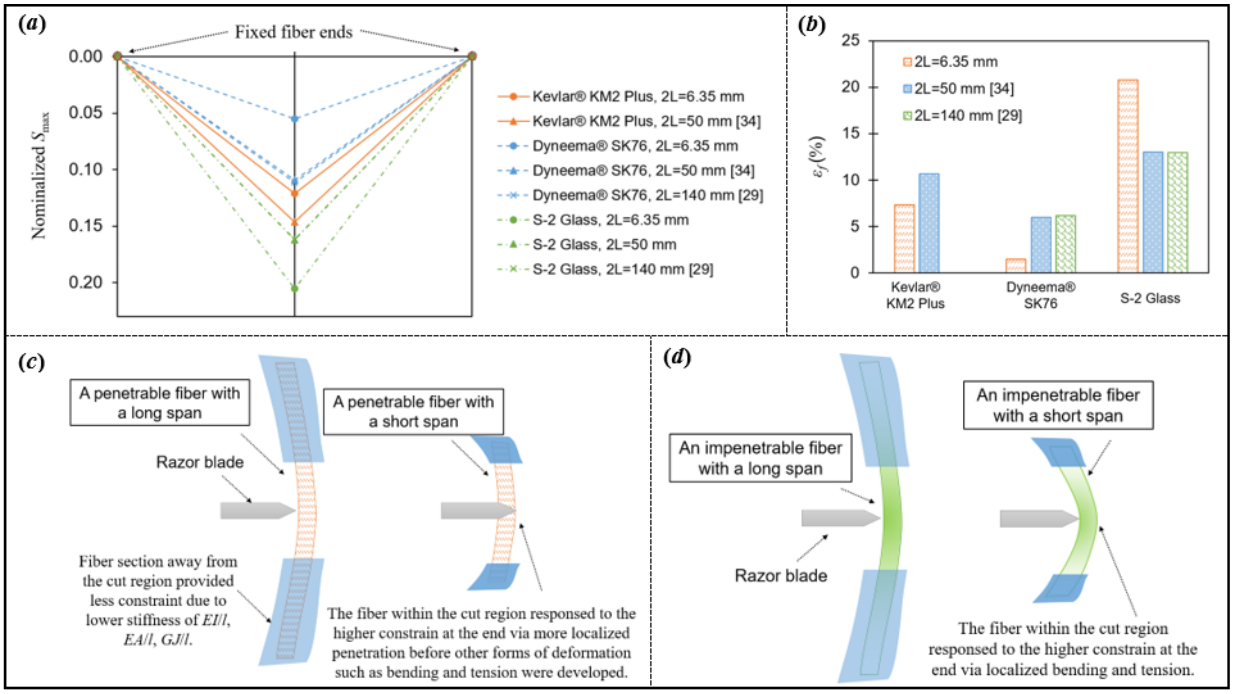

Figure 5.19**.** Fiber length effect on the fiber failure by transverse cut. (*a*) Comparison of triangular geometries of fibers before failure in literature based on the nominalized fiber length; (*b*) Comparison of ε_f developed inside the fibers before failure in literature; (*c*) Cut-induced failure mechanism of a penetrable fiber with different lengths; (*d*) Cut-induced failure mechanism of an impenetrable fiber with different lengths.

5.5.4 Cut angle effect

When the fiber was cut obliquely under dynamic loading conditions, as observed in Section 5.4.7, due to the introduction of F_T, both the Kevlar® KM2 Plus and the Dyneema® SK76 fiber became easier penetrated while the S-2 Glass fiber was more locally deformed.

The maximum tensile strain ε_f developed in the fiber in an oblique cut event was derived in our previous work [45] as Eq. (5-18).

$$\varepsilon_f = \frac{L_1 + L_2}{2L} - 1 \tag{5-18}$$

where L_1 and L_2 represent the length of the fiber astride the blade tip before failure, given as the function of the cut angle and the maximum traveling distance of the blade tip as Eq. (5-19) and Eq. (5-20), respectively.

$$L_1 = L\cos\varphi\sqrt{1+\left(\frac{S_{\max}}{L\cos\varphi}+\tan\varphi\right)^2} \tag{5-19}$$

$$L_2 = L\cos\varphi\sqrt{1+\left(\frac{S_{\max}}{L\cos\varphi}-\tan\varphi\right)^2} \tag{5-20}$$

When the cutting angle φ=0°, Eq. (5-18) degrades into Eq. (5-12), where the fiber was normally cut.

Figure 5.20*a* demonstrates that all fibers were found to have less tensile deformation developed outside the cut region, under the combination of F_N and F_T. Comparison of e_C and E in Figures 5.20*b* and 5.20*c* reveals that the energy dissipation of each fiber was dominated by local deformation/penetration. When the cut angle was small, a large F_N ensured the Kevlar® KM2 Plus fiber to be penetrated successively, whereas F_T caused inter-fibril splitting and accelerated the penetration. Hence, the fiber was unable to dissipate the comparable energy as that under the normal cut. For the non-penetrable S-2 Glass fiber, more localized deformation was promoted by bending, making more energy stored in the fiber, as shown in Figure 5.20*c*. Cut at a large φ, F_N decreased to a level difficult to cut the Kevlar® KM2 Plus fiber transversely, leading to more localized deformation developed during cut process and increasing e_C in Figure 5.20*c*. On the other hand, bending deformation decreased in the S-2 Glass fiber. Both the specific energy component e_C and the total energy dissipated reduced as Figures 5.20*b* and 5.20*c*. Under the dynamic oblique cut, F_N was always able to cut through the Dyneema® SK76 fiber in the transverse direction, which is the possible reason resulting in the decline of the dissipated energy E against the rising of cut angle. The failure mechanisms of Kevlar® KM2 Plus and Dyneema® SK76 fiber under oblique cut

were already illustrated in our previous work [44-45]. Here, we schematically illustrate the failure of S-2 Glass in Figures 5.20*d* and 5.20*e*.

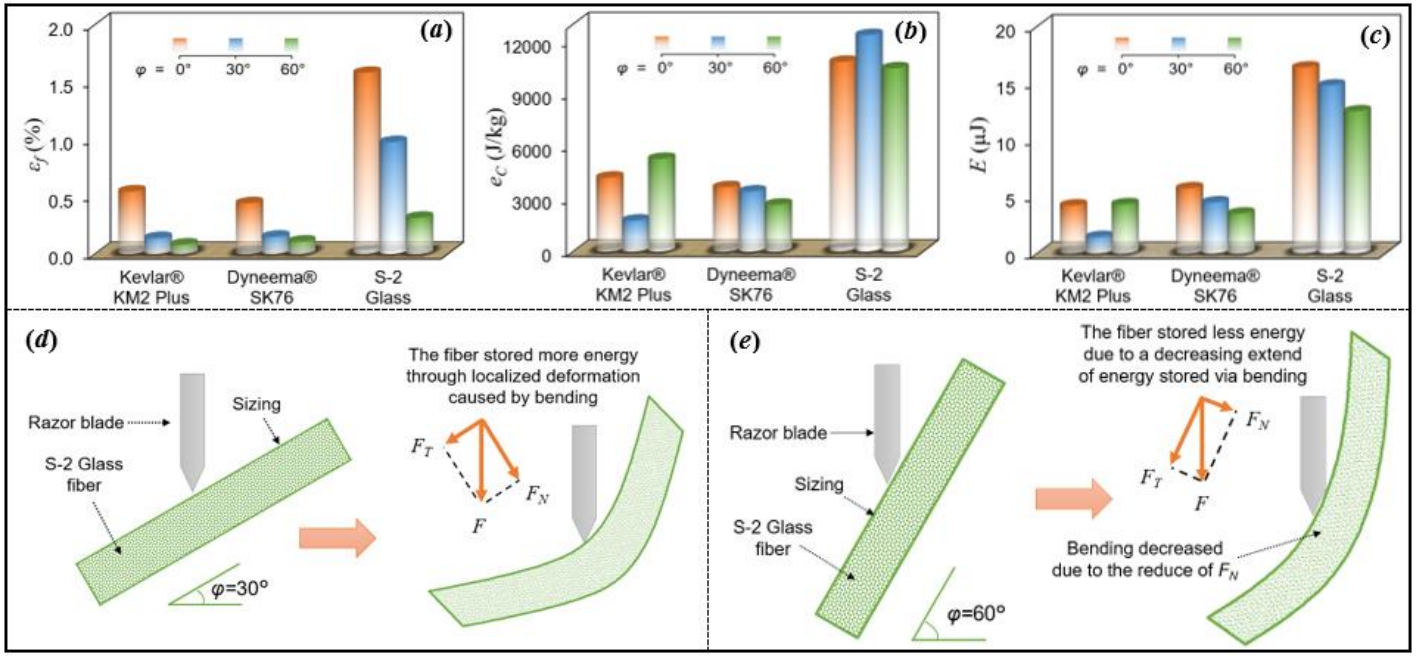

Figure 5.20. Comparison of different fibers obliquely cut by a razor blade. (*a*) ε_f; (*b*) e_C; (*c*) E; (*d*) Failure mechanism of a single S-2 Glass fiber transversely cut at φ=30°; (*e*) Failure mechanism of a single S-2 Glass fiber transversely cut at φ=60°.

5.5.5 Loading rate effect

Section 5.3 reported the failure modes of three types of fibers under dynamic cut were identical with those under quasi-static loading condition: Kevlar® KM2 Plus fiber was partially penetrated followed by tensile failure; Dyneema® SK76 fiber was fully cut through; S-2 Glass cannot be penetrated and was bent astride the blade tip until failed in tension.

Under the normal cut, as the loading rate increased, all single fibers were able to dissipate more energy from the blade through deformation and failure. Obviously, S-2 Glass fiber was capable of dissipating the most energy because of the highest tensile deformation benefit from the non-penetration failure mechanism. Specially, the Dyneema® SK76 fiber has the highest rate-dependent energy dissipating improvement revealed by Figure 5.21*a*: the dissipated energy E increased to ~5.7 times of the E under quasi-static normal cut while the dissipated energies of the Kevlar® KM2 Plus and S-2 Glass fiber only raised by ~50%. Besides, in spite of the rate-induced prominent enhancement in the energy dissipation under axial tension, the cut energy factor of the Dyneema® SK76 fiber still increased by ~195%, as presented in Figure 5.21*b*, which was dramatically higher than the increase of 43% of the Kevlar® KM2 Plus fiber and 79% corresponding to the S-2 Glass fiber. One possible illustration is that the Dyneema® SK76 fiber was completely cut through, and its mechanical properties in the transverse direction were also enhanced by the higher loading rate during the cut process [131-133]. Such illustration can be supported by Figures 5.21*a* and 5.21*c*, via comparing ε_f developed inside each fiber and κ_C and κ_T during each normal cut event, respectively. For Dyneema® SK76 fiber, when the loading speed rose from 1.67 μm/s to 5.34 m/s, ε_f increased by ~191%, which was similar to the variation of δ, and, simultaneously, κ_C and κ_T were nearly constant. On the other hand, due to the tensile-induced failure mechanism in the Kevlar® KM2 Plus and S-2 Glass fiber, under the dynamic cut, the deformation became more localized, which decreased ε_f and the amount of e_T consisting e. Therefore, it is concluded that the failure mechanism of fully penetration results in a rate-independent constitute of dissipated energy (e) contributed by tensile deformation (e_T) and transverse cut through (e_C), although the amount of the energy was low.

Subject to the transverse oblique cut, the total energies dissipated by different fibers were revealed in Figure 5.21*a* to increase with the loading rate, except for the S-2 Glass fiber cut at φ=30°, which is considered to result from the localized deformation intensified under a smaller cut

angle, illustrated in Section 5.5.4. The maximum tensile strain developed outside the cut region decreased under dynamic cut conditions, as present in Figure 5.21*a*.

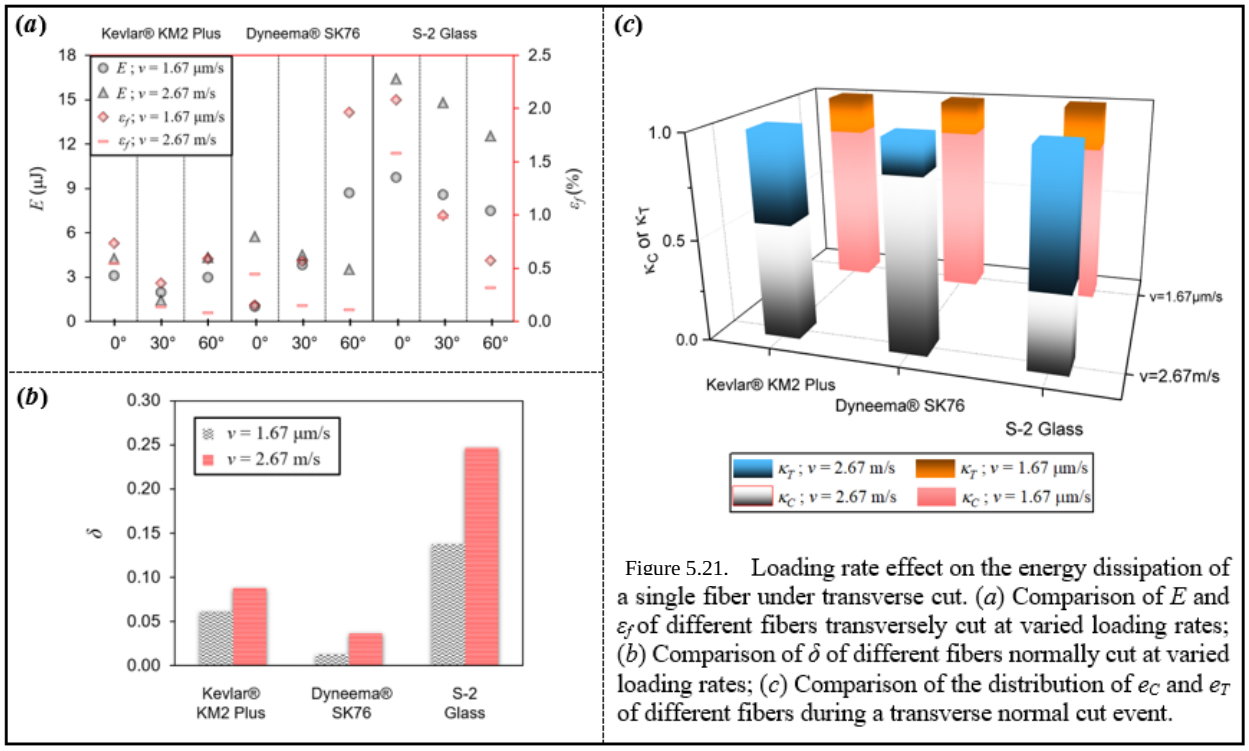

Figure 5.21. Loading rate effect on the energy dissipation of a single fiber under transverse cut. (*a*) Comparison of E and ε_f of different fibers transversely cut at varied loading rates; (*b*) Comparison of δ of different fibers normally cut at varied loading rates; (*c*) Comparison of the distribution of e_C and e_T of different fibers during a transverse normal cut event.

5.6 Conclusions

In this work, cut-induced deformation and failure of single high-performance fibers at a high loading rate were visualized. A reverse impact technique was utilized to apply the dynamic cut load onto the fiber by using a modified miniature Kolsky compression bar. Cut events were captured by an ultra-high-speed camera in combination with an ultra-long working distance objective lens. Quasi-static cut experiments on fibers were performed on a micro-test platform inside an SEM to identify the loading rate effect on the fiber failure. Post-fracture analysis on the failure surfaces of fibers via SEM images further improved the understanding of the fiber failure mechanism under the transverse cut. Three types of fibers were investigated, namely Kevlar® KM2 Plus, Dyneema® SK76, S-2 Glass fiber. In consideration of the mass-efficient energy absorption, cut resistances of different fibers were evaluated by a specific energy, comparing with the energy absorption in the axial tensile experiments performed at varied loading rates. Besides, the effects

of sample length and cut angle on the fiber failure behavior were discussed. Decent findings are concluded as below:

1) Three failure modes were recognized: partially penetration followed by tensile failure, fully cut through and bending-caused brittle failure without penetration, namely corresponding to the Kevlar® KM2 Plus, Dyneema® SK76, and S-2 Glass fiber. The failure modes were not sensitive to the loading rate but closely related to the fiber nanostructure.
2) The high performance in tension of a single fiber was extremely poorly developed when the fiber was transversely cut. Especially, for a Dyneema® SK76 fiber per unit mass failed in a completely cut-through mode, the energy absorbed by tensile deformation outside the cut region was merely 0.6% of the energy absorbed in pure tensile experiments.
3) The hardness of the fiber improved the cut resistance. Impenetrable by the razor blade, a single S-2 Glass fiber per unit mass had a larger tensile strain developed, ~3 times the Dyneema® SK76 fiber. Such tensile deformation dramatically contributed to the energy absorbed by the S-2 Glass fiber during the cut process, which was ~2.9 times that of the Dyneema® SK76 fiber. Synthesis and manufacture of cut-resistance fibers are possibly more effective if the improvement of fiber anti-penetration capability is considered instead of the axial tensile strength.
4) The energy absorptions of investigated fibers increased with the loading rate. Specifically, the amount of energy absorbed by a Dyneema® SK76 fiber rose by 470% when it was cut dynamically. On the other hand, the distribution of the energy contributed by localized penetration and tensile deformation was not sensitive to the loading rate, possibly due to the failure mechanism of completely cut through.
5) Short fibers, having the length/diameter ratio of ~635, became easier penetrated or localized deformed due to the enhancement of constraint by the material away from the cut region. Long fibers with a length/diameter ratio larger than 5000 failed at a similar break angle with identical tensile deformation developed inside the fiber.
6) For the short fibers investigated in this work, increasing the cut angle further decreased the development of the fiber outperformance in tension.

CHAPTER 6. REAL-TIME DAMAGE CHARACTERIZATION FOR GFRCS USING HIGH-SPEED SYNCHROTRON X-RAY PHASE-CONTRAST IMAGING

The following chapter contains content reproduced with permission from the journal article:
Gao J, Kedir N, Kirk C, Hernandez J, Wang J, Paulson S, Zhai X, Horn T, Kim G, Gao J, Fezzaa K, De Carlo F, Shevchenko P, Tallman TN, Sterkenburg R, Palmese G, Chen W (2021). Real-time damage characterization for GFRCs using high-speed synchrotron X-ray phase-contrast imaging. *Composites Part B: Engineering*, 207, 108565. DOI: 10.1016/j.compositesb.2020.108565

6.1 Introduction

Although the fiber-scale experiments in Chapters 4 and 5 provide insight into the cut-induced failure mechanism in the composite materials, the loading speed has been limited within 10 m/s. To detect the microscale failure of the fibers, yarns, and composite strips at high-velocity impact, a more advanced technique is required with a high resolution as well as a sufficient safe working distance.

Current damage and failure detection techniques for composite materials include destructive and non-destructive testing methods. Destructive techniques are not widely employed recently because new damages can be introduced during sample preparation, which disturbs the residual stress around the sectioned area and makes the detected damage and deformation non-representative [134-135]. As a basic type of non-destructive testing (NDT) methods [136], visual inspection provides a cost- and time-efficient way to measure the crack density [137] and conduct micrograph analysis [138]. However, most of the matrixes used for glass fiber-reinforced composites (GFRCs) are opaque. Visual inspection by using optical imaging [139-140], scanning electron microscope (SEM) [141-142], or shearography [143-144], for example, merely capture the surface morphology for estimation of deformation and damage evolution within the entire composite. This is possibly useful in quasi-static loading conditions or for stationary cracks. However, when the loading and crack growth happened in a very short time during a low-velocity impact event, boundary value measurements may become difficult to provide meaningful information regarding the fracture resistance of the material [145]. Alternative NDT methods involve contact methods and non-contact detections [146]. Contact methods usually adhere sensors to the tested composite surface and diagnose the crack location, flaw size and orientation, and other

characterizations based on the information carried by the signal generated during wave propagation, vibration, or electromagnetic response. Reported NDT methods by using contact methods include traditional ultrasonic testing [146], acoustic emission [147], acousto-ultrasonic [148], and vibration measurement [149]. Thermography is a non-contact method applied for damage identification of large-scale composite structures as a type of NDT methods. Basically, this method detects and localizes damage by exciting the tested structure with an external heating source and observing the differences in a temperature distribution [150]. The disadvantages of the aforementioned NDT methods are that detections essentially rely on the sensor's sensitivity, which usually provides an image of the overall damage and lack micrometer resolution and the ability to track the interaction of various damage modes within the material microstructure [135]. Recently, X-ray computed tomography has proven to be a powerful technique to penetrate fiber reinforced plastics (FRPs) and allow the imaging of internal damages at the scale of individual broken fibers. Such high voxel resolution on the order of 1 μm enables detecting and distinguishing primary damage modes of FRPs during deformation and failure [151]. However, these techniques were used to identify key damage features inside the composite in considerable detail by post-impact assessments [152-156] or characterize, in real-time, multiple damage modes and their interactions under quasi-static [157-160] or fatigue [161] loading conditions.

This work aims to extend the application of the synchrotron radiation technique to image the dynamic failure processes of composite materials. Pre-notched S-2 glass/SC-15 unidirectional (UD) and 0°/90° laminated composite beam samples were prepared. Dynamic single-edge notched bending (DSENB) experiments were performed on a modified Kolsky compression bar platform, reversely impacting a sample onto an indenter. Simultaneously, the high-intensity synchrotron X-ray penetrated through the sample, and high-speed phase-contrast imaging (PCI) was employed to capture microscale damages and their interactions and evolutions inside the material within the time span of the impact event. Additional experiments were performed using the optical imaging technique to capture dynamic failure behaviors of GFRCs under similar loading conditions. The radiographic imaging was compared with the optical inspection to illustrate further the potentials of the high-speed synchrotron X-ray PCI technique in detecting dynamic damage initiation and propagation in GFRCs. Such an advanced technique is believed to provide the possibilities to visualize the microscale failure of the composite strip, yarn, and single fiber under transverse high-velocity impact.

6.2 Materials

6.2.1 Fibers and matrix systems

S-2 glass fiber roving was received from AGY (Aiken, SC, USA). A toughened vacuum-assisted resin transfer molding (VARTM) matrix system, SC-15 matrix (Applied Poleramic Inc., Benicia, CA, USA), was used to manufacture the composites. SC-15 matrix is a low-viscosity, two-phase toughened epoxy cured with a cycloaliphatic amine and has been commercialized for applications in defense.

6.2.2 Composite manufacturing

UD composites and cross-ply composites stacked in a $[0°/90°]_{12}$ manner were manufactured and investigated as examples in this work to illustrate the application of high-speed X-ray PCI in damage detection of GFRCs. Manufacturing processes of these GFRCs included unidirectional fabric fabrication, matrix preparation, S-2 glass fiber prepreg formation, prepreg layup, vacuum bagging, curing, and post-curing progression.

Commercial UD glass fiber fabrics are usually stitched transversely or with fine polymer fibers resting on the surface to hold separated roving in position. Studies showed stitching can improve, seriously degrade, or leave unchanged the in-plane mechanical properties of composites, depending on the material, stitching parameters, and loading conditions [162-163]. In addition, stitching can also cause considerable damage by breaking, spreading, and kinking the fibers, by the formation of resin-rich regions, porosity, and resin cracks, as well as by stress gradient effects. In order to fabricate unstitched unidirectional fabric, a filament winding setup was built to wind the S-2 glass roving onto a wooden frame manually. The setup involved an S-2 glass filament delivery apparatus having the fiber roving with a creel assembly and a filament winding apparatus having a detachable wooden frame assembled on a T-slotted frame. As shown in Figure 6.1*a*, the wooden frame was designed with a mandrel possessing a diameter of 15.88 mm to control the rotation of the entire frame and operate the winding process. Filaments were to be wound on two 25.4-mm-diameter rods, which were parallel to the mandrel and transversely supported by two parallel 6.35-mm-diameter rods. Before winding, the wooden frame needed to be mounted onto the T-slotted frame jointed with two aluminum tubes through rail-to-tube holders. First, the mandrel of the wooden frame was assembled with its two ends into the corresponding aluminum

tubes having an inner diameter of 19.1 mm. The movements of the aluminum tubes were then confined by screwing down the threads on the rail-to-tube holders. Furthermore, the axial movement of the mandrel was restrained via wide-seal plastic clamps for firm hose inside tubes, thereby guaranteeing the wooden frame can only rotate along the mandrel and wind enough filaments. Afterward, the wooden frame with filaments was disassembled by unscrewing threads on the rail-to-tube holders and enlarging the distance between two aluminum tubes to start a new filament winding process. Figure 6.1*b* presents the production of wound filaments on many wooden frames. In sequence, these filaments were transversely bonded via the hot-melt adhesive (Hotmelt.com, Edina, MN, USA), as presented in Figure 6.1*c*. Such adhesive was initially in a solid state and melt by the hot-melt glue gun (Hotmelt.com, Edina, MN, USA), which easily wetted the fabric and provided effective adhesion after solidification when the temperature dramatically decreased to room temperature in 2-3 minutes. Finally, the unidirectional fabric was obtained by cutting the winded filaments along the outer edge of the glued area.

The SC-15 matrix was prepared by mixing the epoxy resin and amine with a weight ratio of 100:30 [164]. The matrix was then put inside a vacuum chamber, having the pressure approximately 0.1 MPa below atmospheric pressure at room temperature for 30 minutes. This procedure effectively removed bubbles from the liquid matrix and avoided possible voids in the manufactured composite laminates.

S-2 glass fiber prepregs were made by uniformly pouring the SC-15 matrix onto the unidirectional fabrics. Each unidirectional fabric was first placed on a matrix-wetted nylon peel ply on a flat aluminum plate (see Figure 6.1*c*). The fabric was wetted and then cut along the inner edge of the glued area to prevent the composite from any contamination by the hot-melt adhesive. Figure 6.1*d* presents the S-2 glass fiber prepregs produced. The wetted nylon peel ply can be easily removed from the aluminum plate and simultaneously can prevent the distortion of the wetted filaments on the peel ply during the removement. Subsequently, in Figure 6.1*e*, the peel ply with the wetted filaments was flipped over and carefully placed on the stacked pre-impregnated layers in the designated direction (0° or 90°). Slight compression was applied on the top of the stacked prepregs by using the squeegee to increase the adhesion between individual layers and make it easier to take off the peel ply from filaments with less distortion. As shown in Figure 6.1*f*, the covered peel ply was being taken off to obtain the stacked pre-impregnated fabrics in Figure 6.1*g*. It is noted that the bottom prepreg was directly wetted on a peel ply placed on a release film on a

flat aluminum plate. That peel ply, along with the release film, were the necessary components for vacuum bagging shown in Figure 6.1*h*. Afterward, the other prepregs were stacked accordingly in sequence. The SC-15 matrix has a pot life of more than 6 hours, providing a sufficient time span to finish the layup of 24 pre-preg layers. The stacked prepregs were then vacuum bagged as Figure 6.1*h* and cured at a vacuum pressure of 80 kPa and room temperature for 24 hours [164]. Another 4 hours at atmospheric pressure and room temperature were given for additional curing. Finally, the composite was post-cured at 120 ℃ and atmospheric pressure for 2 hours.

6.2.3 Sample preparation

Composite laminates were sectioned into small beam samples by either a surface grinder or a diamond saw specifically for tailoring GFRCs. Three types of beam samples were obtained as 0°, and 90° UD, and $[0°/90°]_{12}$ composite beams, where 0° is defined to be along the beam span (*S*), and 90° is along the beam width (*B*) as shown in Figure 6.1*i*. The notch on each sample was created by the diamond saw. Due to the unevenness of the vacuum bag, the 0° and 90° UD, and $[0°/90°]_{12}$ composite beams had the thicknesses of 4.76 ± 0.10 mm, 4.76 ± 0.06 mm and 4.88 ± 0.06 mm, respectively. The other dimensions of the composite sample were designed in general accordance with ASTM Standard D5045-14 [165], which is sketched in Figure 6.1*i*.

In order to introduce the application of high-speed X-ray PCI in quantifying the fracture toughness and the transfer of matrix toughness to the mode I interlaminar fracture toughness of the corresponding GFRC [166-167], notched beam samples of the SC-15 matrix having a consistent height of ~ 5 mm and the same aspect ratio determined by ASTM Standard D5045-14 [165] were also prepared for experiments. First, the SC-15 matrix in solution was prepared with the same weight ratio mentioned in Section 2.2. The matrix was poured into the silicone rubber molds with the identical dimension of 50 × 50 mm^2. After that, the matrixes together with the molds were placed in a vacuum chamber for degassing and then cured in the cycle same to the composite. Finally, the obtained bulk matrixes were cut into small beam samples and notched by the diamond saw.

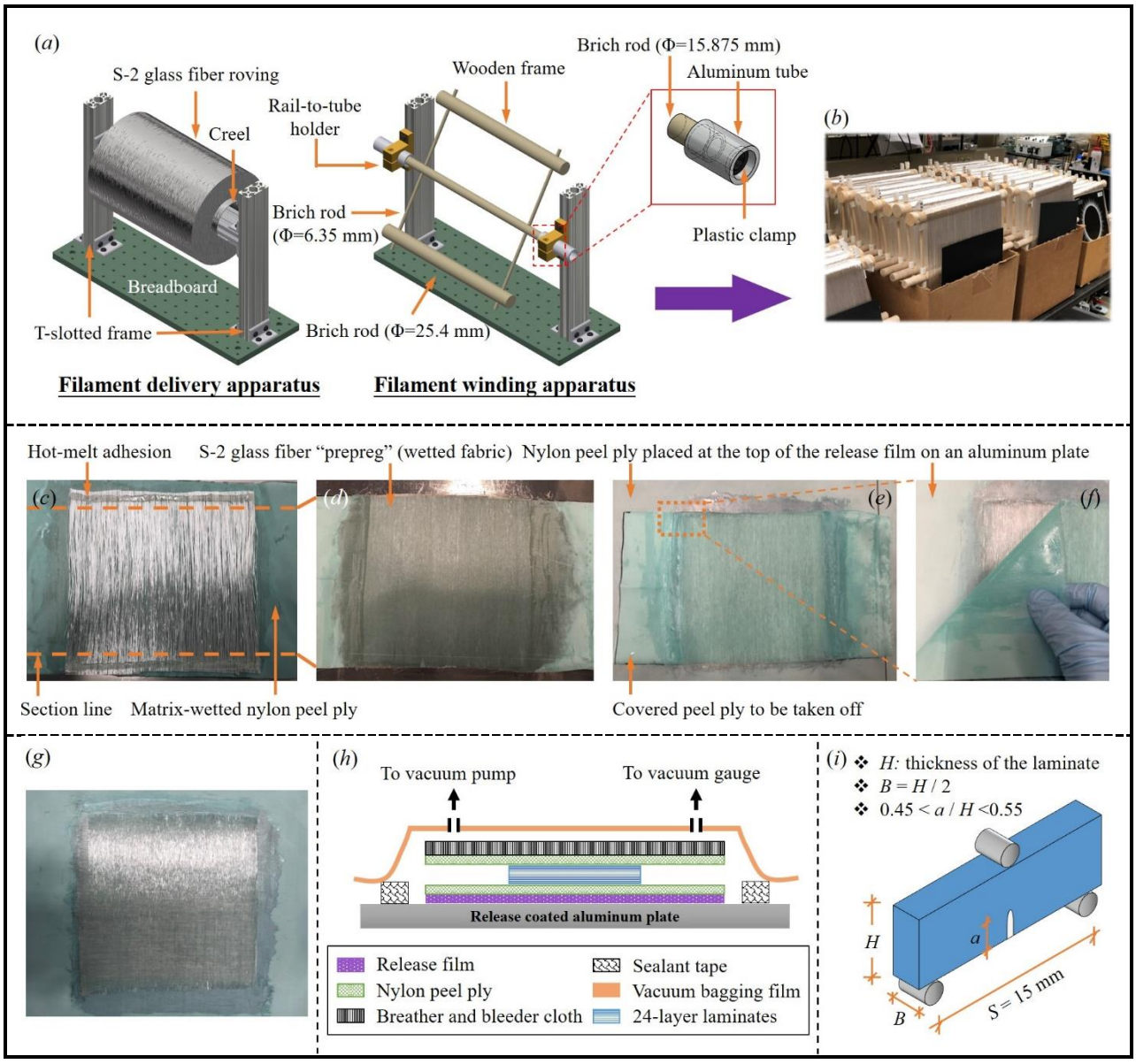

Figure 6.1. Composite manufacturing and sample preparation. (*a*) Schematic of filament winding setup; (*b*) Winded filaments on wooden frames; (*c*) S-2 glass unidirectional fabric; (*d*) S-2 glass fiber prepreg; (*e*) Prepregs layup process; (*f*) Removing covered peel ply; (*g*) Stacked fabrics; (*h*) Vacuum bagging strategy; (*i*) Sample geometry design.

6.3 Experiments

6.3.1 Three-dimensional synchrotron X-ray computed tomography

Interior structures of composite beam samples were characterized by three-dimensional (3D) synchrotron X-ray computed tomography at beamline 2-BM at Advanced Photon Source (APS), Argonne National Laboratory, Lemont, IL, USA. Each sample was first mounted on a rotational stage and rotated over 180°. During this process, a monochromatic X-ray beam with an energy of 40 keV penetrated the mounted sample and reconstructed the internal structures of the composite within 3000 projections, including the fiber distribution and alignment, voids, and defects. The X-ray was then converted into visible light by a single-crystal scintillator, magnified by a 5X microscope objective lens and recorded by FLIR Oryx ORX-10G-51S5M camera used in a fly scan mode where projections were recorded while the sample was continuously rotated. The synchrotron X-ray tomography has a frame size of 2560 × 960 pixels and a voxel size of 1.3 μm. The composite sample was then reconstructed by using the commercialized software Dragonfly 2020.2 (Object Research Systems Inc., Montreal, Canada). The fiber volume fraction (FVF) of the composite can be measured by counting fibers in voxel size. Based on the assumption of the perfect alignment of fibers in small areas, individual slices were randomly selected for the measurement of the FVFs at different locations of the sample.

6.3.2 DSENB experiments integrating with synchrotron X-ray PCI technique

DSENB experiments were performed on a modified Kolsky compression bar, of which the transmission bar was replaced with a fast response quartz load cell (Type 9212; Kistler, NY, USA) due to the space constraints of the X-ray containment hutch at APS beamline 32 ID-B. Figure 6.2*a* schematically illustrates the loading strategy. Upon experiment, the incident steel bar with a diameter of 12.7 mm and length of 1372 mm was impacted by a 305-mm-length air-propelled steel striker with the same diameter. At the opposite end of the incident bar, a C-shape fixture was rigidly installed to support the composite or matrix beam sample. The sample thereby was driven to impact onto a 3-mm-diameter indenter pin assembled on an adapted fixture. Behind the adapted fixture, a load cell captured the load history during each dynamic event. In order to minimize the signal disturbance, the load cell was connected with a rigid backstop. Figure 6.2*c* gives a detailed view of the sample loading side on the Kolsky bar. By the assumption of 1D wave propagation,

the loading speed (v) and time-resolved deflection (S) of the sample at the loading point were given by the bar strain as

$$v(t) = c_B\left[\varepsilon_I(t) - \varepsilon_R(t)\right] \tag{6-1}$$

$$S(t) = \int_0^t v(\tau)\, d\tau \tag{6-2}$$

Here, the bar strain was calculated by the incident (ε_I) and reflected (ε_R) pulses which were measured by a pair of semiconductor strain gauges on the surface of the middle length of the incident bar. The strain gauges were connected in a Wheatstone bridge in a half-bridge configuration. c_B indicates the elastic wave speed of the bar. The output was amplified by a differential amplifier and eventually recorded by an oscilloscope. In order to create a square stress pulse that produces a constant loading speed, a pulse shaper technique was adopted. A single loading stop was used at the strike-impacted end of the incident bar to ensure all the material to deform and fail within a single pulse, avoiding the cyclic loading and overload occurring in the load cell [168-170].

The deformation and failure of the notched composite beam were observed from the side of the sample by integrating the modified Kolsky compression bar with the synchrotron X-ray PCI setup at APS beamline 32 ID-B. Figure 6.2*d* provides a photograph of the setup. The high-energy X-ray beam was generated by APS Undulator A with a period of 33 mm, where the gap between the magnetic poles was varied to 15 mm to see through the composite sample with desired spatial and temporal resolutions. Experiments were performed with the standard operation mode of APS, where 24 bunches of electrons were stored in a circular ring with a circumference of 1140 meters, as shown in Figure 6.2*a*. The X-ray beam spot size was controlled with adjustable 2D slits to 1-3 mm in each direction. A set of slow and fast shutters were applied to provide a short-time window to prevent the potential damage to the optics downstream and the sample due to the excessive exposure to the high-flux X-rays. Before the experiment, the loading platform was aligned with the X-ray beam, and the notch tip was positioned within the field of view (FoV). The reverse impact strategy, by impacting the sample onto the indenter pin, enabled the material deformation and failure at the notch front to always happen inside the FoV. During the experiment, the X-ray beam penetrated the sample and captured the interior fracture information of matrix or composites shown in Figure 6.2*b*. Propagation-based PCI was employed in this work. Fibers, matrix, and the

air after the damage was generated induced spatial variations in the phase of X-rays, γ (x, y, z=0), along with a local curvature to the transmitted wavefront. During free space propagation from the sample to a single crystal Lu3Al5O12:Ce scintillator, the wavefront experienced overlap and interference and modulated the intensity. The variation of the intensity was owing to the propagation effects are proportional to the Laplacian of γ (x, y, z=0), yielding edge enhancement. This is demonstrated as the main benefit of PCI for resolving inhomogeneities and structure changes in low atomic number materials, which are inherently difficult to characterize with contact image radiography [171]. The X-rays were then converted into visible light and projected into a 5X objective lens via a 45-degree mirror. The magnified imaging was finally recorded by the high-speed camera (Shimadzu HPV-X2, Kyoto, Japan) with a frame rate of ~ 0.5-1M fps (frames per second) and an exposure time of 200 ns. The 2D image sequence was calibrated to have a spatial resolution of ~6.4 μm/pixel and the original size of 400 pixels in length and 250 pixels in width. The experiment on each type of sample was repeated 5 times.

For a successful DSENB experiment captured through the high-speed X-ray PCI technique, the timing sequence/synchronization of X-ray open-close time window controlled by slow/fast shutters, Kolsky bar firing, impact event, and image detection was critical. The trigger scheme was aided with a digital delay/pulse generator (DG535). First, a single-shot signal from a DG535 triggered the solenoid valve to launch the striker. A delayed trigger was then sent to the slow shutter to activate the required opening sequence. The time span was determined on average via 10 testing shots prior to the normal experiment. An additional trigger by DG535 was also generated to control the closing of the slow shutter. Within this window, the oscilloscope was triggered when the incident wave passed the strain gauge. Fast shutters and the high-speed camera were triggered by a delayed signal in consideration of the time interval when the stress wave traveled from the strain gauge to the sample at the incident bar end, which ensured the entire dynamic event was imaged within 256 frames at the designated frame rate.

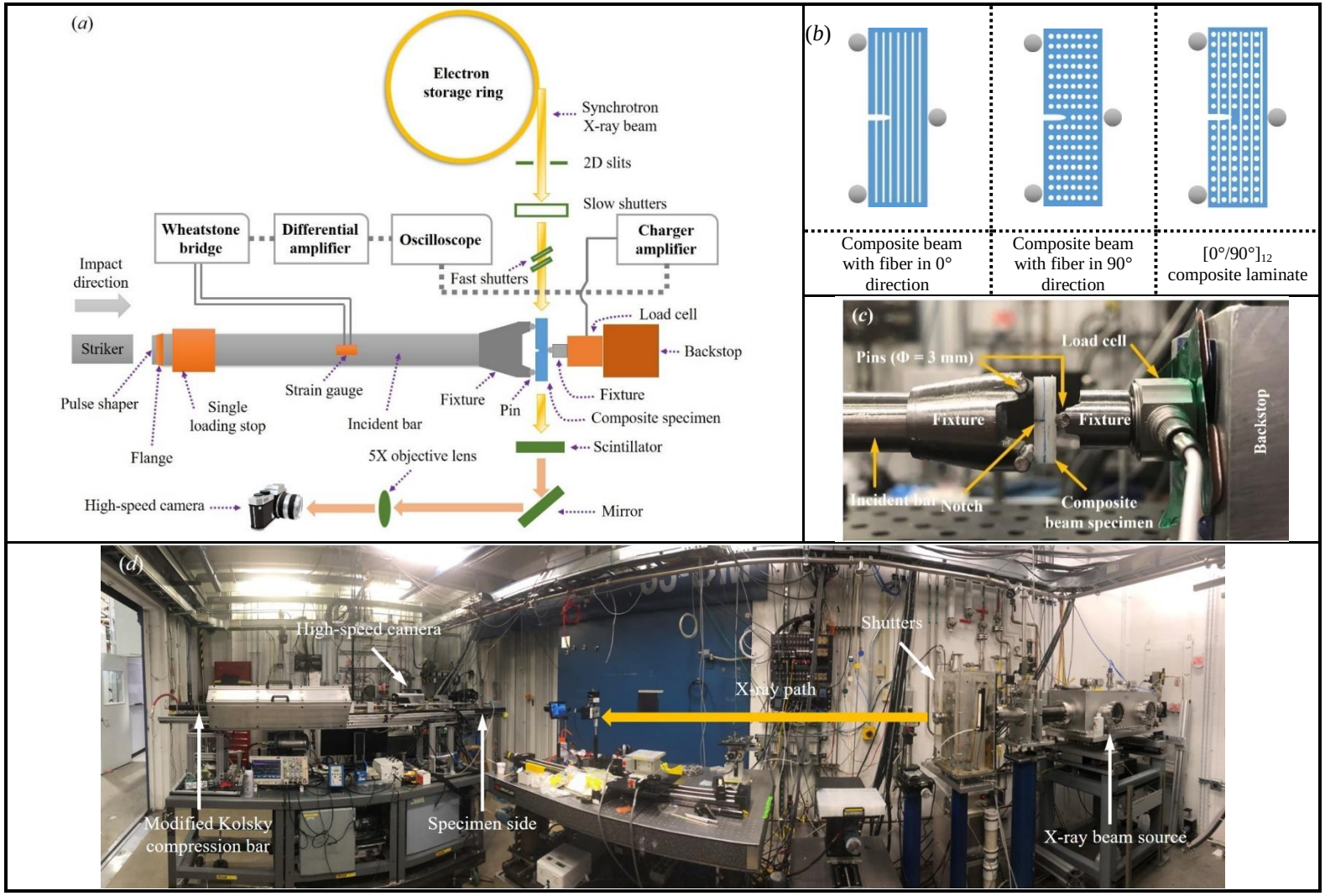

Figure 6.2. Experimental setup of dynamic SENB experiments integrating with synchrotron X-ray PCI technique. (*a*) Schematic of the experimental setup; (*b*) Composite beam sample type; (*c*) A close image about the loading strategy; (*d*) The real picture of the experimental setup at APS beamline 32ID-B. It is noted in (*a*) that the X-ray was in reality penetrating through the sample width (*B*) indicated in Figure 6.1*i* rather than the sample length (*S*).

6.3.3 DSENB experiments integrating with the optical imaging technique

An optical imaging technique was employed to capture a similar dynamic event and compare it with the high-speed X-ray PCI technique. The DSENB experiments adopted the same loading scheme on a modified Kolsky compression bar. A +2 close-up lens was assembled onto the high-speed camera to capture the global deformation and failure of the sample under the dynamic loading. A flash lamp system (Cordin Company, Salt Lake City, USA) was installed to provide a front light source with a typical 42-μs ramp-up time to reach full lamp intensity such that the sample can be illuminated throughout the entire loading event. Additional experiments were performed using a 10X close-up lens to observe the crack initiation and propagation close to the notch tip. Both front and back light sources were used to increase the luminous flux into the decreased FOV. The camera worked in a Trig-Trig mode and was triggered when the incident wave arrived at the strain gauges. An appropriate time delay, equivalent to the travel time of the waveform down to the incident bar end, was determined with caution to visualize the dynamic failure process of the composite at frame rates between 0.5 M and 1M fps. At the same time, the camera outputted a rising signal to activate the strobe light. The flash has a 5-7 ms duration, which ensured a lasting illumination throughout the entire dynamic event.

6.3.4 Scanning Electron Microscopy

Except for the 3D synchrotron X-ray computed tomography, SEM was used to help determine the FVF of the composite. The composite beam samples were polished using conventional metallographic procedures and placed inside the NovaNano SEM (FEI, Hillsboro, OR) for imaging. Image analysis was conducted by ImageJ to obtain the FVFs from 5 images at random locations per sample.

SEM was also utilized in this work to conduct post-fracture analysis on the GFRC samples after the dynamic loading, providing supporting imaging data to validate the real-time experimental observations by high-speed X-ray PCI. High-resolution images, revealing multiple material damage mechanisms and fracture surface morphologies of the samples after sputter coating with platinum, were obtained by NovaNano SEM, operating at a high vacuum with a beam accelerating voltage of 5 kV and spot size of 2.5.

6.4 Results and Discussions

6.4.1 Microstructures of GFRCs

Figures 6.3*a* and 6.3*b* present the reconstructed 3D tomographic images of a unidirectional S-2 glass/SC-15 composite having fibers oriented in 90° and a slice exposing the interior structure of a $[0°/90°]_{12}$ laminated S-2 glass/SC-15 composite, respectively. Single fibers can be identified because the high resolution of the beam source reaches 1.3 μm/voxel size. Moreover, fibers and matrix can be differentiated depending on the intensity of the X-rays penetrating through corresponding materials, making it possible to reveal the distribution of resin-rich regions in composites (see Figure 6.3*a*). The color version of Figure 6.3*a* is included in the online version of the journal, where the fibers were colored yellow, and the matrix was green. In Figure 6.3*b*, multiple plies were stacked in the $[0°/90°]_{12}$ manner, forming the composite laminate. The 3D synchrotron X-ray computed tomography was able to recognize individual plies and resin-rich regions between different plies. Since UD GFRC beam samples used in this work were sectioned from the same UD GFRC plate, samples with fibers uniformly oriented in 0° and 90° were regarded to have the same FVF. The FVF of the UD composite was determined as 64.67 ± 4.38 % by averaging the FVFs of eight individual samples. The FVF of the $[0°/90°]_{12}$ cross-ply composites was obtained as 61.44 ± 3.39 % by using the same method.

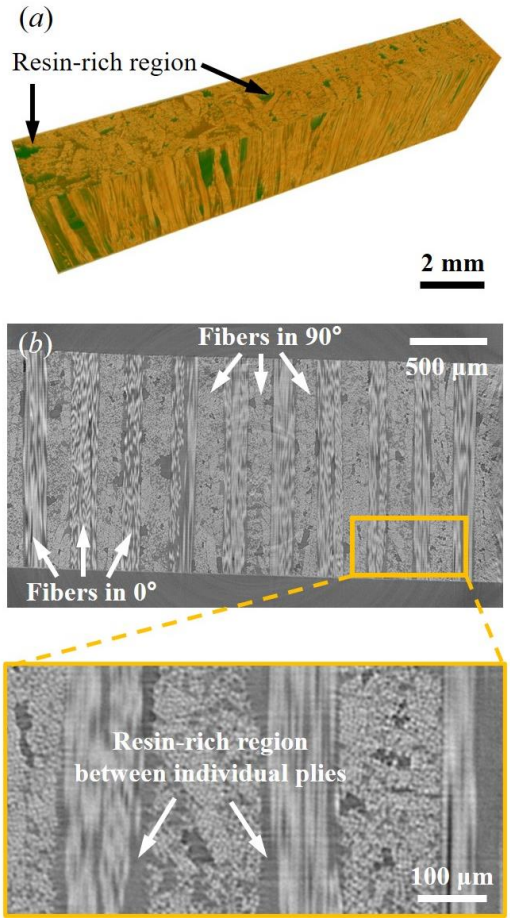

Figure 6.3. Synchrotron X-ray computed tomography images for S-2 glass/SC-15 composites. (*a*) 3D reconstruction for a unidirectional composite with fibers in 90°; (*b*) a slice for a $[0°/90°]_{12}$ laminated composites.

6.4.2 Dynamic fracture of GFRCs with different microstructures

The dynamic failure progressions of different GFRCs, including the fracture initiation, subsequent fracture propagation, and ultimately catastrophic failure, were captured by high-speed X-ray PCI and presented in Figures 6.4, 6.8, 6.13, and the supplementary electronic materials. In each X-ray image, the notch tip was located at the left side of the screen edge while the 3-mm-diameter indenter pin was at the opposite side and out of the screen. Each sample was moving at an identical speed of 6.6 m/s determined by Eq. (6-1) from the left towards the indenter on the right. Fibers oriented in 0° were along the vertical edge of each X-ray image, while the 90° indicated the out-of-plane direction. Crack paths were observed to be consistent for the repeated 5

tests of the individual material type while varying significantly due to the difference in fiber orientations (0° or 90°) within the composite.

6.4.2.1 Dynamic fracture of GFRCs with fiber oriented in 0°

Figure 6.4 shows a typical S-2 glass/SC-15 composite under dynamic loading. The material was firstly compressed as the sample moved towards the indenter. The sample was bent at the loading point. Afterward, in Figure 6.4*b*, the notch was opened due to the increased tensile stress. Having extremely high strength and stiffness in the longitudinal direction, S-2 glass fibers sustained the composite without fiber breakage observed in Figure 6.4*b*, which was verified by SEM images in Figure 6.6*a*. Simultaneously, the increasing stress was transferred from fiber to matrix through their interface. The matrix enveloping the fiber was excessively deformed and yielded, as demonstrated in Figure 6.6*b*, resulting in an increase of energy dissipation and a less amount of the driving force distributed to the notch tip, which significantly improved the overall fracture toughness of the composite. With loading, the stress in either the matrix or the fiber/matrix interface exceeded the corresponding matrix strength or the fiber/matrix interfacial shear strength. A crack was initiated at the radius root of the notch and inclined with an angle of ~ 90° (anti-clockwise direction) to the horizontal direction, indicated in Figure 6.4*c*. It is noted that diagnosis on the origin of the crack from the matrix crack or fiber/matrix interfacial shear debonding is difficult for the current experimental technique because such damage typically develops in less than 10 μm scale. The correlation of Figure 6.4*c* with the load signal in Figure 6.5 revealed that such crack initiation did not significantly degrade the structural stiffness of the sample. Instead, the composite sample kept resisting the dynamic loading as crack propagated along the fiber/matrix interface in Figure 6.4*d*. Subsequently, the crack continuously developed outside the FoV, transversely separating more material within the entire composite. Close to the indenter side, a higher stress concentration resulted in a higher degree of misalignment of the fibers. Interaction between fibers and matrix increased the shear stress developed in the matrix until the matrix yielded, leading to the microcracking in the matrix and the fiber/matrix debonding. Fibers in this area then lost the lateral support while experiencing longitudinal compression due to bending. Consequently, fibers buckled locally [172], as shown in Figure 6.4*e*, followed by the kink band formation. The stiffness of the sample at this time was found to have a dramatical decrease as presented in Figure 6.5. Finally, the sample failed catastrophically in a compressive-shear mode

under the indenter nose. Such shear-driven compressive failures of fibers were rarely observed on the sample surface through post-fracture SEM photographs as shown in Figures 6.6*a* and 6.6*c*, which uncovered the kink band formed within the material.

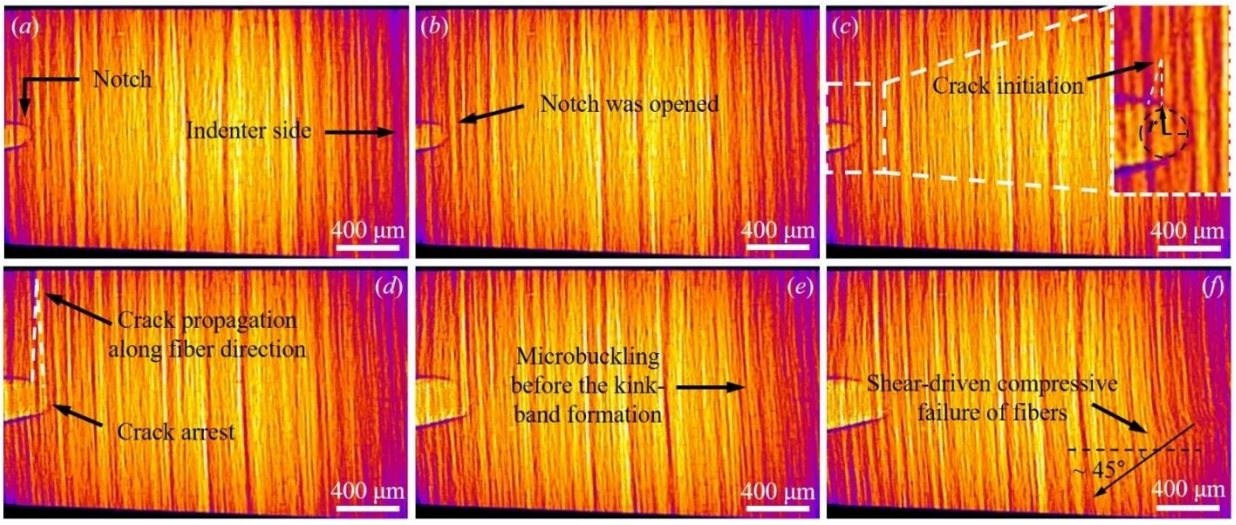

Figure 6.4. Dynamic fracture process of a representative 0° UD GFRC beam sample captured by high-speed X-ray PCI technique. t = (*a*) 0, (*b*) 12.2, (*c*) 18.4, (*d*) 73.4, (*e*) 99.5, (*f*) 120.9 μs. The r was the round notch's root radius.

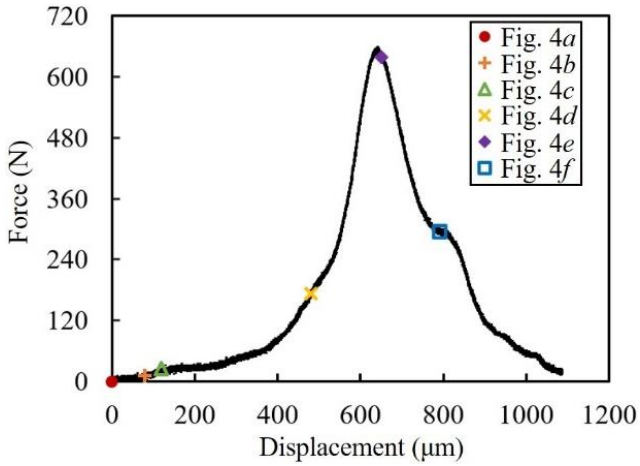

Figure 6.5. Force-displacement curve of the representative 0° UD GFRC beam sample in Figure 6.4.

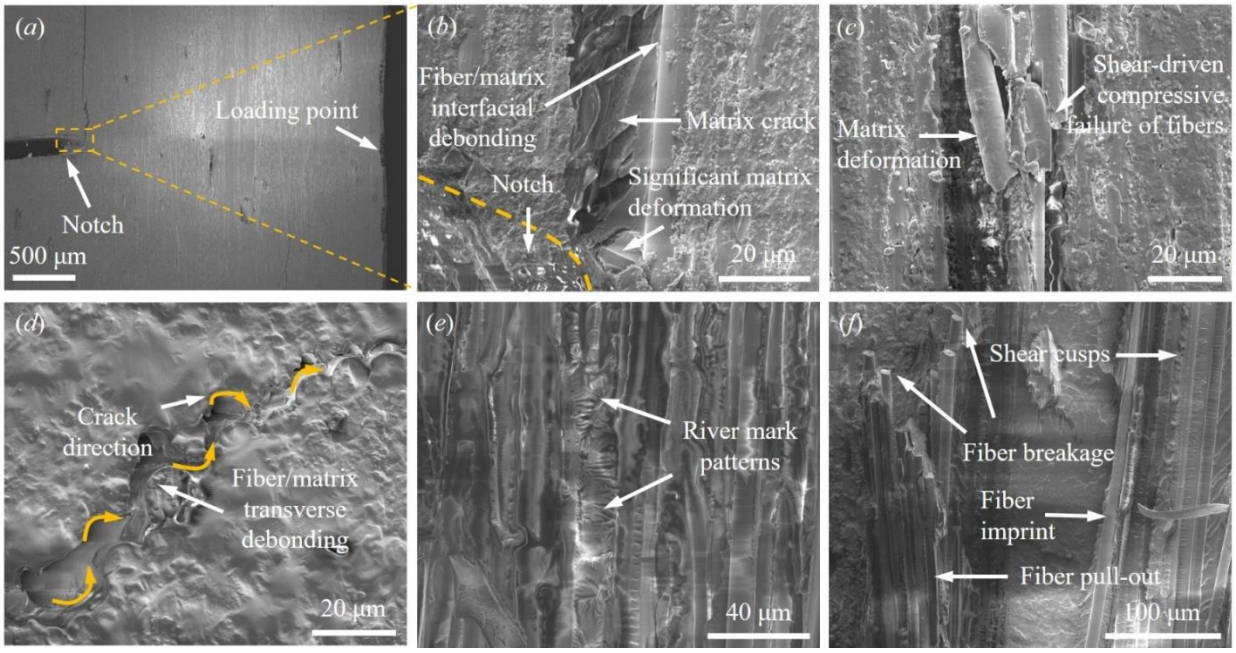

Figure 6.6. SEM images of fracture surfaces of S-2 glass/SC-15 composites. (*a*)-(*c*) A representative 0° UD GFRC beam sample: (*a*) Global fracture morphology close to the notch tip; (*b*) Detailed fracture morphology at the notch tip; (*c*) Detailed fracture morphology close to the loading point. (*d-f*) A representative 90° UD GFRC beam sample: (*d*) Fracture morphology along the crack propagating path; (*e*)-(*f*) Morphologies of the fractured cross-section.

Figure 6.7 compares the dynamic failure of the 0° UD GFRC imaged by high-speed X-ray PCI and optical imaging. The radiographic imaging has a spatial resolution of ~6.4 μm/pixel, and the optical imaging has a resolution of ~33.3 μm/pixel for the +2 close-up lens and ~14.5 μm/pixel for the 10X close-up lens, respectively. As shown in Figure 6.7*a*, although the composite was opaque, the X-rays penetrated through the entire sample and captured the initiated crack inside the composite in the 20-μm scale within 920 ns. On the other hand, the optical imaging used the reflected light as the illumination source and thereby can merely identify the crack initiated close to the sample surface. Hence, the subsurface crack behavior before the surface crack initiation was missed, adding sources of error to quantify the crack velocity and fracture toughness. In addition, the +2 lens does not have the sufficient resolution to identify in vision the delamination, as demonstrated in Figure 6.7*b*. Figure 6.7*c* is a close-up view of the morphology surrounding the notch obtained by the 10X lens. It is revealed that although the resolution was increased by ~1.3 times, the contrast to differentiate various phases was sacrificed, making it visually unrecognizable for the air filling in the opened crack and the real composite material in the vicinity of the crack.

The crack initiation was still challenging to be identified. Figure 6.7*d* is the optical image showing the catastrophic failure of the GFRC sample. It is revealed that the optical method can only capture the macroscopic surface damage morphology owing to the limited resolution. On the other hand, the X-ray image in Figure 6.4*f* is capable of revealing the lower-scale damage mechanism developed inside the GFRC and providing deep insight into the essence of the macroscopic catastrophic failure of the sample.

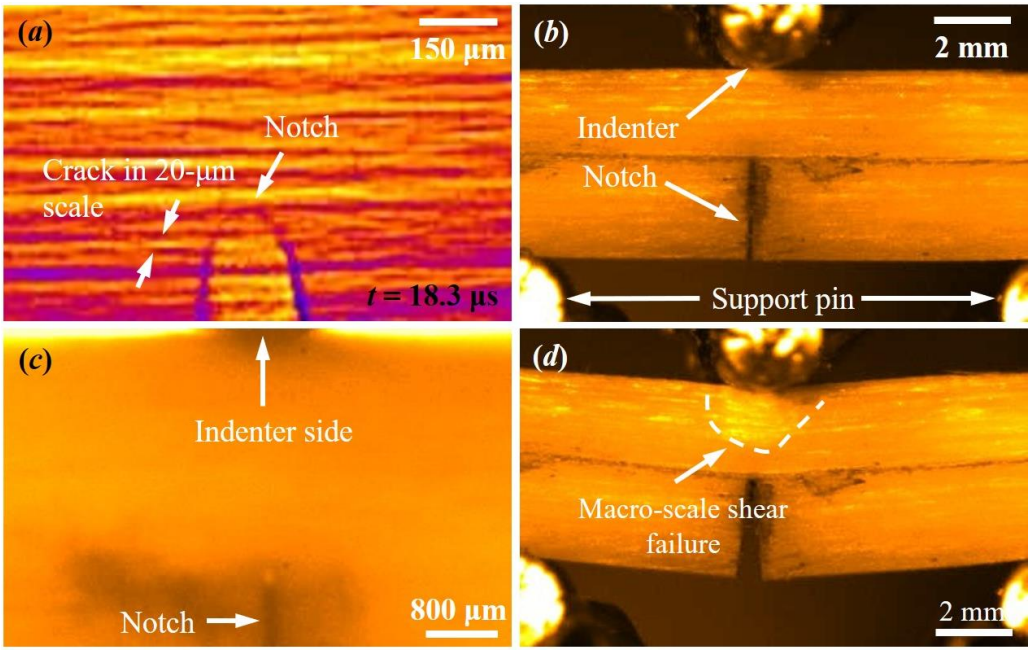

Figure 6.7. Comparison of the dynamic failure of the 0° UD GFRC beam characterized by different techniques. (*a*) Crack initiation in a sample captured by high-speed X-ray PCI; (*b*) A representative sample under dynamic loading captured by optical imaging with +2 lens; (*c*) A representative sample under dynamic loading captured by optical imaging with 10X lens; (*d*) Catastrophic failure of a representative sample captured by optical imaging with +2 lens.

6.4.2.2 Dynamic fracture of GFRCs with fiber oriented in 90°

When fibers were oriented in 90° inside the composite and dynamically loaded, the matrix became the load-bearing component while fibers were merely to toughen the matrix. Since the fiber orientation changed, the X-ray attenuation was correspondingly altered after the X-rays penetrated through the material. Therefore, the structure of intensity shown in Figure 6.8*a* is different from Figure 6.4*a*. The experimental observation was presented as the image sequence in

Figure 6.8, which uncovered the crack initiated exactly at the notch tip (see Figure 6.8*b*). The crack then propagated through the sample to the loading point as Figure 6.8*c* and failed the sample as Figure 6.8*d*. The major toughening mechanisms during crack propagation included crack deflection and fiber bridging. First, fibers embedded inside the composite directed the crack path along the fiber/matrix interface instead of a straight path, as shown in Figure 6.8*c* and verified by the post-fracture image in Figure 6.6*d*. Unevenly distributed resin-rich areas may also disturb the ideally straight crack path and cause the crack branching at the tip presented in Figure 6.8*d*. Such crack deflection increased the energy absorption during crack growth and, in consequence, improved the fracture toughness of the matrix. On the other hand, filaments at the wake behind the crack front transversely connected the crack faces, adding extra pressure to degrade the crack opening (see Figure 6.8*d*). By subsequent lowering the fiber constrain, releasing triaxiality of stress by fiber/matrix transverse debonding, and increasing the size of the damage zone and thereby facilitating more matrix deformation, these bridging elements apparently promoted more energy dissipation toughened the matrix [173]. Lower-scale damage characteristics on the fracture surface of a representative 90° GFRC are presented in SEM images in Figures 6.6*e* and 6.6*f*, where fiber imprint reveals the debonding between fiber and matrix. The river mark patterns and shear cusps, and fiber breakage and pull-out indicate the matrix deformation and fiber failure during the fiber bridging progression. The images were correlated to the load and displacement history in Figure 6.9. Compared with the 0° UD GFRC beam, the 90° UD GFRC beam significantly lowered load-bearing capacity, as demonstrated in Figures 6.5 and 6.9. This is because the failure of the 90° UD GFRC beam was dominated by matrix-related failures, such as the matrix deformation and cracking and fiber/matrix transverse debonding, while fibers embedded in the matrix were only to toughen the matrix. The load capacity of the 90° UD GFRC beam was, thereby, mainly influenced by the matrix property. In contrast, the high strength of S-2 glass fibers contributed to the loading resistance of the 0° UD GFRC beam, resulting in a much higher peak force in Figure 6.5.

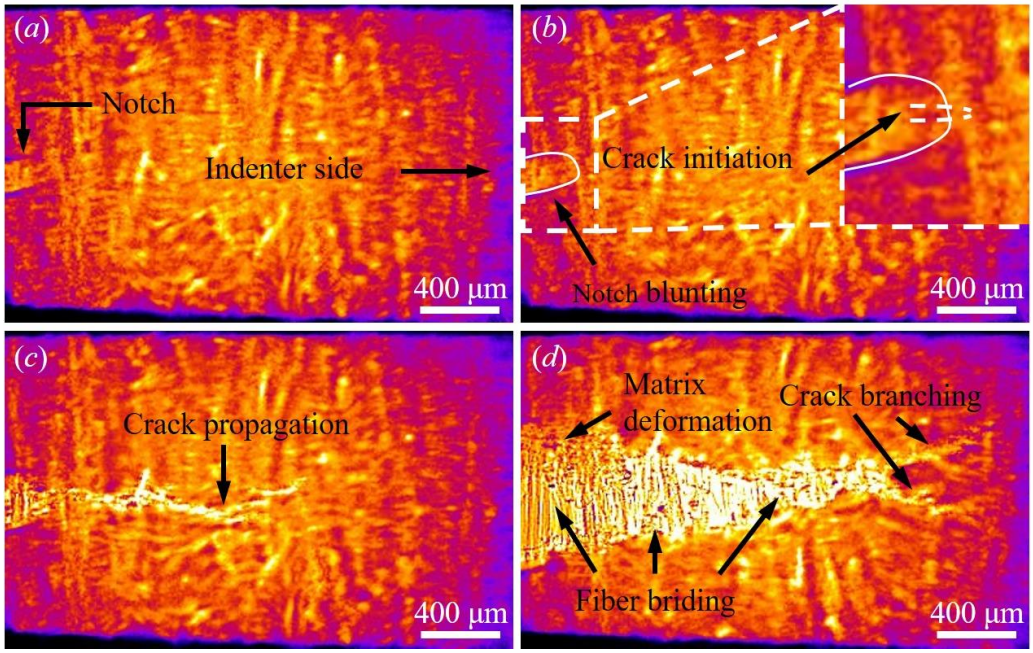

Figure 6.8. Dynamic fracture process of a representative 90° UD GFRC beam sample captured by high-speed X-ray PCI technique. t = (*a*) 0, (*b*) 39.6, (*c*) 60.7, (*d*) 133.4 μs. The 90° indicates the out-of-plane direction.

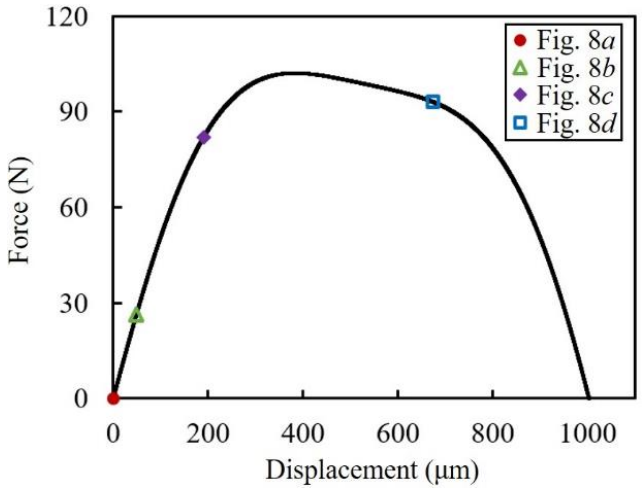

Figure 6.9. Force-displacement curve of the representative 90° UD GFRC beam sample in Figure 6.8.

Figure 6.10 compares the similar crack propagating behavior inside the 90° UD GFRC by high-speed X-ray PCI and optical imaging, where a crack propagates through a region of interest (ROI) having a dimension of 1.32 mm × 0.66 mm. It is demonstrated that high-speed X-ray PCI was able to identify both the crack geometry and crack tip position in real time, while optics only assisted in visualizing the appearance of the crack but failed to capture the crack edge in vision. In order to provide a more quantitative comparison of the characterizations of a propagating crack by two methods, straight paths having an identical length of 330 μm and traversing the crack were sketched in Figures 6.10*a*-6.10*c*, respectively. The brightness of the pixel, which was quantified as the greyscale value (GV), was tracked along each path and compared in Figure 6.11. It is noted that the initial GVs for Figures 6.10*a*-6.10*c* were different because of the difference between the X-rays and visible lights in the given intensity. Therefore, the relative greyscale values (RGVs) were computed. The three GV-distance relations were offset, and the corresponding curves were superposed in Figure 6.11 for comparison. As illustrated in Figure 6.11, the high-speed X-ray PCI technique can identify the crack through an RGV up to 108.3, which was ~12 times the optical method. Furthermore, increasing the magnification of the lens did not improve the RGV for optical imaging. One possible reason is that visualization by virtue of optics is very sensitive to the angle and intensity of the light source. Focusing on the deformation in a smaller area by using a larger-magnification lens can also lose the area that can supply light inputs with different intensities. Hence, the magnified optical images were lack of an effective contrast to differentiate the air and real material beside the crack. In comparison, the high-intensity synchrotron X-ray source penetrated through the composite whilst PCI exploited the phase perturbations introduced by the sample to modulate the intensity recorded at the image receptor and enabled to track in accuracy the crack growth and opening inside the composite [174].

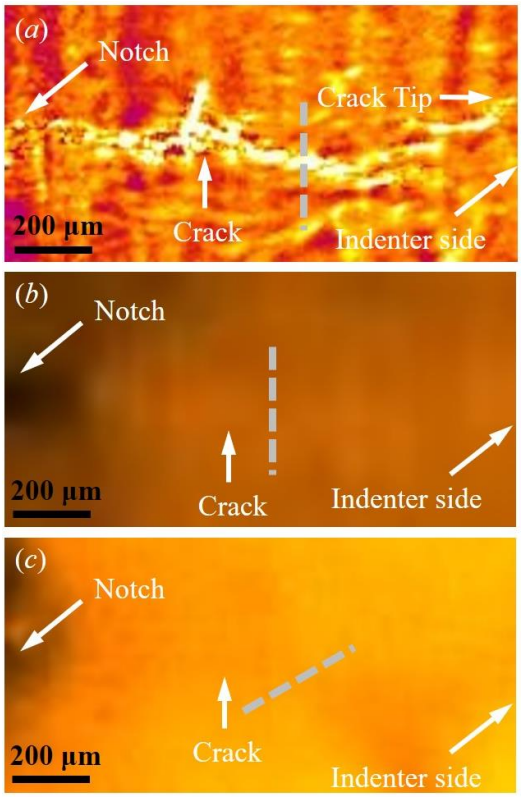

Figure 6.10. Comparison of the crack propagation in the 90° UD GFRC sample characterized by different techniques. (*a*) High-speed X-ray PCI; (*b*) Optical imaging with +2 lens; (*c*) Optical imaging with 10X lens. The 90° indicates the out-of-plane direction.

The similar failure behaviors of the 90° UD GFRC samples captured by different techniques are compared in Figure 6.12 and Figure 6.8*d*. In both the X-ray (Figure 6.8*d*) and optical (Figure 6.12) images, fibers behind the crack tip were transversely debonding with the matrix and bridging the crack. Figure 6.8*d* uncovers that high-speed X-ray PCI can identify the single S-2 glass fiber less than 10-µm scale after it debonded with the matrix. In contrast, optical imaging using the 10X lens had a resolution being 0.44 times the high-speed X-ray PCI and was merely able to recognize the fiber bundles at the 50-µm scale.

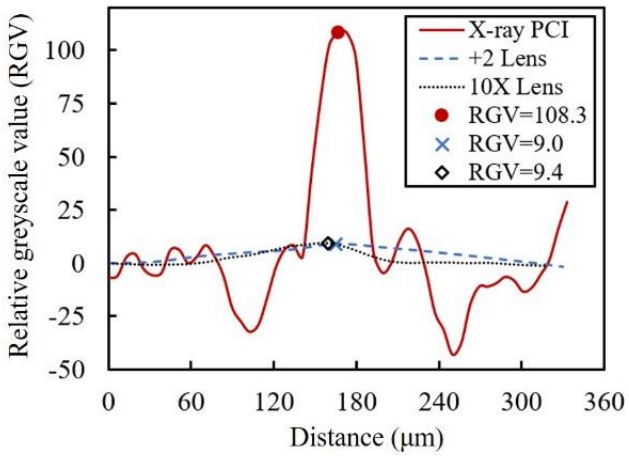

Figure 6.11. RGV variations along the path traversing a crack in growth captured by high-speed X-ray PCI and optical imaging.

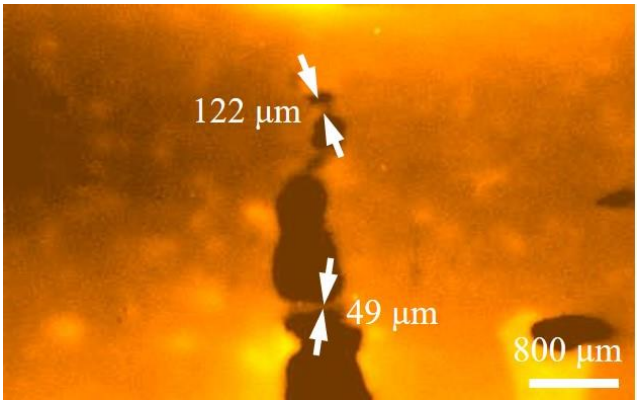

Figure 6.12. Failure behavior of the 90° UD GFRC sample captured by optical imaging with 10X lens.

6.4.2.3 Dynamic fracture of the cross-ply GFRCs

When multiple plies were stacked in the $[0°/90°]_{12}$ manner to form cross-ply composite laminates, the interface between each ply contained a resin-rich region above 10 μm in scale, which was characterized as Figure 6.3*b*. Sandwiched by two areas reinforced with S-2 glass fibers, such resin-rich region enabled more X-rays to penetrate through and, therefore, generated the variation of the X-ray attenuation recorded by the image receptor. Furthermore, the essential threadlike configuration of fibers made it possible to detect fiber orientations either within (0°) or perpendicular (90°) to the observation plane. Figure 6.13*a* presents the morphology of a representative $[0°/90°]_{12}$ laminated composite, where plies in 0°, 90°, and their interfaces were

labeled, and the variation of the X-ray intensity along a path spanning three regions in Figure 6.13*a* was plotted in Figure 6.14. During loading, the crack initiated at the notch tip and propagated along a direction with an angle of ~45° to the horizontal direction (see Figure 6.13*b*) because of the shear stress developed in the composite. The crack split the ply in 90° with the observable deformed matrix, matrix crack, fiber/matrix debonding and fiber bridging shown in Figure 6.13*c*. After traveling through the interface until the next ply in 0°, the crack was arrested and deflected in the 0° fiber direction, as shown in Figure 6.13*c*. The composite sample was delaminated. The opening of the delamination crack is quantified in Figure 6.14, where the alteration of the X-ray intensity distributed along the same path *AB* in Figure 6.13 is plotted. It is noted that GV=85, as a baseline in Figure 6.14, represented the approximate brightness of the fiber-reinforced areas in the image after the X-rays penetrated through the material, which was measured from individual plies. The distance between two intersections (I_1, I_2) of GV=85 and fitted curve at t=0 indicated the width of the resin-rich region connecting two plies. During the dynamic loading, by monitoring the variation of the distance between the intersections of the baseline with the fitted curve, such as I_3I_4, I_5I_6, the crack opening due to delamination can be tracked. In comparison, the optical imaging method was difficult to differentiate a particular lamina in the composite stemming from either a lower-magnification lens or limited phase contrast, revealed by Figure 6.13*d*.

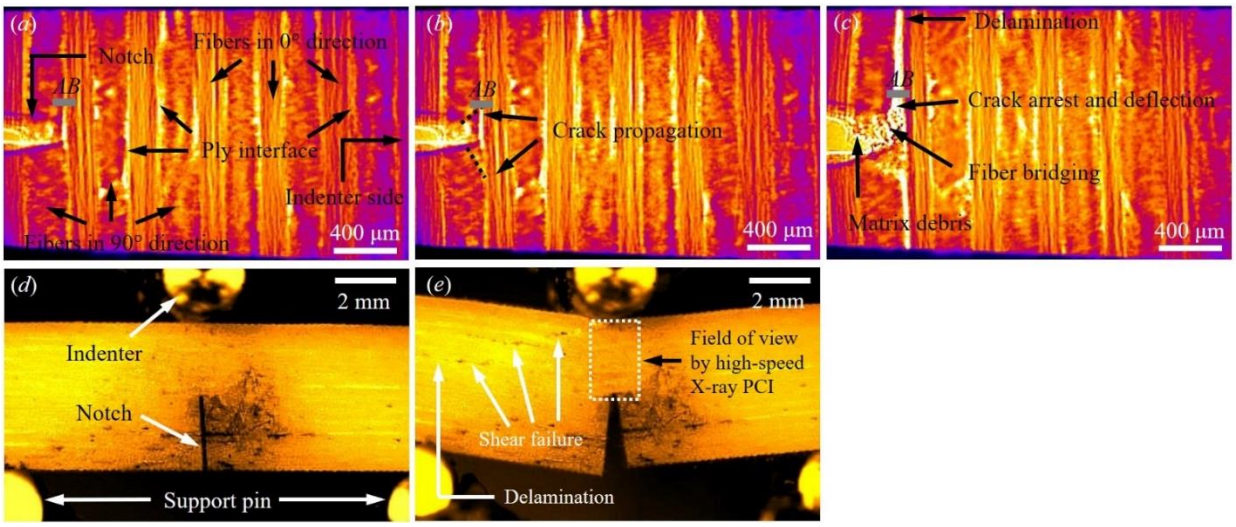

Figure 6.13. Damage characterization for the $[0°/90°]_{12}$ cross-ply GFRC laminates by high speed X-ray PCI at (*a*) t =0, (*b*) t = 38.6 μs, (*c*) t = 78.2 μs, and by optical method at (*d*) t = 0 and when (*e*) the material failure.

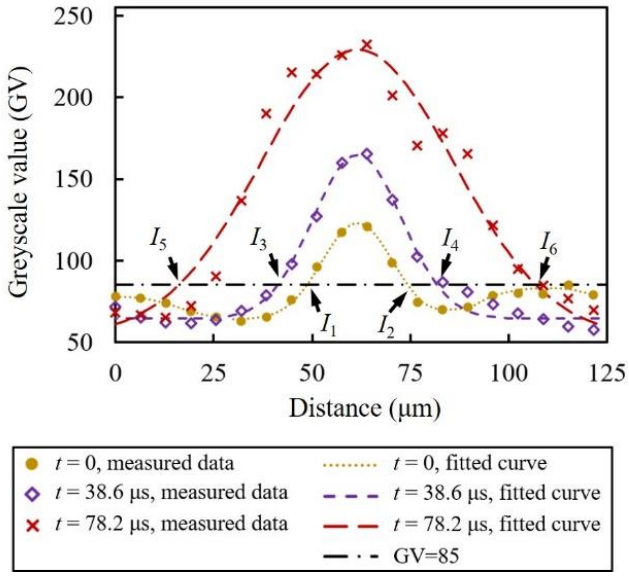

Figure 6.14. Variation of the X-ray intensity along a path spanning two plies at different times in a dynamic event.

6.4.3 X-ray effect on the mechanical properties of GFRCs

X-ray irradiation may destroy the initial structure of the polymer matrix by way of crosslinking, free radical formation, and irreversible bond cleavages, which results in the fragmentation of molecules and formation of saturated and unsaturated groups [174-175]. All these processes may introduce defects inside the matrix material and degrade the fiber/matrix interface, finally changing the mechanical response of the GFRC subjected to the dynamic loading. Nouh et al. [176] reported that the elastic modulus of polyester decreased by ~15% after exposure to the X-rays with a dose of 10 kGy. It is noted that the composite samples in this work were exposed to the X-rays within a short operation time in order of milliseconds to align the sample with the beam source and image the dynamic event. The X-ray dose was calculated on a scale of 10^{-1} kGy based on the assumption that all X-rays were absorbed by the material, which makes it feasible to neglect the effect of the X-ray irradiation on the dynamic failure of the composite. Figure 6.15 compares force-displacement curves of $[0°/90°]_{12}$ laminated samples with identical geometries imaged under X-rays and visible light. Small differences between individual experiments were possibly caused by the sensitivity of the load cell, strain gauge, and variation of the sample dimensions, fiber volume ratios, and notch geometries. Corresponding dynamic failure behaviors recorded can be compared

through Figure 6.13, demonstrating a similar mechanical response of the $[0°/90°]_{12}$ laminated composites under the dynamic loading.

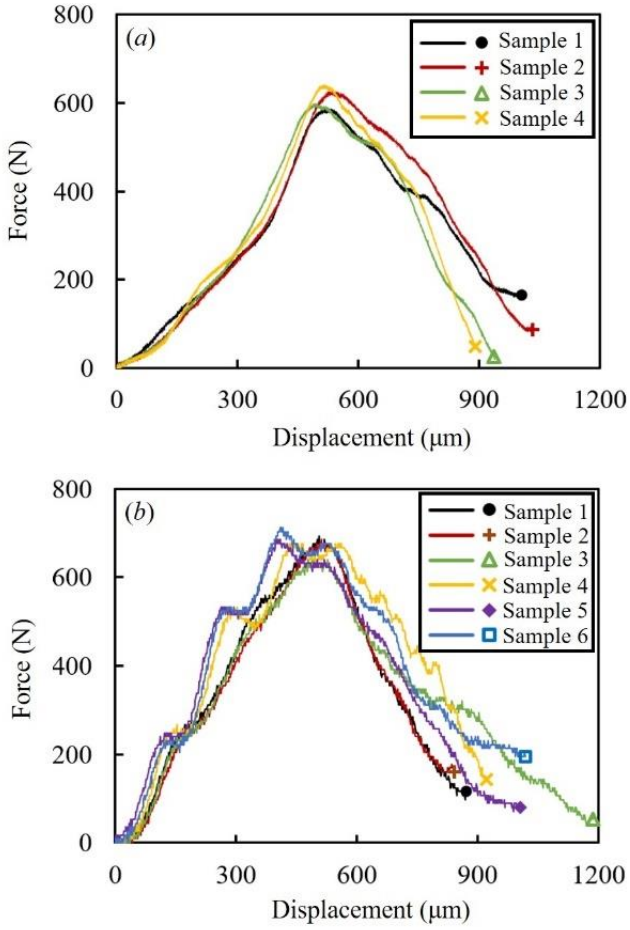

Figure 6.15. Force-displacement curves of various $[0°/90°]_{12}$ cross-ply GFRC laminate samples under synchrotron X-ray and visible light. (*a*) Synchrotron X-ray; (*b*) Visible light.

6.4.4 Limitation of high-speed X-ray PCI

The disadvantage of the high-speed X-ray PCI technique herein proposed is the limitation of the field of view. As introduced in Section 3.2, the 2D slits controlled the X-ray beam spot size within 2.5 mm in each direction. Before each experiment, the sample was aligned until merely a small section of the notch tip located at the left edge of the screen in order to capture the deformation and failure within the material as much as possible. A rectangular box was sketched on the $[0°/90°]_{12}$ cross-ply GFRC sample imaged by optical method with +2 lens in Figure 6.13*e*

to indicate the actual region typically imaged by the high-speed X-ray PCI technique. It is obviously shown that the high-speed X-ray PCI failed to inspect the catastrophic failure mechanism of shear deformation and delamination outside the target area, despite providing a higher-resolution visualization on the crack behavior close to the notch tip. In addition, the current high-speed X-ray PCI technique is limited to in-situ observation. The damage detected could be cumulative through the laminate thickness. Visualizing the damage evolution inside the entire composite through 3D high-speed X-ray PCI needs to be explored in future work.

CHAPTER 7. CONCLUSIONS

High-speed X-ray PCI was employed in this work to visualize in real time the damage evolution within different GFRCs subjected to dynamic loading. Laminated composite plates were first manufactured and sectioned into small beam samples, followed by material characterization by 3D synchrotron X-ray computed tomography and SEM. DSENB experiments were performed on a modified Kolsky compression bar, with the incident bar carrying a pre-notched GFRC beam sample to impact onto a static indenter. Loading information was directly measured by a load cell located behind the indenter, whilst the beam deflection was related to the bar movement calculated from stress waves passing the strain gauge on the incident bar surface. Synchrotron X-rays penetrated the sample from the side, recognized damage-related features developed inside the composite, and were output as a magnified visible light signal for high-speed imaging after processed by a scintillator and 5X objective lens in sequence. UD S-2 GFRCs having fibers in 0° and 90°, and $[0°/90°]_{12}$ laminated composites were investigated. Similar dynamic fracture events were visualized by optical imaging technique for comparison. Benefits and limitation of high-speed X-ray PCI applied in damage diagnoses for GFRCs were uncovered as below:

1) Having synchrotron X-ray penetrating through GFRCs and enhanced phase contrast, high-speed X-ray PCI can visually detect damage initiation inside material in a 20-μm scale.
2) High-speed X-ray PCI can provide real-time microscopic damage monitoring for GFRCs under dynamic loading, thereby generating reliable data to quantify the fracture toughness.
3) With a capability of capturing damage details even less than 10 μm scale like a single fiber, high-speed X-ray PCI provided insights into the fundamental material failure mechanism to understand macroscale structural failure and evaluate material mechanical performance in quantification.
4) By identifying and tracking crack propagation within and between individual plies, high-speed X-ray PCI was useful to reveal the dynamic fracture behavior of laminated GFRCs.
5) The quality of imaging using X-ray PCI relied on the X-ray attenuation traversing the material. Simultaneously, propagation-based PCI was employed to obtain the edge enhancement, making the imaging less sensitive to the external distorting factors such as visible light. Furthermore, the short operating time guaranteed few irradiations on samples investigated and effectively decreased degradation of material mechanical properties.

6) High-speed X-ray PCI had a limited field of view within 2.5 mm in the square. Damage detection was useful to understand fundamental material failure mechanism while was difficult for application in large-scale structural health monitoring for composites. Besides, the current high-speed X-ray PCI technique is limited to in-situ visualization, making the damage inspection likely to be cumulative through the laminate thickness. 3D visualization of the damage evolution inside the entire composite subjected to dynamic loading needs to be explored in future work.

CHAPTER 8. GLOBAL SUMMARY

Transversely impacted by a projectile at the ballistic limit, a composite laminate's failure experienced a transition from the conical deformation to the local perforation. Understanding the transition mechanism contributes to controlling the impact-induced failure and improving the composite's impact resistance. This Ph.D. dissertation aims to promote understanding by performing the low-scale composite strip or fiber impact/loading experiments. The efforts and findings are summarized below:

First, transverse impact experiments by RCC projectiles were conducted on the S-glass and Kevlar® composite strips. Such experiments enabled to isolate the interactions between plies and tows and provide insight into the fundamental material failure mechanism upon the impact. Although a composite strip can be damaged or even failed before the transverse wave deformed the entire sample, the failure of the composite strip was always due to tensile breakage. The S-glass composite strips failed ahead of the RCC projectiles' flat surfaces whilst the Kevlar® composite strips fractured at the projectile corners. It is believed that the stress concentration and anisotropic mechanical properties of fibers can have an impact on the composite's failure close to the impact area. Based on the fiber volume fraction (~50%-60%) investigated in the experiments, the critical velocity region of the composite strip was highly influenced by the fiber type while was not related to the matrix properties. A general trend was revealed that the critical velocity and ballistic limit decreases as the size scale increases from a single fiber to a single-ply composite panel. This indicates that the fiber mobility in the composite material can affect the ballistic limit of the composite panel.

Second, the projectile nose effect on the composite strip's failure was studied. The critical velocities of the S-glass composite strips decreased with the reduction of the round-nose projectiles' nose diameter. Furthermore, the S-glass composite strips had a tensile failure mode in front of both the 40-μm and 400-μm round-nose projectiles. However, a special failure phenomenon was observed for the S-glass composite strip by the 4-μm round-nose projectiles, which were actually razor blades: the S-glass composite strips seemed to be completely cut through by the razor blades when the impact velocities were beyond the upper limit of the critical velocity region. Such a different failure mechanism needs to be further investigated. Besides, the composite strips can be partially failed by different projectiles when the impact velocities increased to a value within the

critical velocity region. Such a partial failure may be different from the projectile nose diameter and also requires further investigation. A reverse impact technique is believed to provide the possibility to visualize the above mechanisms if a more advanced imaging technique was adopted.

To further investigate the particular impact-induced failure phenomenon by the razor blades, single constituent fibers were extracted from the yarns and examined by SEM for the failure by razor blades. A microscopic method was developed, allowing to cut a single fiber at a speed ranging from 1.67 μm/s to 33.3 μm/s and simultaneously observe the failure process. As a type of aramid fiber, a Kevlar® KM2 Plus fiber was partially cut through by a razor blade and finally fractured due to tension. Being a UHMWPE fiber, a Dyneema® SK76 fiber was completed cut through by a razor blade. Different from the above two fibers, a S-2 glass fiber is an inorganic fiber. The razor blade cannot cut into the fiber, so the S-2 glass fiber failed in tension. Such an incision-resistant characteristic enabled the glass fibers to develop more tensile deformation during the transverse cut and thereby absorb more energy.

Afterward, a single-fiber dynamic cut technique was developed and integrated with high-speed optical imaging. Such an integrated technique made it possible to cut a single fiber at a speed up to 10 m/s and simultaneously visualize its deformation and failure process. It was revealed that the failure modes of different fibers did not change when the loading speed increased from 1.67 μm/s to ~5.34 m/s.

As the last technical chapter of this Ph.D. dissertation, an advanced imaging technique, high-speed synchrotron X-ray PCI, was introduced. By integrating such a technique with the modified Kolsky compression bar loading technique, the damage evolution inside an S-2 GFRC beam transversely impacted at a velocity of ~ 6 m/s was successfully characterized. By replacing the objective lens in the high-speed synchrotron X-ray PCI setup, the resolution can be further increased to 1.6 μm/pixel. Integrated with the aforementioned reverse impact technique by a light gas gun setup, such an advanced imaging technique is believed to be capable of visualizing the partial failure and the cut-induced failure mechanism of the composite strips, yarns, and single fibers under transverse impact by different projectiles. The relevant studies can be found in future publications.

CHAPTER 9. FUTURE WORK

As the continued work of this Ph.D. dissertation, the following research is believed to contribute to the understanding of the composites' failure at extreme dynamic environments and improving the impact resistance of the composite structures.

The research effort in the nearest future will be the real-time visualization of the partial failure and the cut-induced failure mechanism of the composite strips and yarns under transverse impact by different projectiles. To successfully conduct such experiments, an integrated technique is required with the high-speed synchrotron X-ray PCI and the reverse impact method by a light gas gun. As concluded in Chapter 7, the high-speed synchrotron X-ray PCI can have a spatial resolution of up to 1.6 μm/pixel. The reverse impact method allows to focus the high-speed camera on a static projectile, making the composite strip's failure always occur within the camera window. The findings will be presented in future publications.

Transverse impact behavior of single fibers is another topic that requires further investigation. Such research enables the isolation of the fiber/fiber or fiber/matrix interactions in yarns and composite strips and focuses on the fundamental material failure mechanism under impact. Despite many experiments on yarns and composites, it has been challenging to evaluate which fiber type can provide the best energy absorption of textiles and composites. The difficulty originated from the fact that the number of fibers composing a yarn and a composite is usually varied for different fiber types. By performing single-fiber transverse impact experiments, the critical velocity regions of different fibers can be quantified as an indicator to evaluate the impact resistance of the fiber materials. Furthermore, by integrating the reverse impact technique and the high-speed synchrotron X-ray PCI, the cut-induced failure mechanism of a single fiber can be visualized. This promotes understanding the cut-induced failure mechanism of a yarn or composite strip as well as the local perforation mechanism of the composite laminate at the ballistic limit.

Being the load-bearing components in the composite materials, the reinforcement fibers need to be sufficiently strong to resist the external loading. The longitudinal tensile properties of the fibers have been improved drastically in the last seven decades. However, experiments on single fibers in this Ph.D. dissertation reveal the axial tensile deformation can be significantly suppressed by the transverse loading, especially by the transverse cut, which is possibly due to the chemical compositions and nanostructures of the fibers. Therefore, it is very promising to design

some nanoscale experiments, develop canonical models for the fibrous materials, and finally modify the fiber via nanotechnology to increase its load-bearing capacities in the transverse direction.

As revealed by the experiments in Chapter 2, there is a general trend that the critical velocity and ballistic limit decreases as the size scale increases from a single fiber to a single-ply composite panel. This indicates that the fiber mobility in the composite material can affect the ballistic limit of the composite panel. The fiber mobility in the composites is related to the fiber/matrix interfacial properties. To examine the fiber mobility effect on the composite's ballistic limit, the fiber/matrix interface needs to be modified, and transverse impact experiments on composite strips with these different fiber/matrix interfaces are required in the future.

Under transverse impact by the projectiles, the composites are subjected to the multi-axial loading in the front of the projectiles or at the projectile corners. Understanding the composite's failure requires a multi-axial loading failure criterion. Different from the metallic materials, the composite's failure by multi-axial loading may be related to the fiber and matrix properties, fiber volume fracture, fiber orientation, stacking method, sample size, and loading rate. Specially, the mechanical response of the composite under dynamic multi-axial loading requires further investigations. Such research is actually in progress by the author of this Ph.D. dissertation.

REFERENCES

1. Bogenfeld R, Kreikemeier J, Wille T. Review and benchmark study on the analysis of low-velocity impact on composite laminates. Eng Fail Anal 2018; 86: 72-99.

2. Abtew MA, Boussu F, Bruniaux P, Loghin C, Cristian I. Ballistic impact mechanisms–a review on textiles and fibre-reinforced composites impact responses. Compos Struct 2019; 223: 110966.

3. National Academies of Sciences, Engineering, and Medicine. Frontiers of Materials Research: A Decadal Survey. Washington, DC: The National Academies Press. 2019.

4. Luz FSD, Lima Junior EP, Louro LHL, Monteiro SN. Ballistic test of multilayered armor with intermediate epoxy composite reinforced with jute fabric. Mater Res 2015; 18: 170-177.

5. Misey J. Analysis of ballistic limit. Ballistic Research Laboratory ARBRL-MR-02815;1978.

6. Akella K, Naik NK. Composite armour—A review. J Indian I SCI 2015; 95(3): 297-312.

7. Sorrentino L, Bellini C, Corrado A, Polini W, Aricò R. Ballistic performance evaluation of composite laminates in Kevlar 29. Procedia Eng 2014; 88: 255-262.

8. Karahan M, Jabbar A, Karahan N. Ballistic impact behavior of the aramid and ultra-high molecular weight polyethylene composites. J Reinf Plast Compos 2015; 34(1): 37-48.

9. Naik NK, Shrirao P. Composite structures under ballistic impact. Compos Struct 2004; 66(1-4): 579-590.

10. Reddy PRS, Reddy TS, Mogulanna K, Srikanth I, Madhu V, Rao KV. Ballistic impact studies on carbon and E-glass fibre based hybrid composite laminates. Procedia Eng 2017; 173: 293-298.

11. Guoqi Z, Goldsmith W, Dharan CH. Penetration of laminated Kevlar by projectiles—I. Experimental investigation. Int J Solids Struct 1992; 29(4): 399-420.

12. Sikarwar RS, Velmurugan R, Gupta NK. Influence of fiber orientation and thickness on the response of glass/epoxy composites subjected to impact loading. Compos B Eng 2014; 60: 627-636.

13. Yaghoubi AS, Liaw B. Influences of thickness and stacking sequence on ballistic impact behaviors of GLARE 5 FML plates: Part I-experimental studies. J Compos Mater 2014; 48(16): 2011-2021.

14. Flanagan MP, Zikry MA, Wall JW, El-Shiekh A. An experimental investigation of high velocity impact and penetration failure modes in textile composites. J Compos Mater 1999; 33(12): 1080-1103.

15. Udatha P, Sesha Kumar CV, Nair NS, Naik NK. High velocity impact performance of three-dimensional woven composites. J Strain Anal Eng 2012; 47(7): 419-431.

16. Ellis RL, Lalande F, Jia H, Rogers CA. Ballistic impact resistance of SMA and spectra hybrid graphite composites. J Reinf Plast 1998; 17(2): 147-164.

17. Muhi RJ, Najim F, de Moura MF. The effect of hybridization on the GFRP behavior under high velocity impact. Compos B Eng 2009; 40(8): 798-803.

18. Pandya KS, Pothnis JR, Ravikumar G, Naik NK. Ballistic impact behavior of hybrid composites. Mater Des 2013; 44: 128-135.

19. Bandaru AK, Vetiyatil L, Ahmad S. The effect of hybridization on the ballistic impact behavior of hybrid composite armors. Compos B Eng 2015; 76: 300-319.

20. Gellert EP, Cimpoeru SJ, Woodward RL. A study of the effect of target thickness on the ballistic perforation of glass-fibre-reinforced plastic composites. Int J Impact Eng 2000; 24(5): 445-456.

21. Ulven C, Vaidya UK, Hosur MV. Effect of projectile shape during ballistic perforation of VARTM carbon/epoxy composite panels. Compos Struct 2003; 61(1-2): 143-150.

22. Zhikharev MV, Kudryavtsev OA, Pavlovskaya MS. Experimental and numerical study of the behavior of a Glass Fiber Reinforced Plastic plate under oblique impact. J Compos Mater 2021; 55(9): 1167-1178.

23. Xie W, Zhang W, Kuang N, Li D, Huang W, Gao Y, Ye N, Guo L, Ren, P. Experimental investigation of normal and oblique impacts on CFRPs by high velocity steel sphere. Compos B Eng 2016; 99: 483-493.

24. Haque BG, Gillespie Jr JW. Penetration and perforation of composite structures. SAT 2013; 2(2.14): 2-14.

25. Pandya KS, Kumar CVS, Nair NS, Patil PS, Naik NK. Analytical and experimental studies on ballistic impact behavior of 2D woven fabric composites. Int J Damage Mech 2015; 24(4): 471-511.

26. Chocron S, King N, Bigger R, Walker JD, Heisserer U, Van der Werff H. Impacts and waves in Dyneema® HB80 strips and laminates. J Appl Mech 2013; 80(3): 031806.

27. Smith JC, McCrackin FL, Schiefer HF. Stress-strain relationships in yarns subjected to rapid impact loading: Part V: wave propagation in long textile yarns impacted transversely. Text Res J 1958; 28(4): 288-302.

28. Bazhenov S, Dukhovskii I, Kovalev P, Rozhkov AN. The fracture of SVM aramide fibers upon a high-velocity transverse impact. Polym Sci Ser A Chem Phys 2001; 43: 61–71.

29. Field JE, Sun Q. High-speed photographic study of impact on fibers and woven fabrics. In: 19th international congress on high-speed photography and photonics. International Society for Optics and Photonics, Cambridge, England, September 1991.

30. Heru Utomo B, Broos J. Dynamic material behavior determination using single fiber impact. In: 25th conference and exposition on structural dynamics (IMAC-XXV), Orlando, Florida, USA, February 2007.

31. Carr DJ. Failure mechanisms of yarns subjected to ballistic impact. J Mater Sci Lett 1999; 18(7): 585-588.

32. Hudspeth M, Chu JM, Jewell E, Lim B, Ytuarte E, Tsutsui W, Horner S, Zheng J, Chen W. (2017). Effect of projectile nose geometry on the critical velocity and failure of yarn subjected to transverse impact. Text Res J 2017; 87(8): 953-972.

33. Phoenix SL, Heisserer U, Van der Werff H, der Jagt-Deutekom V. Modeling and experiments on ballistic impact into UHMWPE yarns using flat and saddle-nosed projectiles. Fibers 2017; 5(1): 8.

34. Hudspeth M, Chen W, Zheng J. Why the Smith theory over-predicts instant rupture velocities during fiber transverse impact. Text Res J 2016; 86(7): 743-754.

35. Lim BH, Chu JM, Gao J, Claus B, Nie Y, Chen W. The effect of projectile nose shape on the critical velocity of high-performance yarn. Fibers 2019; 7(4): 29.

36. Shah K, Sockalingam S. Experimental Investigation of Transverse Loading Behavior of Ultra-High Molecular Weight Polyethylene Yarns. Fibers 2020; 8(10): 66.

37. Song B, Lu WY. Effect of twist on transverse impact response of ballistic fiber yarns. Int J Impact Eng 2015; 85: 1-4.

38. Zhou R. Effects of crimp and slip on laminar and woven fabrics subjected to ballistic impact. Cornell University, New York, 2014.

39. Cunniff PM. Dimensionless parameters for optimization of textile-based body armor systems. In: Proceedings of the 18th international symposium on ballistics. Technomic Publishing Company Inc Lancaster PA, San Antonio, November 1999.

40. Standard NIJ 010106. Ballistic resistance of body armor. National Institute of Justice, US Department of Justice, 2008.

41. Sutherland LS, Soares CG. Impact tests on woven-roving E-glass/polyester laminates. Compos Sci Technol 1999; 59(10): 1553-1567.

42. Jordan JB, Naito CJ, Haque BZ. Quasi-static, low-velocity impact and ballistic impact behavior of plain weave E-glass/phenolic composites. J Compos Mater 2014; 48(20): 2505-2516.

43. Naik NK, Shrirao P, Reddy BCK. Ballistic impact behavior of woven fabric composites: Parametric studies. Mater Sci Eng A Struct Mater 2005; 412(1-2): 104-116.

44. Gao J, Nie Y, Lim BH, Kedir N, Chen W. A microscopic experimental method transversely loading on single high-performance fibers. Exp Mech 2019; 59(5): 669-679.

45. Gao J, Nie Y, Lim BH, Zhai X, Kedir N, Chen W. In-situ observation of cutting-induced failure processes of single high-performance fibers inside a SEM. Compos Part A Appl Sci Manuf 2020; 131: 105767.

46. Hudspeth M, Li D, Spatola J, Chen W, Zheng J. The effects of off-axis transverse deflection loading on the failure strain of various high-performance fibers. Text Res J 2016; 86(9): 897-910.

47. Hazzard MK, Hallett S, Curtis PT, Iannucci L, Trask RS. Effect of fiber orientation on the low velocity impact response of thin Dyneema® composite laminates. Int J Impact Eng 2017; 100: 35-45.

48. Luo Y, Lv L, Sun B, Qiu Y, Gu B. Transverse impact behavior and energy absorption of three-dimensional orthogonal hybrid woven composites. Compos Struct 2007; 81(2): 202-209.

49. García-Castillo SK, Sánchez-Sáez S, Barbero E. Influence of areal density on the energy absorbed by thin composite plates subjected to high-velocity impacts. J Strain Anal Eng Des 2012; 47(7): 444-452.

50. Cantwell WJ, Morton J. The influence of varying projectile mass on the impact response of CFRP. Compos Struct 1989; 13(2): 101-114.

51. Lim BH, Chu JM, Claus B, Nie Y, Chen W. Critical velocity of high-performance yarn transversely impacted by razor blade. Fibers 2018; 6(4): 95.

52. Hazell PJ, Kister G, Stennett C, Bourque P, Cooper G. Normal and oblique penetration of woven CFRP laminates by a high velocity steel sphere. Compos Part A Appl Sci Manuf 2008; 39(5): 866-874.

53. Ansari MM, Chakrabarti A. Ballistic performance of unidirectional glass fiber laminated composite plate under normal and oblique impact. Procedia Eng 2017; 173: 161-168.

54. Zhikharev MV, Sapozhnikov SB, Kudryavtsev OA, Zhikharev VM. Effect of tensile preloading on the ballistic properties of GFRP. Compos B Eng 2019; 168: 524-531.

55. Lomov SV, Ivanov DS, Verpoest I, Zako M, Kurashiki T, Nakai H, Molimard J, Vautrin A. Full-field strain measurements for validation of meso-FE analysis of textile composites. Compos Part A Appl Sci Manuf 2008; 39(8): 1218-1231.

56. Key CT, Alexander CS. Numerical and experimental evaluations of a glass-epoxy composite material under high velocity oblique impacts. Int J Impact E 2020; 137: 103443.

57. Mudric T, Giacomuzzo C, Francesconi A, Galvanetto U. Experimental investigation of the ballistic response of composite panels coupled with a self-healing polymeric layer. J Aerosp Eng 2016; 29(6): 04016047.

58. Garcea SC, Wang Y, Withers PJ. X-ray computed tomography of polymer composites. Compos Sci Technol 2018; 156: 305-319.

59. Cantwell WJ, Morton J. Impact perforation of carbon fiber reinforced plastic. Compos Sci Technol 1990; 38(2): 119-141.

60. Meyer CS, Haque BZG, O'Brien DJ, Getinet N, Jian HY, Bonyi E, Aslan K, Gillespie Jr JW. Mesoscale ballistic damage mechanisms of a single-layer woven glass/epoxy composite. Int J Impact E 2018; 113: 118-131.

61. Chocron S, Nicholls AE, Brill A, Malka A, Namir T, Havazelet D, Werff HV, Heisserer U, Walker JD. Modeling unidirectional composites by bundling fibers into strips with experimental determination of shear and compression properties at high pressures. Compos Sci Technol 2014; 101: 32-40.

62. Gama BA, Gillespie Jr JW. Finite element modeling of impact, damage evolution and penetration of thick-section composites. Int J Impact E 2011; 38(4): 181-197.

63. Nilakantan G, Keefe M, Wetzel ED, Bogetti TA, Gillespie Jr JW. Computational modeling of the probabilistic impact response of flexible fabrics. Compos Struct 2011; 93(12): 3163-3174.

64. Parsons EM, Weerasooriya T, Sarva S, Socrate S. Impact of woven fabric: Experiments and mesostructure-based continuum-level simulations. J Mech Phys Solids 2010; 58(11): 1995-2021.

65. Grujicic M. Multiscale modeling of polymeric composite materials for ballistic protection. In: Advanced Fibrous Composite Materials for Ballistic Protection. Woodhead Publishing, 2016. p. 323-361.

66. Gao J, Lim BH, Zhai X, Nie Y, Kedir N, Chen W. Failure behaviors of single high-performance fibers under transverse dynamic cut. Int J Impact E 2020; 144: 103660.

67. Gao J, Guo Z, Nie Y, Hernandez J, Lim BH, Kedir N, Tallman T, Chen W. Transverse impact on a single layer S-Glass/SC15 epoxy composite strip. In: Proceedings of the American Society for Composites—Thirty-fourth technical conference. Atlanta, September, 2019.

68. Chu JM, Claus B, Parab N, O'Brien D, Sun T, Fezzaa K, Chen W. Visualization of dynamic fiber-matrix interfacial shear debonding. J Mater Sci 2018; 53(8): 5845-5859.

69. Gao J, Chu X, Henry CK, Santos SC, Palmese GR. Highly ductile glassy epoxy systems obtained by network topology modification using partially reacted substructures. Polymer 2021; 212: 123260.

70. Edwards C. Influence of material selection and fabrication process repeatability on mechanical properties of glass-polymer matrix composite structures. Clemson University, Clemson, 2011.

71. DuPont FT. Kevlar® Aramid Fiber: Technical Guide. 2012.

72. Carpenter AJ, Chocron S, Anderson Jr CE. Mesoscale modeling of S-2 glass/SC-15 epoxy composites: Plain-weave architecture. J Compos Mater 2016; 50(5): 685-700.

73. Malkina O, Mahfuz H, Sorge K, Rondinone A, Chen J, More K, Reeves S, Rangari V. Magnetic alignment of SWCNTs decorated with Fe3O4 to enhance mechanical properties of SC-15 epoxy. AIP Adv 2013; 3(4): 042104.

74. Levine S, Nie Y, Chen W. Dynamic transverse debonding of a single fiber. J Dynamic Behavior Mater 2016; 2(4): 521-531.

75. Shokrieh MM, Omidi MJ. Tension behavior of unidirectional glass/epoxy composites under different strain rates. Compos Struct 2009; 88(4): 595-601.

76. Gao J, Kirk CD, Kedir N, Paulson S, Hernandez J, Gao J, Zhai X, Wang J, Horn T, Kim G, De Carlo F, Shevchenko P, Tallman TN, Palmese GR, Sterkenburg R, Chen, W. A method for characterization of multiple dynamic constitutive parameters of FRCs. Compos Sci Technol 2021; 203: 108607.

77. Gao J, Yao W, Liu J. Temperature stress analysis for bi-modulus beam placed on Winkler foundation. Appl Math Mech 2017; 38(7): 921-934.

78. Gao J, Yao W. Thermal stress analysis for bi-modulus foundation beam under nonlinear temperature difference. Int J Comput Methods 2017; 14(01): 1750024.

79. Gao J, Yao W, Ma Y. Analytical and numerical study of graphite IG110 parts in advanced reactor under high temperature and irradiation. Nucl Eng Des 2016; 305: 421-432.

80. Voigt W. Uber die Beziehung zwischen den beiden Elastizitatskonstanten Isotroper Korper, Wied. Ann 1989; 38: 573-587.

81. Sato N, Hojo M, Nishikawa M. Intralaminar fatigue crack growth properties of conventional and interlayer toughened CFRP laminate under mode I loading, Compos Part A Appl Sci Manuf 2015; 68: 202-211.

82. Walker JD, Chocron S. Why impacted yarns break at lower speed than classical theory predicts. J Appl Mech 2011; 78(5): 051021.

83. Phoenix SL, Porwal PK. A new membrane model for the ballistic impact response and V50 performance of multi-ply fibrous systems. Int J Solids Struct 2003; 40(24): 6723-6765.

84. Hudspeth M, Jewell E, Horner S, Zheng J, Chen W. Exploration of wave development during yarn transverse impact. Fibers 2017; 5(2): 17.

85. Yu B, Karthikeyan K, Deshpande VS, Fleck NA. Perforation resistance of CFRP beams to quasi-static and ballistic loading: The role of matrix strength. Int J Impact E 2017; 108: 389-401.

86. De Ruijter C, Van Der Zwaag S, Stolze R, Dingemans TJ. Liquid crystalline matrix polymers for aramid ballistic composites. Polym Composite 2010; 31(4): 612-619.

87. Xie W, Zhang R, Headrick RJ, Taylor LW, Kooi S, Pasquali M, Müftü S, Lee JH. Dynamic strengthening of carbon nanotube fibers under extreme mechanical impulses. Nano Lett 2019; 19(6): 3519-3526.

88. Cunniff PM. An analysis of the system effects in woven fabrics under ballistic impact. Text Res J 1992; 62(9): 495-509.

89. Gama BA, Gillespie Jr JW. Punch shear based penetration model of ballistic impact of thick-section composites. Compos Struct 2008; 86(4): 356-369.

90. Montgomery, TG, Grady PL, Tomasino C. The effects of projectile geometry on the performance of ballistic fabrics. Text Res J 1982; 52(7): 442-450.

91. Tan VBC, Lim CT, Cheong CH. Perforation of high-strength fabric by projectiles of different geometry. Int J Impact Eng 2003; 28(2): 207-222.

92. Abbott NJ. The variation of the geometry of fragment simulators. SCRDE/91/5. The Ballistic Testing of Personal Armour, 1991.

93. Prosser RA. Penetration of nylon ballistic panels by fragment-simulating projectiles: Part II: mechanism of penetration. Text Res J 1988; 58(3): 161-165.

94. Lim BH, Chu JM, Chen W. Mechanical behavior of high-performance yarns transversely loaded by different indenters. Fibers 2018; 6(4): 69.

95. Elices M, Llorca J. Fiber fracture. Gulf Professional Publishing, 2002.

96. Hearle JWS. Fracture of highly oriented, chain-extended polymer fibres. In Fiber fracture (pp. 265-286). Elsevier Science Ltd, 2002.

97. Gupta, PK. Fractography of fiberglass. In Fractography of glass (pp. 185-206). Springer, Boston, MA, USA, 1994.

98. Hearle JW, Lomas B, Cooke WD. Atlas of fibre fracture and damage to textiles. Elsevier, 1998.

99. Hudspeth M, Claus B, Parab N, Lim B, Chen W, Sun T, Fezza K. In situ visual observation of fracture processes in several high-performance fibers. J Dynamic Behavior Mater 2015; 1(1): 55-64.

100. Xu Y. Stabbing resistance of soft ballistic body armour impregnated with shear thickening fluid. The University of Manchester, Manchester, 2017.

101. Nayak R, Crouch I, Kanesalingam S, Ding J, Tan P, Lee B, Miao M, Ganga D, Wang L. Body armor for stab and spike protection, Part 1: Scientific literature review. Text Res J 2018; 88: 812-832.

102. Anctil B, Keown M, Bourget C, Pageau G, Bolduc M, Shewchenko N. Threat assessment and performance evaluation of multi-threat body armour systems. Joint Applied Vehicle Technology/Human Factors & Medicine-NATO RTO Specialists, Koblenz, Germany, 2003.

103. Atanasov SE, Oldham CJ, Slusarski KA, Taggart-Scarff J, Sherman SA, Senecal K, Filocamo SF, McAllister QP, Wetzel ED, Parsons GN. Improved cut-resistance of Kevlar® using controlled interface reactions during atomic layer deposition of ultrathin (< 50 Å) inorganic coatings. J Mater Chem A Mater 2014; 2: 17371-17379.

104. Decker MJ, Halbach CJ, Nam CH, Wagner NJ, Wetzel ED. Stab resistance of shear thickening fluid (STF)-treated fabrics. Compos Sci Technol 2007; 67: 565-578.

105. Gürgen S, Kuşhan MC. The stab resistance of fabrics impregnated with shear thickening fluids including various particle size of additives. Compos Part A Appl Sci Manuf 2017; 94: 50-60.

106. Li W, Xiong D, Zhao X, Sun L, Liu J. Dynamic stab resistance of ultra-high molecular weight polyethylene fabric impregnated with shear thickening fluid. Mater Des 2016; 102: 162-167.

107. Mayo Jr JB, Wetzel ED, Hosur MV, Jeelani S. Stab and puncture characterization of thermoplastic-impregnated aramid fabrics. Int J Impact Eng 2009; 36: 1095-1105.

108. Firouzi D, Foucher DA, Bougherara H. Nylon‐coated ultra high molecular weight polyethylene fabric for enhanced penetration resistance. J Appl Polym Sci 2014; 131: 1-9.

109. Reiners P, Kyosev Y, Schacher L, Adolphe D, Küster K. Experimental investigation of the influence of wool structures on the stab resistance of woven body armor panels. Text Res J 2016; 86: 685-695.

110. Nolan G, Hainsworth SV, Rutty GN. Forces required for a knife to penetrate a variety of clothing types. J Forensic Sci 2013; 58: 372-379.

111. Scott RA(Eds.). Textiles for protection. Elsevier, 2005.

112. Shin HS, Erlich DC, Shockey DA. Test for measuring cut resistance of yarns. J Mater Sci 2003; 38: 3603-3610.

113. Shin HS, Erlich DC, Simons JW, Shockey DA. Cut resistance of high-strength yarns. Text Res J 2006; 76: 607-613.

114. Wang L, Yu K, Zhang D, Qian K. Experimental and theoretical analysis of failure mechanism of UHMWPE Yarn under transverse cut loading. J Text I 2019; 110: 289-297.

115. El Messiry M, Eloufy A, Latif, SA, Eid ES. Evaluation of cutting force of high-performance fibers' dynamic cutting behaviour. J Ind Text 2021; 1528083721990752.

116. Mayo Jr JB, Wetzel ED. Cut resistance and failure of high-performance single fibers. Text Res J 2014; 84: 1233-1246.

117. Lu L, Hou Z, Zhang F, Xie Y, Tang Y. Fracture analysis of a single polyacrylonitrile-based carbon fiber in rigid-fixing and flexible-fixing chopping processes. Text Res J 2017; 87: 1435-1444.

118. Slusarski KA, Taggart-Scarff JK, Wetzel ED. Statistical cut response of high-performance single fibers. Text Res J 2019; 89: 1658-1672.

119. Cline J, Wu V, Moy P. Assessment of the tensile properties for single fibers (No. ARL-TR-8299). US Army Research Laboratory Aberdeen Proving Ground United States, 2018.

120. Sanborn B, DiLeonardi AM, Weerasooriya T. Tensile properties of Dyneema SK76 single fibers at multiple loading rates using a direct gripping method. J Dynamic Behavior Mater 2015; 1(1): 4-14.

121. Hudspeth M, Nie X, Chen W. Dynamic failure of Dyneema SK76 single fibers under biaxial shear/tension. Polymer 2012; 53(24): 5568-5574.

122. McDaniel PB, Deitzel JM, Gillespie Jr JW. Structural hierarchy and surface morphology of highly drawn ultra high molecular weight polyethylene fibers studied by atomic force microscopy and wide angle X-ray diffraction. Polymer 2015; 69: 148-158.

123. Stockdale TA, Strawhecker KE, Sandoz-Rosado EJ, Wetzel ED. A rapid FIB-notch technique for characterizing the internal morphology of high-performance fibers. Mater Lett 2016; 176: 173-176.

124. Strawhecker KE, Sandoz-Rosado EJ, Stockdale TA, Laird ED. Interior morphology of high-performance polyethylene fibers revealed by modulus mapping. Polymer 2016; 103: 224-232.

125. Roenbeck MR, Sandoz-Rosado EJ, Cline J, Wu V, Moy P, Afshari M, Strawhecker KE. Probing the internal structures of Kevlar® fibers and their impacts on mechanical performance. Polymer 2017; 128: 200-210.

126. Arnould O, Siniscalco D, Bourmaud A, Le Duigou A, Baley C. Better insight into the nano-mechanical properties of flax fibre cell walls. Ind Crops Prod 2017; 97: 224-228.

127. Hearle JW (Ed.). High-performance fibres. Elsevier, Amsterdam, 2001.

128. Roenbeck MR, Cline J, Wu V, Afshari M, Kellner S, Martin P, Londono JD, Clinger LE, Reichert D, Lustig SR, Strawhecker KE. Structure–property relationships of aramid fibers via X-ray scattering and atomic force microscopy. J Mater Sci 2019; 54: 6668-6683.

129. Gao X. Tailored interphase structure for improved strength and energy absorption of composites. University of Delaware, Newark, 2006.

130. Chu JM, Claus B, Parab N, O'Brien D, Sun T, Fezzaa K, Chen W. Visualization of dynamic fiber-matrix interfacial shear debonding. J Mater Sci 2018; 53: 5845-5859.

131. Guo Z, Casem D, Hudspeth M, Nie X, Sun J, Chen W, 2016. Transverse compression of two high-performance ballistic fibers. Text Res J 2016; 86: 502-511.

132. Guo Z, Chen W, Zheng J. Improved quasi-static twin-fiber transverse compression of several high-performance fibers. Text Res J 2019; 89: 1595-1613.

133. Sockalingam S, Gillespie JW, Keefe M, Casem D, Weerasooriya T. Transverse compression response of ultra-high molecular weight polyethylene single fibers. J Dynamic Behavior Mater 2017; 1: 7-13.

134. Abrate S. Impact on Laminated Composite Materials. ASME. Appl Mech Rev 1991; 44(4): 155–190.

135. Gómez-del Rıo T, Zaera R, Barbero E, Navarro C. Damage in CFRPs due to low velocity impact at low temperature. Compos B Eng 2005; 36(1): 41-50.

136. Gholizadeh S. A review of non-destructive testing methods of composite materials. Procedia Struct Integr 2016; 1: 50-57.

137. Li C, Ellyin F, Wharmby A. On matrix crack saturation in composite laminates. Compos B Eng 2003; 34(5): 473-480.

138. De Carvalho NV, Pinho ST, Robinson P. An experimental study of failure initiation and propagation in 2D woven composites under compression. Compos Sci Technol 2011; 71(10): 1316-1325.

139. Hung PY, Lau KT, Cheng LK, Leng JS, Hui D. Impact response of hybrid carbon/glass fibre reinforced polymer composites designed for engineering applications. Compos B Eng 2018; 133: 86-90.

~~140.~~ Bourne NK, Parry S, Townsend D, Withers PJ, Soutis C, Frias C. Dynamic damage in carbon-fibre composites. Philos Trans A Math Phys Eng Sci 2016; 374: 20160018.

141. Kim J, Baillie C, Poh J, Mai YW. Fracture toughness of CFRP with modified epoxy resin matrices. Compos Sci Technol 1992; 43(3): 283-297.

142. Zhang L, De Greef N, Kalinka G, Van Bilzen B, Locquet JP, Verpoest I, Seo JW. Carbon nanotube-grafted carbon fiber polymer composites: damage characterization on the micro-scale. Compos B Eng 2017; 126: 202-210.

143. De Angelis G, Meo M, Almond DP, Pickering SG, Angioni SL. A new technique to detect defect size and depth in composite structures using digital shearography and unconstrained optimization. NDT E Int 2012; 45(1): 91-96.

144. Gryzagoridis J, Findeis D, Musonda V. Using digital shearography to visualize and quantify defects in composite aerospace components. In: CD-Proceedings of the 8th South African conference on computational and applied mechanics (SACAM08), Cape Town; March 2008.

145. Liu C, Rosakis AJ, Stout MG. Dynamic fracture toughness of a unidirectional graphite/epoxy composite (No. LA-UR-01-3442). In: Proceedings of the symposium on "Dynamic effects in composite structures", ASME 2001 International Mechanical Engineering Congress & Exposition, New York; November 2001.

146. Katunin A, Dragan K, Dziendzikowski M. Damage identification in aircraft composite structures: a case study using various non-destructive testing techniques. Compos Struct 2015; 127: 1-9.

147. Azadi M, Sayar H, Ghasemi-Ghalebahman A, Jafari SM. Tensile loading rate effect on mechanical properties and failure mechanisms in open-hole carbon fiber reinforced polymer composites by acoustic emission approach. Compos B Eng 2019; 158: 448-458.

148. Schroeder JA, Ahmed T, Chaudhry B, Shepard S. Non-destructive testing of structural composites and adhesively bonded composite joints: pulsed thermography. Compos Part A Appl Sci Manuf 2002; 33(11): 1511-1517.

149. Trendafilova I, Cartmell MP, Ostachowicz W. Vibration-based damage detection in an aircraft wing scaled model using principal component analysis and pattern recognition. J Sound Vib 2008; 313(3-5): 560-566.

150. Yi Q, Tian GY, Yilmaz B, Malekmohammadi H, Laureti S, Ricci M, Jasiuniene E. Evaluation of debonding in CFRP-epoxy adhesive single-lap joints using eddy current pulse-compression thermography. Compos B Eng 2019; 178: 107461.

151. Maire E, Withers PJ. Quantitative X-ray tomography. Int Mater Rev 2014; 59(1): 1-43.

152. Bull DJ, Helfen L, Sinclair I, Spearing SM, Baumbach T. A comparison of multi-scale 3D X-ray tomographic inspection techniques for assessing carbon fiber composite impact damage. Compos Sci Technol 2013; 75: 55-61.

153. Lu T, Chen X, Wang H, Zhang L, Zhou Y. Comparison of low-velocity impact damage in thermoplastic and thermoset composites by non-destructive three-dimensional X-ray microscope. Polym Test 2020; 91: 106730.

154. Leonard F, Stein J, Soutis C, Withers PJ. The quantification of impact damage distribution in composite laminates by analysis of X-ray computed tomograms. Compos Sci Technol 2017; 152: 139-148.

155. Li Y, Sun B, Gu B. Impact shear damage characterizations of 3D braided composite with X-ray micro-computed tomography and numerical methodologies. Compos Struct 2017; 176: 43-54.

156. Zhou H, Li C, Zhang L, Crawford B, Milani AS, Ko FK. Micro-XCT analysis of damage mechanisms in 3D circular braided composite tubes under transverse impact. Compos Sci Technol 2018; 155: 91-99.

157. Scott AE, Mavrogordato M, Wright P, Sinclair I, Spearing SM. In situ fiber fracture measurement in carbon–epoxy laminates using high resolution computed tomography. Compos Sci Technol 2011; 71(12): 1471-1477.

158. Hu X, Wang L, Xu F, Xiao T, Zhang Z. In situ observations of fractures in short carbon fiber/epoxy composites. Carbon 2014; 67: 368-376.

159. Mazars V, Caty O, Couégnat G, Bouterf A, Roux S, Denneulin S, Pailhès J, Vignoles GL. Damage investigation and modeling of 3D woven ceramic matrix composites from X-ray tomography in-situ tensile tests. Acta Mater 2017; 140: 130-139.

160. Garcea SC, Sinclair I, Spearing SM, Withers PJ. Mapping fibre failure in situ in carbon fibre reinforced polymers by fast synchrotron X-ray computed tomography. Compos Sci Technol 2017; 149: 81-89.

161. Garcea SC, Mavrogordato MN, Scott AE, Sinclair I, Spearing SM. Fatigue micromechanism characterisation in carbon fibre reinforced polymers using synchrotron radiation computed tomography. Compos Sci Technol 2014; 99: 23-30.

162. Beier U, Fischer F, Sandler JKW, Altstädt V, Weimer C, Buchs W. Mechanical performance of carbon fibre-reinforced composites based on stitched preforms. Compos Part A Appl Sci Manuf 2007; 38(7): 1655-1663.

163. Hong H, Mingxing Z, Fangueiro R, De Araujo M. Mechanical properties of composite materials made of 3D stitched woven-knitted preforms, J Compos Mater 2010; 44(14): 1753-1767.

164. Gao J, Guo Z, Nie Y, Hernandez J, Lim BH, Kedir N, Tallman T, Chen W. Transverse impact on a single layer S-Glass/SC15 epoxy composite strip. In Proceedings of the American Society for Composites—Thirty-fourth technical conference, Atlanta; September 2019.

165. ASTM D 5045-14. Standard test methods for plane-strain fracture toughness and strain energy release rate of plastic materials. ASTM International, West Conshohocken, PA, 2007.

166. Compston P, Jar PY, Davies P. Matrix effect on the static and dynamic interlaminar fracture toughness of glass-fibeR marine composites. Compos B Eng 1998; 29(4): 505-516.

167. Kim KY, Ye L. Interlaminar fracture toughness of CF/PEI composites at elevated temperatures: roles of matrix toughness and fibre/matrix adhesion. Compos Part A Appl Sci Manuf 2004; 35(4): 477-487.

168. Chen WW, Song B. Split Hopkinson (Kolsky) bar: design, testing and applications. Springer Science & Business Media, 2010.

169. Zhai X, Gao J, Nie Y, Guo Z, Kedir N, Claus B, Sun T, Fezzaa K, Xiao X, Chen WW. Real-time visualization of dynamic fractures in porcine bones and the loading-rate effect on their fracture toughness. J Mech Phys Solids 2019; 131: 358-371.

170. Zhai X, Guo Z, Gao J, Kedir N, Nie Y, Claus B, Sun T, Xiao X, Fezzaa K, Chen WW. High-speed X-ray visualization of dynamic crack initiation and propagation in bone. Acta Biomater 2019; 90: 278-286.

171. Chen WW, Hudspeth MC, Claus B, Parab ND, Black JT, Fezzaa K, Luo SN. In-site damage assessment using synchrotron X-rays in materials loaded by a Hopkinson bar. Trans A Math Phys Eng Sci 2014; 372: 20130191.

172. Budiansky B, Fleck NA. Compressive kinking of fiber composites: A topical review. Appl Mech Rev 1994; 47(6): S246-S250.

173. Hunston DL, Moulton RJ, Johnston NJ, Bascom W. Matrix resin effects in composite delamination: mode I fracture aspects. In Toughened composites. ASTM International; 1987.

174. Magida MM. Study of structural and thermal properties of electron beam irradiated polymethylmethacrylate/bisphenol- A- polycarbonate blends. J Appl Polym Sci 2012; 125(4): 3184-3190.

175. Nathawat R, Kumar A, Kulshrestha V, Vijay YK, Kobayashi T, Kanjilal D. Study of surface activation of PET by low energy (keV) Ni+ and N+ ion implantation. Nuclear Instruments and Methods in Physics Research Section B: Beam Interactions with Materials and Atoms, 2008; 266(21): 4749-4756.

176. Nouh SA, El-Nabarawy HA, Abutalib MM, Bahareth RA. Effect of X-ray irradiation on the structure, thermal and mechanical properties of polyester. Eur Phys J Appl Phys 2013; 62(3): 30201.

PUBLICATIONS AND PRESENTATIONS

Journal Articles

First-author journal articles

[1] **Gao J**, Kirk C, Kedir N, Fezzaa F, Chen W. Transverse impact on a single fiber. 2021, experiments in preparation.

[2] **Gao J**, Kedir N, Kirk C, Fezzaa K, Chen W. Microscale perforation mechanism of Kevlar® KM2 Plus yarns. 2021, experiments in preparation.

[3] **Gao J**, Kedir N, Kirk C, Hernandez J, Zhou F, Tsai JT, Fezzaa K, Shevchenko PD, Tallman TN, Jun MBG, Chen W. Visualizing the failure processes of GFRC strips by integrating reverse impact technique and high-speed synchrotron X-ray phase-contrast imaging. 2021, experiments in preparation.

[4] **Gao J**, Lim BH, Nie Y, Kedir N, Zhai X, Chen W. Increased energy dissipation of several organic high-performance fibers under transverse indentation due to inelastic deformation. 2021, manuscript in preparation.

[5] **Gao J**, Chu JM, Hudspeth M, Sun T, Fezzaa K, Chen W. Multiscale dynamic experiments on fiber-reinforced composites with damage assessment using high-speed synchrotron X-ray phase-contrast imaging. *Composites Part B: Engineering* 2021; Special Issue, *invited paper.*

[6] **Gao J**, Kedir N, Chen W. Characterization of failure of single carbon nanotube fibers under extreme transverse loading. *Journal of the Mechanics and Physics of Solids* 2021; under review.

[7] **Gao J**, Kedir N, Kirk C, Hernandez J, Wang J, Paulson S, Zhai X, Horn T, Kim G, Fezzaa K, De Carlo F, Shevchenko PD, Tallman TN, Sterkenburg R, Chen W. High-speed synchrotron X-ray phase-contrast imaging for evaluating microscale damage mechanisms and tracking cracking behaviors inside cross-ply GFRCs. *Composites Science and Technology* 2021; 210: 108814.

[8] **Gao J**, Guo Z, Hernandez J, Zhou F, Nie Y, Gao J, Lim BH, Kedir N, Zhai X, Wang J, Tsai JT, De Carlo F, Shevchenko PD, Tallman TN, Jun MBG, Palmese GR, Chen W. Transverse impact by RCCs on S-Glass and Kevlar® FRC strips. *Composites Part A: Applied Science and Manufacturing* 2021; 146: 106425.

[9] **Gao J**, Kedir N, Kirk C, Hernandez J, Wang J, Paulson S, Zhai X, Horn T, Kim G, Gao J, Fezzaa K, De Carlo F, Shevchenko P, Tallman TN, Sterkenburg R, Palmese GR, Chen W. Real-time damage characterization for GFRCs using high-speed synchrotron X-ray phase-contrast imaging. *Composites Part B: Engineering* 2021; 207: 108565.

[10] **Gao J**, Kirk C, Kedir N, Paulson S, Hernandez J, Gao J, Zhai X, Wang J, Horn T, Kim G, De Carlo F, Shevchenko PD, Tallman TN, Palmese GR, Sterkenburg R, Chen W. A method for characterization of multiple dynamic constitutive parameters of FRCs. *Composites Science and Technology* 2021; 203: 108607.

[11] **Gao J**, Lim BH, Zhai X, Nie Y, Kedir N, Chen W. Failure behaviors of single high-performance fibers under transverse dynamic cut. *International Journal of Impact Engineering* 2020; 144: 103660.

[12] **Gao J**, Nie Y, Lim BH, Zhai X, Kedir N, Chen W. In-situ observation of cutting-induced failure processes of single high-performance fibers inside a SEM. *Composites Part A: Applied Science and Manufacturing* 2020; 131: 105767.

[13] **Gao J**, Nie Y, Lim BH, Kedir N, Chen W. A microscopic experimental method transversely loading on single high-performance fibers. *Experimental Mechanics* 2019; 59(5): 669-679.

Co-author journal articles

[14] Ellyson B, Fezzaa K, Sun T, Parab N, Finfrock C, Rietema C, Smith D, Copley J, Johnson C, Becker C, Klemm-Toole J, Kirk C, Kedir N, **Gao J**, Chen W, Banerjee R, Clarke K, Clarke A. In-situ imaging and diffraction of TRIP/TWIP Ti-Mo alloys during high strain rate deformation. 2021, manuscript in preparation.

[15] Zhang X, **Gao J**, O'Brien D, Chen W, Ghosh S. Parametrically homogenized continuum damage mechanics (PHCDM) models for analyzing composite structures. *Composites Science and Technology* 2021; under review.

[16] Kedir N, Hernandez J, Lim BH, **Gao J**, Zhai X, Nie Y, Tallman TN, Chen W. (2021). Time-dependent response of carbon fiber reinforced plastic (CFRP) to irradiation by a short pulse near-infrared (NIR) laser. *Journal of Laser Applications* 2021; under review.

[17] Tadevich JT, Bhagat ND, Lim BH, **Gao J**, Chen W, Merrell GA. Power-optimizing repair distal biceps rupture: stronger and safer. *Journal of Hand Surgery* 2021; under review.

[18] Copley JA, Ellyson B, Klemm-Toole J, **Gao J**, Kedir N, Kirk C, Chen W, Parab N, Sun T, Fezzaa K, Clarke K, Clarke AJ. HiSPoD as a preparatory tool for improving design of high-rate, time-resolved synchrotron x-ray diffraction experiments. *Journal of Synchrotron Radiation* 2021, accepted.

[19] Kedir N, Garcia E, Kirk C, **Gao J**, Guo Z, Zhai X, Sun T, Fezzaa K, Sampath S, Chen W. Impact damage of narrow silicon carbide (SiC) ceramics with and without environmental barrier coatings (EBCs) by various foreign object debris (FOD) simulants. *Surface and Coatings Technology* 2021; 407: 126779.

[20] Kedir N, Garcia E, Kirk C, Guo Z, **Gao J**, Zhai X, Sun T, Fezzaa K, Sampath S, Chen W. In situ characterization of foreign object damage (FOD) in environmental-barrier-coated silicon carbide (SiC) ceramic. *Journal of the American Ceramic Society* 2020; 103(8): 4586-4601.

[21] Chen D, Narayanan N, Federici E, Yang Z, Zuo X, **Gao J,** Fang F, Deng M, Campanella OH, Jones OG. Electrospinning Induced Orientation of Protein Fibrils. *Biomacromolecules* 2020; 21(7): 2772-2785.

[22] Zhai X, Nie Y, **Gao J,** Kedir N, Claus B, Sun T, Fezzaa K, Chen W. The effect of loading direction on the fracture behaviors of cortical bone at a dynamic loading rate. *Journal of the Mechanics and Physics of Solids* 2020; 142: 104015.

[23] Nie Y, Claus B, **Gao J**, Zhai X, Kedir N, Chu J, Sun T, Fezzaa K, Chen W. In Situ observation of adiabatic shear band formation in aluminum alloys. *Experimental Mechanics* 2020; 60(2): 153-163.

[24] Zhai X, **Gao J**, Nie Y, Guo Z, Kedir N, Claus B, Sun T, Fezzaa K, Xiao X, Chen W. Real-time visualization of dynamic fractures in porcine bones and the loading-rate effect on their fracture toughness. *Journal of the Mechanics and Physics of Solids* 2019; 131: 358-371.

[25] Zhai X, **Gao J**, Liao H, Kirk C, Balogun YA, Chen W. Mechanical behaviors of auxetic polyurethane foam at quasi-static, intermediate and high strain rates. *International Journal of Impact Engineering* 2019; 129: 112-118.

[26] Zhai X, Guo Z, **Gao J**, Kedir N, Nie Y, Claus B, Sun T, Xiao X, Fezzaa K, Chen W. High-speed X-ray visualization of dynamic crack initiation and propagation in bone. *Acta Biomaterialia* 2019; 90: 278-286.

[27] Lim BH, Chu JM, **Gao J**, Claus B, Nie Y, Chen W. The effect of projectile nose shape on the critical velocity of high-performance yarn. *Fibers* 2019; 7(4): 29.

Conference Proceedings

[1] **Gao J**, Kedir N, Kirk C, Hernandez J, Zhai X, Wang J, Tallman TN, Fezzaa K, Chen W. Real-Time Visualization of Damage Progression Inside GFRP Composites via High-Speed X-Ray PCI Technique. *Proceedings of the Society for Experimental Mechanics 14th International Congress*, Orlando, Florida, USA, digital forum, Sep 14-17, 2020.

[2] **Gao J**, Kedir N, Kirk C, Hernandez J, Wang J, Zhai X, Horn T, Kim G, Fezzaa K, De Carlo F, Shevchenko PD, Tallman TN, Sterkenburg R, Chen W. In-situ Observation of Dynamic Damage Evolution Inside GFRCs Through High-Speed X-ray PCI. *Proceedings of the American Society for Composites—Thirty-fifth Technical Conference*, Hoboken, New Jersey, USA, digital forum, Sep 23-24, 2020.

[3] **Gao J**, Guo Z, Nie Y, Hernandez J, Lim BH, Kedir N, Tallman TN, Chen W. Transverse Impact on a Single Layer S-Glass/SC15 Epoxy Composite Strip, *Proceedings of the American Society for Composites—Thirty-fourth Technical Conference*, Atlanta, Georgia, USA, Sep 23-25, 2019.

Conference Abstracts

[1] **Gao J**, Kedir N, Hernandez JA, Tallman TN, Chen W. Projectile nose effect on failure of fiber-reinforced composite strips characterized by reverse impact technique. *Mach Conference*, digital forum, Apr 7-9, 2021.

[2] Clarke A, Coury F, Copley J, Guo Y, Klemm-Toole J, Ellyson B, **Gao J**, Gus Becker C, Milligan B, Finfrock C, Johnson C, Clarke K, Chen W, Parab N, Sun T, Fezzaa K, Kaufman M. Non-Equiatomic, Multi-Phase TRIP/TWIP Multi-Principal Element Alloys. *The Minerals, Metals & Materials Society Annual Meeting & Exhibition*, San Diego, California, USA, Feb 23-27, 2020.

[3] Clarke A, Ellyson B, Copley J, Coury F, Klemm-Toole J, Guo Y, **Gao J**, Gus Becker C, Milligan B, Finfrock C, Johnson C, Clarke K, Chen W, Parab N, Sun T, Fezzaa K. TRIP/TWIP of Structural Metallic Alloys for Performance in Extreme Environments. *The Minerals, Metals & Materials Society Annual Meeting & Exhibition*, San Diego, California, USA, Feb 23-27, 2020.

[4] Copley J, Coury F, Klemm-Toole J, **Gao J**, Guo Y, Clarke K, Ellyson B, Becker C, Milligan B, Frinfrock C, Johnson C, Parab N, Fezzaa K, Sun T, Chen W, Clarke A. Toughness Enhancing Deformation Mechanisms in the CoCrNi Family of MPEAs. *1st World Congress on High Entropy Alloys*, Seattle, Washington, USA, Nov 11-20, 2019.

[5] Chen W, Hudspeth M, Guo Z, Lim BH, **Gao J**. Experimental studies on impact failure of soft body armors at micro to macro size scales. Abstracts of Papers of *the American Chemical Society*, Vol 257, Washington, DC, USA, 2019.

[6] Chu JM, Claus B, Lim BH, **Gao J**, O'Brien D, Sun T, Fezzaa K, Chen W. Interfacial failure mechanisms of different single FRPC under transverse tensile loading. *Mach Conference*, Annapolis, Maryland, USA, Apr 3-5, 2019.

Posters

[1] **Gao J**, Gao J, Zhang X, Meyer C, O'Brien D, Haque B, Palmese G, Ghosh S, Gillespie JW, Chen W. Real-time damage visualization in composites. *Materials in Extreme Dynamic Environments Collaborative Research Alliance (MEDE CRA) Fall Meeting*, digital forum, Oct 15, 2020.

[2] **Gao J**, Gao J, Palmese G, Chen W. Real-time damage visualization in composites under transverse impact. *Enterprise for Multiscale Research of Materials (EMRM) Research Management Board (RMB)*, Baltimore, Maryland, USA, Jan 14, 2020.

[3] **Gao J**, Gao J, Palmese G, Chen W. Transverse impact on FRP composite strips. *Materials in Extreme Dynamic Environments (MEDE) Fall Meeting*, Baltimore, Maryland, USA, Oct 17, 2019.

Conference Presentations

[1] **Gao J**, Gao J, Zhang X, O'Brien D, Meyer C, Palmese G, Ghosh S, Chen W. Multiscale dynamic experiments on glass fiber reinforced composites. *Composites CMRG Teleconference*, Oral Presentation, digital forum, May 25, 2021.

[2] **Gao J**, Kedir N, Hernandez J, Tallman TN, Chen W. Projectile nose effect on failure of fiber-reinforced composite strips characterized by reverse impact technique. *Mach Conference*, Oral Presentation, digital forum, April 7, 2021.

[3] **Gao J**, Kedir N, Kirk C, Wang J, Paulson S, Zhai X, Hernandez J, Horn T, Kim G, Sterkenburg R, Gao J, Fezzaa K, De Carlo F, Shevchenko PD, Tallman TN, Palmese G, Chen W. In-situ observation of dynamic damage evolution inside GFRCs through high-speed X-ray PCI. *The American Society for Composites—Thirty-fifth Technical Conference*, Oral Presentation, digital forum, Sep 14, 2020.

[4] **Gao J**, Gao J, Zhang X, O'Brien D, Meyer C, Haque B, Palmese G, Ghosh S, Gillespie Jr JW, Chen W. Real-time damage visualization in composites. *Materials in Extreme Dynamic Environments (MEDE) Fall Meeting*, Oral Presentation, digital forum, Oct 15, 2020.

[5] **Gao J**, Gao J, Zhang X, O'Brien D, Meyer C, Haque B, Palmese G, Ghosh S, Gillespie JW, Chen W. Real-time visualization in glass fiber reinforced composites. *Composites CMRG Summer Meeting*, Oral Presentation, digital forum, Aug 11, 2020.

[6] **Gao J**, Kedir N, Kirk C, Wang J, Paulson S, Zhai X, Hernandez J, Horn T, Kim G, Gao J, Fezzaa K, De Carlo F, Shevchenko PD, Tallman TN, Sterkenburg R, Palmese G, Chen W. Real-time visualization of dynamic fractures in GFRC by high-speed synchrotron X-ray PCI. *The Society for Experimental Mechanics 14th International Congress*, Oral Presentation, digital forum, Aug 15, 2020.

[7] **Gao J**, Gao J, Zhang X, Xiao Y, O'Brien D, Meyer C, Palmese G, Ghosh S, Chen W. Real-time visualization of dynamic fractures in GFRP by high-speed synchrotron X-ray PCI. *Composites CMRG Teleconference*, Oral Presentation, digital forum, May 12, 2020.

[8] **Gao J**, Guo Z, Nie Y, Hernandez J, Lim BH, Kedir N, Gao J, Palmese G, Chen W. Transverse impact on unidirectional fiber-reinforced polymer composite strips. *The American Society for Composites—Thirty-fourth Technical Conference*, Oral Presentation, Atlanta, Georgia, USA, Sep 23, 2019.

[9] **Gao J**, Gao J, Palmese G, Chen W. Transverse impact on FRP composite strips. *Materials in Extreme Dynamic Environments (MEDE) Fall Meeting*, Oral Presentation, Baltimore, Maryland, USA, Oct 17, 2019.

[10] **Gao J**, Levine SE, Chu J, Gao J, Palmese G, Chen W. Multi-scale real-time damage visualization in composites. *Composites CMRG Summer Meeting*, Oral Presentation, Newark, Delaware, USA, Aug 2, 2019.

[11] **Gao J**, Levine SE, Chu J, Gao J, Palmese G, Chen W. Multi-scale real-time damage visualization in composites. *Composites CMRG Teleconference*, Oral Presentation, digital forum, Jul 9, 2019.

[12] **Gao J**, Chen W. Real-time visualization of failure behaviors of single high-performance fibers. *Purdue University School of Materials Engineering 7th Annual Soft Materials Summer Research Symposium*, Oral Presentation, West Lafayette, Indiana, USA, Jun 25, 2019.

[13] **Gao J**, Chu JM, O'Brien D, Chen W. Interfacial failure mechanisms of different single FRPC under transverse tensile loading. *Mach Conference*, Oral Presentation, Annapolis, Maryland, USA, Apr 4, 2019.